FLUID FLOW INDUCED BY OSCILLATING BODIES AND FLOWS IN CYCLONES

By

Baoshe Yan

Submitted in accordance with the requirements for

the degree of Doctor of Philosophy

The University of Leeds

Department of Applied Mathematical Studies

November 1991

Abstract

In this thesis the following aspects have been investigated: (i) the numerical solutions for unsteady 2-dimensional, incompressible viscous fluid flows induced by a harmonically oscillating cascade, and (ii) the fluid flows in industrial cyclones and their separation efficiencies. In the first part of the thesis we deal with fluid flows induced by harmonically oscillating cascades of cylinders with different cross sectional shapes. Numerical solutions for large amplitude oscillations of a cascade of normal flat plates are obtained by using a finite-difference method and it is found that solutions are in good agreement with some related experimental results. For small amplitude oscillations a perturbation method, series truncation technique and finite-difference methods are used to obtain solutions for cascades of normal flat plates and square cylinders. By assuming that the streaming Reynolds number is O(1) then the outer streaming flows for cascades of square cylinders, normal flat plates and circular cylinders are investigated numerically for the streaming Reynolds number R_s up to 70. Conformal mapping, grid generation and boundary element methods are used to deal with the different geometries in order to determine the outer potential flows. For small values of the streaming Reynolds number it is found experimentally that the flow remains symmetrical and the numerically predicted fluid flow is in good agreement with the experimental results. As the value of the streaming Reynolds number increases then it is found experimentally that the flow develops asymmetries and this occurs when $8 \lesssim R_s \lesssim 9$, and the numerically predicted results are also in good agreement with

the experimental data. A stability analysis is presented for the outer streaming flow for the cascade of circular cylinders which reveals the reasons for the break-down in the symmetry.

In the second part of the thesis the fluid flow in industrial cyclones has been investigated numerically. The influence of various aspects of the design parameters of the cyclone have been studied numerically and some important factors which affect the separation efficiency of the cyclone are identified. Numerical results are also compared with some existing experimental data and there is good agreement. Correlations for both the loss factor and d_{50}, the 50% cut-off particle diameter, with other parameters and operating conditions of the cyclone performance have been developed using a regression method with the existing experimental results. Finally, the separation efficiency of a small personal cyclone (10mm in diameter) is also investigated.

Acknowledgements

I am truly indebted to Professor D. B. Ingham for his enthusiastic help and supervision throughout my studies for a Ph.D. Further, I would also like to thank Professor B. R. Morton, for his constant encouragement and for providing the experimental results used in this thesis, Drs. M. I. G. Bloor, M. D. Savage, T. Tang and X. Wen and Mr. Y. Yuan for all their help during my studies. I gratefully acknowledge the Chinese government, the Health and Safety Executive and the Overseas Research Students Scholarship Committee for their financial supports of this research.

Part of the work in chapter 2 of this thesis was presented at the 6th International Conference on Numerical Methods in Laminar and Turbulent Flow, Swansea, July 1989 (Ingham and Yan (1989)) and part of the work in chapter 2 has now been accepted for publication in Computer and Fluids (Ingham *et al.* (1990b)). The work in chapter 3 has been accepted for publication in Acta Mechanica (Ingham and Yan (1991)) and part of the work in chapter 5 was presented at the 6th International Conference on Numerical Methods in Laminar and Turbulent Flow, Stanford, U.S.A., July 1991 (Yan and Ingham (1991)). Part of the work presented in chapter 5 has been submitted to Journal of Fluids Mechanics (Yan *et al.* (1991)) and the work in chapter 6 was presented at the 4th Annual Conference of the Aerosol Society, University of Surrey, U.K., April 1990 (Yan *et al.* (1990)).

Contents

Nomenclature for Section 1:

a: amplitude of the oscillation of the cascade,

b: angular frequency of the oscillation,

d: typical size of the body (=diameter for a circular bar or the length of a side of a square bar or the length of a normal flat,

h: mesh size for space variable,

$\mathcal{L}$: half distance between two successive cylinders (see Figs.1.5-1.7),

L: $=\mathcal{L}/d$,

R_e: Reynolds number, $=abd/\nu$,

R_b: frequency Reynolds number, $=bd^2/\nu$,

R_s: streaming Reynolds number, $=a^2b/\nu$,

t^*: time,

t: non-dimensional time, $=bt^*$,

U_∞: typical velocity, $=ab$,

U_P: potential flow speed at the outer edge of the boundary-layer,

(u, v): velocities in the x and y directions, respectively,

(x^*, y^*): dimensional coordinate system,

(x, y): non-dimensional coordinate system fixed in space,

(X, Y): non-dimensional coordinate system fixed in space,

(α, η): coordinate system in the computational domain,

x_L: left limit of solution domain in the (x, y) plane,

x_R: right limit of the solution domain in the (x, y) plane,

X_L: left limit of solution domain in the (X, Y) plane,

X_R: right limit of solution domain in the (X, Y) plane,

Greek:

ϕ: perturbation function to the O(ε) steady streamfunction,

ψ: streamfunction in the (x, y) plane,

Ψ: streamfunction in the (X, Y) plane,

Ψ_0: O(1) streamfunction,

$\Psi^{(s)}$: O(ε) steady streamfunction,

$\Psi_{1i}^{(u)}$: i=1, 2, O(ε) unsteady streamfunction, respectively,

Ψ_2, Ψ_3: $O(\varepsilon^2)$, $O(\varepsilon^3)$ streamfunctions,

ω: vorticity,

ω_0: O(1) vorticity,

$\omega^{(s)}$: O(ε) steady vorticity,

ε: =a/d,

τ: mesh size for time,

ν kinematic viscosity of the fluid,

δ_u thickness of the unsteady boundary-layer.

Nomenclature for Section 2:

Latin

C: angular momentum of the flow at the cyclone entry,

d_{50}: the particle diameter for which fifty percent separation efficiency is achieved, i.e. the 50% cut size,

D_i: inlet diameter of cyclone,

E_m: separation efficiency of cyclone (main flow),

E_b: separation efficiency in the top boundary-layer,

E_o: overall efficiency of cyclone,

h_0: length of the cylindrical portion of cyclone,

h_1: length of the vortex finder,

Le: overflow leakage, $=Q_L/Q$, or $=Q_{Lv}/Q$,

Q: total flux of fluid through cyclone,

Q'_L: meridional flux of fluid through the top boundary-layer,

Q_L: leakage of fluid through the top boundary-layer,

Q_{Lv}: leakage of fluid through the top boundary-layer between the equilibrium point for a particle with size d and the top wall,

Q_s: flux of fluid through main flow,

R, z, λ: cylindrical coordinate system,

R_1: a variable in R-direction determined by ensuring ψ=1 joins with vortex finder tangentially,

R_c: radius of the cylindrical portion of the cyclone,

R_E: a variable in the R-direction which varies within (R_1, R_c)

R_o: radius of the overflow,

R_f: ratio of the flux of fluid through the underflow to the total flux of fluid through the cyclone,

R_{in}: inlet Reynolds number, $=D_i W_o/\nu$,

R_u: radius of the underflow tube,

S_{QL}: a scale for the flux of fluid in the boundary-layer at top wall of the cyclone,

t_{Rz}: $=R_c/Z_c$,

T_v: thickness of the vortex finder,

u, v, w: velocity components in R, z, λ directions, respectively,

U: main flow velocity component in the R-direction at the outer edge of the top boundary-layer,

U_{sc}: $= Q/(2\pi R_c Z_c)$, scale for velocity u,

V_{sc}: $= Q/(2\pi R_c^2)$, scale for velocity v,

W_{sc}: $= W_0$, scale for velocity w,

V_0: vertical velocity at annulus entry of the cyclone,

W: main flow spin velocity at the outer edge of the top

boundary-layer,

W_0: average spin velocity at the entry to the cyclone,

Z_c: length of the conical portion of the cyclone,

Greek:

α: equivalent loss factor,

α^*: full angle of the conical portion of cyclone,

μ: coefficient of viscosity of the fluid,

ν: kinematic viscosity of the fluid,

η: a boundary-layer variable which measures the distance normal to the top wall of the cyclone,

η_0: a constant value such that $0<\eta_0<1$ which satisfies $f(\eta)=0$ (see equations (8.5.4),

η_d: an equilibrium point which satisfies equation (8.5.12),

ρ: density of the fluid,

ρ_p: density of the particle,

ψ: streamfunction,

δ: thickness of the boundary-layer on the top wall of cyclone,

Subscripts:

i: inlet conditions,

k: values used by Kelsall (1952).

List of Figures

List of Tables

CHAPTER 1 GENERAL INTRODUCTION

1.1 Oscillatory Flows

The problem of fluid flow induced by a harmonically oscillating cylinder (or cylinders) has for a long time received much attention, theoretically, experimentally and numerically. The early theoretical and experimental work was mainly performed when there is only one oscillating body and usually this has been a circular cylinder. Typically, the problem investigated is that of the two-dimensional fluid flow induced by a cylinder (or cylinders), with a typical dimension d and of infinite length, which oscillates harmonically in the direction which is perpendicular to the axis of the cylinder in an incompressible, viscous fluid which is otherwise at rest. The x^*-component of the displacement $s(t^*)$ of the oscillation may be written as a function of time t^* as

$$s(t^*)=a \sin(bt^*) \qquad (1.1.1)$$

where a and b are the amplitude and angular frequency of the oscillation, respectively.

It has been identified, see for example Riley (1967), that the flow induced by the harmonic oscillation can be characterized by the following parameters, namely

(i) R_e, the Reynolds number with the length scale based on the typical size of the body, d, and the maximum speed of the

oscillation, U_∞=ab, i.e. R_e=abd/ν, where ν is the coefficient of kinematic viscosity of the fluid.

(ii) R_b, the Reynolds number with the length scale based on the typical size of the body and the speed on the frequency of the oscillation b, i.e. $R_b=bd^2/\nu$,

(iii) ε, the ratio of the amplitude of the oscillations, a, to the typical size of the body, d, i.e. ε=a/d,

(iv) R_s, the streaming Reynolds number with the length scale based on the amplitude of the oscillation and the speed on the maximum speed of oscillation, i.e. $R_s=a^2b/\nu$,

It should be noted that only two of the above parameters are independent, for example if R_e and R_b are taken to be the two independent parameters then ε and R_s can be expressed as follows

$$\varepsilon = R_e/R_b \qquad R_s = R_e^2/R_b \qquad (1.1.2)$$

Experimentally, the first report of the presence of an induced steady circulation over vibrating plates was due to Faraday (1831) and then further observations of induced steady motion in a tube was made by Dvorak (1874). Typically, the fluid flow induced by a harmonically oscillating body with a small value of the parameter ε consists of two components, namely an unsteady velocity component which is periodic in time, t^*, and a steady component of the flow. This steady component of the flow is usually referred to as 'streaming flow' or 'steady streaming' or 'secondary flow'. It is this streaming flow which has interested scientists for more than a hundred years. In order to illustrate the streaming flow phenomena **Fig.1.1** shows a photograph, taken by Tatsuno, of the streaming flow induced by a harmonically oscillating circular cylinder in an

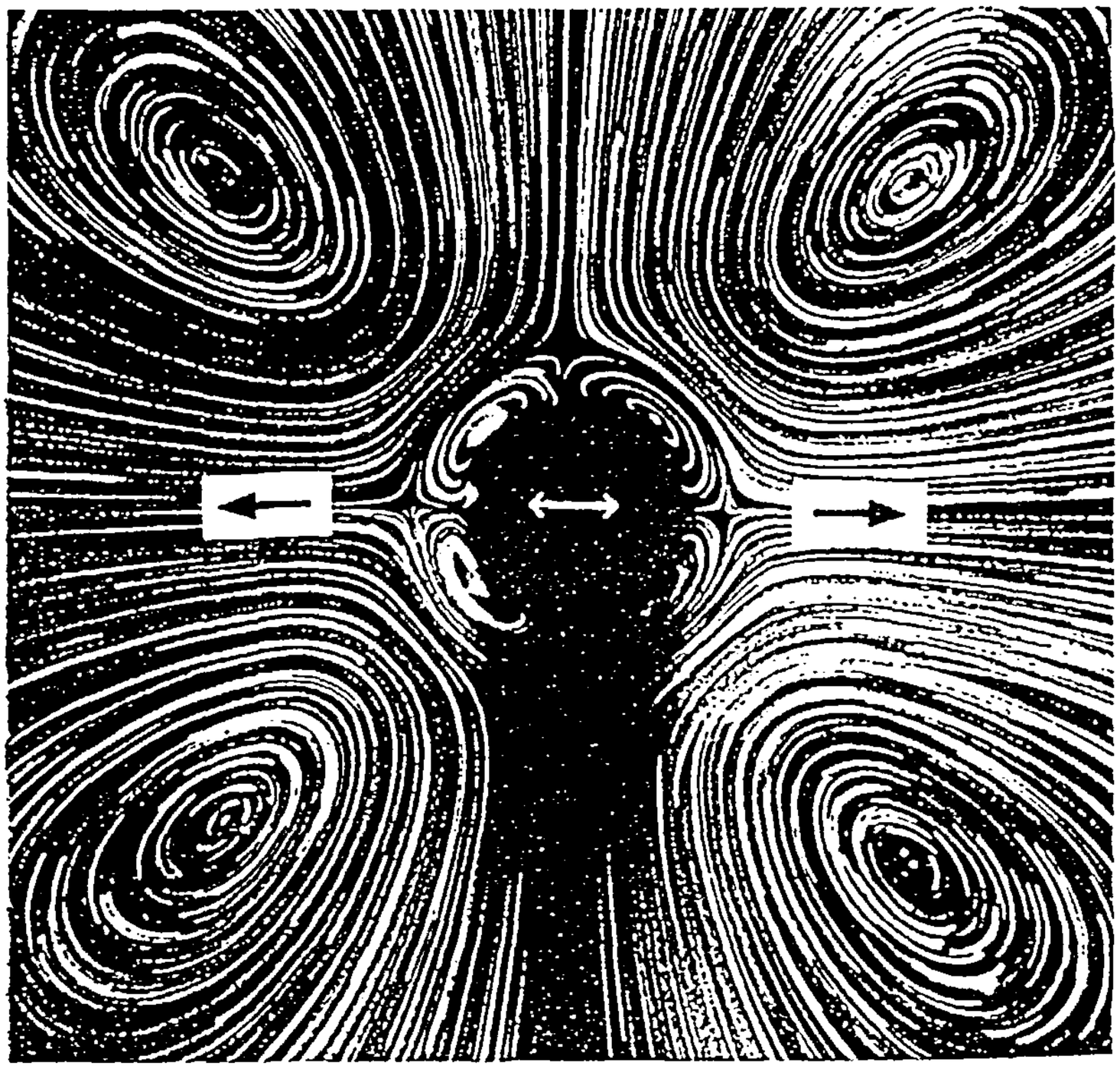

Fig.1.1 Streaming flow patterns around a harmonically oscillating circular cylinder.

incompressible viscous fluid which is otherwise at rest, the ⟷ indicates the direction of the oscillation and the direction of the streaming flow is also shown on the picture. After the work of Faraday and Dvorak, both hydrodynamicists and acousticists have investigated streaming flows in various flow regimes which depend on the parameters R_e, R_b, R_s and ε. Numerous experimental work has been reported in the cases when $\varepsilon \ll 1$ for various values of the parameter R_b, see for example Carrière (1929), Andrade (1931), Schlichting (1932), Holtsmark *et al.* (1954), Tatsuno (1973, 1974, 1980), Bertelsen (1974) and Kim and Troesch (1989).

Almost all the early experimental investigations were performed

with $\varepsilon \ll 1$ and when the oscillating body is a long circular cylinder but quite different results were obtained for different values of R_b. For the induced streaming flow Carrière (1929) showed that when R_b is small then the direction of the streaming flow was towards the body along the axis of oscillation at an O(1) distance from the body whilst when R_b is large then the experimental results of Andrade (1931), Schlichting (1932) and Holtsmark *et al.* (1954) showed the streaming flow in the opposite direction. An explanation of these controversial sets of experimental results has long been established and we will return to this later.

Theoretically, using the boundary-layer technique Schlichting (1932) investigated the non-linear effects of periodic oscillating flows in the case when $\varepsilon \ll 1$, $R_b \gg 1$ and $R_s \ll 1$. He studied the fluid flow induced by an oscillating circular cylinder in a fluid at rest when $R_s \ll 1$ whilst his experimental results were for $R_s \gg 1$. It can be shown, see for example Schlichting (1932), that the potential velocity at the outer edge of the boundary-layer, due to a body performing harmonic oscillations as described in equation (1.1.1), may be found in the form

$$U(x', t^*) = U_p(x')\cos(bt^*), \qquad (1.1.3)$$

where U_p is the potential flow velocity at the outer edge of the boundary-layer. Standard boundary-layer techniques then result in the following well-known first-order Stokes solution in the boundary-layer,

$$u_1' = U_p[\cos(bt^*) - e^{-\eta}\cos(bt^*-\eta)] \qquad (1.1.4)$$

where $\eta = y'(b/2\nu)^{1/2}$, x' and y' are independent variables along and

normal to the surface of the oscillating body, respectively, and u' (and later v') are the velocity components along (and normal to) the surface of the body.

It can also be shown that the second-order term for the velocity contains two components, i.e. both a steady and an unsteady part. The unsteady component contains terms of the form $\cos(2bt^*)$ and $\sin(2bt^*)$. It was Schlichting (1932) who first recognised that at the outer edge of the Stokes-layer the magnitude of the steady part of the second-order boundary velocity (tangential velocity) may be non-zero and proportional to the pressure gradient along the surface of the body. That is to say that the 'inner' streaming layer induced by the oscillation may extend further than the Stokes-layer into the potential flow and the zero steady tangential velocity boundary condition on the outer edge of the Stokes-layer should therefore be abandoned.

The streaming flow outside the Stokes-layer is actually driven by the tangential velocity along the outer edge of the Stokes-layer, as mentioned in the last paragraph. In the case when the frequency of the oscillations is large, i.e. $R_b \gg 1$, then for a fixed body dimension, the thickness of the unsteady Stokes-layer, $\delta_u = (\nu/b)^{1/2}$, becomes very small and as a result the steady tangential velocity at the outer edge of the Stokes-layer can be assumed to be located at the surface of the oscillating body.

The third- and fourth-order boundary-layer effects on an oscillating body were investigated by Andres and Ingard (1953a) where both R_e and $R_b \gg 1$ and $\varepsilon \ll 1$, i.e. the linearisation of the boundary-layer equations is valid. The third-order effects are purely periodic with angular frequency b and 3b whilst the

fourth-order effects contain both an unsteady and a steady component, the ratio of this steady correction to the $O(\varepsilon)$ steady solution is $O(\varepsilon^2)$.

For a valid boundary-layer approximation to the Navier-Stokes equations the thickness of the Stokes-layer should be very small compared to the body dimension, i.e.

$$\left(\frac{\delta_u}{d}\right)^2 = \frac{\nu}{bd^2} = \frac{1}{R_b} \ll 1 \qquad (1.1.5)$$

Thus when R_b is very small the boundary-layer theory breaks down and Andres and Ingard (1953b) solved the Stokes-Oseen equations. They found, theoretically, that when $\varepsilon \ll 1$ and $R_b \ll 1$ the streaming flow near the body is in the opposite direction to that when R_b is very large, $R_b \gg 1$ (see Andres and Ingard (1953a)). Their analysis is, of course, only valid for $R_e \ll 1$ since $R_e = \varepsilon R_b$.

As observed earlier, most of the early work on harmonically oscillating flows was performed when ε is very small. This has the advantage for theoretical investigators that a perturbation technique (with perturbation parameter ε) may be employed. Using the full Navier-Stokes equations, Holtsmark *et al.* (1954) have considered a perturbation solution, for $\varepsilon \ll 1$, for both unbounded and bounded flows, for the case of a harmonically oscillating circular cylinder and hence their result is valid for $R_b = O(1)$ and $R_e \ll 1$. The first-order solution was obtained explicitly and the formal solution for the $O(\varepsilon)$ correction was also given. Calculations for the perturbation quantities were facilitated by the tabulation of some specialised functions, related to the Hankel function. Experiments were also performed which supported their theory even for $R_e = O(1)$.

This is not surprising since, as explained by Riley (1967), the flow structures are quite similar for $R_e \ll 1$ and $R=O(1)$ and the solutions for the $O(\varepsilon)$ steady streaming are identical to each other in each of these two cases. By extending the solutions of Holtsmark *et al.* (1954) so that they are valid for large values of R_b, Raney *et al.* (1954) showed that the steady streaming in the Stokes-layer increases in thickness as R_b decreases.

It has long been understood that the conformal mapping technique is a very useful technique for solving the Navier-Stokes equations. This is because there is no substantial complexity introduced into the governing equations other than by adding a Jacobian. Segel (1961) used a conformal transformation to study the flow between two concentric circular cylinders with the outer cylinder performing small amplitude, low frequency harmonic oscillations, i.e. his analysis is valid for $\varepsilon \ll 1$ and $R_b \ll 1$.

Taking ε and $R_b^{-1/2}$ as the perturbation parameters, Riley (1967) examined, in his excellent review article, the fluid flow induced by a harmonically oscillating cylinder (not necessarily a circular cylinder). The unbounded ambient viscous fluid was at rest at infinity and he considered a wide range of parameters, namely $R_e \ll 1$, $R_e=O(1)$, $R_b \gg 1$ and $R_s=O(1)$. By using an 'outer' and 'inner' expansion technique, up to second-order accuracy, steady and unsteady solutions were obtained in both the 'inner' and 'outer' flow regions. Using a similar perturbation and 'outer' and 'inner' expansion techniques, Wang (1968) also studied the fluid flow induced by an oscillating circular cylinder in the case of small Reynolds number flows such that $\varepsilon \ll R_e \ll 1/\varepsilon$ with the value of ε being very small.

The controversial experimental observations of Carrière (1929), Andrade (1931), Schlichting (1932) and Holtsmark *et al.* (1954) for the streaming flow induced by the oscillating circular cylinder were explained some time ago and reviewed, for example, by Riley (1967) (also see Rott (1964) and Stuart (1963)). When $R_b \gg 1$ the viscous length $(\nu/b)^{1/2}$ is small compared with the geometric length d, thus the leading term (of the first-order 'inner solution') of the streaming flow (see Riley (1967)) shows that within the Stokes-layer the steady part of the tangential velocity undergoes a change of sign. The direction of the tangential velocity is such that outside the Stokes-layer fluid is carried over the surface of the body and out away from the body along the direction of the oscillation. So the fluid adjacent to the surface of the body within the boundary-layer flows in the opposite direction to that outside the Stokes-layer. Continuity of fluid within the boundary-layer is maintained by the streamlines forming closed loops. As R_b decreases, the viscous length $(\nu/b)^{1/2}$ increases and the Stokes-layer increases in thickness until we see, at an O(1) distance from the body, streaming in the opposite direction to that when R_b is very large. What we are seeing in this case is the inner part of the closed streamlines which are originally associated with the Stokes-layer.

When R_s is very small the outer streaming flow is governed by the biharmonic equation. This flow vanishes far from the body but on the surface of the body it matches with the inner streaming flow and takes the tangential velocity at the outer edge of the Stokes-layer(Riley (1967), Telionis (1981)).

When $R_s \geq O(1)$, the $O(\varepsilon)$ outer streaming flow induced by the harmonic oscillation of a body is governed by the full steady

Navier-Stokes equations with R_s the streaming Reynolds number as the governing parameter (Riley (1967)). This steady Navier-Stokes equations can be solved for the streaming flow on any solution domain. The importance of the streaming Reynolds number was theoretically first recognized by Stuart (1963, 1966) although in the earlier work of Andres and Ingard (1953a/b) the authors did mention that the structure of the streaming flow depends only on the streaming Reynolds number. For $\varepsilon \ll 1$, $R_s \geq O(1)$ implies that $R_b \gg 1$ so the Stokes-layer is very thin. Numerically, Haddon and Riley (1979) solved the Navier-Stokes equations, based on the analysis of Riley (1967), for the $O(\varepsilon)$ outer streaming flow outside the Stokes-layer in the closed domain between two concentric circular cylinders that Bertelsen (1974) considered in his experiments for $R_s=90$ and 400 and they found a good agreement between their experimental results.

When $R_s \gg 1$ the outer streaming flow has the character of a boundary-layer structure with a boundary-layer thickness $O(R_s^{-1/2}d)$ (Stuart (1966)). Using a perturbation scheme, Stuart solved the boundary-layer equations for the outer streaming flow by introducing a small artificial perturbation parameter, σ say, finding that the solution converges in practice as far as $\sigma=1$. Stuart (1966) predicted that a collision of the boundary-layers will take place resulting in the emergence of a jetlike flow along the axis of the oscillation. Later, Davidson and Riley (1972) examined in detail the structure of this outer boundary-layer for an oscillating cylinder with an elliptical cross section for various aspect ratios. They confirmed, experimentally, the existence of the jetlike outer flow (near the surface of the body). Using a perturbation scheme with a perturbation parameter $R_s^{-1/2}$ and higher-order boundary-layer

techniques, Riley (1975) studied the steady streaming due to an oscillating circular cylinder in the case when $R_s \gg 1$ and $\varepsilon \ll 1$. His results show good agreement with those obtained experimentally by Bertelsen (1974). Another important piece of work which should be mentioned here is that of Duck and Smith (1979) who investigated the oscillatory fluid flow between two concentric circular cylinders when the inner cylinder performs small amplitude oscillations (i.e. $\varepsilon \ll 1$). Using a perturbation and series expansion technique they studied the streaming flow due to the oscillations for both $R_s \ll 1$ and $R_s \gg 1$. The effect of the outer cylinder on the solution in the 'inner' layer was discussed and they found that as the radius of the outer cylinder tended to infinity their solutions tended to those obtained by Riley (1967) and Wang (1968) in the case when there was no outer cylinder. A flow model appropriate for large values of R_s and a large value of the ratio of radius of the outer cylinder to that of the inner cylinder was also presented which gave details of the outer streaming flow structure between these two cylinders. More recently, work on the fluid flows when the values of R_b and ε are small has also been performed theoretically by Amin (1988). He investigated the fluid flow induced by an oscillating circular cylinder using 'outer' and 'inner' expansion techniques and he indicated that the work of Andres and Ingard (1953b) is unnecessarily complicated.

Recently, some work on flows induced by a harmonically oscillating body with a cross-section other than circular has been reported. Tamada and Miyagi (1974) investigated the streaming flow induced by a symmetric Joukowski profile. Their analysis was based on the theory of Schlichting (1932) and is applicable to the case

when $R_b \gg 1$ and $R_s \ll 1$. The experimental investigation of this problem can be found in Tatsuno's work (1980) where the streaming flow initiated by a cylinder with a fan-shaped cross section was also studied experimentally. In the case when the oscillating body is a square cylinder Tatsuno (1974) showed, experimentally, for $\varepsilon \ll 1$ and $R_b \lesssim 4$ that the structure of the induced streaming flow consists of four symmetric vortices around the square cylinder with one in each quadrant of the square, see **Fig.1.2a**. The direction of the flow at an O(1) distance from the cylinder is towards the cylinder along the direction of the oscillation. As the value of R_b increases from about 4 then newly created vortices appear near the cylinder, so that there are now eight vortices situated around the square with two in each quadrant, see **Fig.1.2b**. As R_b increases further from

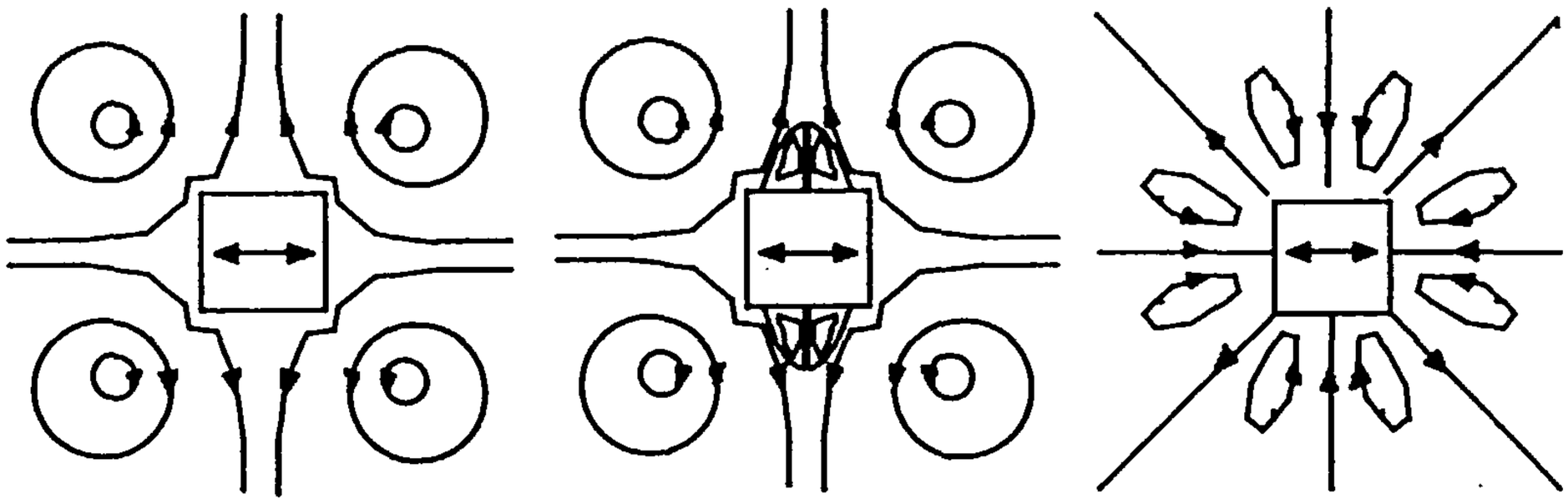

Fig.1.2 Streaming flow patterns around a harmonically oscillating square cylinder.

about 100 all these vortices become of comparable strength, see **Fig.1.2c**. Irani (1982) and Pattani and Olson (1987, 1988) used a finite element method in order to investigate the fluid flow induced by a harmonically oscillating cylinder in an unbounded viscous fluid. Irani concentrated on the flow induced by a square cylinder

for large amplitudes of oscillations, whereas Pattani and Olson (1987, 1988) investigated the flow induced by both a circular cylinder and a square cylinder and in the parameter range $\varepsilon \ll 1$ and $R_s \geq O(1)$.

Kim and Troesch (1989) extended the work of Haddon and Riley (1979) to include the fluid flow between two cylinders with the inner cylinder being square but the outer one being circular. Conformal mapping and finite-difference techniques were used to study the outer streaming flow when $R_s = O(10)$. The conformal mapping technique made it easier to deal with the complex geometry and their numerical results compare well with their experimental investigations.

Historically, the streaming phenomenon induced by the oscillating body was the domainant interest of many experimental investigators and less attention was paid to the unsteady flow pattern at different times during a period of the harmonic oscillation. Williamson (1985) investigated the fluid flow induced by large amplitude oscillations of a circular cylinder ($\varepsilon = O(1)$). His attention was focused on the instantaneous flow patterns (instantaneous recirculating flows) induced by the oscillations of the cylinder at different times. Also in Williamson's work (1985) the flow induced by two circular cylinders oscillating in phase and the effect of varying the distance between the axes of the cylinders was investigated experimentally.

Tabakova and Zapryanov (1982) and Zapryanov *et al.* (1988) used conformal mappings and 'inner' and 'outer' expansion techniques to investigate the streaming flow initiated by two circular cylinders with parallel axes. They considered two cases, namely, (i) when the

cylinders oscillate in phase and parallel to the plane containing their axes, and (ii) when the cylinders are equal in diameter and oscillate in phase but perpendicular to the plane containing their axes. Their methods were based on a perturbation analysis and their results are valid for $R_b \gg 1$ and $\varepsilon \ll 1$.

To sum up, **Fig.1.3** shows a schematic diagram of the parameter

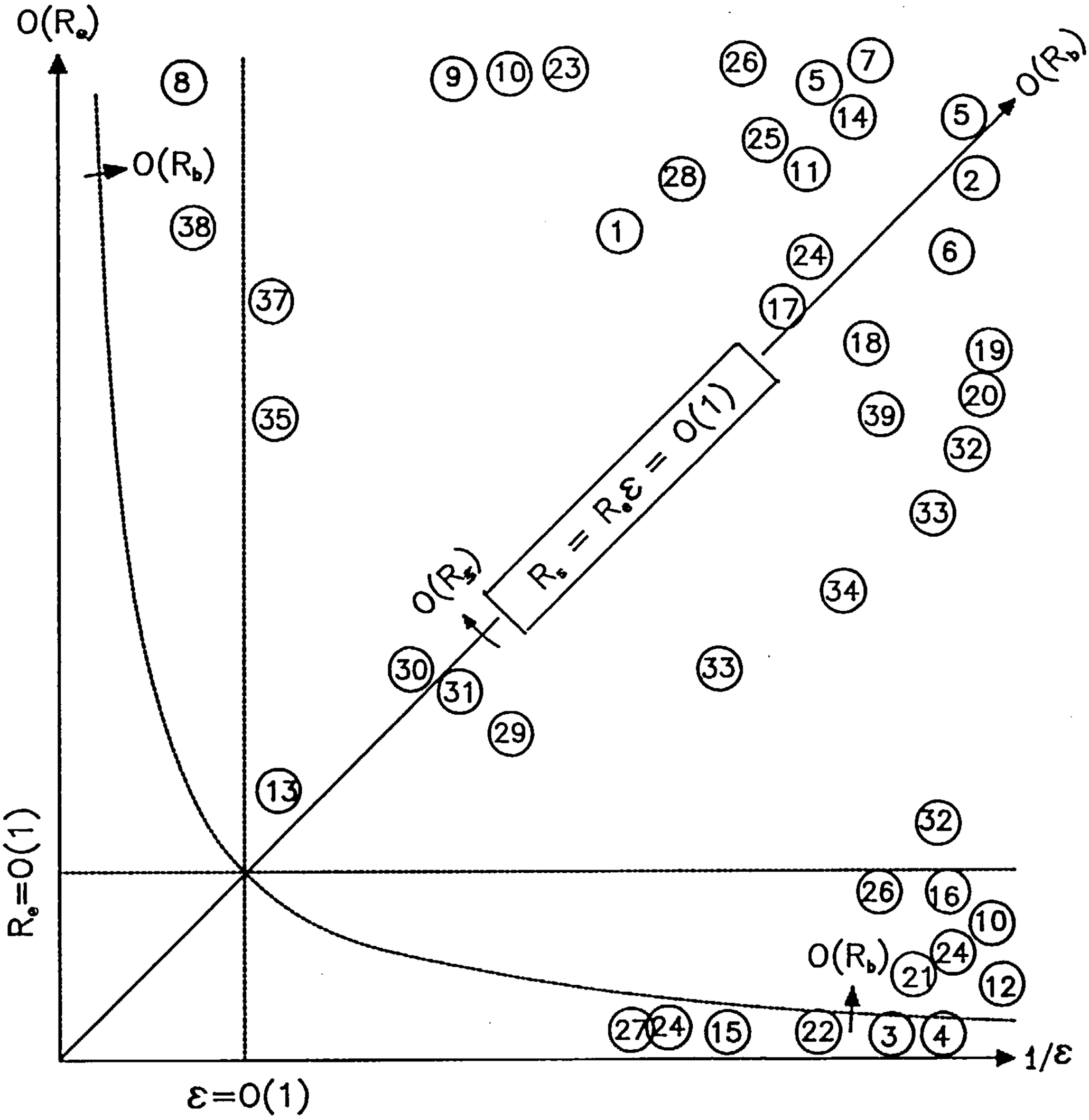

Fig.1.3 Schematic diagram of the parameter ranges of the oscillatory flows reviewed in this thesis (see table.1.1 for details).

ranges investigated by previous authors when considering the fluid flow induced by an oscillating body (or bodies) with different cross sectional shapes and Table 1.1 gives a brief description of the authors, date, body shape, methods used and the parameter ranges considered for each of the investigations reviewed in this thesis.

No.	Authors	Dates	Shapes	Parameters	Methods
1	Andrade	1931	C.C.	$R_s \gg 1$, $\varepsilon \ll 1$	Exp.
2	Andres & Ingard	1953a	C.C.	$R_e \gg 1$, $R_b \gg 1$, $\varepsilon \ll 1$	B.L.
3	Andres & Ingard	1953b	C.C.	$R_e \ll 1$, $R_b \ll 1$, $\varepsilon \ll 1$	S.O.A.
4	Amin	1988	C.C.	$R_b \ll 1$, $\varepsilon \ll 1$	O.I.E.
5	Bertelsen *et al.*	1973	C.C.C.	R_s=0.75, 90, 400, $\varepsilon \ll 1$	Exp.
6	Bertelsen *et al.*	1973	C.C.C. & C.C.	$R_s \leq O(1)$, $\varepsilon \ll 1$	P.M. & Num.
7	Bertelsen	1974	C.C.	R_s=60, 90, 400, ε=1/20, 1/24	Exp.
8	Bittleston	1986	C.C.A.	$R_e \leq 150$, $O(1) \leq \varepsilon \ll 100$	Exp. & Num.
9	Davidson & Riley	1972	E.C.	$R_s \gg 1$, $\varepsilon \ll 1$	B.L. & Num.
10	Duck & Smith	1979	C.C. & C.C.C.	$\varepsilon \ll 1$, $R_s \ll 1$; $R_s \gg 1$	P.M., C.P. & Num.
11	Haddon & Riley	1979	C.C.C.	R_s=90, 400, $\varepsilon \ll 1$	Num.
12	Holtsmark *et al.*	1954	C.C. & C.C.C.	$R_e \ll 1$, $\varepsilon \ll 1$, $R_b = O(1)$	P.M.
13	Ingham *et al.*	1990b	F.P.C.	$\varepsilon = O(1)$, $R_e = R_b \leq 30$	Exp. & Num.

Table 1.1 The oscillatory flows reviewed in this thesis (to be continued).

No.	Authors	Dates	Shapes	Parameters	Methods
14	Kim & Troesch	1989	S.C.	R_s=O(10), $\varepsilon \ll 1$	Exp. & Num.
15	Lane	1955	Sphere	$R_e \ll 1$, $\varepsilon \ll 1$, R_b=O(1)	P.M.
16	Tamada & Miyagi	1974	J.C.	$R_s \ll 1$, $R_b \gg 1$ $\varepsilon \ll 1$	P.M. & C.M.
17	Morton & Ingham	1990	S.C.	$0.3 \leq R_s \leq 35$, ε=0.05	Exp.
18	Pattani & Olson	1987	S.C.	$2 \leq R_b \leq 120$, $0.06 \leq \varepsilon \leq 0.1$	Num.
19	Pattani & Olson	1987	C.C.	$1 \leq R_b \leq 324$, $0.038 \leq \varepsilon \leq 0.046$	Num.
20	Pattani & Olson	1988	C.C.	R_b=278, $0.038 \leq \varepsilon \leq 0.046$	Num.
21	Raney *et al.*	1954	C.C. & C.C.C.	$R_e \ll 1$, R_b=O(1)	P.M.
22	Rayleigh	1883	Tube, Plate	$R_s \ll 1$, $\varepsilon \ll 1$	P.M.
23	Riley	1965	S.M.C.	$R_s \gg 1$, $\varepsilon \ll 1$	O.I.E.
24	Riley	1967	G.C.	R_s=O(1), $R_e \ll 1$, R_e=O(1), $R_b \ll 1$, $\varepsilon \ll 1$	O.I.E.
25	Riley	1975	C.C	$R_s \gg 1$, $\varepsilon \ll 1$	B.L.
26	Schlichting	1932	C.C. C.C.	$R_s \gg 1$, $\varepsilon \ll 1$ $R_s \ll 1$, $\varepsilon \ll 1$	Exp. B.L.
27	Segel	1961	C.C.C.	$R_b \ll 1$, $\varepsilon \ll 1$	C.M.
28	Stuart	1966	C.C.	$R_s \gg 1$, $\varepsilon \ll 1$	B.L.,P.M & F.M
29	Tatsuno	1973	C.C.	$R_b < 100$, $0.092 < \varepsilon < 0.9$	Exp.

Table 1.1 The oscillatory flows reviewed in this thesis (to be continued).

No.	Authors	Dates	Shapes	Parameters	Methods
30	Tatsuno	1974	S.C.	$2 \le R_b < 1282$, $0.02 \le \varepsilon \le 0.3$	Exp.
31	Tatsuno	1974	D.S.C.	$O(1) \le R_b < 6400$ $0.02 \le \varepsilon \le 0.16$	Exp.
32	Tatsuno	1980	C.C.	$R_b = 278$, $\varepsilon = 0.046$	Exp.
33	Tatsuno	1980	T.C.	$R_b = 156$, $0.0238 \le \varepsilon \le 0.308$; $R_b = 2345$, $\varepsilon = 0.0424$	Exp.
34	Tatsuno	1980	J.C.	$55 \le R_b \le 1334$ $0.0046 \le \varepsilon \le 0.064$	Exp.
35	Tatsuno & Bearman	1990	C.C.	$0.78 \le R_b \le 25.5$, $0.24 \le \varepsilon < 2.39$	Exp.
36	Wang	1968	C.C.	R_e small, $\varepsilon \ll R_e \ll 1/\varepsilon$	O.I.E.
37	Williamson	1985	C.C.	$R_b = 4587$, $0 < \varepsilon \le 6.37$;	Exp.
38	Williamson	1985	T.C.C.	$R_b = 4587$, $1.1 < \varepsilon \le 8.5$	Exp.
39	Zaprryanov *et al.*	1988	T.C.C.	$R_b \gg 1$, $\varepsilon \ll 1$	O.I.E. & C.M.

Table 1.1 The oscillatory flows reviewed in this thesis. The notation is as follows: B.L.—boundary-layer method, C.C.—circular cylinder, C.C.A.—circular cylinder array, C.C.C.—concentric circular cylinders, C.M.—conformal mapping method, D.S.C.—diagonally oscillating square cylinder, E.C.—elliptic cylinder, Exp.—experimental method, F.M.—Fettis' method, F.P.C.—flat plate cascade, G.C.—general cylinder, J.C.—Joukowski- cross-section cylinder, Num.—numerical method, O.I.E.—outer and inner expansion method, P.M.—perturbation method, S.C.—square cylinder, S.F.—steady flow, S.M.C.—symmetrical cylinder, S.O.A.—Stokes-Oseen approximation method, T.C.C.—two circular cylinders in parallel, T.C.—triangular cylinder.

1.2 The Fluid Flow in an Industrial Cyclone

Over many years a great deal of effort has been devoted to obtaining a better working knowledge of industrial cyclones. This has been due in no small part to the apparent simplicity of operation and design inherent in this device. Conceptually the principle of operation is straightforward. Fluid containing particles of a different density, or even two fluids, is injected tangentially at high speed into a vessel of circular cross section. The high rotational vorticities so generated produce centrifugal accelerations which cause the particles to move relative to the fluid and therefore offer the possibility of separation or classification subject to some means of collecting the distinct phases. The very high radial accelerations produced allow for a relatively rapid migration of particles thus allowing a large rate of volume flux through the equipment.

Fig.1.4 shows the typical geometry of a conical cyclone. It can be seen that the main body of the cyclone is a conical vessel, usually of small included angle, α^* say, surrounded by a cylindrical section with a lid. At the top of the cylindrical section there are one or more inlet nozzles which direct the feed tangentially into the upper part of the body. Most of the fluid, which is fed into the cyclone through the tangential inlet (inlets), leaves through a tube, known as the vortex finder or overflow, which is located centrally through the lid. At the apex of the cone there is an orifice, called the underflow, through which the rest of the fluid entering the cyclone is allowed to leave. The high speed fluid through the inlet of the cyclone produces strong centrifugal forces which cause the particles to move relative to the fluid and towards the side wall of

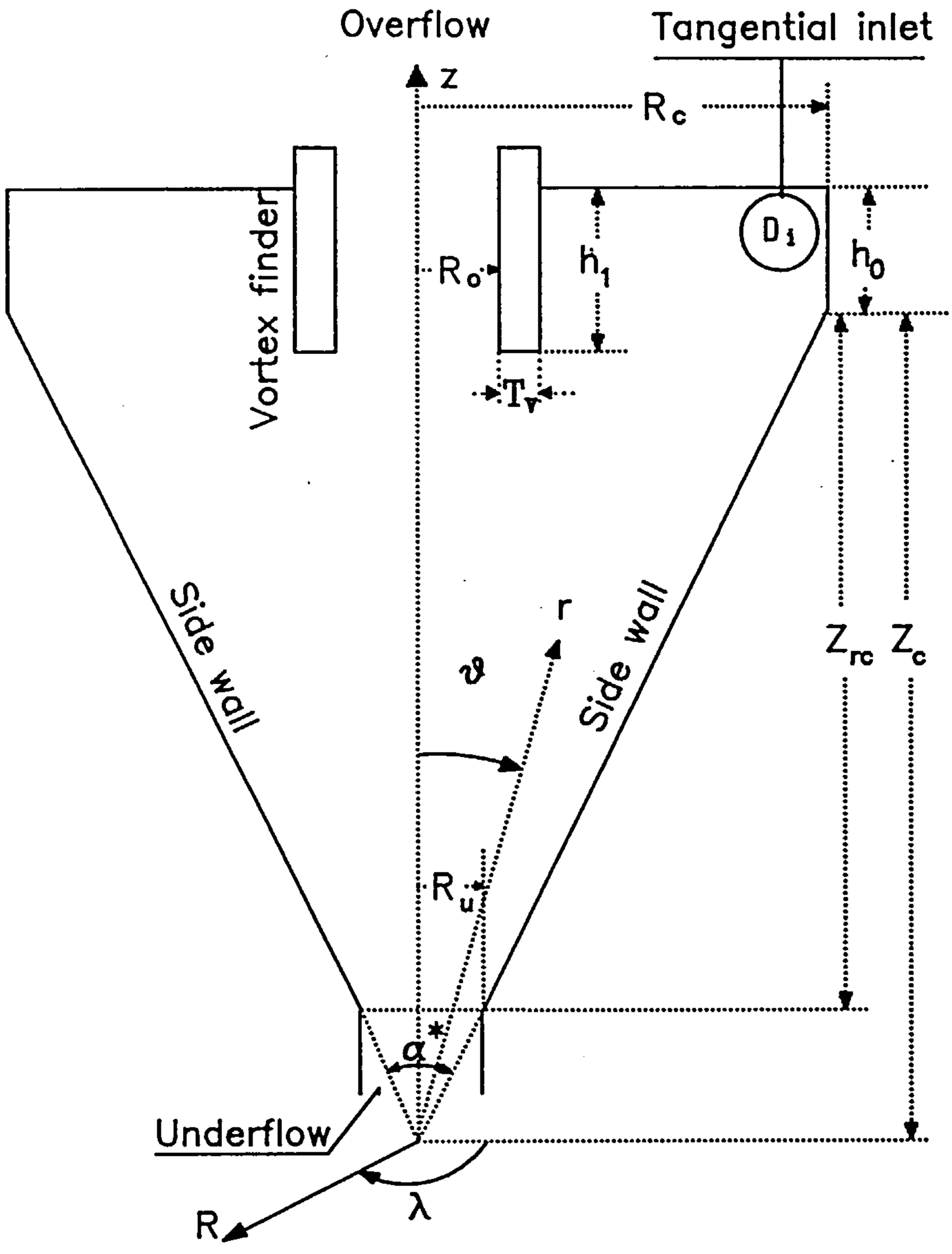

Fig.1.4 The cyclone geometry and the coordinate systems.

the cyclone, as a result some particles with higher densities or larger sizes may be moved to the side wall before being discharged to the underflow and hence are separated. The centrifugal forces, produced by the fluid with the tangential speed, may not be large enough to move the particles with smaller sizes or lower densities to the side wall before these particles are discharged to the

overflow and these particles are consequently not separated. A cyclone can be operated with different fluids: one which operates with a liquid is referred to as a hydrocyclone, whilst one operating with a gas is called a gas cyclone or simply a cyclone. However the basic principle of separation is identical in both cases.

On entry into the cyclone the fluid passes through a nozzle which generates high speeds and then the fluid goes through what is effectively an expansion where streamlines diverge and quite significant energy losses may occur. Also the fluid has to adjust to the no slip conditions at the solid boundaries across boundary-layers and, again, energy losses will arise. Account is usually taken of these energy losses by regarding the effective azimuthal velocity (spin velocity) at entry to the cyclone as a proportion (less than unity) of the actual entry spin velocity. The constant of the proportionality is called the loss factor, α say. The fluid then spirals down the outer parts of the cyclone and, since most of the fluid leaves through the vortex finder, spirals up to the inner region around the axis of the cyclone. In the absence of any losses, so that angular momentum is conserved, the reduction in radius of curvature of the streamlines in the horizontal planes cause the spin velocity to increase and so increase the radial acceleration of the fluid. The very high fluid speeds which arise near the axis produce a low pressure and this results in a gas liquid interface in the case of a hydrocyclone. If this core region communicates with the atmosphere then an air core is formed. Otherwise, if the pressure is sufficiently low then the liquid vaporises and a vapour core is formed. In the upper part of the cyclone the rapid motion down the wall of the cyclone causes a

toroidal vortex to be formed which usually extends beyond the lower end of the vortex finder. Clearly some radial motion must exist and this will play a significant part in determining whether a particle will be separated or not since the radial acceleration simply gives an indication of the migration of a particle relative to the surrounding fluid. The means of removal of separated dense particles from the device relies on the intricate mechanics of the boundary-layers on the solid boundaries.

Because the Reynolds number of flow in the cyclone is generally very large, boundary-layers in which inertial and viscous stresses balance, form on the walls of the cyclone. In the main flow the motion of the fluid around the axis is maintained by a pressure gradient directed towards the axis. Because the pressure is a constant across a boundary-layer, and within the boundary-layer spinning motion is attenuated through the action of the viscosity, an imbalance exists between pressure and inertial stresses. This imbalance causes fluid in the boundary-layer to be driven in the direction of the pressure gradient giving rise to secondary flows. In the case of the boundary-layer on the side wall of the cyclone, a component of the radial pressure gradient drives fluid through the boundary-layer towards the vertex of the core and this assists in the removal of dense solid particles through the underflow. However, the boundary-layer on the lid drives the fluid which has just entered towards the vortex finder where it escapes to the overflow carrying with it particles which have not been subjected to the full separating mechanism of the cyclone. This is commonly referred to as the 'short circuit flow' or 'leakage effect' or even simpler 'leakage'.

The very simplicity of the cyclone operation has probably dictated the course followed by many investigations. The fact that the mechanism of particle separation seemed straightforward together with the readily available information on particle drag at low concentration levels allowed intuition to play a significant part in the development of the parameter grouping relevant to the operation of the cyclone. This in turn was supported by extensive experimental investigations into the separation efficiency, the meaning of which, although it can be defined in a variety of ways, is adequately conveyed by its title. Not surprisingly, with this volume of data available and the intuitive understanding of the role played by various parameters it was possible to develop quite successful empirical formulae which predicted the performance of cyclones. There are several ways to measure the separation efficiency of a cyclone, the most important and frequently used one is the 50% cut size, d_{50} say, i.e. the diameter of the particle which has a 50% separation efficiency.

Among the large number of investigations on the cyclones, Rietema (1961) published an extensive piece of work on the design and performance of the cyclone. However the first major review work on the cyclone (hydrocyclone) was published by Bradley (1965) and more recently there has been an excellent review of all aspects of the operations of hydrocyclones by Svarovsky (1984).

The first major contribution towards an understanding of the fluid mechanics of the cyclone is due to Kelsall (1952). He studied experimentally the velocity distributions within the cyclone and his results have frequently been used as a standard by later investigators. From the results of Kelsall (1952) it is clear that

the spin velocity in the cyclone is almost independent of z. In fact, away from the axis of the cyclone the spin velocity w satisfies wR^m=constant and Kelsall showed for his experiments that m≈0.84. It should be noted that m=1 gives the free vortex flow which inviscid theory predicts. There is a sharp transition from the near free vortex flow to solid rotation which occurs near the axis of the cyclone.

As cyclones became more widely used, problems in the operation and the need for a more fundamental and theoretical study became apparent. It was recognised that a better understanding of the fluid mechanics was required and it was probably at this stage that the complexity of the flow problem became manifest. This, and again the fact that the cyclone operated by centrifugal separation, dictated that early theoretical investigations concentrated on the spin velocity. Fontein and Dijksman (1953), recognising that in the majority of the cyclone the spin velocity was likely to be that associated with a free vortex whilst near the axis of the cyclone solid body rotation existed, suggested that the spin velocity was of the form $k_1/R + k_2R$, where R is the radial distance from the axis of the cyclone and k_1 and k_2 are constants to be determined. However no values of k_1 and k_2 were given by Fontein and Dijksman. This relationship would be of value if k_1 and k_2 were allowed to vary with R, in particular k_1 should be zero for small values of R.

Ohasi and Maeda (1958) investigated experimentally the velocity distributions in a hydrocyclone by taking photographs of the loci of the particles within the cyclone. Errors due to density differences and the centrifugal force were taken into consideration for the radial velocity component. The experimental setup used was similar

to that of Kelsall (1952) but with a much shorter vortex finder. Ohasi and Maeda (1958) found, by taking averages at different levels in the cyclone that m≈0.79.

Kelsall's excellent work (1952), as mentioned earlier, supplied the type of information which was much needed in order to obtain some insight into the fundamentals of the fluid mechanics of the cyclone. Indeed, using Kelsall's data, Rietema (1961) solved the azimuthal component of the Navier-Stokes equations assuming a constant eddy viscosity. His results show a strong similarity with the experimentally determined spin velocity profiles but no detailed comparisons were made.

Knowles *et al.* (1973) also studied the velocity distributions within a cyclone which has no air core. In order to obtain the velocity profiles high speed movies of droplets of anisole were taken in two perpendicular horizontal directions and the analysis of these films gave results for the velocity distributions. The cyclone setup was one which was recommended by Rietema (1961) and was performed in similar conditions to those described by Kelsall (1952) and Ohasi & Maeda (1958). However, they found that m≈0.25.

The early emphasis on just the spin velocity is understandable but with the benefit of hindsight it is probably true to say that this emphasis was, to some extent, misplaced. When the cyclone is used to separate dispersed dense particles the later work of Bloor and Ingham (1974) has shown that it is the spin velocity in the outer region of the cyclone which is of significance. Of course it is in this region where this velocity component is most easily determined theoretically because generally speaking viscous losses have not become significant. However, when a dispersed light phase

is to be separated then the magnitude of the velocity near the axis is of paramount importance.

The recent major contributions to the understanding of the fluid mechanics in the cyclone were, perhaps, due to Bloor and Ingham. Many research papers which involve various aspects of the cyclone such as velocity distributions, the separation efficiency and entry conditions etc., have been published by Bloor and Ingham since the early 1970's. In fact they (see Bloor and Ingham (1973a)) obtained the cross-plane velocities in the form

$$q_r = \frac{1}{r^2 \sin\theta}\frac{\partial\psi}{\partial\theta} = \frac{1}{2}B(r\theta)^{-1/2}\left(\frac{3\alpha^*}{2} - \theta\right) \qquad (1.2.1)$$

$$q_\theta = \frac{1}{r\sin\theta}\frac{\partial\psi}{\partial r} = -\frac{3}{2}Br^{-1/2}\theta^{1/2}\left(\frac{\alpha^*}{2} - \theta\right) \qquad (1.2.2)$$

where ψ is the streamfunction and B is a constant which can be evaluated by the knowledge of the operating conditions and the geometry of the cyclone. Their results predicted, as pointed out by Ferguson (1989), the locus of the zero axial velocity to be at $\theta=0.3\alpha^*$, whilst the experimental work of Bradley (1965a) gives $\theta=0.305\alpha^*$. Having obtained the cross-plane velocities Bloor and Ingham (1975) then obtained the spin velocity profile assuming that the viscosity was of an anisotropic nature. Actually it was assumed that the flow was inviscid in the cross-plane and viscous in the λ-plane (see **Fig.1.4** for the co-ordinate system) and the flow was turbulent. Using the three velocity profiles available they also obtained the efficiency curves for particle separation.

Having obtained the basic flow model in the cyclone, Bloor and Ingham (1976) investigated the boundary-layer flow near the walls of the cyclone. A Pohlhausen and a finite-difference technique were

used to solve the momentum integral equations and a comparison between these two methods was made. Later the presence of particles in the boundary-layer flow was also investigated by Bloor *et al.* (1980) and Laverack (1980a, 1980b).

Boysan *et al.* (1982) suggested a mathematical model for the turbulent gas flow in a cyclone. They assumed that the flow was incompressible and the turbulence was modelled using a Reynolds stress technique and closure was obtained by relating the Reynolds stresses to the time averaged fluctuating velocity components.

More recently, an investigation of the influence of the entry conditions on the separation efficiency of a cyclone has been performed by Bloor and Ingham (1987). By solving the inviscid flow equations they suggested three models for the vorticity distributions at the entry of the cyclone and found that the following model gives the best representation of the flow in the cyclone, especially in those of Kelsall (1952) and Knowles *et al.* (1973).

> 'Induced azimuthal vorticity model: An inlet flow where the fluid enters the cyclone with angular velocity which varies with the radius of the cyclone, corresponding to an axial component of vorticity. The geometry of the cyclone then ensures than an azimuthal component of vorticity is generated.'

The velocity distributions obtained by Bloor and Ingham were based on the assumption that the cyclone is conical in shape. In order to deal with a practical cyclone more precisely, Ferguson (1989) extended the work of Bloor and Ingham to include a recirculation region in the cylindrical part of the cyclone. He investigated both viscous and inviscid flows in the cyclone by using

numerical techniques and found that a very good model for the entry conditions is vital for predicting the flow in the cyclone.

1.3 Outline of the Thesis

Almost all investigations on the flow due to a harmonically oscillating body have been performed when there is only one, or at most two, oscillating bodies. The oscillatory flows induced by a cascade of cylinders has not as yet been reported. So in the first part of this thesis we investigate the fluid flows induced by cascades of various shaped cylinders which oscillate harmonically in an unbounded, incompressible viscous fluid which is otherwise at rest. For the study of the problem of viscous flow through an array of cylinders such as the cascade mentioned earlier, apart from the interest from an academic point of view, it also has a number of important industrial applications, including the modelling of flows through a porous material and in the construction of certain heat exchangers. Several cascades have been studied but in this thesis we concentrate on three, namely,

(i) A cascade of normal flat plates. The cascade is assumed to consist of an infinite number of flat plates which are of infinitesimal thickness in the x^*-direction, of uniform width d in the y^*-direction and of infinite extent in the z^*-direction. The plates occupy the plane $x^*=0$ at time $t^*=0$ with edges at $y^*=-\frac{d}{2}+2k\mathcal{L}$ and $y^*=\frac{d}{2}+2k\mathcal{L}$, where $k=0, \pm1, \pm2,\ldots,$ and $\mathcal{L}$ is the half-width of the plates plus gap, see Fig.1.5.

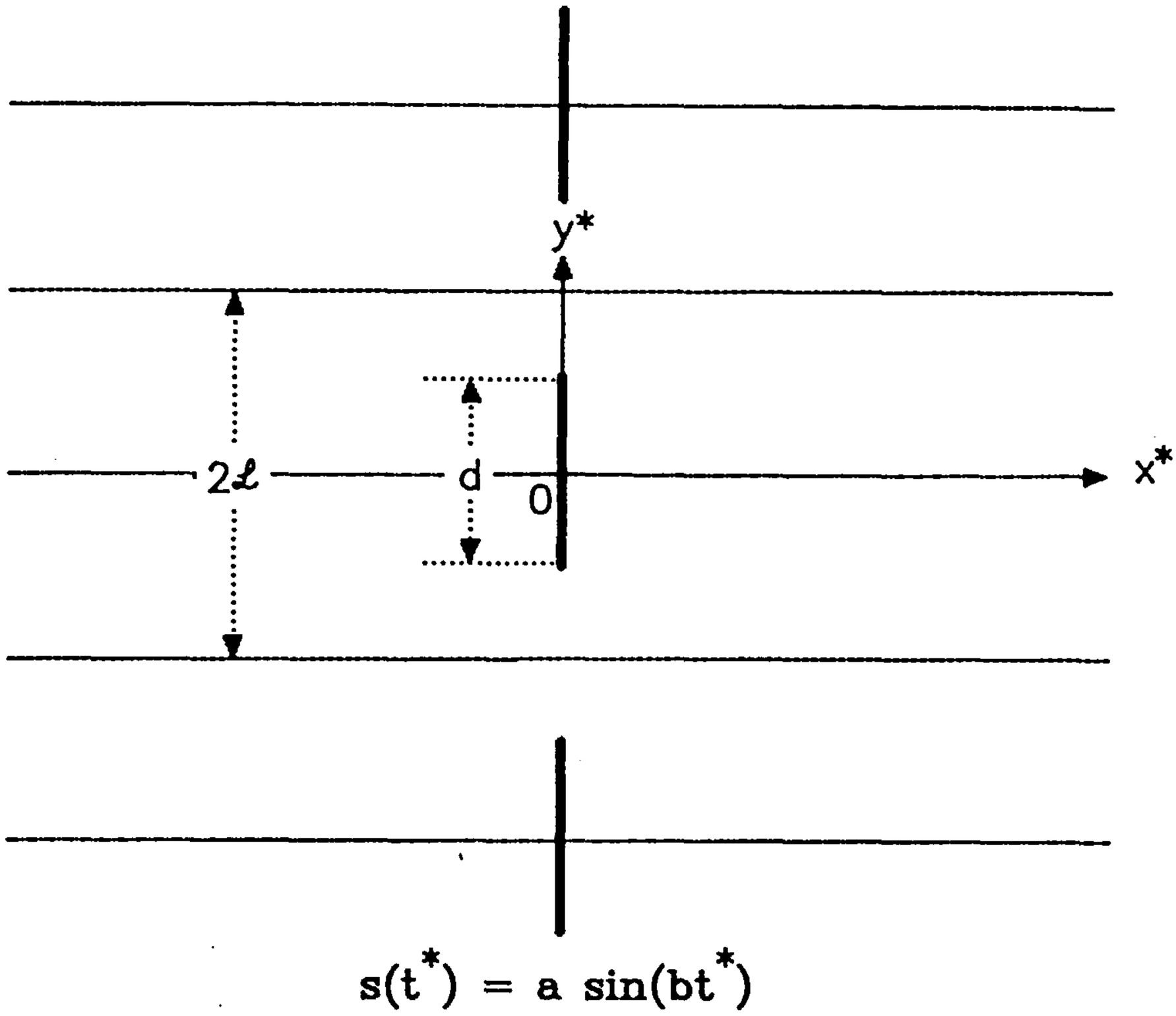

Fig.1.5 The geometry of the cascade of normal flat plates.

(ii) A cascade of square cylinders. The cascade is assumed to consist of an infinite number of square cylinders which have a width d in the x^*- and y^*-directions and of infinite extent in the z^*-direction. The cylinders occupy the space between the planes $x^*=-\frac{d}{2}$, $x^*=\frac{d}{2}$, $y^*=-\frac{d}{2}+2k\ell$ and $y^*=\frac{d}{2}+2k\ell$ at time $t^*=0$, where k=0, ±1, ±2,..., see Fig.1.6.

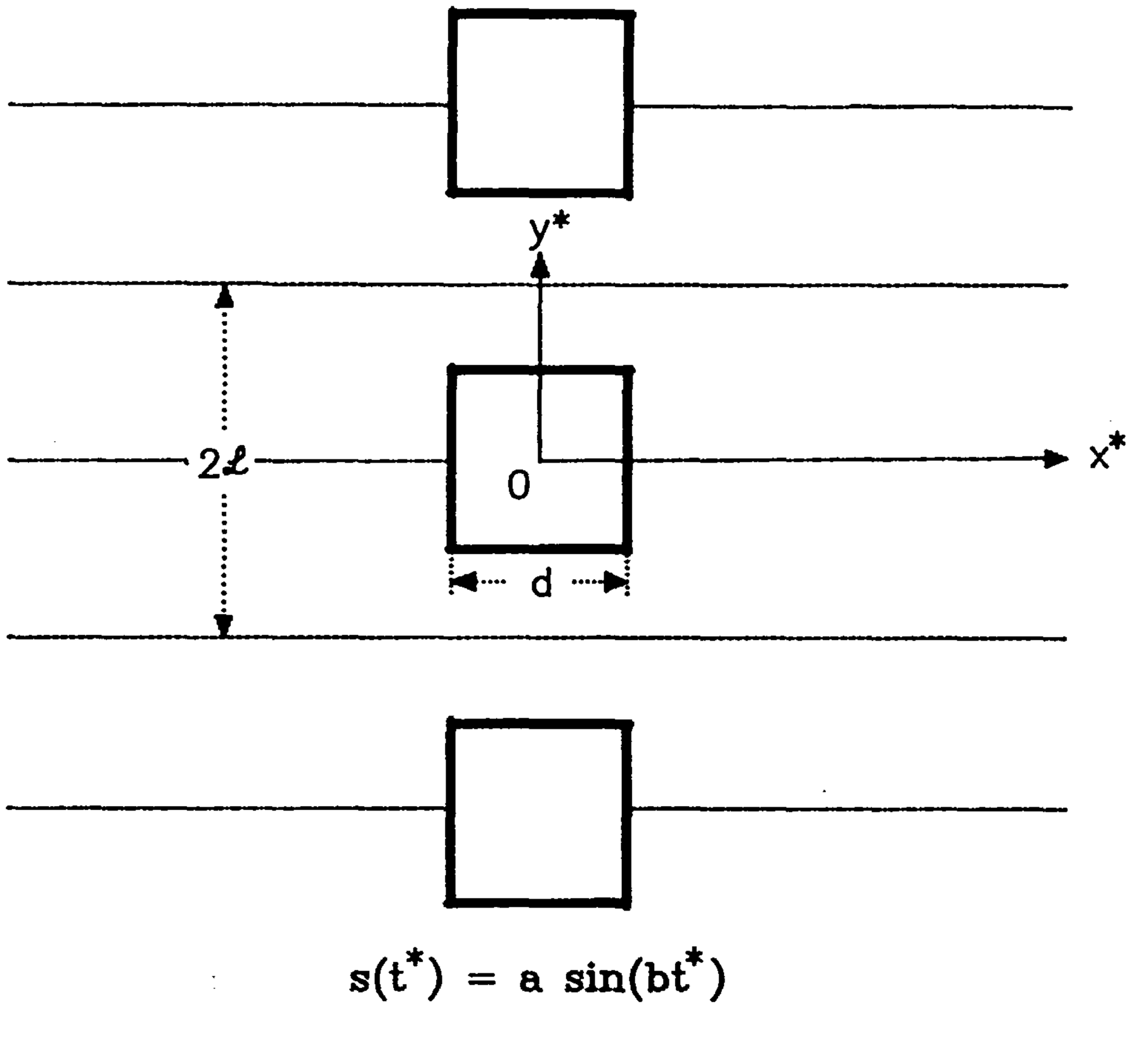

$$s(t^*) = a \sin(bt^*)$$

Fig.1.6 The geometry of the cascade of square cylinders.

(iii) A cascade of circular cylinders. The cascade is assumed to consist of an infinite number of circular cylinders of uniform diameter d whose axes occupy the plane $x^*=0$ at time $t^*=0$ with each axis at $y^*=2k\ell$, where k=0, ±1, ±2,..., see **Fig.1.7.**

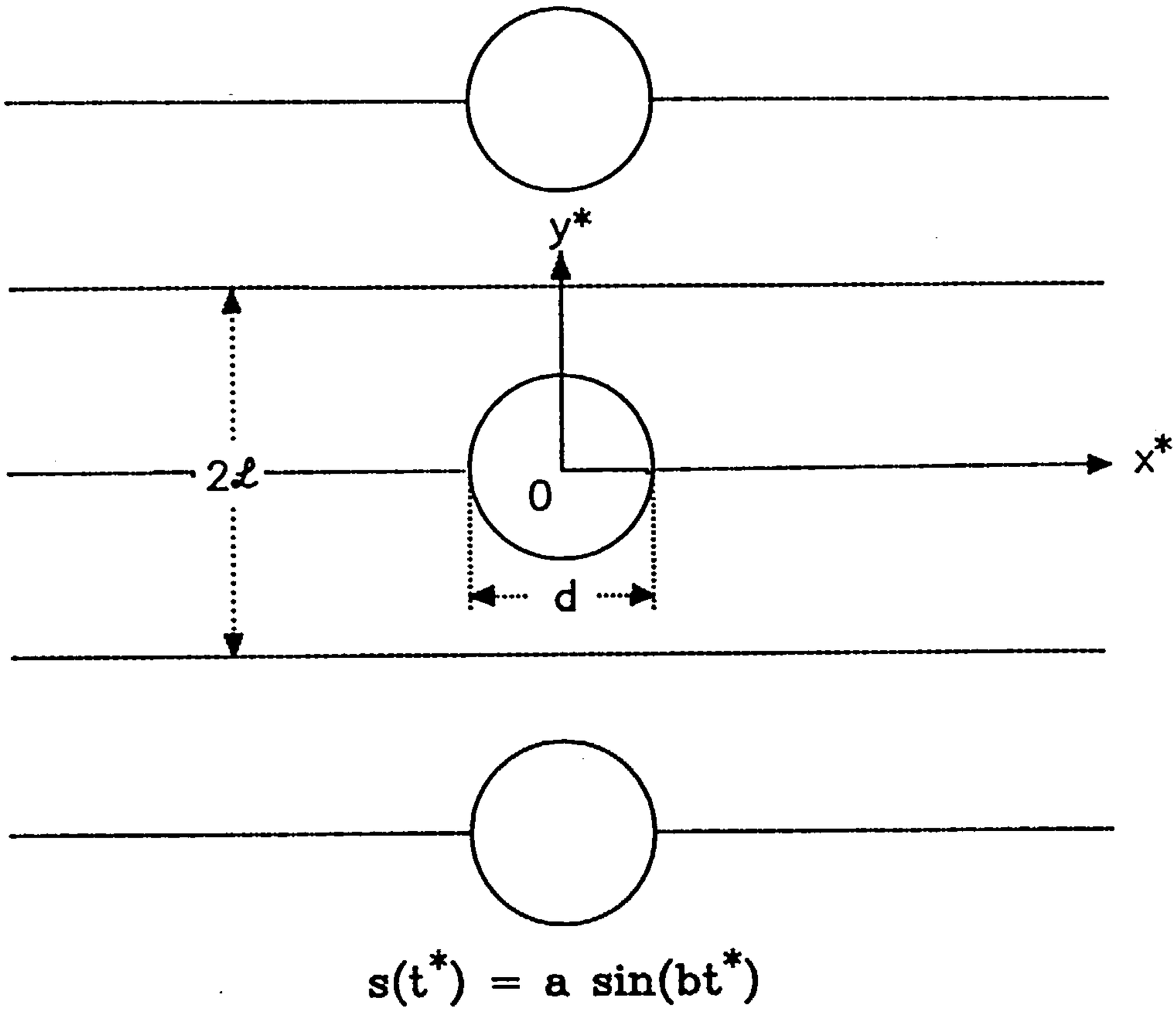

$$s(t^*) = a \sin(bt^*)$$

Fig.1.7 The geometry of the cascade of circular cylinders.

The motion of the flow is assumed to be laminar and two-dimensional throughout chapters 2 to chapter 5 and the x^*-component of the displacement of the oscillations of the cascade at time t^* is given by equation (1.1.1). With respect to rectangular Cartesian coordinates (x^*, y^*), the governing equations of the flow may be written in the form

$$\frac{\partial u^*}{\partial t^*} + u^* \frac{\partial u^*}{\partial x^*} + v^* \frac{\partial u^*}{\partial y^*} = - \frac{1}{\rho} \frac{\partial P^*}{\partial x^*} + \nu \nabla^2 u^* \qquad (1.3.1)$$

$$\frac{\partial v^*}{\partial t^*} + u^* \frac{\partial v^*}{\partial x^*} + v^* \frac{\partial v^*}{\partial y^*} = - \frac{1}{\rho} \frac{\partial P^*}{\partial y^*} + \nu \nabla^2 v^* \qquad (1.3.2)$$

$$\frac{\partial u^*}{\partial x^*} + \frac{\partial v^*}{\partial y^*} = 0 \qquad (1.3.3)$$

where (u^*, v^*) are the velocity components of the flow. It is usual to work with non-dimensional quantities and b^{-1}, d and U_∞ (=ab) are used as scales for time, length and speed, respectively. Then the non-dimensional governing equations, in terms of the streamfunction, ψ, and vorticity, ω, can now be written as follows

$$\frac{\partial \omega}{\partial t} + \varepsilon\left\{\frac{\partial \psi}{\partial y}\frac{\partial \omega}{\partial x} - \frac{\partial \psi}{\partial x}\frac{\partial \omega}{\partial y}\right\} = \frac{1}{R_b}\nabla^2\omega \qquad (1.3.4)$$

$$\nabla^2\psi = -\omega \qquad (1.3.5)$$

where

$$\omega = \frac{\partial v}{\partial x} - \frac{\partial u}{\partial y} \qquad (1.3.6)$$

is the scalar vorticity and the streamfunction ψ is defined in terms of the velocity components (u, v) by

$$u = \frac{\partial \psi}{\partial y}, \qquad v = -\frac{\partial \psi}{\partial x}. \qquad (1.3.7)$$

The equations (1.3.4)-(1.3.7) have been solved for different values of the parameters ε, R_e, R_b and R_s subject to the appropriate boundary conditions depending on the parameter ranges considered.

Ingham *et al.* (1990a) have investigated, both numerically and experimentally, the two-dimensional steady flow through a uniform cascade of normal flat plates. They have shown that the length of the wake bubble behind the plate when the blockage ratio is unity is proportional to the Reynolds number. In chapter 2 we extend this work to include the two-dimensional flow which is induced by a

cascade of normal flat plates which perform harmonic oscillations. In most of the calculations it has been assumed that the non-dimensional amplitude of the oscillation, ε, is O(1) and numerical results have been obtained for values of R_e up to 30. The numerical results compare well with some related experimental results. Some results for very large amplitude oscillations (ε=1000) are also discussed.

When only one body oscillates in a fluid at rest and $\varepsilon \ll 1$ then the Stokes-layer near the body generated by the oscillation becomes thicker as R_b decreases. The question arises as to what happens when there is more than one oscillating body? In chapter 3 both a series truncation and a numerical technique is used to study the flow due to an oscillating cascade of both normal flat plates and square cylinders. It is assumed that $\varepsilon \ll 1$ and R_b is O(1), i.e. there are no boundary-layers on the surface of the cascade. We use a perturbation method, with parameter ε, and the separation of variables method. The resulting coupled set of partial differential equations for the O(1) flow are then solved by both a numerical and a series truncation method. Further, a numerical technique is employed to obtain both the steady and unsteady flows for the $O(\varepsilon)$ approximation.

In chapter 4 we focus attention mainly on the streaming flows induced by a harmonically oscillating cascade of both square cylinders and normal flat plates in the case when $\varepsilon \ll 1$ and $R_s \geq O(1)$. The conformal transformation technique is employed to obtain the boundary values for the steady streaming tangential velocity which is required when the governing equations for the streaming flow is to be solved. A special central finite-difference scheme has been

used to solve the full steady state Navier-Stokes equations which govern the outer streaming flow and numerical results have been obtained for values of R_s up to 70 for both cascades.

In chapter 5 the streaming flow induced by an oscillating cascade of circular cylinders is obtained numerically for $\varepsilon \ll 1$ and for streaming Reynolds numbers up to 100. A grid generation method is first used to transfer the physical geometry onto a simpler mathematical domain and then the Navier-Stokes equations are solved on the newly transformed plane. Some related experimental investigations show that when R_s is sufficiently large, the streaming flow induced by the oscillating cascade is no longer symmetrical and an asymmetrical flow develops. Therefore in chapter 5 we solve numerically the steady state Navier-Stokes equations which govern the outer streaming flow due to the oscillating cascade of circular cylinders subject to both symmetrical and asymmetrical boundary conditions. Numerical results show that the break-down of symmetry occurs when $8<R_s<9$. In order to identify the reason for this break-down, a stability analysis is presented for two model problems.

Although cyclones can be used to separate solids from solids, solids from liquids and even liquids from liquids, in this thesis we will study cyclones which are used to separate solid particles from a fluid, either a liquid or a gas. The main purpose of the work in the second part of this thesis is to predict theoretically and numerically the separation efficiency of a cyclone as a function of different operating conditions and cyclone design. Because the underlying fluid mechanics of the cyclone governs the separating

process, some of the work in this thesis involves also an investigation of the fluid flow within the cyclone. In particular we investigate the following aspects:

(i) The velocity distributions in the cyclone.

(ii) The influence of the cyclone geometry on the separation efficiency.

(iii) The influence of the operating conditions on the separation efficiency.

(vi) Comparisons of our mathematically predicted results with some available experimental data.

(v) Correlations of d_{50} and the loss factor α with the cyclone geometry and operating conditions.

In chapter 6 we investigate how different estimations of (i) the angular momentum at the entry of the cyclone affect the cross-plane velocity distribution, (ii) the vorticity in the recirculation region affect the cross-plane flow pattern, and (iii) the angular momentum at the entry of the cyclone and the vorticity in the recirculation region affect the separation efficiency of the cyclone.

Based on the mathematical model for the fluid flow in the cyclone as described in chapter 6, we investigate in chapter 7 the the effects of the cyclone geometry and operating conditions on the separation efficiency of the cyclone. The effects of most of the parameters involved in the cyclone configuration have been investigated numerically. It is found that the most important parameter which affects the separation efficiency of the cyclone is the spin velocity at the entry to the cyclone.

Having studied the influence of the cyclone geometry and the

operating conditions on the separation efficiency of a cyclone, we then, in chapter 8, compare our theoretically and numerically predicted results with the available experimental data such as those of Stairmand (1951), Smith *et al.* (1979) and Kim and Lee (1990). As d_{50} and the loss factor α are two very important factors involved in estimating the performance of a cyclone, in chapter 8 we also apply a regression analysis to correlate d_{50} and the loss factor α with the cyclone geometry and operating conditions using some of the available experimental data.

Since the small personal cyclone, which is typically 10mm in diameter, is extensively used in the mining and health and safety industries we therefore identify in chapter 9 the differences in the cyclone performance between the small personal cyclones and the larger cyclones investigated in chapters 6 to 8. Also in chapter 9 we demonstrate how our numerical methods can be applied to the small personal cyclone.

Finally, in chapter 10 some general conclusions are made and suggestions for further studies on both the oscillatory flow problems and the industrial cyclone are presented.

CHAPTER 2 NUMERICAL SOLUTIONS FOR THE FLUID FLOWS INDUCED BY LARGE AMPLITUDE HARMONIC OSCILLATIONS OF A CASCADE OF NORMAL FLAT PLATES

2.1 Introduction

As observed in chapter 1, most investigations of the fluid flow induced by oscillating bodies have been performed when $\varepsilon \ll 1$ and $R_b \gg 1$, i.e. the amplitude of the oscillations is very small compared with the dimension of the body whilst the frequency of the oscillations is high. However, recently Williamson (1985) studied, experimentally, the two-dimensional laminar fluid flow induced by two circular cylinders which perform large amplitude and low frequency oscillations, typically $\varepsilon = O(1)$ and $R_b = 4587$ and the effect of varying the distance between the two axes of the cylinders was investigated. His attention was mainly focused on the vortices that are generated along the axis of the oscillation of the cylinders.

For the fluid flow past through more than two bodies, Gordon (1978) solved the steady two-dimensional fluid flow with a uniform velocity at infinity, past an array of circular cylinders using a finite-difference method for Reynolds numbers up to 20. The array of the cylinders was arranged such that all the axes of the cylinders were parallel to the z^* axis and there was an infinite number of cylinders in the y^*-direction and a finite number of rows in the x^*-direction, and the distribution of cylinders in the x^*-y^* plane

was symmetrical about the x^* axis. Later, Bittleston (1986) extended Gordon's work to both the steady and oscillating cases and calculated the fluid flow due to an array of cylinders, both circular and elliptical, such that the distribution of cylinders was periodic in both the x^* and y^* directions. Using a grid generation method and a finite-difference technique he was able to obtain both the steady and unsteady solutions of the full Navier-Stokes equations. The parameter range for his steady solutions was $0 \leq R_e \leq 200$ whilst the parameter ranges for his unsteady solutions were: $0 \leq R_e \leq 150$ and $\varepsilon = O(1)$ to $O(10^2)$. Ingham *et al.* (1990a) investigated the two-dimensional steady flow through a uniform cascade of normal flat plates, see **Fig.1.5**, and, with a careful treatment of the singularity in the vorticity at the corners of the plates, they were able to obtain solutions for values of R_e up to 500.

The use of circular and elliptical cylinders makes it easier for investigators to solve the Navier-Stokes equations in terms of the streamfunction and the vorticity as there are no singularities in the vorticity in the solution domain, see for example Gordon (1978) and Bittleston (1986). However, singularities arise in the vorticity near the corners of the cylinders when the array consists of cylinders with sharp corners such as normal flat plates. It is these singularities that make the numerical calculations more difficult.

In this chapter we investigate the two-dimensional fluid flow induced by a cascade of normal flat plates which perform harmonic oscillations in the direction normal to the plane of the plates in an unbounded incompressible fluid which is otherwise at rest. The Navier-Stokes equations are written in terms of the streamfunction

and vorticity and are solved using an implicit second-order-accurate finite-difference scheme which is based on a modified procedure to preserve accuracy and iterative convergence at large values of the Reynolds numbers. Singularities in the vorticity near the edges of the plates are treated in the way which is similar to that developed by Moffatt (1964) in the steady case. Interest is mainly concentrated on small and moderate values of the Reynolds number as much more computation time is needed in order to obtain accurate solutions at large values of the Reynolds number. Therefore, in this chapter we mainly present results for $\varepsilon = O(1)$ and for values of R_e up to 30. However, the numerical scheme is applicable to any value of ε and the Reynolds number. Also in this chapter an asymptotic approximation is developed which is valid at large distances from the cascade in order for the numerical scheme to adequately deal with the boundary conditions at large distances from the cascade.

2.2 Governing Equations and Boundary Conditions

The cascade considered is assumed to consist of an infinite number of normal flat plates as described in chapter 1 (see **Fig.1.5**) and the harmonic oscillation of the cascade is given by (1.1.1). The non-dimensional governing equations for the flow are equations (1.3.4)-(1.3.7) and due to the symmetry of the physical geometry, we need only consider the flow in the non-dimensional region $-\infty < x < \infty$, $0 \le y \le \mathcal{L}/d \equiv L$.

Equations (1.3.4)-(1.3.7) now must be solved subject to the boundary conditions

$$\psi = y\cos(t), \quad \frac{\partial\psi}{\partial x} = 0, \quad \text{on } x = \varepsilon\sin(t), \ 0 \le y \le \frac{1}{2} \qquad (2.2.1a)$$

LEEDS UNIVERSITY LIBRARY

$$\psi = \omega = 0, \qquad \text{on } y = 0 \text{ and } y = L, \ -\infty < x < \infty \tag{2.2.1b}$$

$$\frac{\partial\psi}{\partial x} \longrightarrow 0, \quad \frac{\partial\psi}{\partial y} \longrightarrow 0, \quad \omega \longrightarrow 0, \quad \text{as } x \longrightarrow \pm\infty, \ 0 \le y \le L \tag{2.2.1c}$$

Clearly the numerical implementation of the boundary condition (2.2.1a) is not easy so we consider the problem with the coordinate system fixed in the cascade. We therefore make the following coordinate transformation,

$$\left.\begin{aligned} Y &= y \\ X &= x - \varepsilon \sin(t) \\ \Psi(X,Y,t) &= \psi(X,y,t) - y\cos(t) \end{aligned}\right\} \tag{2.2.2}$$

Then the equations (1.3.4)-(1.3.7) become

$$\frac{\partial\omega}{\partial t} + \varepsilon\left(\frac{\partial\Psi}{\partial Y}\frac{\partial\omega}{\partial X} - \frac{\partial\Psi}{\partial X}\frac{\partial\omega}{\partial Y}\right) = \frac{1}{R}\left(\frac{\partial^2\omega}{\partial X^2} + \frac{\partial^2\omega}{\partial Y^2}\right) \tag{2.2.3}$$

b

$$\frac{\partial^2\Psi}{\partial X^2} + \frac{\partial^2\Psi}{\partial Y^2} = -\omega \tag{2.2.4}$$

where

$$U = \frac{\partial\Psi}{\partial Y}, \qquad V = -\frac{\partial\Psi}{\partial X} \tag{2.2.5}$$

$$\omega = \frac{\partial V}{\partial X} - \frac{\partial U}{\partial Y} \tag{2.2.6}$$

and the boundary conditions (2.2.1) become

$$\Psi = 0, \quad \frac{\partial\Psi}{\partial X} = 0, \quad \text{on } X = 0\pm, \ 0 \le Y \le \frac{1}{2} \tag{2.2.7a}$$

$$\left.\begin{aligned} &\Psi = \omega = 0, && \text{on } Y = 0, \ -\infty < X < \infty \\ &\Psi = -L\cos(t), \ \omega = 0, && \text{on } Y = L, \ -\infty < X < \infty \end{aligned}\right\} \tag{2.2.7b}$$

$$\frac{\partial\Psi}{\partial X} \longrightarrow 0, \quad \frac{\partial\Psi}{\partial Y} \longrightarrow -\cos(t), \quad \omega \longrightarrow 0, \quad \text{as } X \longrightarrow \pm\infty, \ 0 \le Y \le L \tag{2.2.7c}$$

For viable computations we must limit the length of the computational region in the X−direction to $X_L \le X \le X_R$, say, without introducing any significant errors into the computations, see **Fig.2.1**,

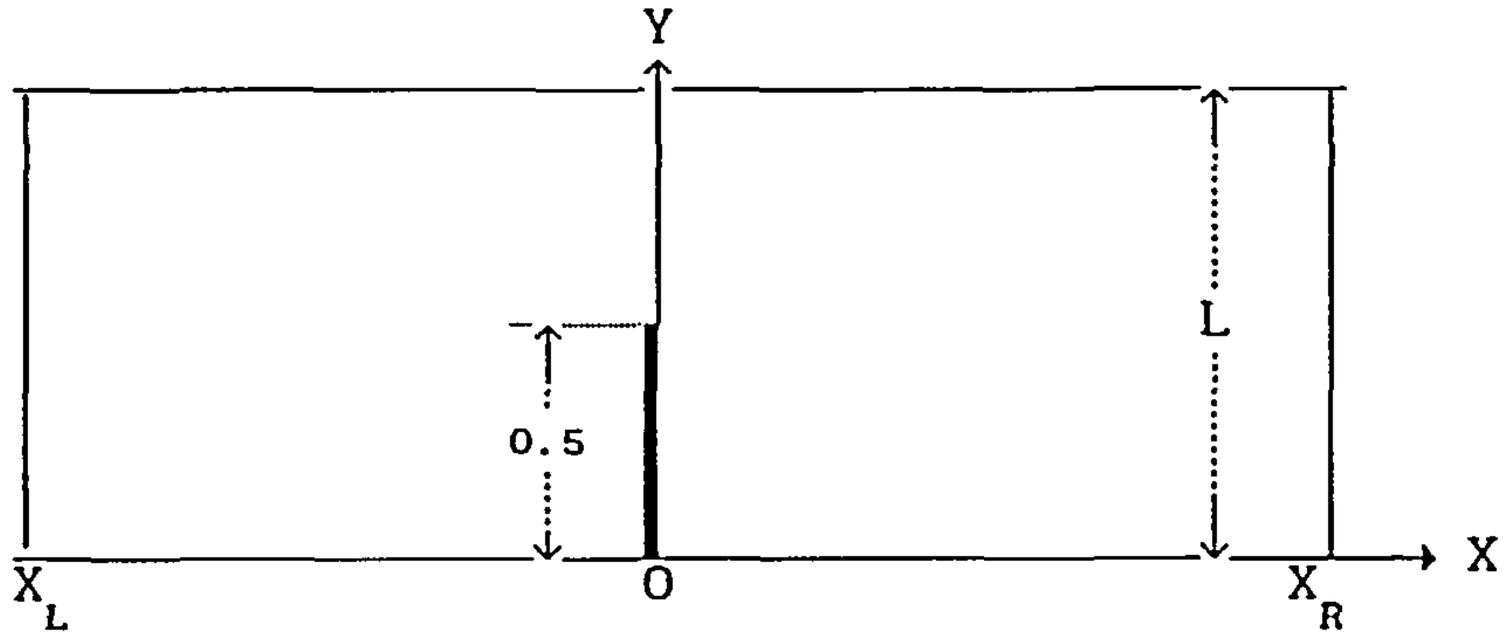

Fig.2.1 The geometry of the computational domain.

As quantities change more rapidly near the cascade than at large values of $|X|$ we introduce the following coordinate transformation

$$\begin{cases} \alpha = \begin{cases} h+\ln(1+D(X-h)) & X > h \\ -h-\ln(1-D(X+h)) & X < -h \end{cases} \\ \eta = Y \end{cases} \qquad (2.2.8)$$

where D is a constant which can be adjusted. In this chapter we take

$$h = \ln (1+Dh), \qquad (2.2.9)$$

where h is a constant mesh size in the η-direction, so that all the meshs in the region $[-2h \le X \le 2h,\ 0 \le Y \le L]$ are square. The governing equations (2.2.3)-(2.2.6) may now be written, for $|\alpha| > h$,

$$\frac{\partial \omega}{\partial t} + (\varepsilon EU \pm \frac{E^2}{R_b})\frac{\partial \omega}{\partial \alpha} + \varepsilon V\frac{\partial \omega}{\partial \eta} = \frac{1}{R_b}(E^2\frac{\partial^2 \omega}{\partial \alpha^2} + \frac{\partial^2 \omega}{\partial \eta^2}) \qquad (2.2.10)$$

$$E^2\left(\frac{\partial^2\Psi}{\partial\alpha^2} \mp \frac{\partial\Psi}{\partial\alpha}\right) + \frac{\partial^2\Psi}{\partial y^2} = -\omega \qquad (2.2.11)$$

with

$$U = \frac{\partial\Psi}{\partial y}, \qquad V = -E\,\frac{\partial\Psi}{\partial\alpha} \qquad (2.2.12)$$

$$\omega = E\frac{\partial V}{\partial\alpha} - \frac{\partial U}{\partial y} \qquad (2.2.13)$$

where $E = D\exp(\mp(\alpha\pm h))$ and the upper and lower signs refer to $\alpha > h$ or $\alpha < -h$, respectively. The governing equations for $\alpha = 0$ are those given in (2.2.3)-(2.2.6) except with α replacing X.

We determine the vorticity on the plate of the cascade at points other than at the edge of the plate using the method of Woods (1954), which gives

$$\omega_B = \frac{3U_B}{h} - \frac{3\Psi_I}{h^2} - \frac{\omega_I}{2} \qquad (2.2.14)$$

where the subscript B denotes a value at a boundary grid point and the subscript I at the first internal grid point along the inward normal to the solution domain at the point B. The quantity U_B is the velocity of the plate (in the (X, Y) co-ordinate system) in the X-direction at the point B.

In order to reduce the solution domain in which we seek a solution we investigate the asymptotic solution of the Navier-Stokes equations for large positive values of X. Using a method similar to that described for a steady state problem by Wilson (1969), Bramley and Dennis (1984) and Ingham *et al.* (1990a), we write, for large positive values of X,

$$\Psi = -Y\cos(t) + e^{-\alpha X}f(Y,t) \qquad (2.2.15)$$

where α (> 0) is an unknown constant and f(Y,t) is an unknown function. It is clear that (2.2.15) satisfies the boundary condition (2.2.7c). Substituting expression (2.2.15) into equations (2.2.3)-(2.2.6) and neglecting terms $O(e^{-2\alpha X})$ and higher, we obtain

$$(\varepsilon\alpha\cos(t) + \frac{\partial}{\partial t})\left(\alpha^2 f + \frac{\partial^2 f}{\partial Y^2}\right) = \frac{1}{R_b}\left(\frac{\partial^4 f}{\partial Y^4} + 2\alpha^2\frac{\partial^2 f}{\partial Y^2} + \alpha^4 f\right) \qquad (2.2.16)$$

We now look for a separable solution of this partial differential equation. Further, as the solution is periodic in Y we assume that $f = \sin(\beta Y)F(t)$, where β is a constant to be determined, and we obtain

$$\frac{dF}{dt} + \alpha\varepsilon\cos(t)F = \frac{1}{R_b}(\alpha^2-\beta^2)F \qquad (2.2.17)$$

In order to obtain solutions which are periodic in time then $\alpha = \beta$ and

$$F(t) = \tilde{c}\ \exp(-\beta\varepsilon\sin(t)) \qquad (2.2.18)$$

where $\tilde{c}$ is an unknown constant; hence

$$\Psi = -Y\cos(t) + \tilde{c}\ \exp(-\beta X)\ \exp(-\beta\varepsilon\sin(t))\ \sin(\beta Y) \qquad (2.2.19)$$

In order to satisfy the boundary conditions (2.2.7b) we require that $\beta = \beta_i = i\pi/L$ (i=1, 2, 3,...) and the leading terms in the expansion (2.2.19) are when $\beta = \beta_1 = \pi/L$.

For X < 0, a similar procedure may be followed and finally we obtain

$$\Psi = -Y\cos(t) + \tilde{c}_{1,2}\exp(\mp\frac{\pi}{L}X)\ \exp(-\frac{\pi}{L}\varepsilon\sin(t))\ \sin(\frac{\pi}{L}Y)$$

$$\text{as } X \longrightarrow \pm\infty,\ 0 \le Y \le L \qquad (2.2.20)$$

where $\tilde{c}_1$ and $\tilde{c}_2$ are constants to be determined for $X > 0$ and $X < 0$, respectively, and the upper (lower) signs correspond to $X > (<) 0$. Implementation of the boundary conditions (2.2.20) is rather complex so we eliminate the constants $\tilde{c}_1$ and $\tilde{c}_2$. This leads to the following asymptotic boundary condition,

$$\frac{\partial \Psi}{\partial X} = \mp \frac{\pi}{L}(\Psi + Y\cos(t)), \qquad \text{as } X \longrightarrow \pm \infty \qquad (2.2.21)$$

which in terms of α becomes

$$E\frac{\partial}{\partial \alpha}(\Psi + y\cos(t)) = \mp \frac{\pi}{L}(\Psi + y\cos(t)) \qquad \text{as } \alpha \longrightarrow \pm \infty \qquad (2.2.22)$$

One grid point that needs special attention is the corner of the plate (S in Fig.2.2) where the vorticity is singular.

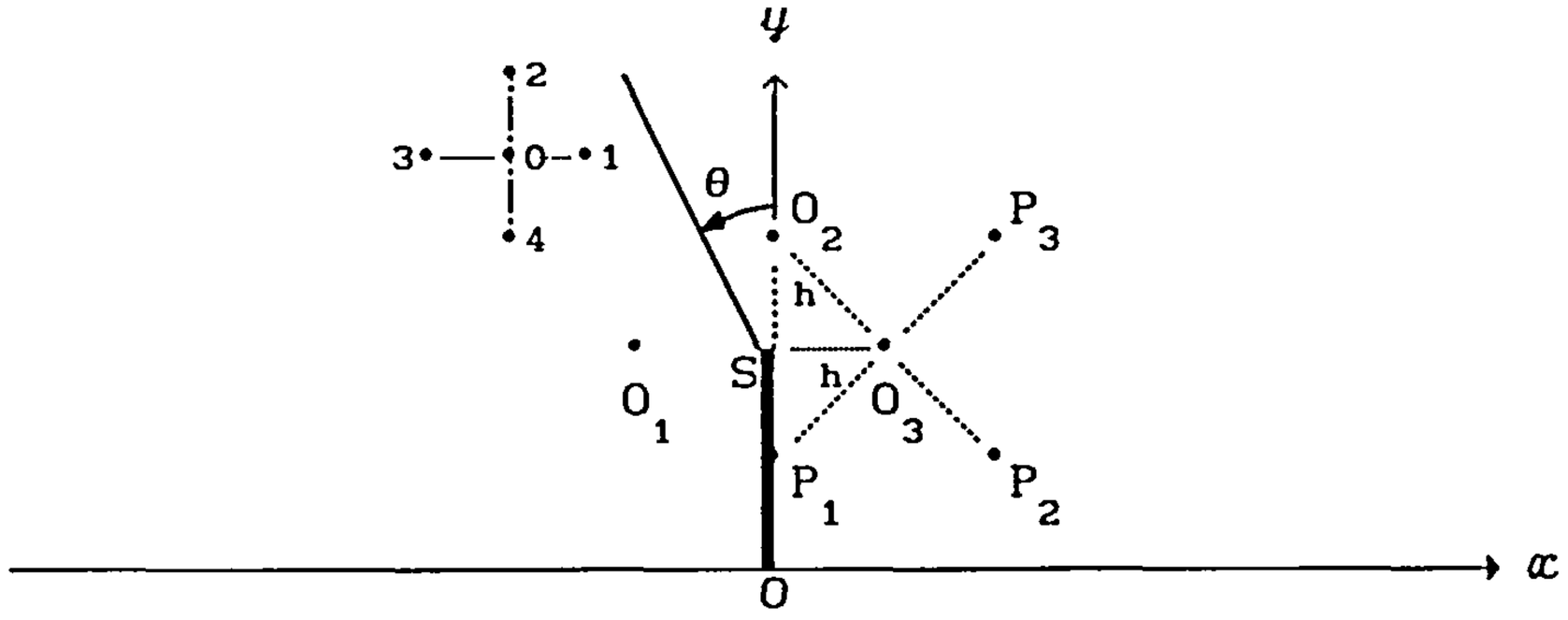

Fig.2.2 Singular & typical grid points in (α, y) plane.

At the points O_1, O_2 and O_3, which are internal grid points near the point S (see Fig.2.2), the usual finite-difference scheme can not be used. Two ways of dealing with this singularity will be discussed in the next section.

2.3 Numerical Procedure and Singularity at the Sharp Corner

A Crank-Nicolson scheme is used to solve the vorticity equation (2.2.10) except that the non-linear terms are treated in a similar way to the method described by Dennis and Hudson (1978) and Ingham *et al.* (1990a) for a similar steady problem in which second-order accuracy is maintained. The choice of the constant D in equation (2.2.9) means that at for $X = 0$ and $0 \le Y \le L$ the mesh is square and there are no difficulties encountered in writing down the finite-difference equations on this line. If h and τ are the mesh sizes in space and time, respectively, and the subscripts 0, 1, 2, 3 and 4 denote the grid points (ih, jh), (ih+h, jh), (ih, jh+h), (ih-h, jh) and (ih, jh-h), respectively, then the finite-difference representation of equations (2.2.10) and (2.2.11) become

$$c_1^{k+1}\omega_1^{k+1}+c_2^{k+1}\omega_2^{k+1}+c_3^{k+1}\omega_3^{k+1}+c_4^{k+1}\omega_4^{k+1}-c_o^{k+1}\omega_o^{k+1}+\Omega(\omega^k)=0 \qquad (2.3.1)$$

$$b_1\Psi_1^{k+1}+b_2\Psi_2^{k+1}+b_3\Psi_3^{k+1}+b_4\Psi_4^{k+1}-b_o\Psi_o^{k+1}+h^2\omega_o^{k+1}=0 \qquad (2.3.2)$$

where

$$c_1^{k+1}=\begin{cases}E_o^2-hE_o(R_eU_o^{k+1}\pm E_o)/2+h^2(R_eU_o^{k+1}\pm E_o)^2/8 & |\alpha|>h\\ 1-hR_eU_o^{k+1}/+h^2R_e^{\,2}(U_o^{k+1})^2/8 & |\alpha|\le h\end{cases} \qquad (2.3.3)$$

$$c_2^{k+1}=1-hR_eV_o^{k+1}/2+h^2R_e^{\,2}(V_o^{k+1})^2/8 \qquad (2.3.4)$$

$$c_3^{k+1}=\begin{cases}E_o^2+hE_o(R_eU_o^{k+1}\pm E_o)/2+h^2(R_eU_o^{k+1}\pm E_o)^2/8 & |\alpha|>h\\ 1+hR_eU_o^{k+1}/+h^2R_e^{\,2}(U_o^{k+1})^2/8 & |\alpha|\le h\end{cases} \qquad (2.3.5)$$

$$c_4^{k+1}=1+hR_eV_o^{k+1}/2+h^2R_e^{\,2}(V_o^{k+1})^2/8 \qquad (2.3.6)$$

$$c_o^{k+1}=c_1^{k+1}+c_2^{k+1}+c_3^{k+1}+c_4^{k+1}+2R_bh^2/\tau \qquad (2.3.7)$$

$$\Omega(\omega^k)=c_1^k\omega_1^k+c_2^k\omega_2^k+c_3^k\omega_3^k+c_4^k\omega_4^k-(c_o^k-2R_bh^2/\tau)\omega_o^k \qquad (2.3.8)$$

$$b_1 = \begin{cases} E_o^2(1 \mp h/2) & |\alpha| > h \\ 1 & |\alpha| \leq h \end{cases} \qquad (2.3.9)$$

$$b_3 = \begin{cases} E_o^2(1 \pm h/2) & |\alpha| > h \\ 1 & |\alpha| \leq h \end{cases} \qquad (2.3.10)$$

$$b_2 = b_4 = 1 \qquad (2.3.11)$$

$$b_o = b_1 + b_2 + b_3 + b_4 \qquad (2.3.12)$$

where the superscripts k represent the value of the function at time $t = k\tau$.

The matrix associated with the set of finite-difference equations (2.3.1) is diagonally dominant under all circumstances. This is because the coefficient of each grid value, c_i^{k+1} (i = 1, 2, 3, 4 and k = 1, 2, 3,...), may be expressed in the form

$$\gamma^2(1+2\mu+2\mu^2) \qquad (2.3.13)$$

and for all values of γ and μ this expression is always greater than zero. Thus

$$c_0^{k+1} > c_1^{k+1} + c_2^{k+1} + c_3^{k+1} + c_4^{k+1} \qquad (2.3.14)$$

and the matrix associated with the set of finite-difference equations (2.3.2) is also always diagonally dominant. Hence an over relaxation iterative scheme may be employed in order to reduce the number of iterations required for convergence. It should be noted that in the unsteady case considered here the convergence may be quicker than that in the steady case because the diagonal dominance is improved in the unsteady case and this can be seen from (2.3.7).

It should also be noted that the iterative procedure may be

used at every mesh point except the points O_1, O_2 and O_3 since the evaluation of ω at these three points involves knowledge of the value of ω at the point S, which is infinite. In order to determine the value of the vorticity at these three points we employ two methods.

Method I uses the modified finite-difference scheme described above except that the finite-difference grid is rotated through 45° at the points O_1, O_2 and O_3, see **Fig.2.2.** Thus, for example, the values of the functions are used at the points $P_1(0, \frac{1}{2} - h)$, $P_2(2h, \frac{1}{2} - h)$, $P_3(2h, \frac{1}{2} + h)$ and $O_2(0, \frac{1}{2} + h)$ to determine the vorticity at the point O_3 and similarly for the points O_1 and O_2. The possibility of being able to use this technique was brought about by the choice of the constant D. This method has been used very successfully in other related problems by Dennis and Smith (1980) and Bramley and Dennis (1984) and full details of this method are to be found in these papers.

An alternative method, II, of dealing with the singularity in the vorticity near S is based on the theory which is valid for steady state flows and was developed by Moffatt (1964) and later by Lugt and Schwiderski (1964), see for example Bramley and Dennis (1984) and Badr *et al.* (1985). For unsteady flows equations (2.2.3) and (2.2.4) near the corner S reduce to

$$R_b \frac{\partial}{\partial t}\nabla^2\Psi = \nabla^4\Psi \qquad (2.3.15)$$

We now look for a solution near S in the form

$$\Psi = \sum_{i=1}^{\infty} r^{\lambda_i} G_i(\theta, t) \qquad (2.3.16)$$

where (r, θ) are the polar coordinates shown in Fig.2.2, $\lambda_1 < \lambda_2 < \ldots$ are some unknown constants and $G_i(\theta, t)$ are unknown functions of θ and t. Substituting expression (2.3.16) into equation (2.3.15) and retaining only the leading terms as $r \longrightarrow 0$ on both sides of the equation gives

$$R_b\, r^{\lambda_1-2}\, \frac{\partial}{\partial t}\left\{ \frac{\partial^2 G_1}{\partial \theta^2} + \ldots \right\} \sim r^{\lambda_1-4}\left\{ \frac{\partial^4 G_1}{\partial \theta^4} + \ldots \right\} \qquad (2.3.17)$$

It is seen that the term of order r^{λ_1-2} on the left hand side of this equation is small compared with the term in r on the right hand side of the equation. This indicates that the form of the solution as obtained for the steady flow is appropriate for the unsteady flow if R_b is not large. Therefore on substituting expansion (2.3.16) into the governing equation, $\nabla^4\Psi = 0$, and solving subject to the boundary conditions (2.2.7a) gives

$$\Psi \sim r^{3/2}\left(A^*(t)\left(\tfrac{1}{3}\cos\left(\tfrac{3\theta}{2}\right) + \cos\left(\tfrac{\theta}{2}\right)\right) + B^*(t)\left(\sin\left(\tfrac{\theta}{2}\right) - \sin\left(\tfrac{3\theta}{2}\right)\right)\right)$$

$$+ r^2 C^*(t)(1 - \cos(2\theta)) + r^{5/2}\left(D^*(t)\left(\cos\left(\tfrac{\theta}{2}\right) - \cos\left(\tfrac{5\theta}{2}\right)\right) + \right.$$

$$\left. + E^*(t)\left(\sin\left(\tfrac{\theta}{2}\right) - \sin\left(\tfrac{5\theta}{2}\right)\right) + \ldots \right. \qquad (2.3.18)$$

and therefore

$$\omega \sim r^{-1/2}\left(-2A^*(t)\cos\left(\tfrac{\theta}{2}\right) + 2B^*(t)\sin\left(\tfrac{\theta}{2}\right)\right) - 4C^*(t)$$

$$+ r^{1/2}\left(-6D^*(t)\cos\left(\tfrac{\theta}{2}\right) - 6E^*(t)\sin\left(\tfrac{\theta}{2}\right)\right) + \ldots \qquad (2.3.19)$$

where $A^*(t)$, $B^*(t)$, $C^*(t)$, $D^*(t)$ and $E^*(t)$ are some unknown functions of t. These five functions are determined at each time level and during each iteration by using values of either, or both,

Ψ and ω at points near S (but not the points O_1, O_2 and O_3). This results in five equations in five unknowns. Once A^*, B^*, C^*, D^* and E^* have been evaluated at a given time then the values of the vorticity at the points O_1, O_2 and O_3 may be determined from expression (2.3.19).

It should be noted that the expansion (2.3.19) is only valid provided that r is sufficiently small and the larger the value of R_b then the smaller is the mesh size that is required to obtain an accurate solution. Ingham *et al.* (1990a) have pointed out that in the steady flow situation the inclined finite-difference scheme near the point S does not give accurate results even at Reynolds number zero and we have also found in this oscillatory flow that this method is inaccurate. Hence all the results presented in this chapter have been obtained using the method II.

Having obtained the finite-difference equations (2.3.1) and (2.3.2) we now use an iterative procedure in order to obtain their solution. The point relaxation iteration method is used and ω_B^{k+1}, ω_o^{k+1} and Ψ_o^{k+1} are obtained from the following expressions

$$(\omega_B^{k+1})^{m+1}=(1-\lambda_B)(\omega_B^{k+1})^m+\lambda_B(3U_B^{k+1}/h-3\Psi_I^{k+1}-\tfrac{1}{2}\omega_I^{k+1})^m \qquad (2.3.20)$$

$$(\omega_o^{k+1})^{m+1}=(1-\lambda_I)(\omega_o^{k+1})^m+\lambda_I(C_1^{k+1}\omega_1^{k+1}+C_2^{k+1}\omega_2^{k+1}$$

$$+C_3^{k+1}\omega_3^{k+1}+C_4^{k+1}\omega_4^{k+1}+\Omega(\omega^k)/c_o^{k+1})^m \qquad (2.3.21)$$

$$(\Psi_o^{k+1})^{m+1}=(1-\lambda_I)(\Psi_o^{k+1})^m+\lambda_I(B_1\Psi_1^{k+1}+B_2\Psi_2^{k+1}$$

$$+B_3\Psi_3^{k+1}+B_4\Psi_4^{k+1}+h^2\omega_o^{k+1}/b_o)^m \qquad (2.3.22)$$

respectively, where $C_i^{k+1}= c_i^{k+1}/c_o^{k+1}$ and $B_i= b_i/b_o$ (i = 1, 2, 3, 4). The superscript m on the right hand side of the above equations

refer to the most recent estimates of ω_B^{k+1}, ω_o^{k+1} and Ψ_o^{k+1} and λ_I and λ_B are relaxation parameters.

The order of the solution procedure was as follows:

(i) At time $t = (k+1)\tau$ one complete iteration for all the internal grid points, except O_1, O_2 and O_3, was performed using expression (2.3.21).

(ii) One complete iteration over all the internal grid points was performed using expression (2.3.22).

(iii) The values of ω at points O_1, O_2 and O_3 were then determined using expressions (2.3.18) and (2.3.19).

(iv) The boundary values of ω were calculated using expression (2.3.20).

(v) The boundary conditions at $X = X_L$ and $X = X_R$ were satisfied using condition (2.2.21).

(vi) If $$\sum \left| 1 - \frac{(\omega^{k+1})^m}{(\omega^{k+1})^{m+1}} \right| > \varepsilon_1 \qquad (2.3.23)$$

where the summation refers to all the grid points and ε_1 is a pre-assigned tolerance, then go to (i).

(vii) Otherwise Ψ_0^{k+1}, ω_0^{k+1}, Ψ_B^{k+1} and ω_B^{k+1} are the solutions for time $t = (k+1)\tau$. We now use these solutions at time $(k+1)\tau$ as the initial guesses of the solution at the time $(k+2)\tau$ and the above procedure is repeated.

For a given value of ε_1 and R_b the calculations were started at time $t = 0$ with the steady state solution with the cascade moving at its maximum speed using the method described by Ingham *et al.* (1990a). The calculations were carried out until t was sufficiently large so that the solution had almost reached a 'periodic' solution.

It should be noted that due to the non-linear terms in the governing equation a purely periodic solution will never be reached everywhere. So the term 'periodic' here means a solution which at time t is very little different from the solution at time $t-2\pi$ for all sufficiently large values of t. Further, as the solution decays to zero at large distances from the cascade then these non-linear effects will not be important in this region.

2.4 Flow Visualisation Experiments

In this section we describe the experimental methods by which some experimental results related to this thesis were obtained.*

A general schematic layout of the equipment in the Geophysical Fluid Dynamics Laboratory at Monash University is shown in Fig.2.3. The experiments were performed in a large rectangular tank of length 2m, width 0.36m filled to a depth of approximately 0.20m with water. Within this tank there is a smaller perspex tank of length 1m, width 0.14m and filled with water to a depth of approximately 0.12m and the smaller tank is fixed at about 0.04m above from the bottom of the larger tank. The temperature of the water in the outer tank was refrigerated and carefully controlled by having a large recirculation of water in the tank so that the temperature on the boundary of the inner tank may be assumed constant. The water in the outer tank was slightly cooled so that there was no loss of heat from either the side or the bottom of the small tank. On top of the small tank there was placed a sheet of perspex, which was covered with bubble plastic in order for it to float. The perspex is painted

---

* All experimental results used in this thesis were obtained by professor B. R. Morton at Monash University, Australia.

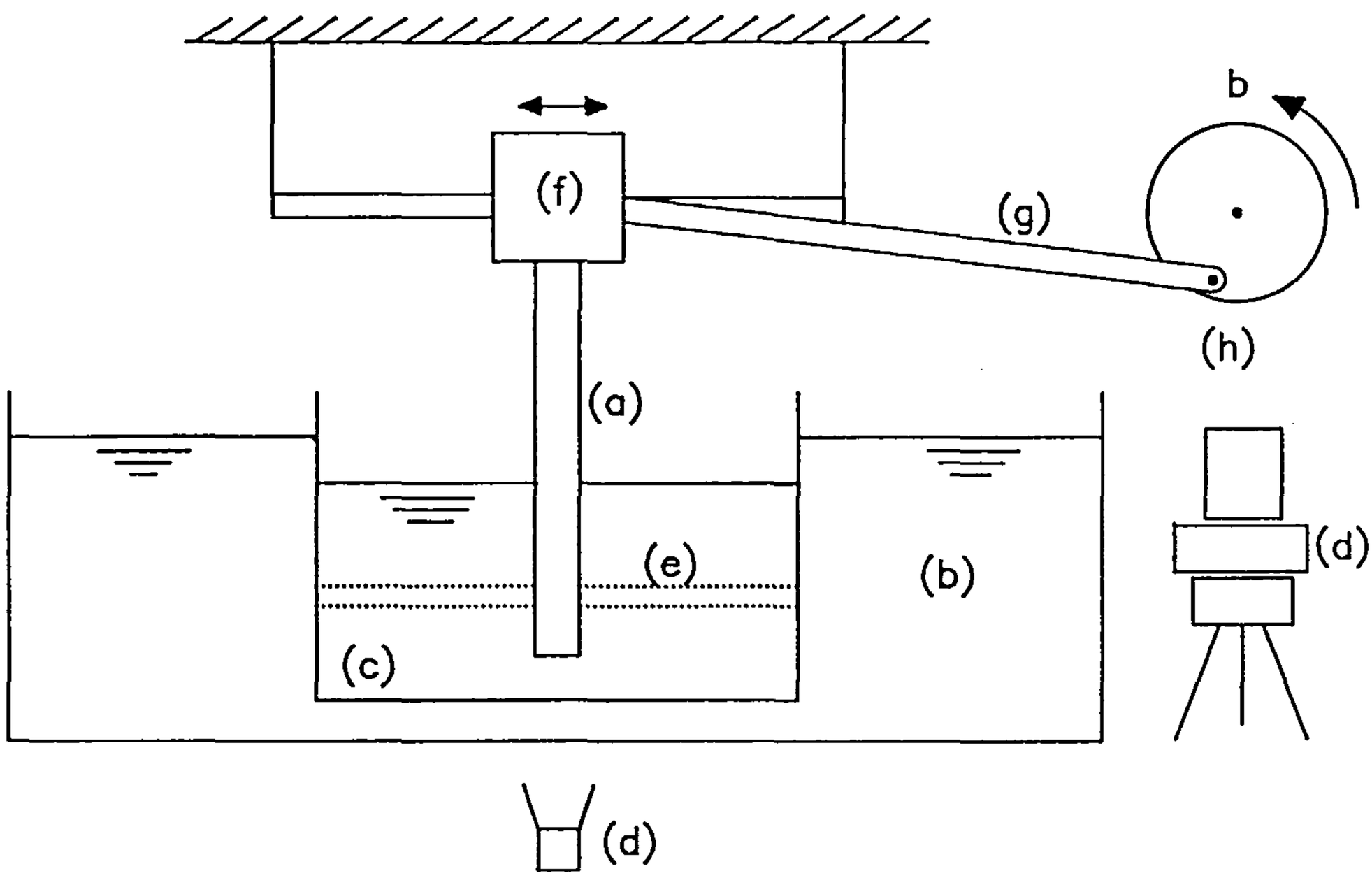

Fig.2.3 Schematic diagram of the experimental apparatus in the Geophysical Fluid Dynamics Laboratory at Monash University, Australia. (a) the cascade, (b) the refrigerated outer tank, (c) the inner tank, (d) the camera, (e) illuminated strip of light, (f) a trolley which is free to move horizontally (the double arrows indicate the motion is harmonic), (g) connecting rod and (h) a geared-down D.C permanent magnet motor with a number of fixed displacement cams.

black in order to reduce the reflection of the light and to increase the contrast in the photographs. However, the main aim of the covering of the top of the small tank was to reduce water evaporation from the surface which causes recirculations. As we are investigating both the instantaneous flow and the second-order effects (in chapter 5) it is absolutely essential that as much care as possible is taken in eliminating thermally driven flows albeit

they are very small. Throughout the experiments the temperature in the test tank was taken at numerous positions within the tank. It was found that typically the temperature in the test tank was position independent, being 12.2°C±0.1°C, whilst the ambient temperature was 19.6°C and the dew point temperature 8.4°C. The closeness of the small tank temperature and the dew point temperature ensures that only a very small amount of evaporation takes place. The surface temperature is higher than the side wall temperature but this just ensures that the water is thermally stratified.

Harmonic oscillations were achieved by using a geared-down D.C. permanent magnet motor with a number of fixed displacement cams. From the cam a connecting rod is attached to a freely moving trolley which runs on top of the large tank. The cascades are firmly fixed to the trolley such that they are vertical and at right angles to the axis of the small tank. The cascade of normal flat plates was made from a thin aluminum plate with teeth of uniform width 0.01m and separated by uniform gaps of 0.01m, i.e. L = 1. Also cascades of rectangular bars and circular cylinders were made from perspex, the rectangular bars were of 0.01m×0.02m rectangular sections (0.01m×0.01m in the case of the square cylinders) whilst the circular cylinders were of diameter 0.01m. Both the square bars and circular cylinders were mounted such that they were 0.01m apart and lie in a plane. The cascades were mounted such that

the teeth of the cascade were about 0.002m above the bottom of the tank and extend out of the water. This configuration minimizes the end effects.

The visualisation was achieved by seeding the entire water with

polyester spheres used in Dulux emulsion paints. These spheres are coated with titanium oxide and have a mean diameter 17μm and only 3% of the mass of particles having a diameter greater than 30μm. The specific gravity varies but is generally within about 5% of that of water and hence the particles settle out of suspension extremely slowly. It is found they stay long enough in suspension for the purpose of photography over a period of about ten hours. However, the tank is stirred every four hours when performing the experiments. Further the length of time taken between photographing different runs varies according to the frequency and amplitude of the previous oscillation. It was found in all experiments performed here that if 20 minutes is left between each set of runs then the residual motion in the tank is minimal when viewing the flow.

The marker particles are illuminated using light from good quality projectors with slits in their focal planes focused into thin horizontal sheets of light between 0.002 and 0.005m thickness in the working section. Two opposed projectors were required to obtain records adequately illuminated both upstream and downstream of the cascade from either side of the tank with one projector upstream and one downstream at the moment of the record. The recording camera was fixed under the tanks and looked vertically down the face of the centre body of the cascade and the thickness of the light sheet in the working section was chosen to illuminate just sufficient particles for a clear record in an exposure time which was variable according the period of oscillation of the cascade and the type of flows of interest. For the unsteady instantaneous flow (in this chapter) the exposure time was 2 to 4 seconds whilst for

the streaming flow it was about 10 times the period of oscillation of the cascade.

2.5 Results and Discussion

Numerical results have been obtained over a wide range of small and moderate values of R_e and R_b. However, in this chapter we concentrate mainly on the case when $R_e = R_b$ as the results obtained when R_e and R_b are of comparable size show the same general flow structure as when $R_e = R_b$. The results presented here have been obtained using mesh sizes h = 1/20, 1/30 and 1/40 and $\tau = \pi/20$, $\pi/40$ and $\pi/60$.

Most of the results presented correspond to $\tau = \pi/60$ and h = 1/40 and the graphical results given are almost indistinguishable from those obtained using the slightly coarser mesh. At small values of R_b the very coarse mesh is quite adequate. Various values of X_L and X_R were taken but it was found that $-X_L = X_R = 10$ was sufficiently large so that any larger values produced almost graphically indistinguishable results. Several values of L have been investigated but in this chapter we concentrate on L = 1. Results obtained with other values of L show the same general flow characteristics. The tolerance, ε_1, was chosen such that all values of ψ were accurate to at least two significant digits. The values of the relaxation parameters varied according to the values of the Reynolds numbers, R_e and R_b, but typically $\lambda_I \sim 1.2$ and $\lambda_B \sim 0.2$ have been found appropriate.

In the steady state situation, with the coordinates fixed in the body, the length of the recirculating eddy behind each plate of the cascade, L_b, is approximately $0.1R_e$, see Ingham *et al.* (1990a),

and in a related problem Smith (1985) also obtained a similar result, see **Fig.2.4**. Of course, in the harmonically oscillating cascade situation the eddy length will vary with time and the length of the eddy was measured when the cascade had reached its maximum velocity, i.e. at times $t = k\pi$ ($k = 1, 2, 3, \ldots$) for various values of R_e. **Fig.2.4** also shows the variation of L_b as a function of R_e at time $t = 10\pi$. At times $t = k\pi$, where k is an integer greater than 10 then the values of L_b are graphically indistinguishable from those obtained when $t = 10\pi$. Since in the oscillating case the cascade is

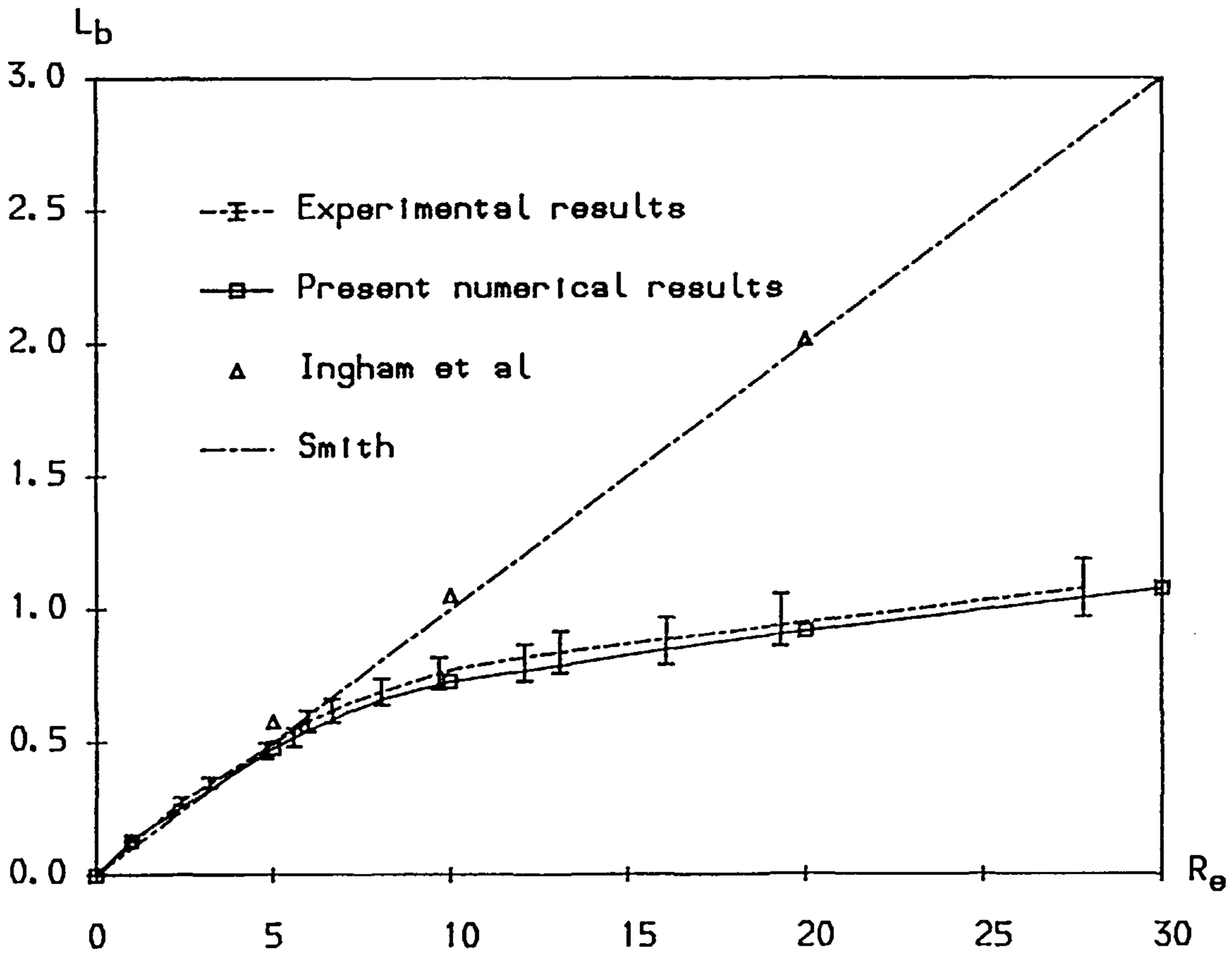

Fig.2.4 The length of the recirculating eddy behind each plate of the cascade as a function of the Reynolds number, R_e, in the steady case as obtained by Ingham *et al.* (1990a) and Smith (1985) and in the unsteady case considered here at $t=10\pi$ and $R_e=R_b$.

at its local maximum Reynolds number when at the centre of its oscillation it is not therefore surprising that the eddy length will be less than that obtained in the corresponding steady state configuration, see **Fig.2.4.**

Both the time at which the recirculating eddies behind the plates of the cascade begin to form and the time variation of the length of the eddy behind the plates, L_b, depend on the Reynolds number. The length of the eddy as a function of time for Reynolds numbers $R_e = R_b = 1$, 5, 10, 20 and 30 is shown in **Fig.2.5.** It is observed that, as expected, the larger the values of R_e the earlier the eddy appears and the longer is the eddy at a given time. Further the eddy length is not a maximum when the cascade is moving at its maximum speed. As the time approaches $(k+0.5)\pi$ then the eddy length begins to grow very quickly and eventually becomes infinite at time $t = (k+0.5)\pi$ (k, an integer) and therefore it is very difficult to determine accurately the value of L_b for $(k+0.4)\pi < t < (k+0.5)\pi$.

In the experimental investigation, periods of oscillation in the range 25-200 seconds were used and this corresponds to values of the Reynolds number of between 3 and 28. If much shorter periods of oscillations are used then the flow becomes asymmetric and it is therefore not possible to compare the results with those calculated numerically. A further difficulty that arises when one compares the experimental and numerical results at a particular cascade displacement is that the camera only records the average flow over the period of the film exposure time. In all the results presented in this chapter a film exposure time of between 2 and 4 seconds has

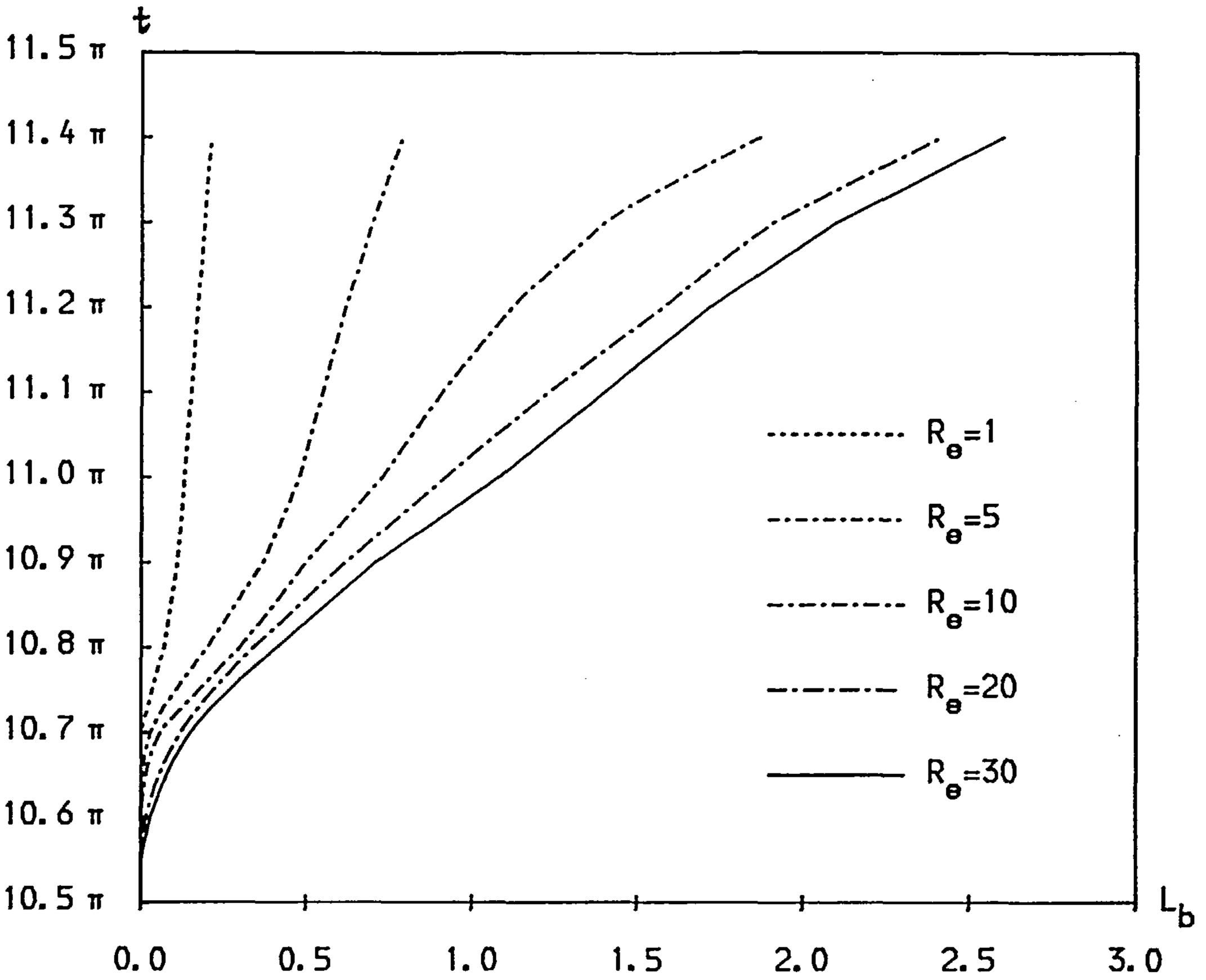

Fig.2.5 The length of the recirculating eddy behind each plate of the cascade as a function of time t for various values of Reynolds number R_e $(=R_b)$.

been used. Any shorter period of film exposure does not give sufficient time for the flow streamlines to be identified. The finiteness of the exposure time has two effects, namely,

(i) the flow patterns are not as sharp as those obtained when determining the corresponding steady state problem, see Ingham *et at.* (1990a), and

(ii) the streamline flow shown on the photographs are an average of the flow over the exposure time.

Several photographs were taken at different frequency of oscillations and with an exposure time T (T = 2 or 4 seconds, normally) such that the cascade passes through its mean position at time T/2. The length of the corresponding eddy as a function of R_e is shown in **Fig.2.4.** During most of the time interval of the exposure the length of the recirculating eddy behind each plate grows linearly with time, see **Fig.2.5,** and hence the assumption made in plotting the data on **Fig.2.4** that the eddy length during the exposure is its mean value during the exposure seems to be reasonable. There is also some experimental error in measuring exactly the length of the recirculating eddy and the limit of the experimental error is shown in **Fig.2.4.** The larger the value of the Reynolds number then the larger will be the experimental error because of the averaging process. It is observed that the numerically predicted value for the eddy length falls within the experimental data points although there is a tendency for the experimental data to be, on average, slightly higher than the numerical predictions. However, bearing in mind all the experimental difficulties that occur, the agreement between the theoretical and experimental results is encouraging. As an example of the experimental observations **Fig.2.6** shows the streamlines when the Reynolds number are 5.6, 6.7, 13.1 and 27.8 and the cascade is passing through its mean position T/2 seconds after the film exposure has started. Although the cascade consists of 7 plates only the flow near two of the plates is shown since if all seven plates are shown much detail is lost in the flow in the recirculating eddies behind the plates. It is seen that the flow is symmetrical but the termination of the eddy is not too clear and there is some

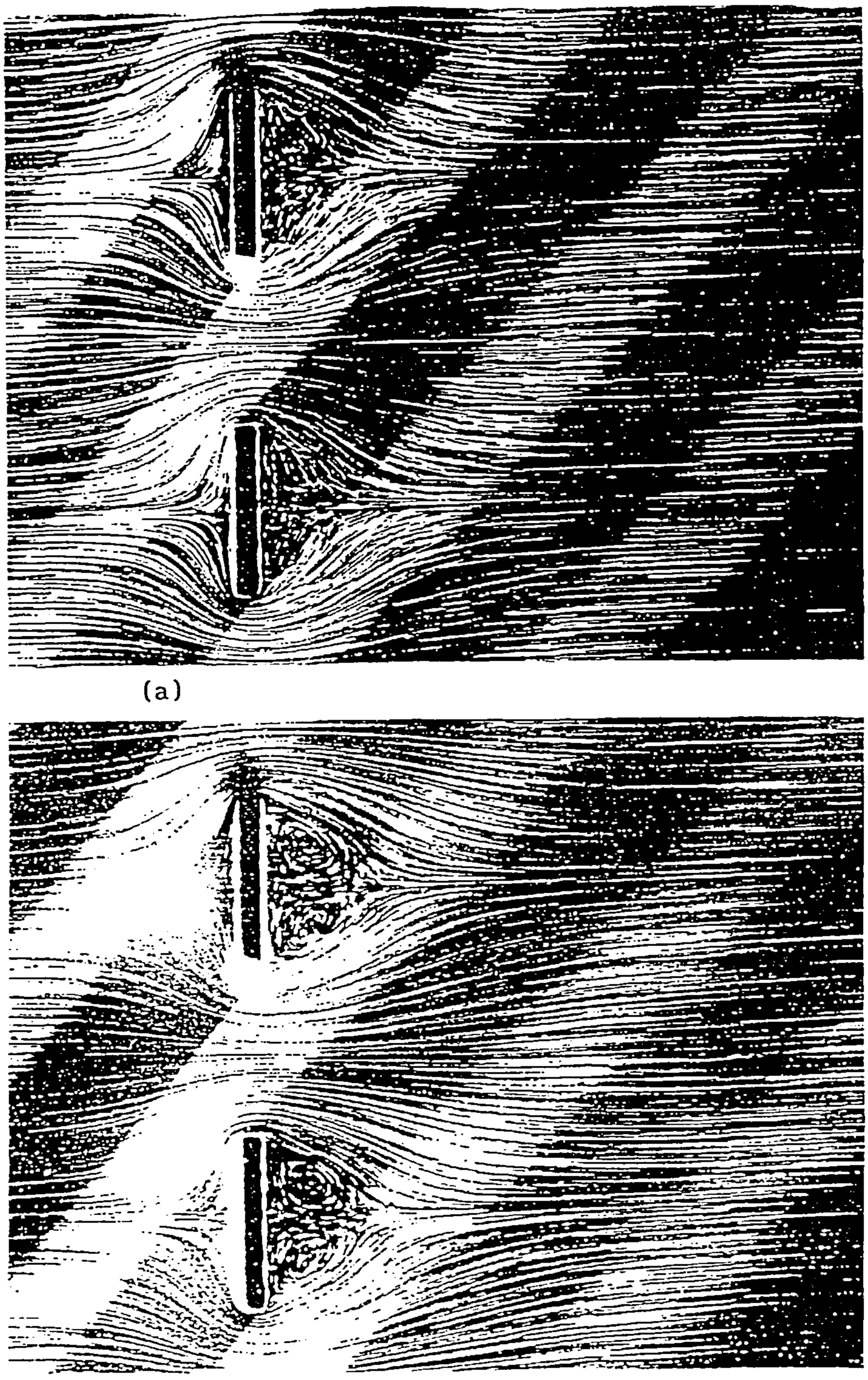

(a)

(b)

Fig.2.6 The instantaneous streamlines obtained experimentally at the time when cascade passes through its mean position ($R_e = R_b$). (to be continued).

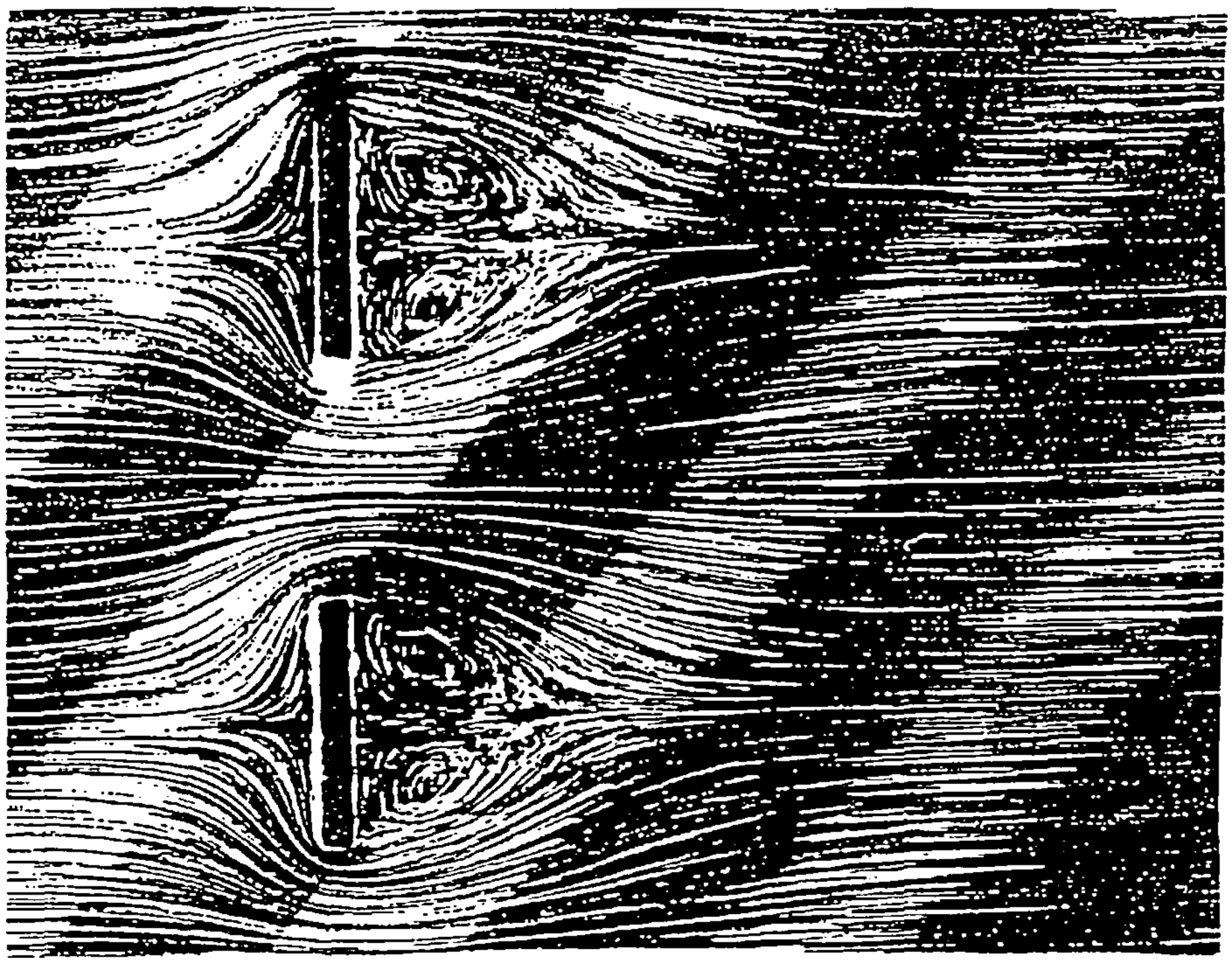

(c)

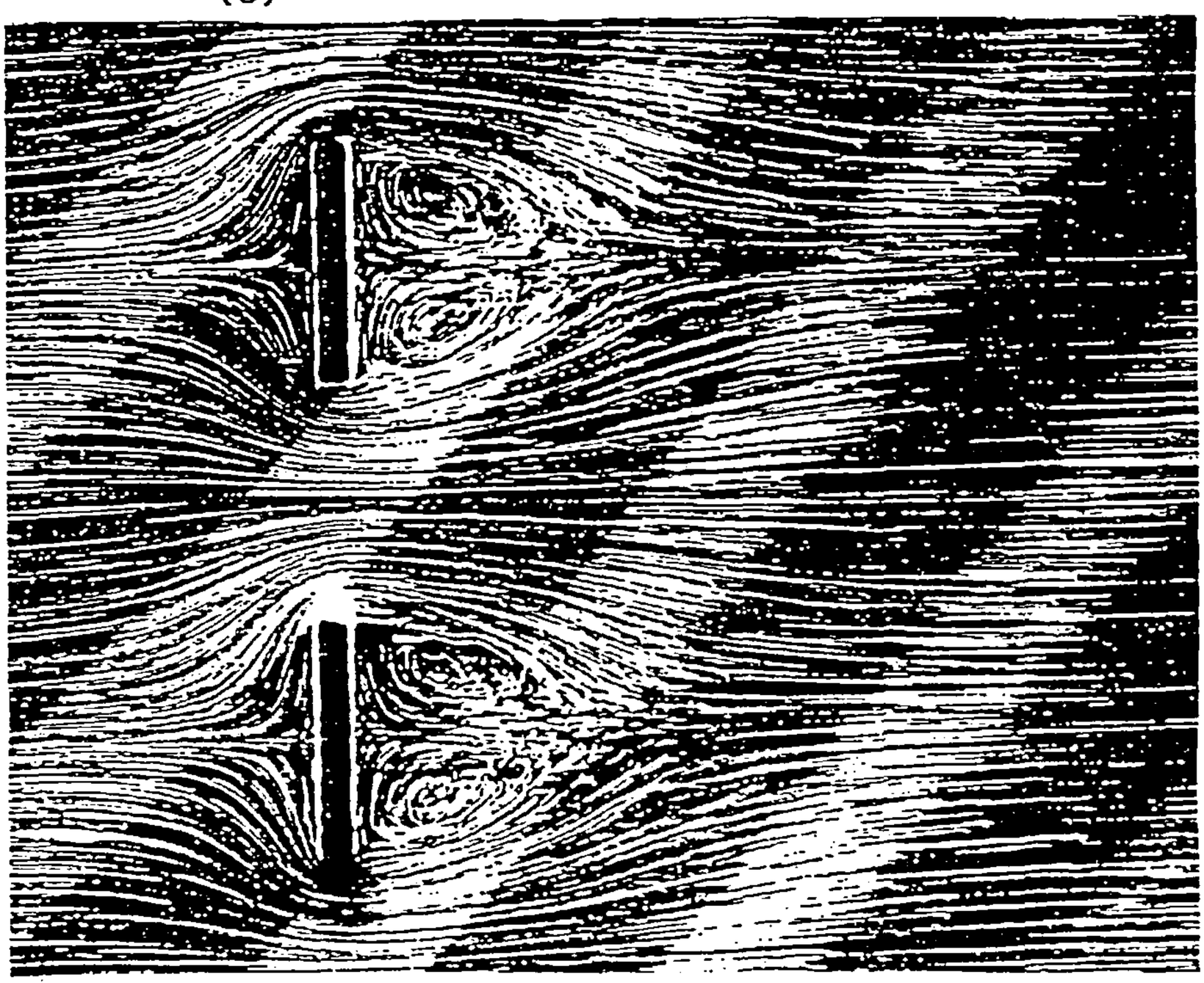

(d)

Fig.2.6 The instantaneous streamlines obtained experimentally at the time when cascade passes through its mean position ($R_e = R_b$). (a) $R_e = 5.6$, (b) $R_e = 6.7$, (c) $R_e = 13.1$, (d) $R_e = 27.8$.

uncertainty in the flow directions. It is seen that the flow separates from the edges of the plates forming an attached bubble consisting of a vortex pair. All these can be seen in our numerical predictions for $R_e = R_b = 5.6$, 6.7, 13.1 and 27.8 which are plotted in **Fig.2.7a**, **Fig.2.7b**, **Fig.2.7c** and **Fig.2.7d**, respectively. A clear agreement between the numerical and experimental results can be observed from **Fig.2.6** and **Fig.2.7**. The diagonal patterns in **Fig.2.6** are caused by the use of light sources slanting rearwards to the left and forwards to the right; these produce bright diagonal bands where the marker particles are illuminated by both sources, and darker bands of roughly half the intensity when one beam is obstructed by a tooth of the cascade.

Numerically it has been found that after $t = 10\pi$ all the results presented here have reached their 'periodic' states, i.e. the results obtained at time t and those obtained obtained at time $t+2\pi$ are graphically indistinguishable everywhere in space, see section 2.3 for a full discussion. **Fig.2.8** shows the streamlines as obtained from the numerical scheme with the co-ordinate system fixed in the cascade for $R_e = R_b = 10$ at several values of time between $t = (10.5+1/40)\pi$ and $t = 11.5\pi$. At time $t = 10.5\pi$ the cascade has come to rest at its maximum positive amplitude. After one further time interval, $t = (10.5+1/40)\pi$, then the cascade has moved to the left and set up a circulation, in the upper part of the upstream flow near the cascade, which is not attached to the cascade. This is in direct contrast to the conventional recirculating flow behind a bluff body. As time increases this recirculation becomes weaker and disappears after a short interval of time. The recirculating eddy behind the plate of the cascade does not appear immediately but by

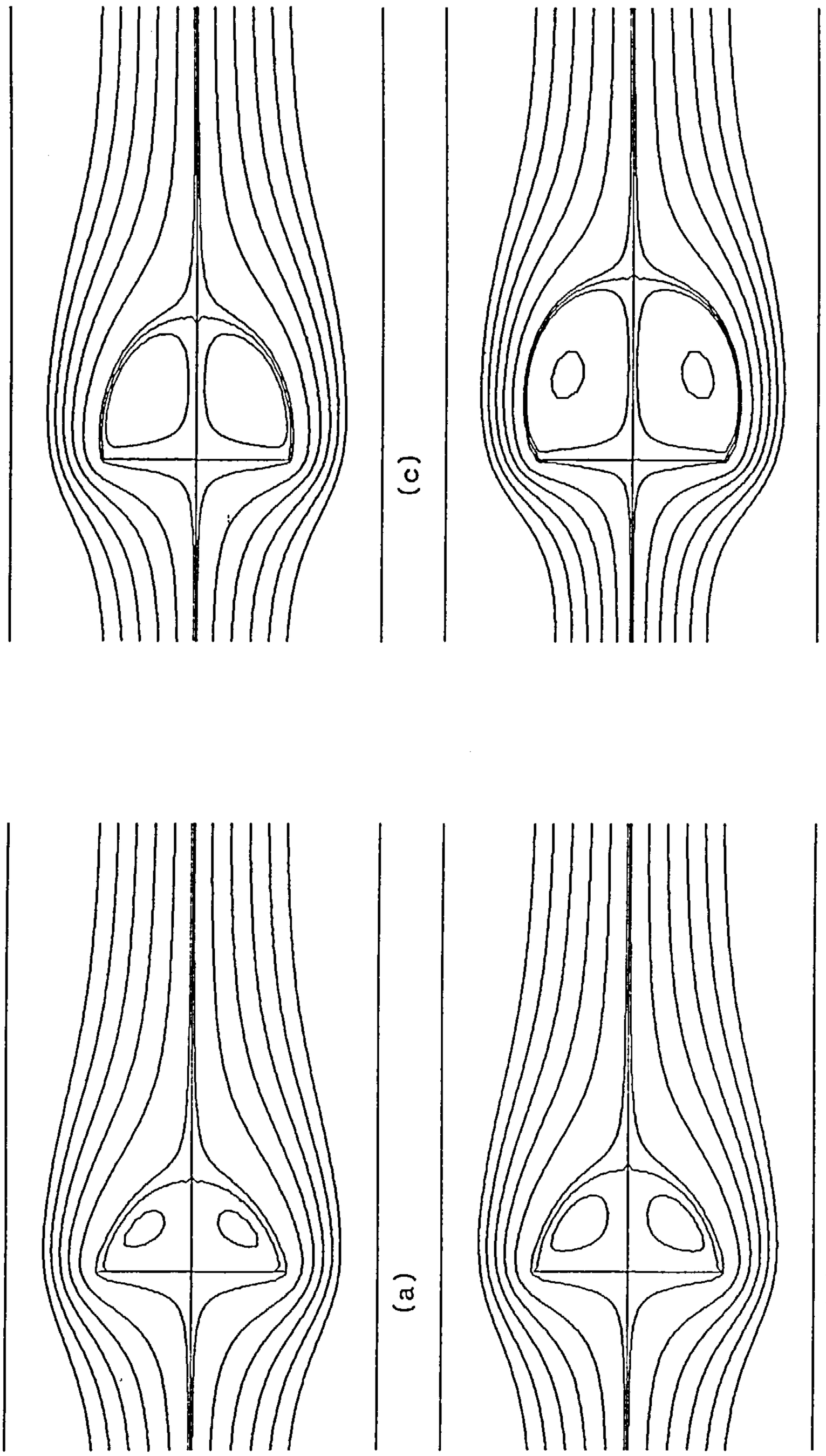

Fig.2.7 The instantaneous streamlines obtained numerically when cascade passes through its mean position at $t = 11\pi$ ($R_e = R_b$). (a) $R_e = 5.6$, (b) $R_e = 6.7$, (c) $R_e = 13.1$, (d) $R_e = 27.8$.

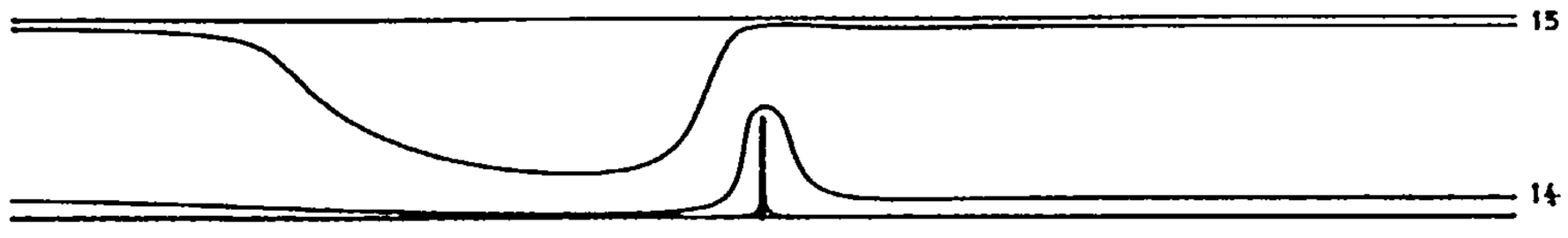

(a)

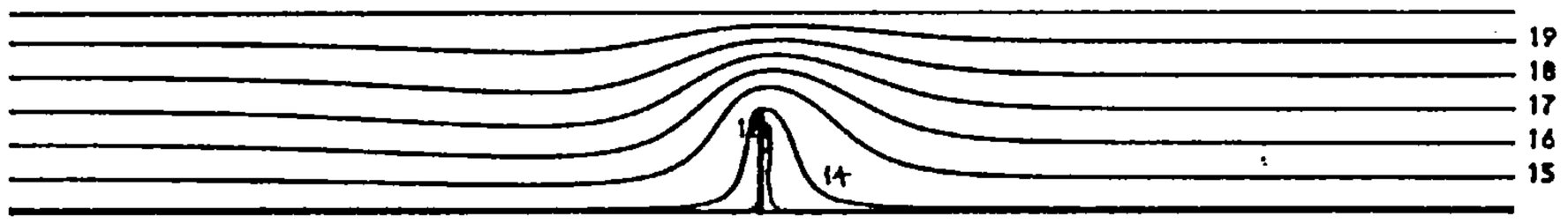

(b)

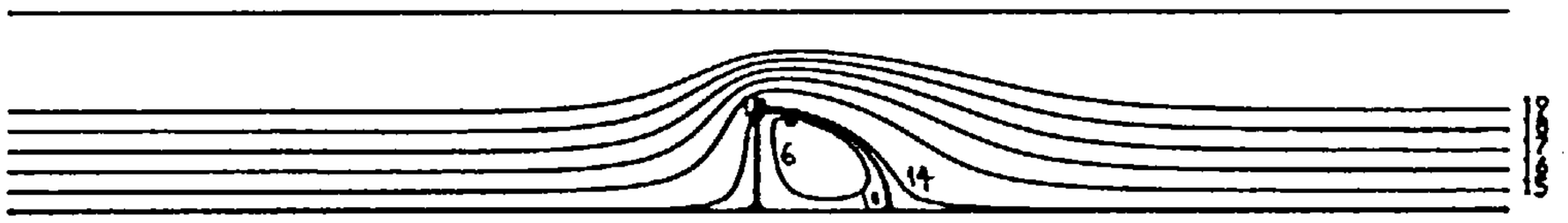

(c)

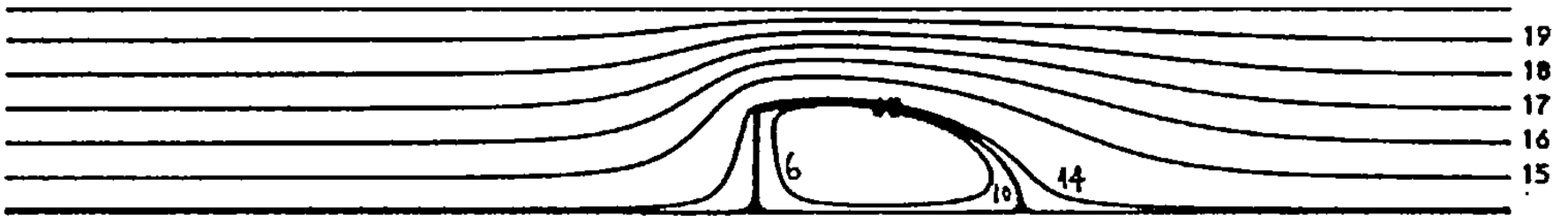

(d)

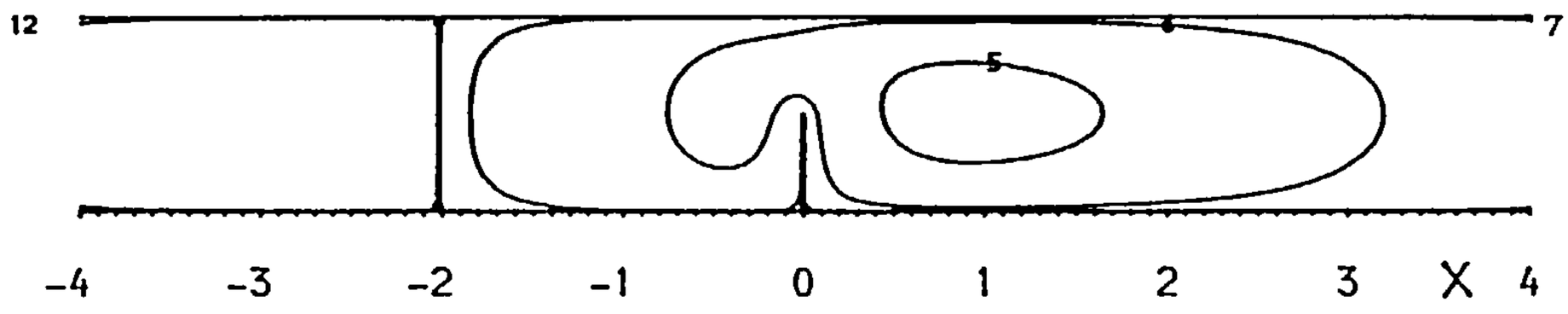

(e)

Fig.2.8 The streamlines Ψ obtained numerically for $R_e=R_b=10$ at different times t. Streamlines labelled 1, 2,..., 19 correspond to Ψ = -0.5, -0.4, -0.3, -0.2, -0.1, -0.01, -0.1×10^{-3}, -0.1×10^{-5}, -0.1×10^{-9}, 0, 0.1×10^{-9}, 0.1×10^{-5}, 0.1×10^{-3}, 0.01, 0.1, 0.2, 0.3, 0.4, 0.5, respectively. (a) $t=(10.5+1/40)\pi$, (b) $t=10.7\pi$, (c) $t=11\pi$, (d) $t=11.3\pi$, (e) $t=11.5\pi$.

the time $t = 10.7\pi$ the eddy has been formed, see **Fig.2.8**, This bubble becomes longer and larger as time increases and it is again interesting to note that the length of the recirculating region at time $t = 11\pi$, i.e. when the cascade is moving at its maximum speed, has not reached its maximum value but it continues to grow until the cascade comes to rest at time $t = 11.5\pi$. At this time the velocity is zero at the body and at infinity but is finite, albeit small, near the cascade. Just before the cascade comes to rest the flow near the plates of the cascade develops a 'bubble' structure and this is presented in **Fig.2.8** at time $t = 11.5\pi$. At time $t = 11.5\pi$ the cascade starts to move in the positive x-direction and the whole process that occurred for $10.5\pi \leq t < 11.5\pi$ starts to develop for $11.5\pi \leq t < 12.5\pi$ except that the cascade is now moving in the opposite direction and the flow has almost periodic behaviour of period 2π.

In order to illustrate the streamline pattern as shown in **Fig.2.8** at a time immediately after the plate has come to rest experimental evidence was sought. Bearing in mind that this flow pattern only exists for a short period of time and that the exposure time of the photograph is limited to a minimum of 2 seconds in order to obtain some detail of the flow streamlines then it may be expected that it would be very difficult to observe such a flow. However, if extreme care is taken then such flows may be observed and **Fig.2.9** shows two such flow patterns for $R_e = R_b = 13.1$. These were obtained using a 2 seconds exposure starting with the plate at its maximum amplitude at $x^* = \pm a$. At the Reynolds number involved this implies that the exposure time was (1/30)th of the period of the

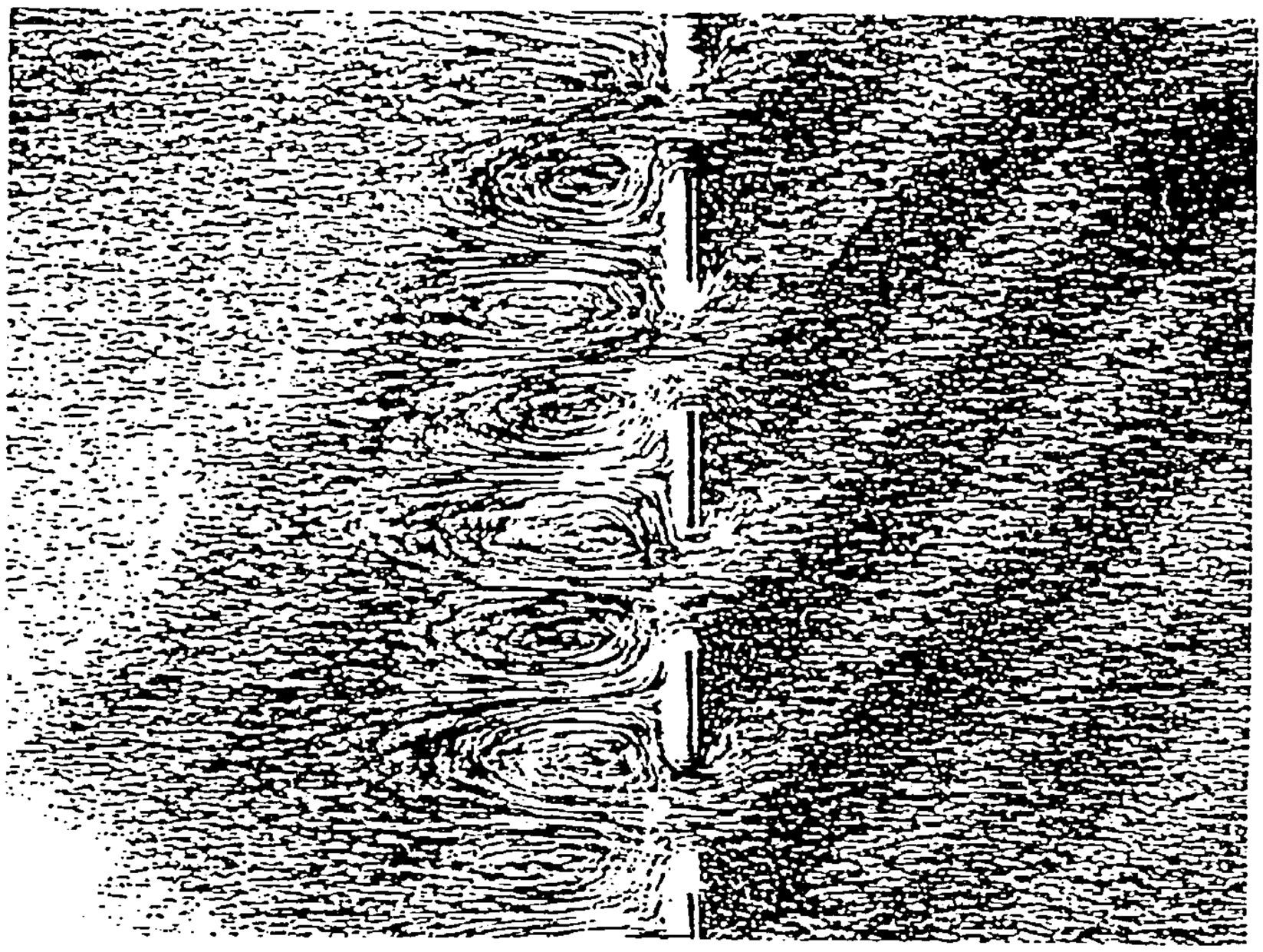

(a)

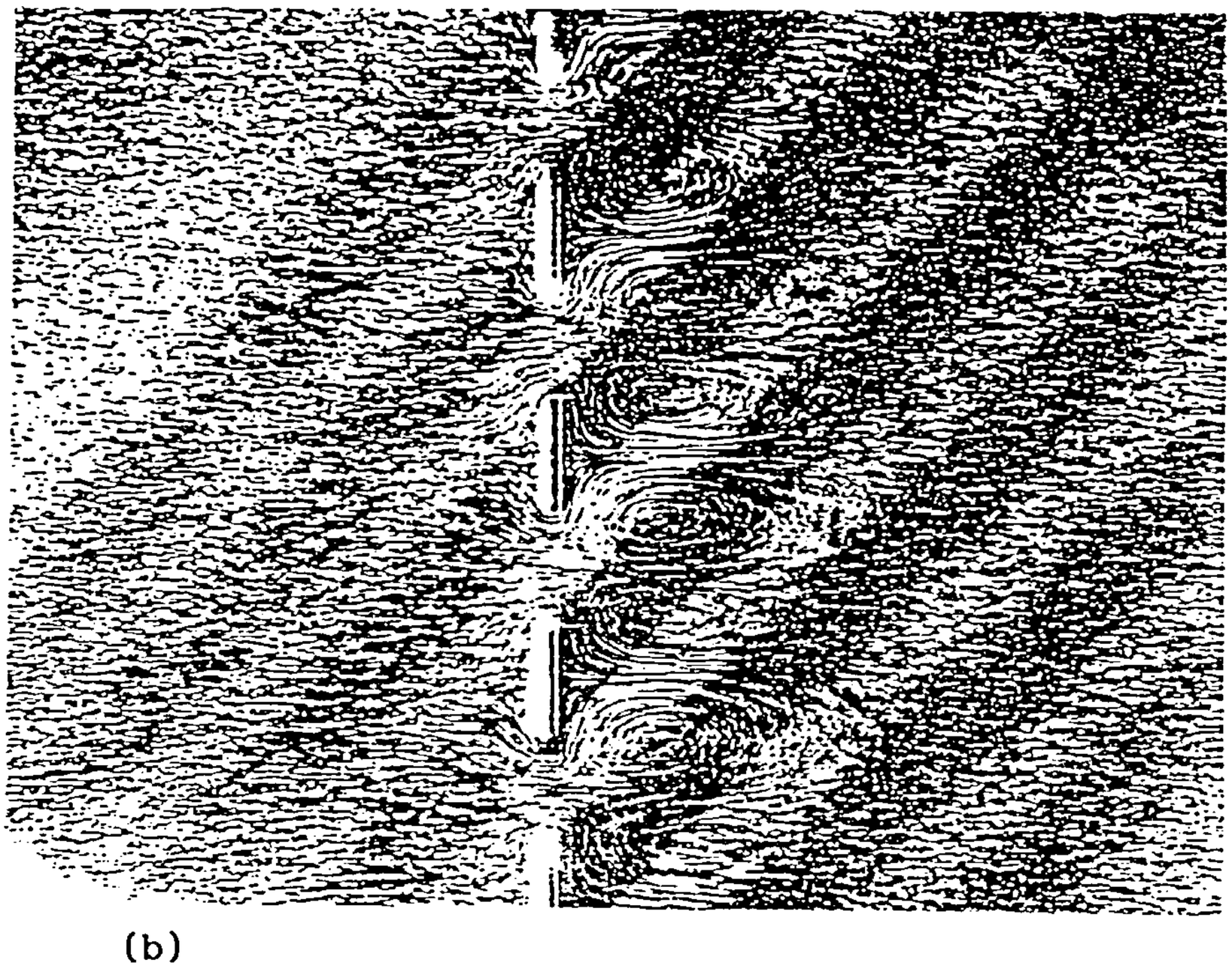

(b)

Fig.2.9 The flow patterns for $R_e = R_b = 13.1$ soon after the cascade has come to rest (exposure time = 2 seconds). (a) Right end, (b) Left end.

oscillation. Hence **Fig.2.9** represents the numerical solution at approximately the mid time of the photograph exposure time. It is observed that there is reasonable agreement between the results obtained in **Fig.2.9** and the numerical predictions of **Fig.2.10** at time $t = (10.5+2/40)\pi$ and $t = (11.5+2/40)\pi$ and that the results obtained in **Fig.2.9a** and **Fig.2.9b** show very similar flow streamlines except that one is the mirror image of the

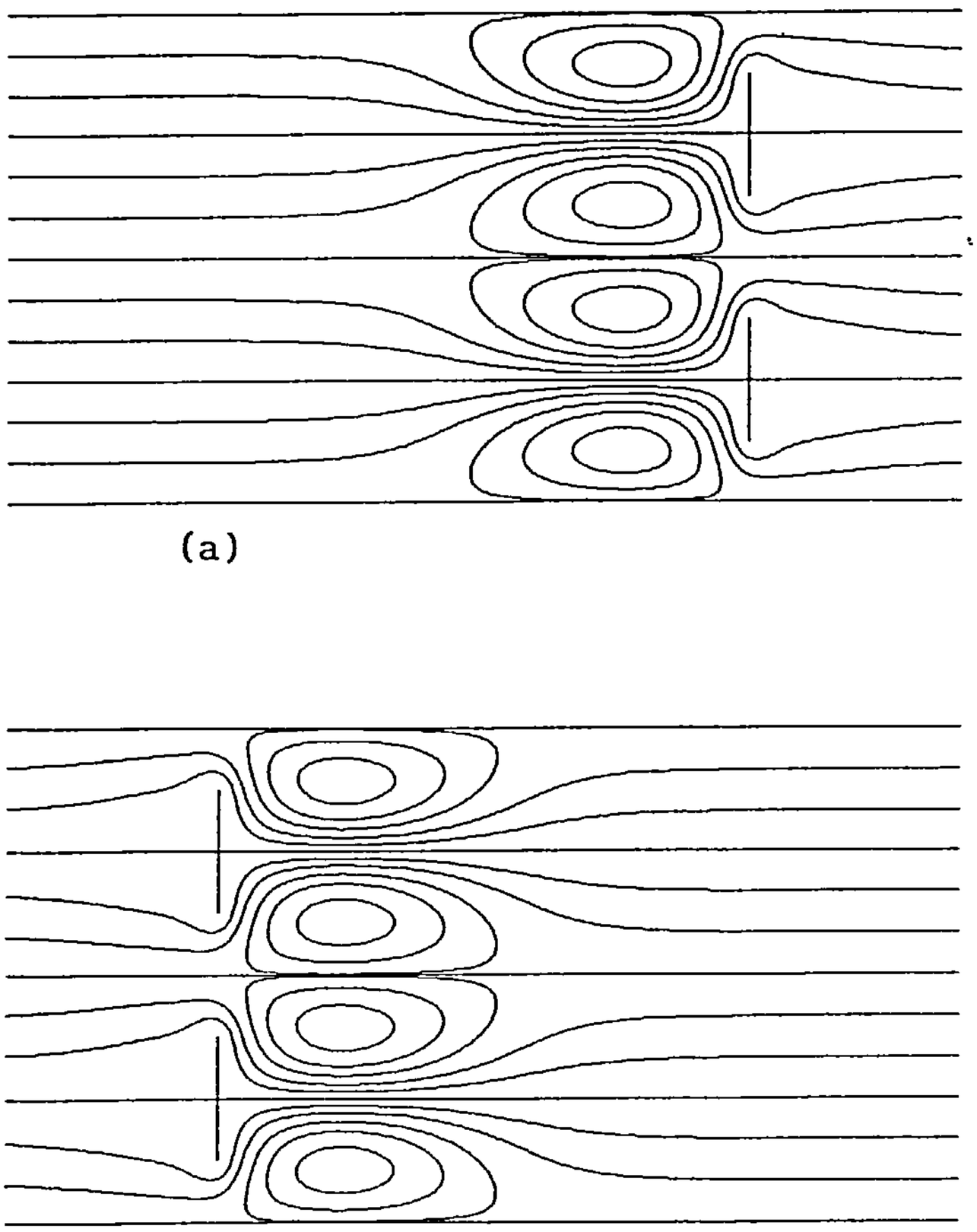

(a)

(b)

Fig.2.10 The instantaneous streamlines obtained numerically for $R_e = R_b = 27.8$ soon after the cascade has come to rest. (a) Right end: at $t = (10.5+2/40)\pi$, (b) Left end: at $t = (11.5+2/40)\pi$.

other and these can also be observed from the numerical results shown in **Fig.2.10a** and **Fig.2.10b**.

Fig.2.11 shows the length of the recirculating eddy, L_b, behind each plate of the cascade at time $t = k\pi$ (k is an integer greater or equal to 10) for $R_e = 10$ and various values of R_b. It is observed that L_b becomes shorter as the value of R_b increases, i.e. ε decreases. This is to be expected since in this limit of parameter

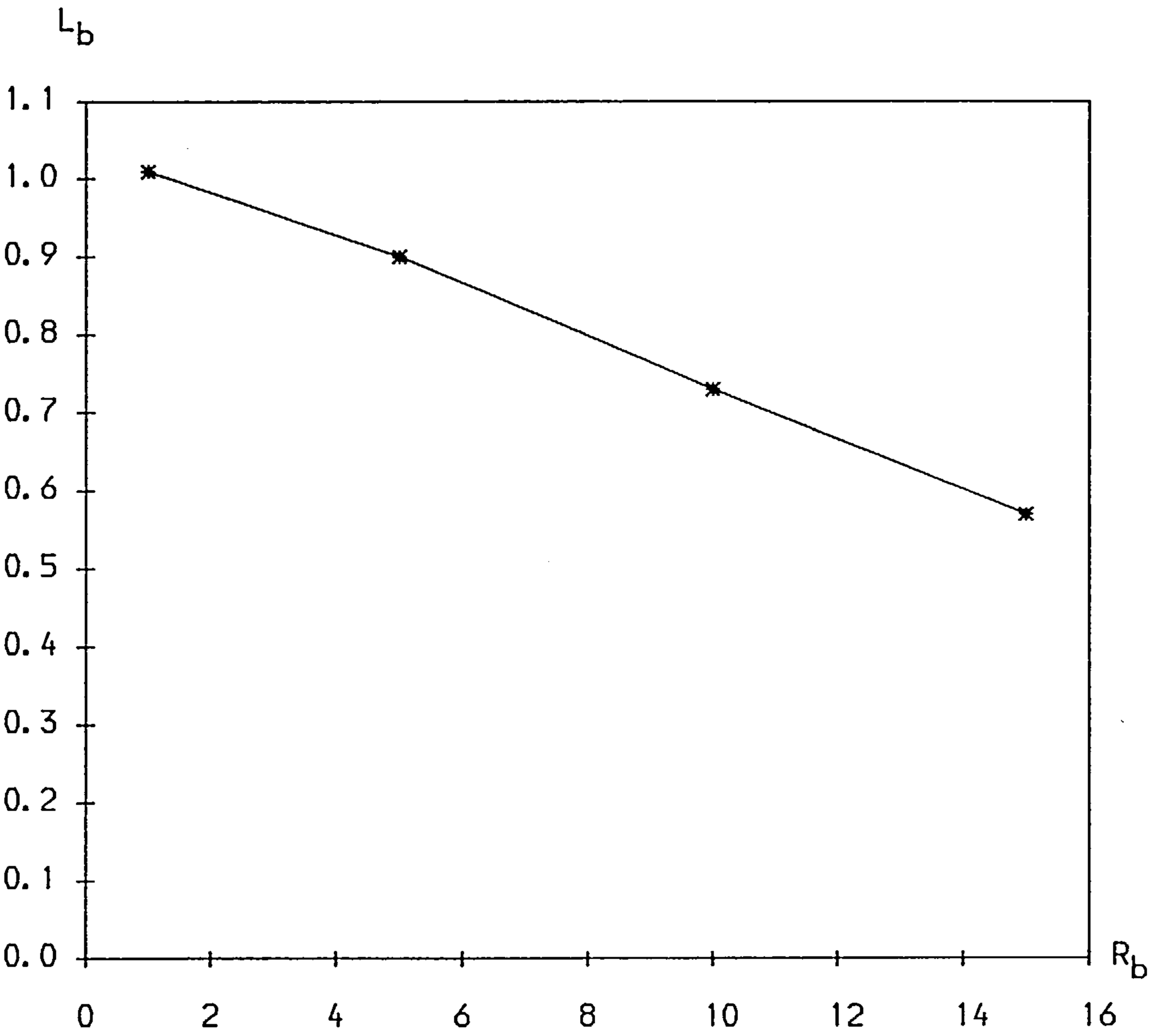

Fig.2.11 The length of the recirculating eddy behind each plate of the cascade at $t=12\pi$ as a function of the Reynolds number R_b for $R_e=10$.

space steady streaming occurs and a Stokes-layer is formed on the plates of the cascade. On the other hand, as R_b becomes smaller, i.e. ε becomes larger, the eddy appears to get longer and at $R_b = 1$ the value of L_b is 1.04 and this represents a length of approximately $0.1R_e$. This is not surprising because the governing equations (2.2.3) and (2.2.4) are dominated by the time independent terms and therefore the steady state flow as given by Ingham *et al.* (1990a), may be an appropriate approximation and in this case the length of the recirculating eddy behind each plate is $0.1R_e$ as R_b tends to zero. Actually as $\varepsilon \longrightarrow \infty$ the flow will become quasi-steady and we will return this later.

Using the transformation (2.2.2) the solution of the problem with the coordinate system fixed in space can be obtained. **Fig.2.12** shows the streamlines for $R_e = R_b = 10$ for various values of time between $t = (10.5+1/40)\pi$ and $t = 11.5\pi$. At time $t = 10.5\pi$ the cascade is at its maximum amplitude in the positive x-direction and at time $t = 10.5\pi+\pi/40$ it has just started to move from rest in the negative x-direction. It is observed that the fluid is being pumped around the plate from infront of the plate to the low pressure area being produced behind the plate. In front of the plate is one large recirculating eddy whilst behind there are two recirculating flows. Clearly the flows alternate in the directions of their recirculations. As time increases and the cascade approaches its mean position the two recirculating regions behind the cascade are swamped in intensity by the flow emanating from just in front of the cascade and these two recirculations disappear. This general flow picture continues right up to the point where the cascade comes to rest at its maximum amplitude with a negative x-displacement. This

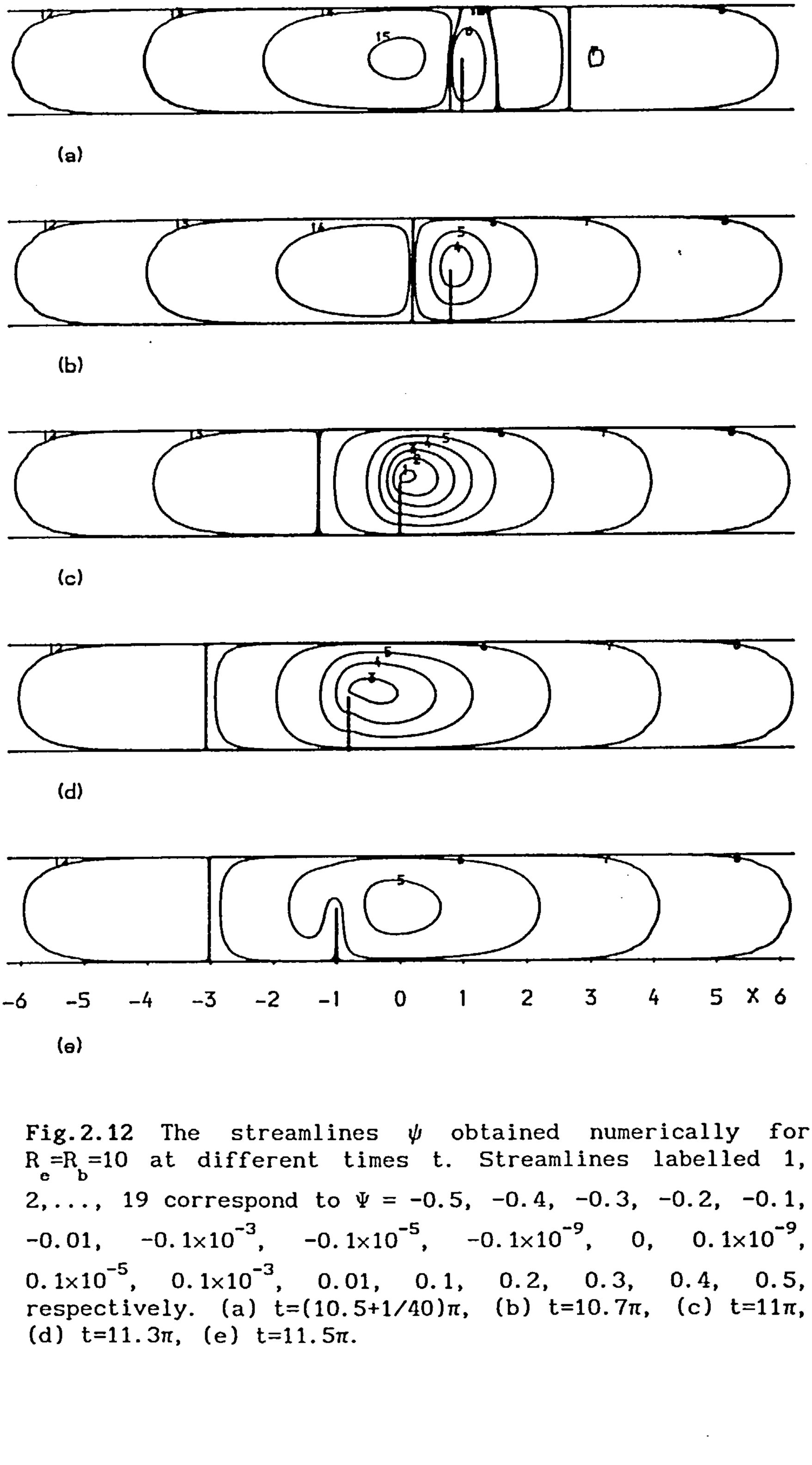

Fig.2.12 The streamlines ψ obtained numerically for $R_e=R_b=10$ at different times t. Streamlines labelled 1, 2,..., 19 correspond to Ψ = -0.5, -0.4, -0.3, -0.2, -0.1, -0.01, -0.1×10^{-3}, -0.1×10^{-5}, -0.1×10^{-9}, 0, 0.1×10^{-9}, 0.1×10^{-5}, 0.1×10^{-3}, 0.01, 0.1, 0.2, 0.3, 0.4, 0.5, respectively. (a) $t=(10.5+1/40)\pi$, (b) $t=10.7\pi$, (c) $t=11\pi$, (d) $t=11.3\pi$, (e) $t=11.5\pi$.

process repeats itself over the next time interval of π except that the cascade is travelling in the positive x-direction and the whole process is repeated every 2π time intervals. It is also seen that the fluid ahead of the plate is almost stationary as is the flow which is behind the recirculation region and this is predicted in Fig.2.12.

As observed above, see Fig.2.12, there is always a secondary circulation generated which is in the opposite direction to the primary circulation at a distance ahead of the cascade. The line, M, which separates the two counter rotating circulations occurs at a station which is almost y independent. The x-component of the distance between the line M and the plane of the cascade, L_d, varies with time and the Reynolds number and the variation of L_d as a function of time t is shown in Fig.2.13 for different values of the Reynolds number R_e ($=R_b$). It is observed that as the Reynolds number increases the length L_d decreases. This is to be expected since, no matter what the value of the parameter ε, if the Reynolds number is sufficiently large then there will be a region very close to the cascade where the flow oscillates from being in front to being behind the cascade. Further this motion will take place in a Stokes boundary-layer which decreases in thickness as the Reynolds number increases.

For a given value of the Reynolds number, R_e, the value of L_d becomes smaller as R_b increases and the variation of L_d as a function of R_b is shown in Fig.2.14 for $R_e = 10$. As R_b increases, for a given value of R_e, then ε decreases and a Stokes-layer develops on the surface of the plates of the cascade. Therefore L_d

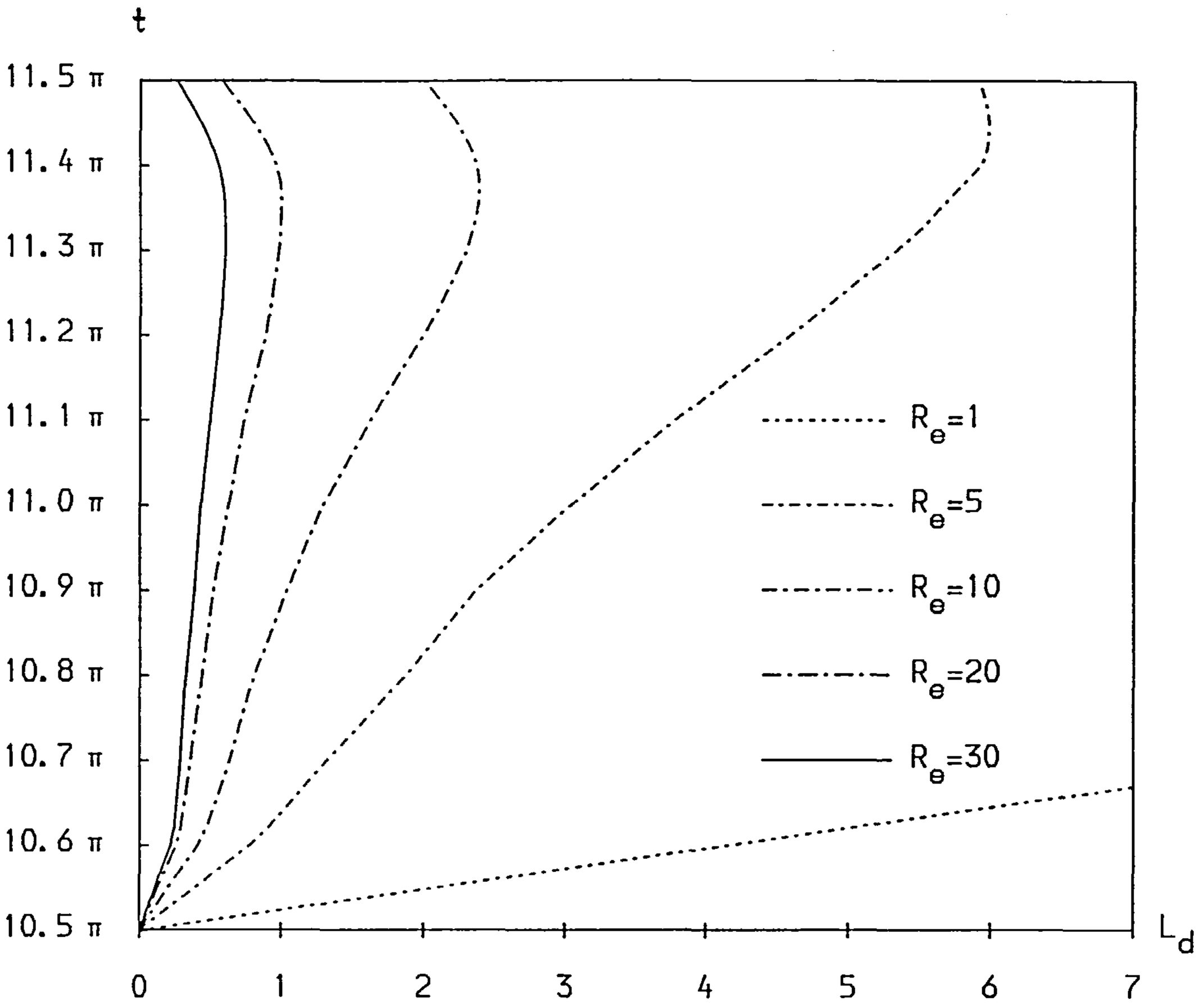

Fig.2.13 Distance between the line, M, dividing the counter rotating circulations and the plane of the cascade as a function of time for $R_e=R_b$.

will decrease and this is shown in Fig.2.14. However, if R_b decreases then ε increases and the flow is then governed by the quasi-steady flow equations and the Stokes-layer becomes very thick. Therefore the division between the two counter rotating circulations becomes large as indicated in Fig.2.14.

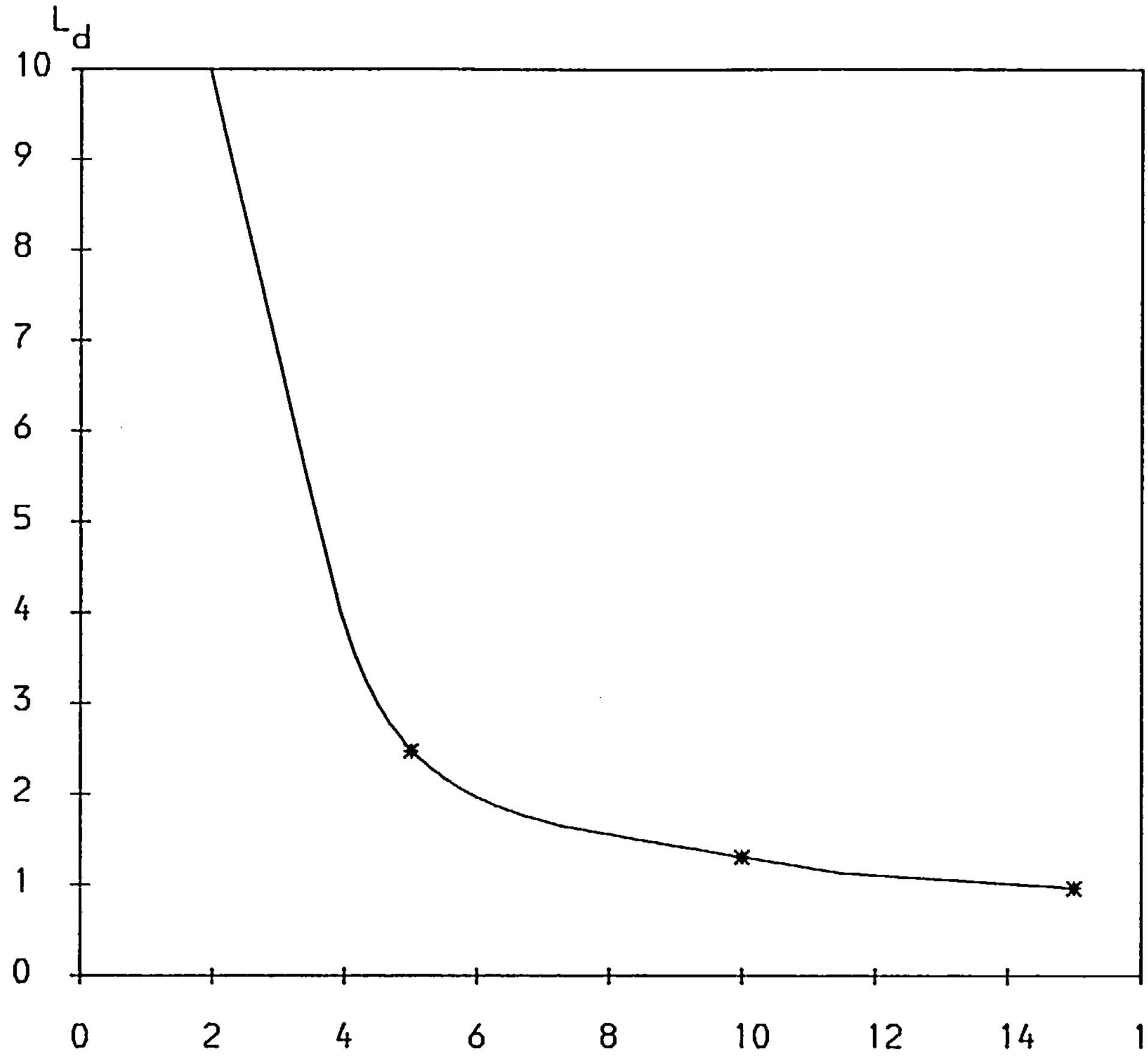

Fig.2.14 Distance between the line, M, dividing the counter rotating circulations and the plane of the cascade as a function of the Reynolds number R_b for R_e=10.

In all the calculations performed for $\varepsilon = 1$ it is observed that the length of the wake bubble behind the body, L_b, starts to be developed soon after the cascade moves from its position of instantaneous rest. Then L_b increases in length until the cascade comes to rest again, see Fig.2.5. However when $\varepsilon \gg 1$, i.e. $R_e \gg R_b$, this is not true and the unsteady flow may become quasi-steady. In this case the flow at time t may be approximately found by solving the

steady state Navier-Stokes equations for the instantaneous Reynolds number and the recirculating region behind the body will increase (decrease) in size as the cascade accelerates (decelerates) and disappear when the instantaneous Reynolds number is zero. In order to illustrate this phenomena numerical results were obtained for R_e = 10 and ε = 1000 and the results shown in **Fig.2.15** for different values of the time t.

The length of the bubble behind the body for R_e = 10 and ε = 1000 as a function of t for half a period of oscillation is plotted in **Fig.2.16** along with the results obtained by Ingham *et al.* (1990a) on solving the corresponding steady state problem. It is observed that there is very little difference between two sets of results and this suggests that for R_e = 10 a value of ε=1000 may be considered sufficiently large for the flow to be considered quasi-steady.

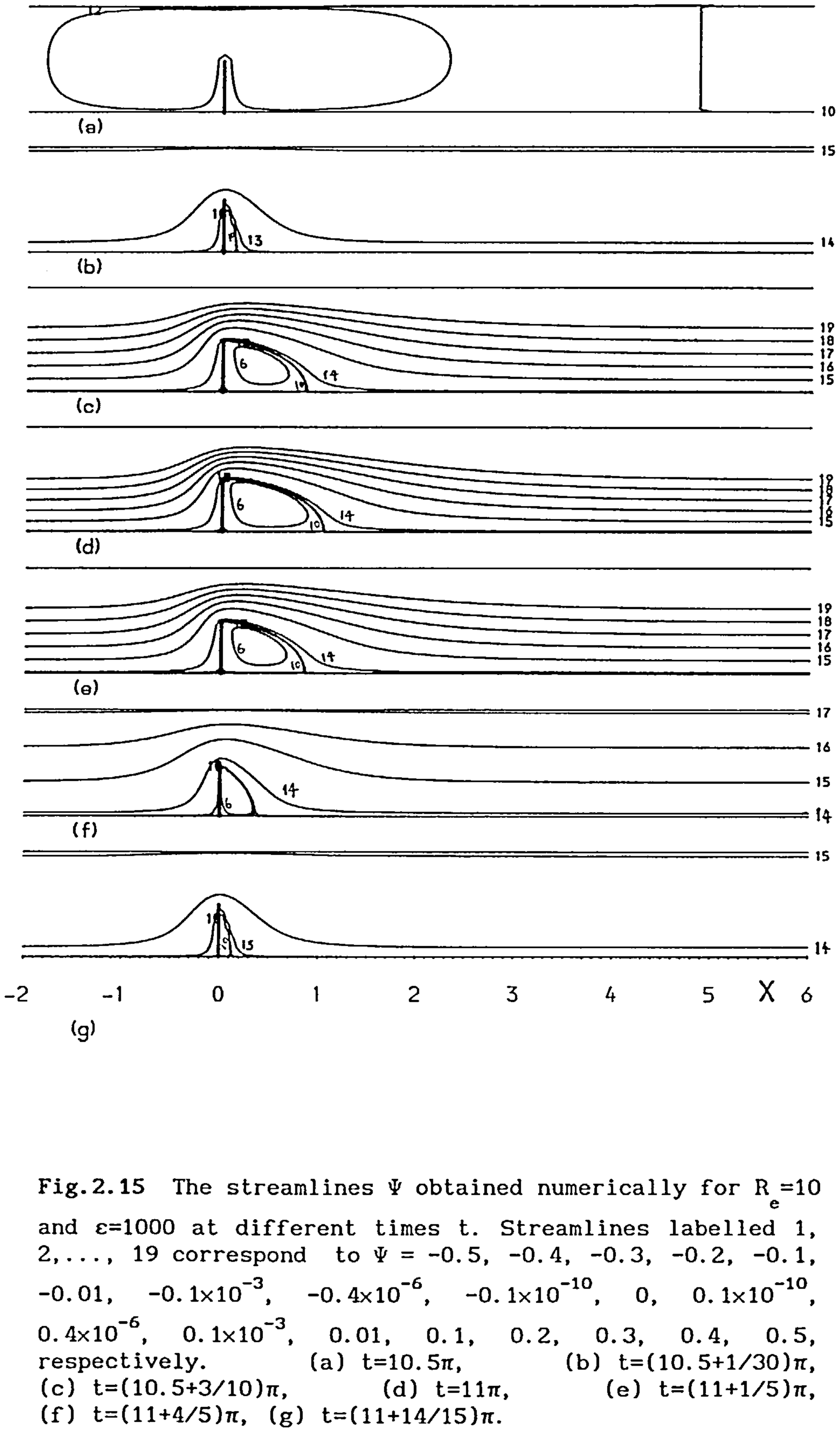

Fig.2.15 The streamlines Ψ obtained numerically for $R_e=10$ and $\varepsilon=1000$ at different times t. Streamlines labelled 1, 2,..., 19 correspond to Ψ = -0.5, -0.4, -0.3, -0.2, -0.1, -0.01, -0.1×10^{-3}, -0.4×10^{-6}, -0.1×10^{-10}, 0, 0.1×10^{-10}, 0.4×10^{-6}, 0.1×10^{-3}, 0.01, 0.1, 0.2, 0.3, 0.4, 0.5, respectively. (a) $t=10.5\pi$, (b) $t=(10.5+1/30)\pi$, (c) $t=(10.5+3/10)\pi$, (d) $t=11\pi$, (e) $t=(11+1/5)\pi$, (f) $t=(11+4/5)\pi$, (g) $t=(11+14/15)\pi$.

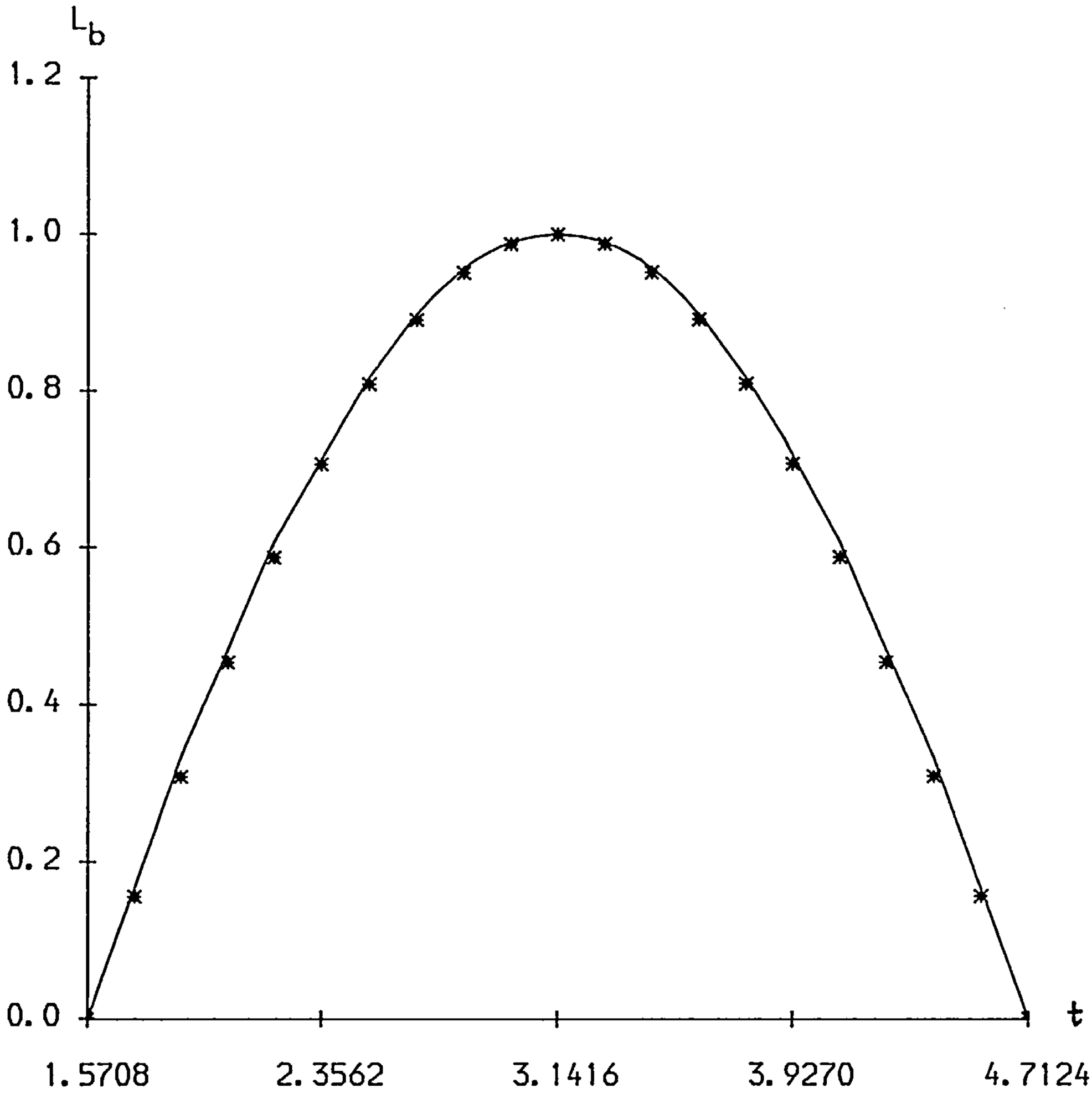

Fig.2.16 The length of the recirculating eddy behind each plate of the cascade as a function of t for R_e=10 and ε=1000. ——— present work, * Ingham *et al.* (1990a).

2.6 Conclusions

A finite-difference scheme which is suitable for a wide range of two-dimensional incompressible, viscous, unsteady problems has been used to solve the oscillating cascade flow. By carefully

dealing with the singularity in the vorticity near the sharp edge of the plate and the boundary conditions at large distances from the body, accurate numerical results have been obtained for the fluid flow induced by an oscillating cascade of normal flat plates for different values of the Reynolds number up to 30 and $\varepsilon = O(1)$. However, the numerical methods used in this chapter can be used for larger values of the Reynolds number and other values of ε, especially for $\varepsilon \geq O(1)$. Numerical results obtained by numerical means show a very good agreement with those obtained experimentally.

CHAPTER 3 NUMERICAL SOLUTIONS FOR THE FLUID FLOWS INDUCED BY A SMALL AMPLITUDE HARMONICALLY OSCILLATING CASCADE

3.1 Introduction

In chapter 2 we have investigated the fluid flow induced by an oscillating cascade of normal flat plates for $\varepsilon = O(1)$ and $R_e \leq 30$ and in this chapter we study the same problem but for $\varepsilon \ll 1$ and $R_b = O(1)$. This problem has been previously studied by Holtsmark *et al.* (1954) when there is just one circular cylinder performing harmonic oscillations. They demonstrated that for very small values of ε the inner streaming layer increases in thickness as R_b decreases. Tatsuno (1974) investigated, experimentally, the streaming flow between two concentric circular cylinders of which the inner one performs harmonic oscillations with $R_b = O(1)$, he found that for small values of ε the streaming flow has an 'inner' flow structure, i.e. the direction of the flow is along the axis of the oscillation and towards the the inner cylinder. Tatsuno (1974) has also studied, experimentally, the streaming due to a harmonically oscillating square cylinder. He showed that for small values of ε and R_b (≈ 26.01) there is an inner layer structure with four vortices which are symmetrically situated around the square and the direction of the streaming flow is along the axis of the oscillations and towards the cylinder. These four vortices develop into eight vortices with two in each quadrant when R_b is larger, 119.7 say. In

this chapter we investigate the flow induced by a cascade of normal flat plates and a cascade of square cylinders which perform harmonic oscillations in an unbounded, incompressible fluid which is otherwise at rest. We concentrate on the case when $\varepsilon \ll 1$ and $R_b = O(1)$, i.e. no boundary-layers exist, and investigate how the value of R_b affects the streaming flow due to the oscillations. We use a perturbation method with ε the small parameter and use the method of separation of variables. The resulting coupled set of partial differential equations for the O(1) flow are then solved by both a numerical and a series truncation method. Further, a numerical technique is employed to obtain both the steady and unsteady flow for the $O(\varepsilon)$ approximation.

3.2 Governing Equations and Perturbation Procedures

In this chapter the fluid flow induced by the oscillations of two infinite cascades of bodies have been investigated, namely, (i) a cascade of normal flat plates and (ii) a cascade of square cylinders, see **Fig.1.5** and **Fig.1.6.**

The fluid at large distances from the cascade is assumed to be at rest and the displacement of the cascade has only a non-zero component in the x^*-direction and it is given by expression (1.1.1). The non-dimensional governing equations in terms of ψ and ω can be written as (1.3.4)-(1.3.5).

Due to the symmetry of the problem we need only consider the flow in the regime $-\infty < x < \infty$ and $0 \leq y \leq L$, see **Fig.3.1**, for the geometry of the solution domain for the cascade of normal flat plates,

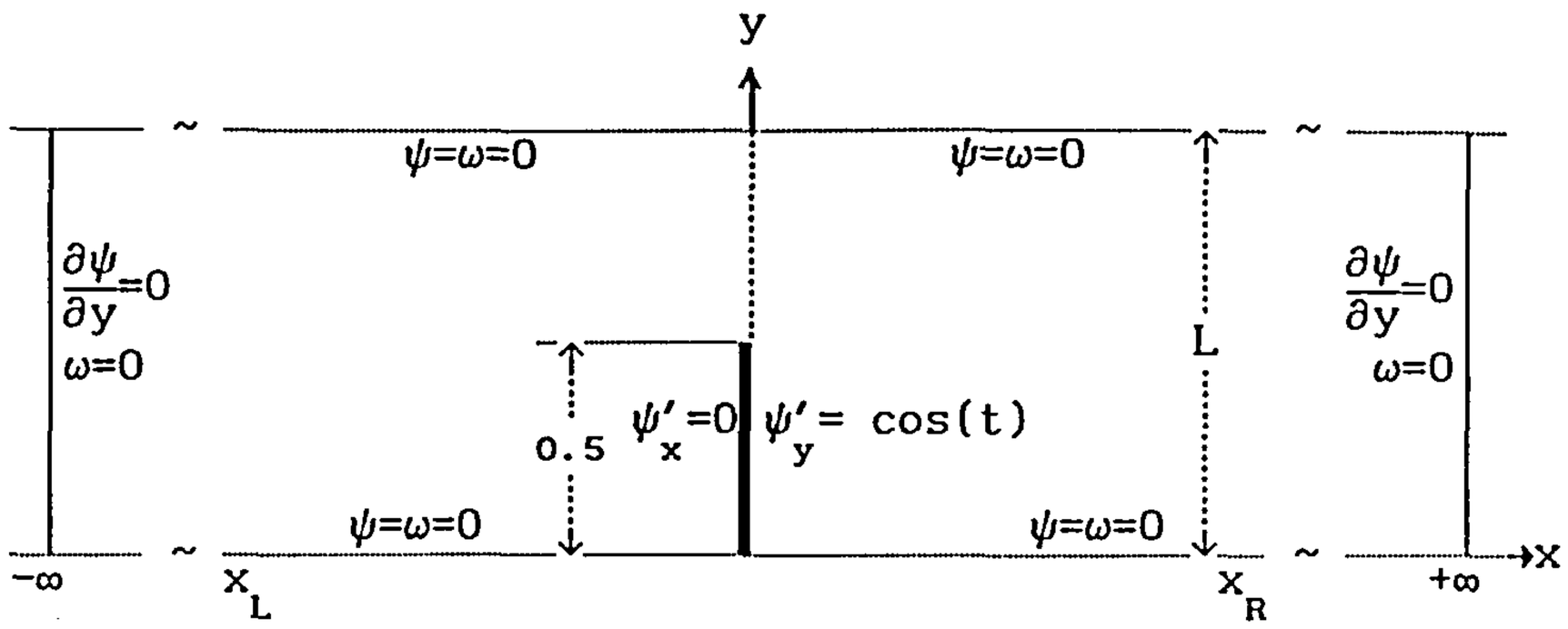

Fig.3.1 The geometry of the solution domain for the cascade of normal flat plates.

In order to illustrate the method used we will describe in detail the formulation for the cascade of the normal flat plates but the extension of the method to deal with cascade of square cylinders is straightforward and has therefore not been included.

Equations (1.3.4)-(1.3.5) must be solved subject to boundary conditions (2.2.1), namely,

$$\psi = y\cos(t), \quad \frac{\partial\psi}{\partial x} = 0 \qquad \text{on } x = \varepsilon\sin(t)\pm,\ 0 \le y \le \frac{1}{2} \qquad (3.2.1a)$$

$$\psi = \omega = 0 \qquad \text{on } y = 0 \text{ and } y = L,\ -\infty<x<\infty \qquad (3.2.1b)$$

$$\frac{\partial\psi}{\partial x} \longrightarrow 0, \quad \frac{\partial\psi}{\partial y} \longrightarrow 0, \quad \omega \longrightarrow 0 \quad \text{as } x \longrightarrow \pm\infty,\ 0 \le y \le L \qquad (3.2.1c)$$

Due to the difficulty in dealing with the boundary condition on the oscillating body, i.e. condition (3.2.1a), we introduce the transformation (2.2.2) and fix the co-ordinate system, (X, Y), in the body. Then the governing equations (1.3.4)-(1.3.5) become (2.2.3)-(2.2.4) which need to be solved subject to boundary conditions (2.2.7), namely,

$$\Psi = 0, \quad \frac{\partial \Psi}{\partial X} = 0 \quad \text{on } X = 0+ \text{ and } X = 0-, \quad 0 \le Y \le \frac{1}{2} \qquad (3.2.2a)$$

$$\Psi = \omega = 0 \qquad \text{on } Y = 0, \quad -\infty \le X \le \infty \qquad (3.2.2b)$$

$$\Psi = -L\cos(t), \quad \omega=0 \qquad \text{on } Y = L, \quad -\infty \le X \le \infty \qquad (3.2.2c)$$

$$\frac{\partial \Psi}{\partial Y} \longrightarrow -\cos(t), \quad \omega \longrightarrow 0 \qquad \text{as } X \longrightarrow \pm\infty, \quad 0 \le Y \le L \qquad (3.2.2d)$$

As we have assumed that ε is small so we look for a solution of equations (1.3.4) and (1.3.5) in the form

$$\psi=\psi_0(x,y,t)+\varepsilon(\psi_1^{(u)}(x,y,t)+\psi_1^{(s)}(x,y))+O(\varepsilon^2) \qquad (3.2.3a)$$

$$\omega=\omega_0(x,y,t)+\varepsilon(\omega_1^{(u)}(x,y,t)+\omega_1^{(s)}(x,y))+O(\varepsilon^2) \qquad (3.2.3b)$$

where the superscripts (s) and (u) denote the steady and unsteady components of the $O(\varepsilon)$ perturbations, respectively.

Substituting (3.2.3) into equations (1.3.4) and (1.3.5) and equating the coefficients of the same powers of ε we obtain

$O(1)$ terms:

$$\frac{\partial \omega_0}{\partial t} = \frac{1}{R_b}\nabla^2\omega_0 \qquad (3.2.4a)$$

$$\nabla^2\psi_0 = -\omega_0 \qquad (3.2.4b)$$

$O(\varepsilon)$ terms:

$$\frac{\partial \omega_1^{(u)}}{\partial t} + \left\{\frac{\partial(\omega_0,\psi_0)}{\partial(x,y)}\right\}^{(u)} = \frac{1}{R_b}\nabla^2\omega_1^{(u)} \qquad (3.2.5a)$$

$$\nabla^2\psi_1^{(u)} = -\omega_1^{(u)} \qquad (3.2.5b)$$

$$\left\{\frac{\partial(\omega_0,\psi_0)}{\partial(x,y)}\right\}^{(s)} = \frac{1}{R_b}\nabla^2\omega_1^{(s)} \qquad (3.2.6a)$$

$$\nabla^2\psi_1^{(s)} = -\omega_1^{(s)} \qquad (3.2.6b)$$

In the co-ordinate system fixed in the body we write Ψ and ω in the forms

$$\Psi=\Psi_0(X,Y,t)+\varepsilon(\Psi_1^{(u)}(X,Y,t)+\Psi_1^{(s)}(X,Y))+O(\varepsilon^2) \qquad (3.2.7a)$$

$$\omega=\omega_0(X,Y,t)+\varepsilon(\omega_1^{(u)}(X,Y,t)+\omega_1^{(s)}(X,Y))+O(\varepsilon^2) \qquad (3.2.7b)$$

which on substituting into equations (2.2.3)-(2.2.4), and collecting up the same powers of ε, gives,

O(1) terms:

$$\frac{\partial\omega_0}{\partial t} = \frac{1}{R_b}\nabla^2\omega_0 \qquad (3.2.8a)$$

$$\nabla^2\Psi_0 = -\omega_0 \qquad (3.2.8b)$$

$O(\varepsilon)$ terms:

$$\frac{\partial\omega_1^{(u)}}{\partial t} + \left\{\frac{\partial(\omega_0,\Psi_0)}{\partial(X,Y)}\right\}^{(u)} = \frac{1}{R_b}\nabla^2\omega_1^{(u)} \qquad (3.2.9a)$$

$$\nabla^2\Psi_1^{(u)} = -\omega_1^{(u)} \qquad (3.2.9b)$$

$$\left\{\frac{\partial(\omega_0,\Psi_0)}{\partial(X,Y)}\right\}^{(s)} = \frac{1}{R_b}\nabla^2\omega_1^{(s)} \qquad (3.2.10a)$$

$$\nabla^2\Psi_1^{(s)} = -\omega_1^{(s)} \qquad (3.2.10b)$$

3.3 The O(1) Approximation Using The Series Truncation Method

The first-order approximation is now governed by equations (3.2.4) along with the boundary conditions (3.2.1) with $\varepsilon=0$. We therefore look for a solution in the form

$$\psi_0 = f_0(x,y)\sin(t) + F_0(x,y)\cos(t) \qquad (3.3.1a)$$

$$\omega_0 = g_0(x,y)\sin(t) + G_0(x,y)\cos(t) \qquad (3.3.1b)$$

where $f_0(x,y)$, $F_0(x,y)$, $g_0(x,y)$ and $G_0(x,y)$ are unknown functions which have to be determined. Substituting expressions (3.3.1) into equations (3.2.4) and equating like terms of sin(t) and cos(t) leads to the set of partial differential equations

$$\nabla^2 f_0 = -g_0 \qquad (3.3.2a)$$

$$\nabla^2 F_0 = -G_0 \qquad (3.3.2b)$$

$$\nabla^2 g_0 = -R_b G_0 \qquad (3.3.2c)$$

$$\nabla^2 G_0 = R_b g_0 \qquad (3.3.2d)$$

Bearing in mind that both the governing equations and the boundary conditions are symmetrical about x=0 the boundary conditions (3.2.1) may now be written in the form

$$\left.\begin{aligned} &f_0 = 0, \quad F_0 = y, \\ &\frac{\partial f_0}{\partial x} = 0, \quad \frac{\partial F_0}{\partial x} = 0. \end{aligned}\right\} \quad \text{on } x = 0,\ 0 \le y \le \frac{1}{2} \qquad (3.3.3a)$$

$$f_0 = F_0 = g_0 = G_0 = 0 \quad \text{on } y = 0 \text{ and } y = L,\ -\infty < x < \infty \qquad (3.3.3b)$$

$$\frac{\partial f_0}{\partial x} = 0, \quad \frac{\partial f_0}{\partial y} = 0, \quad \frac{\partial F_0}{\partial x} = 0, \quad \frac{\partial F_0}{\partial y} = 0, \quad g_0 = G_0 = 0 \quad \text{as } x \to \infty,\ 0 \le y \le L \qquad (3.3.3c)$$

$$\frac{\partial f_0}{\partial x} = \frac{\partial F_0}{\partial x} = \frac{\partial g_0}{\partial x} = \frac{\partial G_0}{\partial x} = 0 \quad \text{on } x = 0,\ \frac{1}{2} \le y \le L \qquad (3.3.3d)$$

and solutions are only sought for x>0. Since y=0 and y=L are

streamlines, with help from boundary condition (3.3.3b), it can be shown that boundary condition (3.3.3c) may be written as follows:

$$f_0,\ F_0,\ g_0 \text{ and } G_0 \longrightarrow 0 \quad \text{as } x \rightarrow \infty,\ 0 \le y \le L \qquad (3.3.3c)$$

Because of the periodic nature of the cascade in the y direction we assume that the functions f_0, F_0, g_0 and G_0 may be expressed in the following forms

$$f_0(x,y) = \sum_{n=1}^{\infty} f_{0n}(x)\sin\frac{n\pi y}{L} \qquad (3.3.4a)$$

$$F_0(x,y) = \sum_{n=1}^{\infty} F_{0n}(x)\sin\frac{n\pi y}{L} \qquad (3.3.4b)$$

$$g_0(x,y) = \sum_{n=1}^{\infty} g_{0n}(x)\sin\frac{n\pi y}{L} \qquad (3.3.4c)$$

$$G_0(x,y) = \sum_{n=1}^{\infty} G_{0n}(x)\sin\frac{n\pi y}{L} \qquad (3.3.4d)$$

where $f_{0n}(x)$, $F_{0n}(x)$, $g_{0n}(x)$ and $G_{0n}(x)$ (n=1, 2, 3,...) are unknown functions of x which are to be determined.

Substituting expressions (3.3.4) into the equations (3.3.2) and assuming that the infinite series may be differentiated term by term twice then we obtain the following four infinite sets of ordinary differential equations,

$$\sum_{n=1}^{\infty}\left\{\frac{d^2 f_{0n}}{dx^2} - \left(\frac{n\pi}{L}\right)^2 f_{0n}\right\}\sin\frac{n\pi y}{L} = -\sum_{n=1}^{\infty} g_{0n}\sin\frac{n\pi y}{L} \qquad (3.3.5a)$$

$$\sum_{n=1}^{\infty}\left\{\frac{d^2 F_{0n}}{dx^2} - \left(\frac{n\pi}{L}\right)^2 F_{0n}\right\}\sin\frac{n\pi y}{L} = -\sum_{n=1}^{\infty} G_{0n}\sin\frac{n\pi y}{L} \qquad (3.3.5b)$$

$$\sum_{n=1}^{\infty}\left\{\frac{d^2 g_{0n}}{dx^2} - \left(\frac{n\pi}{L}\right)^2 g_{0n}\right\}\sin\frac{n\pi y}{L} = -R_b\sum_{n=1}^{\infty} G_{0n}\sin\frac{n\pi y}{L} \qquad (3.3.5c)$$

$$\sum_{n=1}^{\infty}\left\{\frac{d^2G_{0n}}{dx^2} - (\frac{n\pi}{L})^2G_{0n}\right\}\sin\frac{n\pi y}{L} = R_b\sum_{n=1}^{\infty}g_{0n}\sin\frac{n\pi y}{L} \qquad (3.3.5d)$$

and these equations are identically satisfied if

$$\frac{d^2f_{0n}}{dx^2} - (\frac{n\pi}{L})^2f_{0n} = -g_{0n} \qquad (n=1,\ 2,\ 3,\ldots) \qquad (3.3.6a)$$

$$\frac{d^2F_{0n}}{dx^2} - (\frac{n\pi}{L})^2F_{0n} = -G_{0n} \qquad (n=1,\ 2,\ 3,\ldots) \qquad (3.3.6b)$$

$$\frac{d^2g_{0n}}{dx^2} - (\frac{n\pi}{L})^2g_{0n} = -R_bG_{0n} \qquad (n=1,\ 2,\ 3,\ldots) \qquad (3.3.6c)$$

$$\frac{d^2G_{0n}}{dx^2} - (\frac{n\pi}{L})^2G_{0n} = R_bg_{0n} \qquad (n=1,\ 2,\ 3,\ldots) \qquad (3.3.6d)$$

On substituting equation (3.3.6d) into (3.3.6c) and making the assumption that $G_{0n} \in C^4(-\infty,\ +\infty)$ then we obtain

$$\frac{d^4G_{0n}}{dx^4} - 2(\frac{n\pi}{L})^2\frac{d^2G_{0n}}{dx^2} + [(\frac{n\pi}{L})^2+R_b^2]\ G_{0n} = 0$$

$$(n=1,\ 2,\ 3\ldots) \qquad (3.3.7)$$

The corresponding characteristic equations are

$$\lambda^4 - 2(\frac{n\pi}{L})^2\lambda^2 + [(\frac{n\pi}{L})^2 + R_b^2] = 0 \qquad (3.3.8)$$

and the roots are given by

$$\lambda_{n1} = A_n(\cos\frac{\theta_n}{2} + i\sin\frac{\theta_n}{2}) \qquad (3.3.9a)$$

$$\lambda_{n2} = -A_n(\cos\frac{\theta_n}{2} + i\sin\frac{\theta_n}{2}) \qquad (3.3.9b)$$

$$\lambda_{n3} = A_n(-\cos\frac{\theta_n}{2} + i\sin\frac{\theta_n}{2}) \qquad (3.3.9c)$$

$$\lambda_{n4} = A_n(\cos\frac{\theta_n}{2} - i\sin\frac{\theta_n}{2}) \qquad (3.3.9d)$$

where $A_n=\left[(\frac{n\pi}{L})^4+R_b^2\right]^{1/4}$ (n=1, 2, 3,...) are the magnitudes of λ_{ni} (i=1, 2, 3, 4) and θ_n (n=1, 2, 3,...) are the arguments of λ_{n1}.

Hence the solutions of equations (3.3.7) have the form

$$G_{0n}(x)= e^{\alpha_n x}(c_{n1}\cos(\beta_n x)+c_{n2}\sin(\beta_n x))+ e^{-\alpha_n x}(c_{n3}\cos(\beta_n x)+c_{n4}\sin(\beta_n x)) \qquad (3.3.10)$$

where $\alpha_n= A_n\cos\left(\frac{\theta_n}{2}\right)$ and $\beta_n= A_n\sin\left(\frac{\theta_n}{2}\right)$ (n=1, 2, 3,...). Finite solutions are only possible if $c_{n1}= c_{n2}= 0$ and then, from equation (3.3.6d), we obtain

$$g_{0n}(x)= \frac{1}{R_b}\left\{ \left[\alpha_n^2-\beta_n^2-(\frac{n\pi}{L})^2\right] G_{0n}+ 2\alpha_n\beta_n e^{-\alpha_n x}\left[c_{n3}\sin(\beta_n x)-c_{n4}\cos(\beta_n x)\right]\right\} \qquad (n=1, 2,...) \qquad (3.3.11)$$

Now from equations (3.3.6) we have

$$\frac{d^2}{dx^2}(G_{0n}+R_b f_{0n})-(\frac{n\pi}{L})^2(G_{0n}+R_b f_{0n}) = 0 \qquad (n=1, 2, 3,...) \qquad (3.3.12a)$$

$$\frac{d^2}{dx^2}(g_{0n}-R_b F_{0n})-(\frac{n\pi}{L})^2(g_{0n}-R_b F_{0n}) = 0 \qquad (n=1, 2, 3,...) \qquad (3.3.12b)$$

and therefore

$$G_{0n} + R_b f_{0n} = k_{n1}\, e^{\frac{n\pi x}{L}} + k_{n3}\, e^{-\frac{n\pi x}{L}} \qquad (n=1, 2, 3,...) \qquad (3.3.13a)$$

$$g_{0n} - R_b F_{0n} = -k_{n2} e^{\frac{n\pi x}{L}} + k_{n4}\, e^{-\frac{n\pi x}{L}} \qquad (n=1, 2, 3,...) \qquad (3.3.13b)$$

where k_{ni} (n=1, 2, 3,..., i=1, 2, 3, 4) are unknown constants.

Because we require solutions which are finite then $k_{n1}=k_{n2}=0$ (n=1, 2, 3,...) and we obtain

$$f_{0n}(x)=\left\{k_{n3}e^{-\frac{n\pi x}{L}} - G_{0n}\right\}\Big/R_b \qquad (n=1,\ 2,\ 3,\ldots) \qquad (3.3.14a)$$

$$F_{0n}(x)=\left\{k_{n4}e^{-\frac{n\pi x}{L}} + g_{0n}\right\}\Big/R_b \qquad (n=1,\ 2,\ 3,\ldots) \qquad (3.3.14b)$$

Applying the boundary conditions (3.3.3d) we now find that

$$k_{n3}=(\alpha_n c_{n3}-\beta_n c_{n4})\frac{L}{n\pi} \qquad (n=1,\ 2,\ 3,\ldots) \qquad (3.3.15a)$$

$$k_{n4}=(\alpha_n C_{\alpha n} c_{n3}+\beta_n C_{\beta n} c_{n4})\frac{L}{n\pi R_b} \qquad (n=1,\ 2,\ 3,\ldots) \qquad (3.3.15b)$$

where $C_{\alpha n} = 3\beta_n^2-\alpha_n+(\frac{n\pi}{L})^2$, $C_{\beta n}= 3\alpha_n^2-\beta_n-(\frac{n\pi}{L})^2$ (n=1, 2, 3,...).

Boundary conditions (3.3.3a) may now be written in the form

$$\sum_{n=1}^{\infty} f_{0n}(0)\ \frac{n\pi}{L}\ \cos\frac{n\pi y}{L} = 0 \qquad 0 \le y \le \frac{1}{2} \qquad (3.3.16a)$$

$$\sum_{n=1}^{\infty} F_{0n}(0)\ \frac{n\pi}{L}\ \cos\frac{n\pi y}{L} = 1 \qquad 0 \le y \le \frac{1}{2} \qquad (3.3.16b)$$

and on using expressions (3.3.15) then $f_{0n}(0)$ and $F_{0n}(0)$ can be expressed in the terms of c_{n3} and c_{n4} as follows,

$$f_{0n}(0)=\frac{L\alpha_n-n\pi}{n\pi R_b}\ c_{n3} - \frac{L\beta_n}{n\pi R_b}\ c_{n4}$$

$$(n=1,\ 2,\ 3,\ldots) \qquad (3.3.17a)$$

$$F_{0n}(0)= \frac{\alpha_n L_n+n\pi M_n}{n\pi R_b^{\,2}}\ c_{n3} + \frac{\beta_n (C_{\beta n}-2n\pi\alpha_n)}{n\pi R_b^{\,2}}\ c_{n4}$$

$$(n=1,\ 2,\ 3,\ldots) \qquad (3.3.17b)$$

where $L_n = 3\beta_n^2 - \alpha_n^2 + (\frac{n\pi}{L})^2$, $M_n = 2\beta_n - L_n$ (n=1, 2, 3,...).

As it is impossible to solve infinite sets of equations we terminate all the infinite series after N terms. Although the constants c_{ni} (n=1, 2, 3,... and i=1, 2, 3, 4) will depend on the value of N we will assume that the value of N is sufficiently large that this effect is negligible and continue to use c_{ni} whatever the value of N. Later calculations will confirm the validity of this assumption. Further, for convenience we will take N to be an even positive integer.

Multiplying both expressions in (3.3.16) by $\cos\frac{m\pi y}{L}$ (m=1, 3, 5,..., N-1) and integrating the resulting expressions with respect to y between 0 and $\frac{1}{2}$ gives

$$\sum_{n=1}^{N} f_{0n}(0)\ \frac{n\pi}{L} \int_0^{1/2} \cos\frac{n\pi y}{L}\ \cos\frac{m\pi y}{L}\ dy = 0 \qquad (3.3.18a)$$

$$\sum_{n=1}^{N} F_{0n}(0)\ \frac{n\pi}{L} \int_0^{1/2} \cos\frac{n\pi y}{L}\ \cos\frac{m\pi y}{L}\ dy = \int_0^{1/2} \cos\frac{m\pi y}{L}\ dy \qquad (3.3.18b)$$

(m=1, 3, 5,..., N-1)

Now equations (3.3.18) form N equations but involve 2N unknown coefficients. Therefore we require N further conditions and these are obtained by using the last two conditions in (3.3.3d), i.e.

$$\sum_{n=1}^{\infty} \frac{d}{dx}\ g_{0n}(0)\ \sin\frac{n\pi y}{L} = 0 \qquad (\tfrac{1}{2} \le y \le L) \qquad (3.3.19a)$$

$$\sum_{n=1}^{\infty} \frac{d}{dx}\ G_{0n}(0)\ \sin\frac{n\pi y}{L} = 0 \qquad (\tfrac{1}{2} \le y \le L) \qquad (3.3.19a)$$

Equations (3.3.19) are now multiplied by $\sin\frac{m\pi y}{L}$ (m=1, 3, 5,..., N-1) and integrated with respect to y from $\frac{1}{2}$ to L and we obtain

$$\sum_{n=1}^{N} \frac{d}{dx} g_{0n}(0) \int_{1/2}^{L} \sin\frac{n\pi y}{L} \sin\frac{m\pi y}{L}\, dy = 0 \quad (\tfrac{1}{2} \le y \le L) \qquad (3.3.20a)$$

$$\sum_{n=1}^{N} \frac{d}{dx} G_{0n}(0) \int_{1/2}^{L} \sin\frac{n\pi y}{L} \sin\frac{m\pi y}{L}\, dy = 0 \quad (\tfrac{1}{2} \le y \le L) \qquad (3.3.20b)$$

$$(m= 1,\ 3,\ 5,\ldots N-1)$$

where

$$\frac{d}{dx} g_{0n}(0) = \left[\alpha_n (2\beta_n^2 - M_n) c_{n3} + \beta_n (2\alpha_n^2 + M_n) c_{n4}\right] \frac{1}{R_b} \qquad (3.3.21a)$$

$$\frac{d}{dx} G_{0n}(0) = -\alpha_n c_{n3} + \beta_n c_{n4} \qquad (n=1,\ 2,\ 3,\ldots,N) \qquad (3.3.21b)$$

Equations (3.3.18) and (3.3.20) form a linear system of 2N equations and 2N unknowns c_{n3} and c_{n4} (n=1, 2,..., N) which has to be solved numerically and then using expressions (3.3.15) all the unknown coefficients in the solution may be determined.

3.4 The O(1) Solution Using a Numerical Technique

In this section we solve equations (3.2.8) subject to the boundary conditions (3.2.2). As in section 3.3 we write

$$\Psi_0 = f_0(X,Y)\sin(t) + F_0(X,Y)\cos(t) \qquad (3.4.1a)$$

$$\omega_0 = g_0(X,Y)\sin(t) + G_0(X,Y)\cos(t) \qquad (3.4.1b)$$

where f_0, F_0, g_0 and G_0 are unknown functions of X and Y to be determined. On substitution of expressions (3.4.1) into equations (3.2.8) and equating terms in sin(t) and cos(t), we obtain

$$\nabla^2 f_0 = -g_0 \qquad (3.4.2a)$$

$$\nabla^2 F_0 = -G_0 \qquad (3.4.2b)$$

$$\nabla^2 g_0 = -R_b G_0 \qquad (3.4.2c)$$

$$\nabla^2 G_0 = R_b g_0 \qquad (3.4.2d)$$

which have to be solved in $X \geq 0$ subject to the boundary conditions

$$\left.\begin{array}{ll} f_0 = 0, & F_0 = 0, \\ \dfrac{\partial f_0}{\partial X} = 0 & \dfrac{\partial F_0}{\partial X} = 0 \end{array}\right\} \quad \text{on } X = 0,\ 0 \leq Y \leq \frac{1}{2} \qquad (3.4.3a)$$

$$\left.\begin{array}{ll} f_0 = F_0 = g_0 = G_0 = 0 & \text{on } Y = 0,\ X > 0 \\ f_0 = 0,\ F_0 = -L,\ g_0 = G_0 = 0 & \text{on } Y = L,\ X > 0 \end{array}\right\} \qquad (3.4.3b)$$

$$\left.\begin{array}{ll} \dfrac{\partial f_0}{\partial Y} = 0, & \dfrac{\partial F_0}{\partial Y} = -1 \\ g_0 = 0,\ G_0 = 0 & \end{array}\right\} \quad \text{as } X \longrightarrow \infty,\ 0 \leq Y \leq L \qquad (3.4.3c)$$

$$\frac{\partial f_0}{\partial X} = \frac{\partial F_0}{\partial X} = \frac{\partial g_0}{\partial X} = \frac{\partial G_0}{\partial X} = 0 \qquad \text{on } X = 0,\ \frac{1}{2} \leq Y \leq L \qquad (3.4.3d)$$

bearing in mind that the flow is symmetrical about X=0.

A standard second-order accurate central finite-difference discretisation of equations (3.4.2) was made and the resulting set of coupled finite-difference equations solved using a relaxation procedure. The numerical procedure used is similar to that described in chapter 2 and therefore the full details are not presented. However one or two points are worthy of mention.

As the flow changes most rapidly in the vicinity of the plates it is advisable to use a finer mesh in this vicinity. This was achieved by introducing the co-ordinate transformation (2.2.8).

At large distances from the cascade we assume that the flow approaches its asymptotic value exponentially in X, and the asymptotic solution has been found in chapter 2 as (2.2.20), or

alternatively, as equation (2.2.21) which in terms of f_o and F_o becomes

$$\frac{\partial f_o}{\partial X} = -\frac{\pi}{L} f_o \qquad \text{as } X \longrightarrow \infty,\ 0 \le Y \le L \qquad (3.4.8)$$

$$\frac{\partial}{\partial X}(F_o + Y) = -\frac{\pi}{L}(F_o + Y) \qquad \text{as } X \longrightarrow \infty,\ 0 \le Y \le L \qquad (3.4.9)$$

In practice the boundary conditions (3.4.8) and (3.4.9) have to be applied at a finite value of X and these are taken to be $X = X_L$, to represent the condition at $X = -\infty$, and $X = X_R$ for $X = +\infty$. The values of $|X_L|$ and $|X_R|$ have to be taken to be sufficiently large so that any increase in these values results in a negligible change in the calculated solution.

Another difficulty which arises is that the vorticity on the plate is unknown and in order to determine this we use the method devised by Woods (1954), namely we write

$$g_{OB} = -\frac{3f_{OI}}{h^2} - \frac{g_{OI}}{2} + O(h^2),\ G_{OB} = -\frac{3F_{OI}}{h^2} - \frac{G_{OI}}{2} + O(h^2) \qquad (3.4.10)$$

where the suffices B and I refer to the value on the body and the first internal grid point normal to the body.

Also the solution near the point $(0, \frac{1}{2})$ requires special attention since the vorticity is infinite at this point. In order to deal with this singularity two methods have been used, namely,

Method *I*: we use the inclined finite-difference scheme as described in detail by Ingham *et al.* (1990a). The discretisation of the functions g_o and G_o at the grid points (h, 0.5), (0, 0.5+h) and (-h, 0.5) using a square mesh of size h involves the values of g_o and G_o at the point $(0, \frac{1}{2})$. To overcome this difficulty we rotate the mesh through 45° so that the solution at the point (h, 0.5), for

example, may be obtained in terms of the functions at the points (0, 0.5-h), (2h, 0.5-h), (2h, 0.5+h) and (0, 0.5+h) rather than at the points (0, 0.5), (h, 0.5-h), (2h, 0.5) and (h, 0.5+h).

Method *II*: We use the analysis similar to that described in section 2.3. In the vicinity of the rigid wall the Navier-Stokes equations (1.3.4)-(1.3.5) and (3.2.8) may be written in terms of f_0 and F_0 in the following form,

$$\nabla^4 f_0 = 0 \qquad (3.4.11)$$

$$\nabla^4 F_0 = 0 \qquad (3.4.12)$$

these have to be solved subject to the boundary conditions (3.4.3a) and equations (3.4.11) and (3.4.12) now give the solutions for g_0 and G_0, exactly the same as in equations (2.3.18) and (2.3.19) except that Ψ and ω in chapter 2 are replaced by f_0 (or F_0) and g_0 (or G_0), respectively. The coefficients appearing in equations (2.3.19) are determined in the same way as described in section 2.3 and are therefore not presented here.

Both methods *I* and *II* have been used and it is found that they give similar results but with method *II* giving the more accurate solutions for a given mesh size. Therefore throughout the remainder of this chapter method *II* has been employed.

3.5 O(ε) Solutions

Now we seek the solutions of equations (3.2.9) and (3.2.10) subject to the boundary conditions (3.2.2). It is well known that for this kind of problem in which harmonic oscillations occur that there exist terms in the solution in both sin(2t) and cos(2t) due to

the non linearity of the problem. Hence we write

$$\Psi_1^{(u)} = f_1(X,Y)\sin(2t) + F_1(X,Y)\cos(2t) \qquad (3.5.1a)$$

$$\omega_1^{(u)} = g_1(X,Y)\sin(2t) + G_1(X,Y)\cos(2t) \qquad (3.5.1b)$$

where f_1, F_1, g_1 and G_1 are some unknown functions to be determined. Substituting expressions (3.4.1) and (3.5.1) into equations (3.2.9) and (3.2.10) and collecting up terms with the same coefficients in cos(2t), sin(2t) and those independent of the time t gives

$$\nabla^2 g_1 = \mathcal{X}_0 - 2R_b G_1 \qquad (3.5.2a)$$

$$\nabla^2 G_1 = \mathcal{F}_0 + 2R_b g_1 \qquad (3.5.2b)$$

$$\nabla^2 \omega_1^{(s)} = \ell_0 \qquad (3.5.2c)$$

$$\nabla^2 f_1 = -g_1 \qquad (3.5.2d)$$

$$\nabla^2 F_1 = -G_1 \qquad (3.5.2e)$$

$$\nabla^2 \Psi_1^{(s)} = -\omega_1^{(s)} \qquad (3.5.2f)$$

where

$$\mathcal{X}_0 = \frac{R_b}{2}\left\{\frac{\partial(G_0, f_0)}{\partial(X,Y)} + \frac{\partial(g_0, F_0)}{\partial(X,Y)}\right\} \qquad (3.5.3a)$$

$$\mathcal{F}_0 = \frac{R_b}{2}\left\{\frac{\partial(G_0, F_0)}{\partial(X,Y)} - \frac{\partial(g_0, f_0)}{\partial(X,Y)}\right\} \qquad (3.5.3b)$$

$$\ell_0 = \frac{R_b}{2}\left\{\frac{\partial(g_0, f_0)}{\partial(X,Y)} + \frac{\partial(G_0, F_0)}{\partial(X,Y)}\right\} \qquad (3.5.3c)$$

The boundary conditions (3.2.2) can now be written,

$$\left.\begin{aligned} f_1 &= F_1 = 0 \\ \frac{\partial f_1}{\partial X} &= \frac{\partial F_1}{\partial X} = 0 \end{aligned}\right\} \qquad \text{on } X = 0,\ 0 \le Y \le \frac{1}{2} \tag{3.5.4a}$$

$$\left.\begin{aligned} f_1 = F_1 = g_1 = G_1 = 0 \qquad & \text{on } Y = 0, \quad |X| > 0 \\ f_1 = F_1 = g_1 = G_1 = 0 \qquad & \text{on } Y = L, \quad |X| > 0 \end{aligned}\right\} \tag{3.5.4b}$$

$$\frac{\partial f_1}{\partial Y} = 0, \quad \frac{\partial F_1}{\partial Y} = 0, \quad g_1 = G_1 = 0 \qquad \text{as } |X| \to \infty,\ 0 \le Y \le L \tag{3.5.4c}$$

$$\Psi_1^{(s)} = \frac{\partial \Psi_1^{(s)}}{\partial X} = 0 \qquad \text{on } X = 0,\ 0 \le Y \le \frac{1}{2} \tag{3.5.5a}$$

$$\Psi_1^{(s)} = \omega_1^{(s)} = 0 \qquad \text{on } Y = 0 \text{ and } Y = L,\ |X| > 0 \tag{3.5.5b}$$

$$\frac{\partial \Psi^{(s)}}{\partial Y} = 0, \qquad \omega_1^{(s)} = 0 \quad \text{as } |X| \to \infty,\ 0 \le Y \le L \tag{3.5.5c}$$

It should be noted that unlike the O(1) solution, the flow may be symmetrical or antisymmetrical about $X = 0$.

Following the derivation of the asymptotic boundary condition in section 2.2, and the boundary conditions on the plate for the O(1) formulation we obtain,

$$\frac{\partial f_1}{\partial X} = -\frac{\pi}{L} f_1, \quad \frac{\partial F_1}{\partial X} = -\frac{\pi}{L} F_1 \qquad \text{as } X \to \pm\infty,\ 0 \le Y \le L \tag{3.5.6}$$

$$\frac{\partial \Psi_1^{(s)}}{\partial X} = -\frac{\pi}{L} \Psi_1^{(s)} \qquad \text{as } X \to \pm\infty,\ 0 \le Y \le L \tag{3.5.7}$$

and

$$\left.\begin{aligned} g_{1B} &= -\frac{3f_{1I}}{h^2} - \frac{g_{1I}}{2} \\ G_{1B} &= -\frac{3F_{1I}}{h^2} - \frac{G_{1I}}{2} \end{aligned}\right\} \qquad X = 0,\ 0 < Y < \frac{1}{2} \tag{3.5.8}$$

$$\omega_{1B}^{(s)} = -\frac{3\Psi_{1I}^{(s)}}{h^2} - \frac{\omega_{1I}^{(s)}}{2} \qquad X = 0,\ 0 < Y < \frac{1}{2} \tag{3.5.9}$$

Again a second-order accurate central finite-difference discretisation of the equations (3.4.2) and (3.2.10) was made and the resulting set of coupled finite-difference equations solved in a similar manner to that described in section 3.4.

3.6 Results and Discussion

Results were obtained using a central finite-difference discretisation and an iterative process for values of the frequency Reynolds number, R_b =1, 5, 10, 50, 100 and 200 with mesh sizes h=1/40, 1/60 and 1/80. All the results presented in this chapter were obtained with h=1/80 but the results obtained with h=1/60 are graphically indistinguishable from those obtained using h=1/80. Further, when R_b is small a mesh size of h=1/40 is found to be adequate but as R_b increases then the flow field changes more rapidly near the plate and therefore a smaller value of h is required in order to adequately describe the flow field. In order to illustrate the numerical method we present results only for L=1 although calculations have been performed over a wide range of values of L and the results show the same general flow characteristics. Several values of X_R and X_L have been tried and it was found that for the values of R_b considered, a value of about 15 (the exact value depends on the mesh size employed in the X-direction) gave results which were graphically indistinguishable from those obtained using $-X_L=X_R\approx 10$. In the series truncation method the series was truncated after N=100, 150 and 200 terms and it was found that a value of N=200 was sufficiently large in order to obtain solutions which are correct everywhere to less than 1%.

Fig.3.2 shows the instantaneous streamline pattern for R_b=5 for

various values of time using the series truncation and the numerical scheme for the **O**(1) solution. It is seen that the two methods give solutions which are almost the same and this agreement is typical of the results obtained. At time $t=2n\pi$ (n an integer) the plate is moving from left to right and is at its maximum speed. The plate starts to slow down and by the time $t=2n\pi+0.3\pi$ the recirculation region that existed at time $t=2n\pi$ and centred at $x\approx6$ has been annihilated. The plate continues to slow down and comes to rest when $t=2n\pi+0.5\pi$. As the plate then starts to move from right to left it develops a recirculating flow around the plate in the opposite direction to the original recirculating flow. The new recirculating flow becomes stronger and the original one becomes weaker and this phenomena persists until $t=2n\pi+\pi$ and then the whole process is repeated.

Fig.3.3b shows the instantaneous streamline pattern for $R_b=50$ for various values of time using the numerical scheme for the O(1) solution. The results obtained using the series truncation method show very little difference and are shown in **Fig.3.3a**. The solution for $R_b=50$ shows a similar behaviour to that obtained for $R_b=5$ except that the development of the counter rotating eddy is not so pronounced and this is to be expected as the effects of diffusion are much smaller at this value of the Reynolds number.

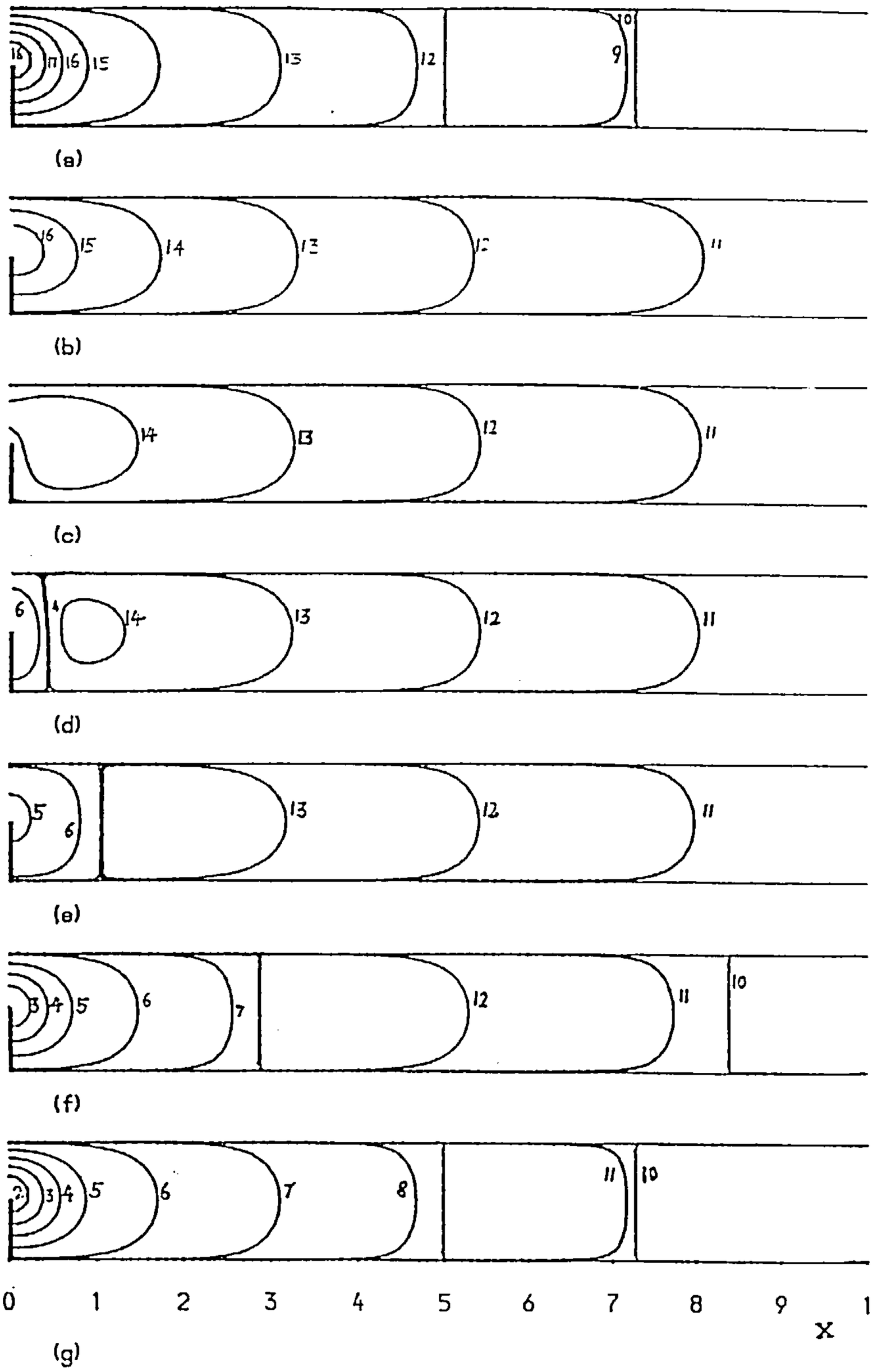

Fig.3.2a The instantaneous streamlines for the first-order unsteady solutions obtained from the series truncation method for $R_b=5$ at different times, t. (a) $t=2n\pi$, (b) $t=(2n+0.3)\pi$, (c) $t=(2n+0.5)\pi$, (d) $t=(2n+16/30)\pi$, (e) $t=(2n+0.6)\pi$, (f) $t=(2n+0.8)\pi$, (g) $t=(2n+1)\pi$. The streamline labelled 1, 2,..., 19 corresponds to $\psi=-0.5$, -0.4, -0.3, -0.2, -0.1, -0.01, -0.0001, -0.1×10^{-6}, -0.1×10^{-10}, 0, 0.1×10^{-10}, 0.1×10^{-6}, 0.0001, 0.01, 0.1, 0.2, 0.3, 0.4, 0.5, respectively, and n is an integer.

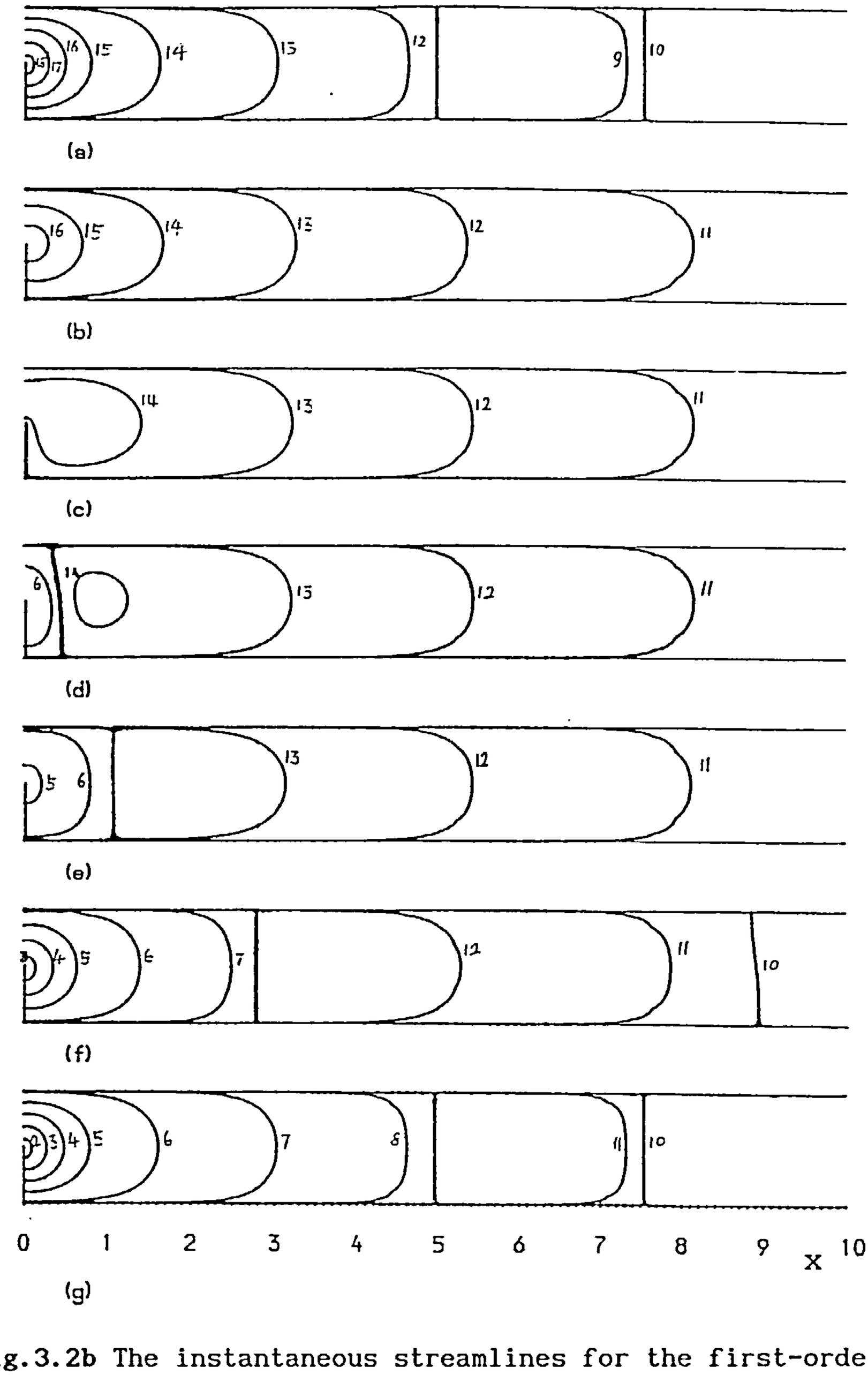

Fig.3.2b The instantaneous streamlines for the first-order unsteady solutions obtained from the the numerical method for $R_b=5$ at different times, t. (a) $t=2n\pi$, (b) $t=(2n+0.3)\pi$, (c) $t=(2n+0.5)\pi$, (d) $t=(2n+16/30)\pi$, (e) $t=(2n+0.6)\pi$, (f) $t=(2n+0.8)\pi$, (g) $t=(2n+1)\pi$. The values of the streamfunction are the same as those given in the caption to Fig.3.2a.

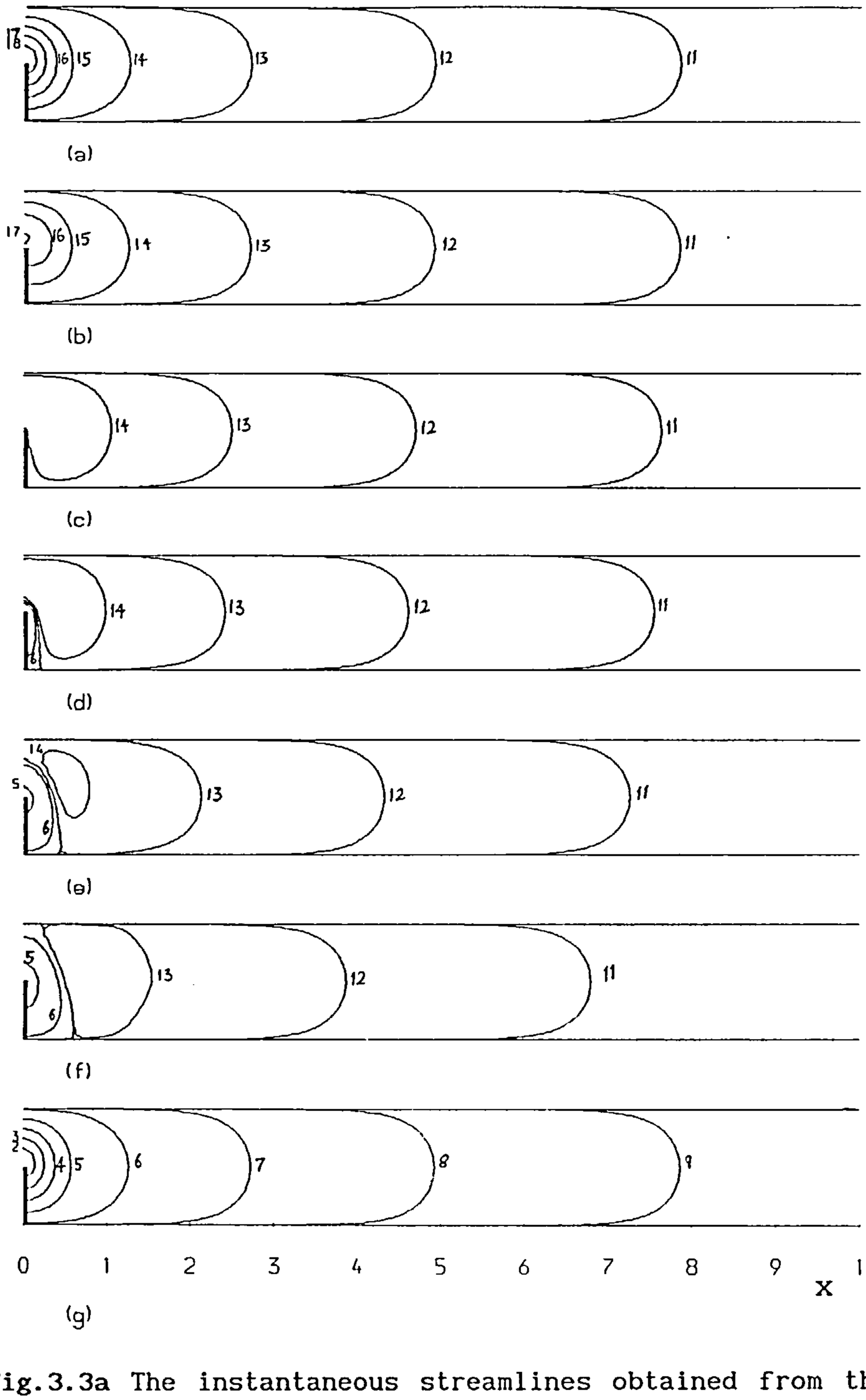

Fig.3.3a The instantaneous streamlines obtained from the series truncation method for the first-order unsteady solution for R_b=50 at different times, t. (a) t=2nπ, (b) t=(2n+0.3)π, (c) t=(2n+0.5)π, (d) t=(2n+16/30)π, (e) t=(2n+0.6)π, (f) t=(2n+19/30)π, (g) t=(2n+1)π. The values of the streamfunction are the same as those given in the caption to Fig.3.2a.

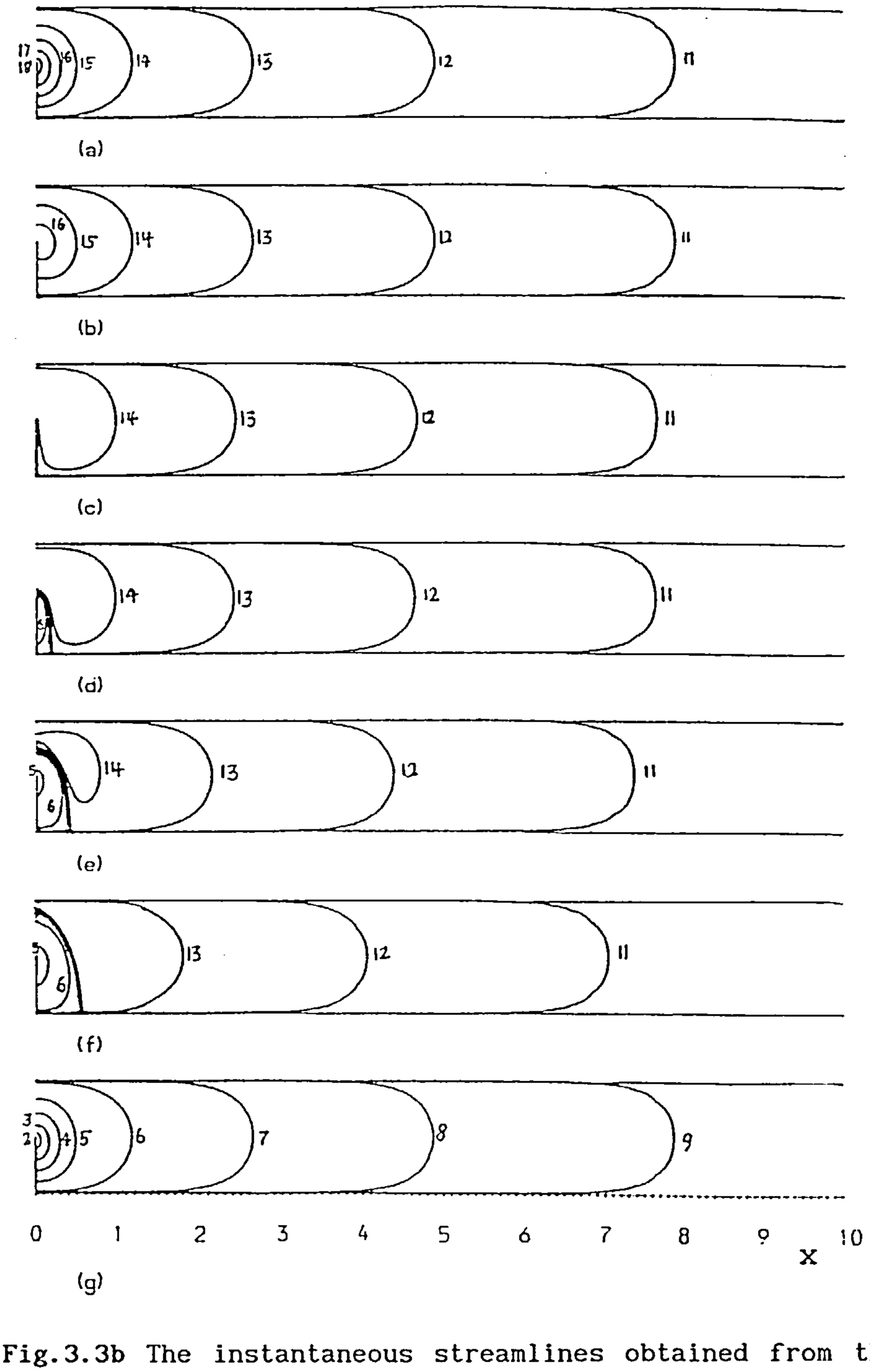

Fig.3.3b The instantaneous streamlines obtained from the numerical method for the first-order unsteady solution for R_b=50 at different, times t. (a) $t=2n\pi$, (b) $t=(2n+0.3)\pi$, (c) $t=(2n+0.5)\pi$, (d) $t=(2n+16/30)\pi$, (e) $t=(2n+0.6)\pi$, (f) $t=(2n+19/30)\pi$, (g) $t=(2n+1)\pi$. The values of the streamfunction are the same as those given in the caption to Fig.3.2a.

The steady streamlines for R_b=1, 5, 10, 50 and 100 are shown in Fig.3.4. It is observed that the vortex motion becomes stronger as the parameter R_b increases. This is to be expected since increasing R_b is equivalent to increasing the frequency of the oscillations of the cascade. This implies pumping more energy into the system and hence the strength of the vortex motion must increase. In order to demonstrate this phenomena more clearly the variation of the steady vertical velocity as a function of X at Y=1/2 for R_b=1, 5, 10, 50, 100 and 200 is shown in **Fig.3.5**. This figure also illustrates that the larger the values of R_b the larger the velocity gradients near the plate and hence the need for the finer mesh which is employed near X=0 in order to obtain accurate solutions.

Figs.3.4 and 3.5 illustrate that as R_b increases then the position of the centre of the vortex gets closer to the plate. Fig.3.6 shows the variation of the X-component of the distance of the centre of the vortex, D_v, as a function of R_b. As the parameter R_b increases we expect that the flow will consist of an outer inviscid flow and a viscous inner flow and therefore we may expect the value of D_v to decrease as R_b increases.

Numerical results have also been obtained for a grid of rectangular cylinders rather than the normal flat plates. In particular detailed solutions have been obtained when the cylinders are of square cross section, see **Fig.1.6**, and when L=1. The singularity in vorticity that occurs at the corners of the squares was treated in a similar way to the singularity at the edges of the plates and all other details are very similar to those presented in chapter 2 for the cascade of normal flat plates and are therefore not presented.

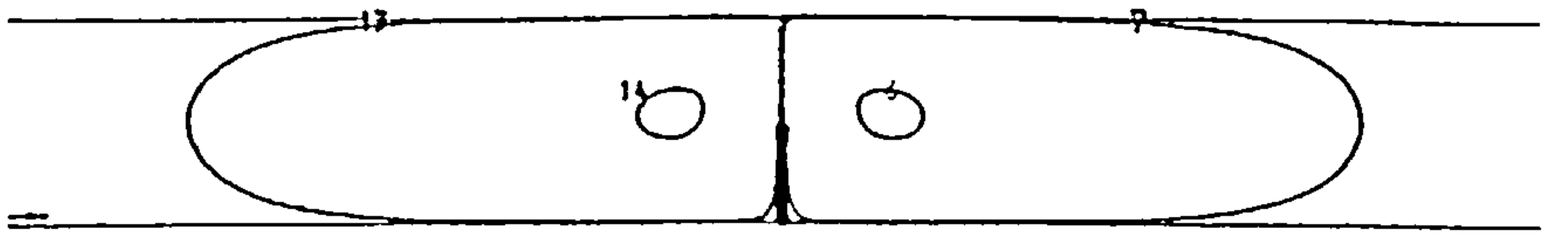

(a)

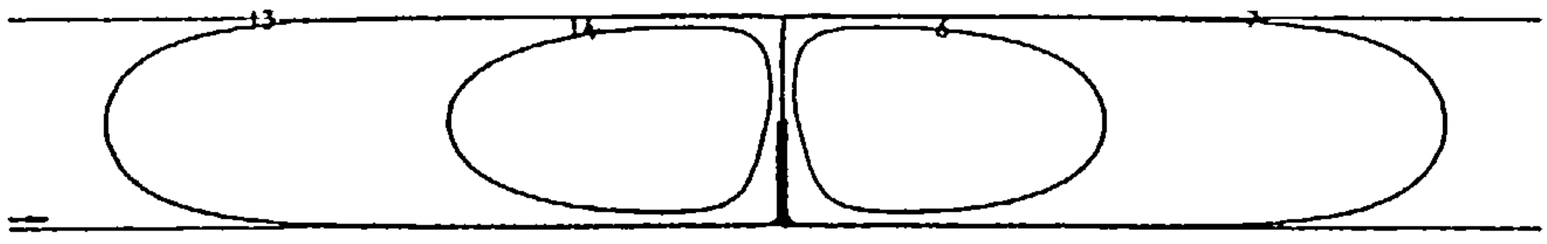

(b)

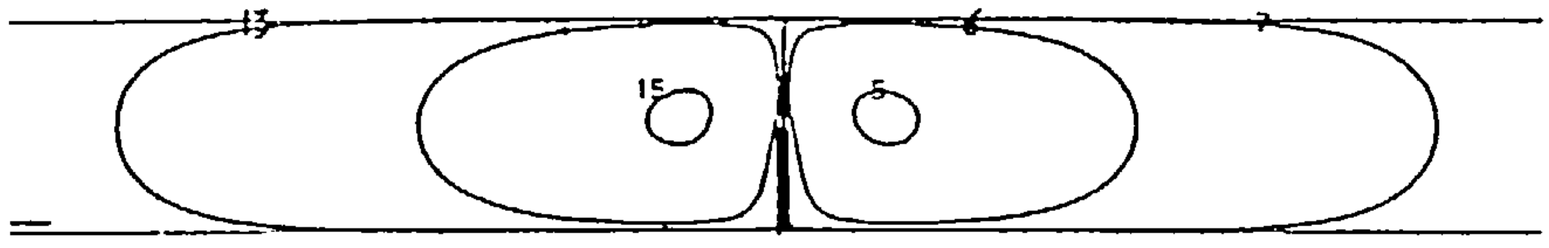

(c)

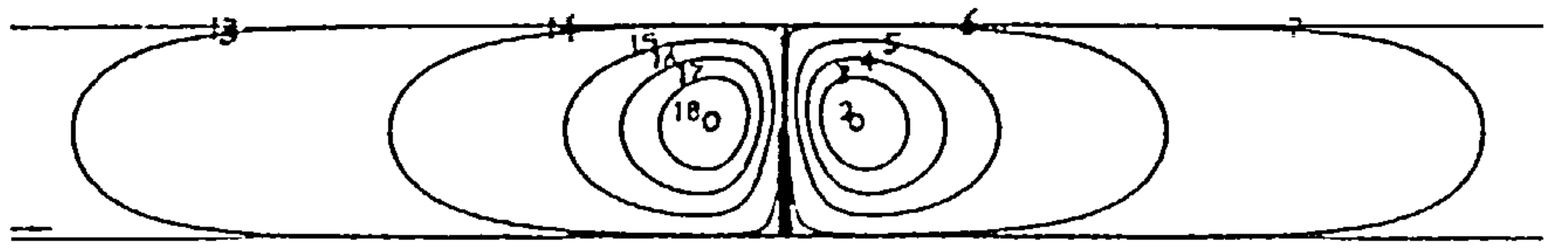

(d)

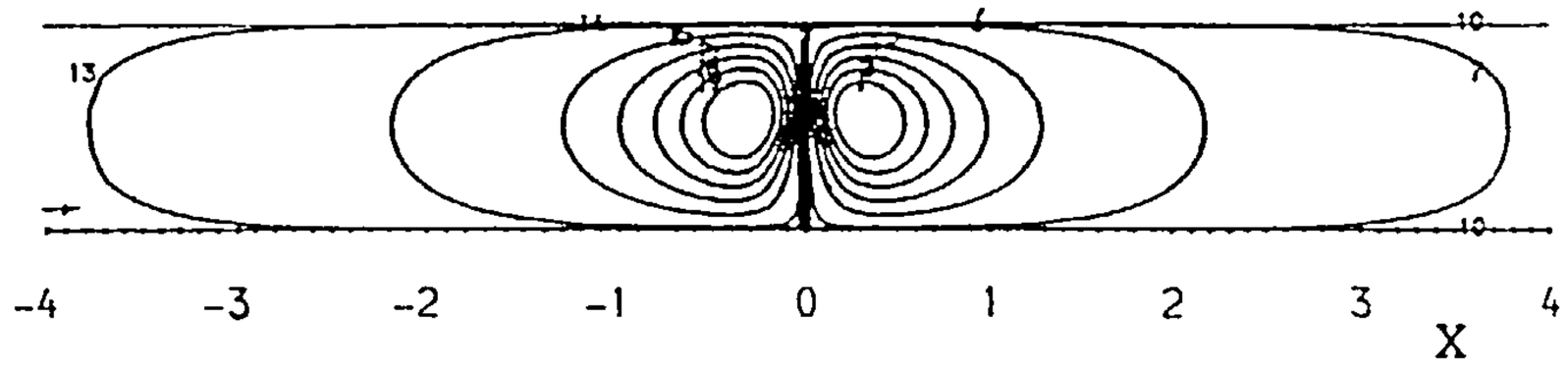

(e)

Fig.3.4 The streaming streamlines (Eulerian) for various values of R_b. (a) R_b=1, (b) R_b=5, (c) R_b=10, (d) R_b=50, (e) R_b=100. The values of the streamfunction are the same as those given in the caption to Fig.3.2a.

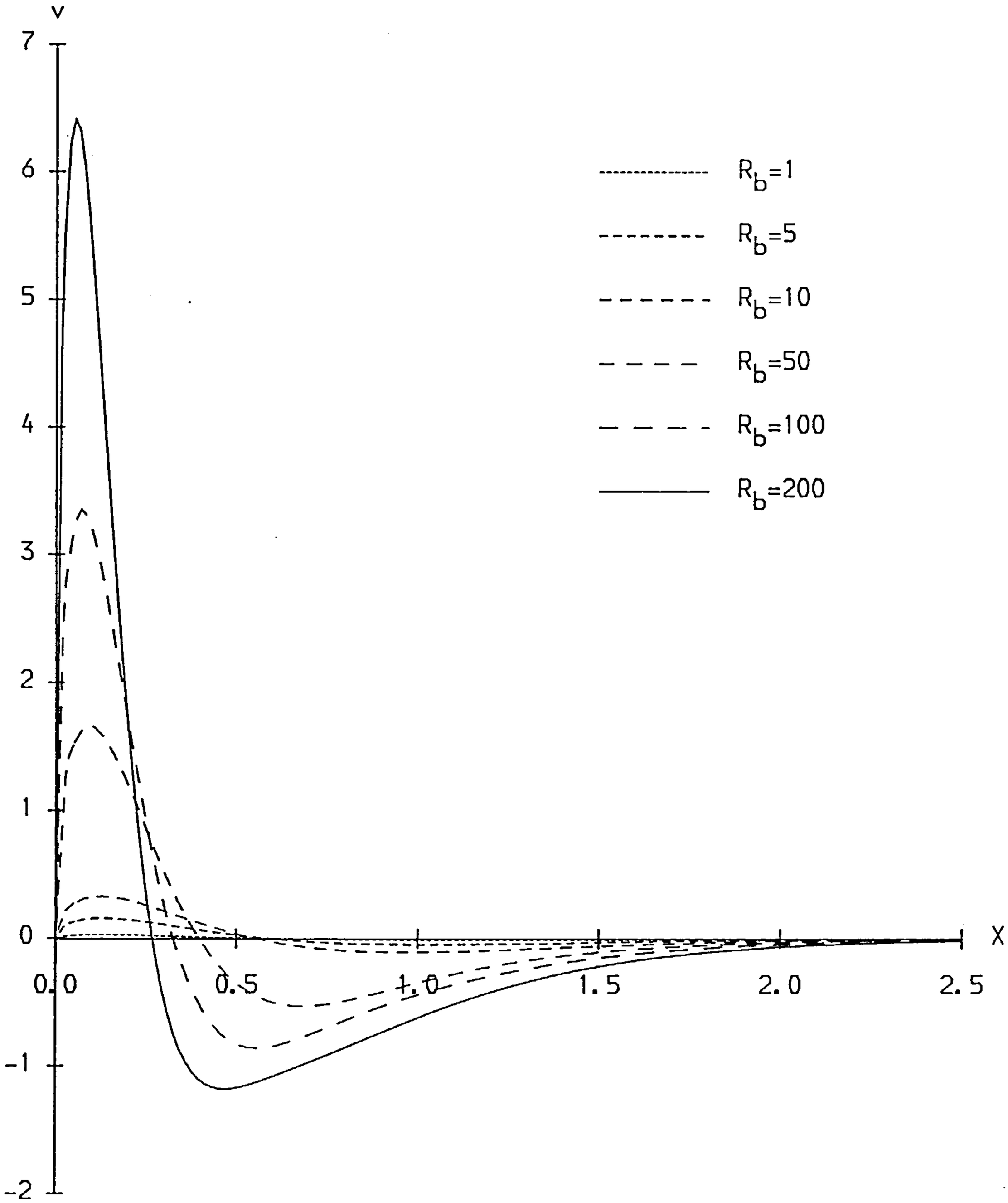

Fig.3.5 The vertical velocity as a function of X at Y=0.5 for R_b=1, 5, 10, 50, 100 and 200.

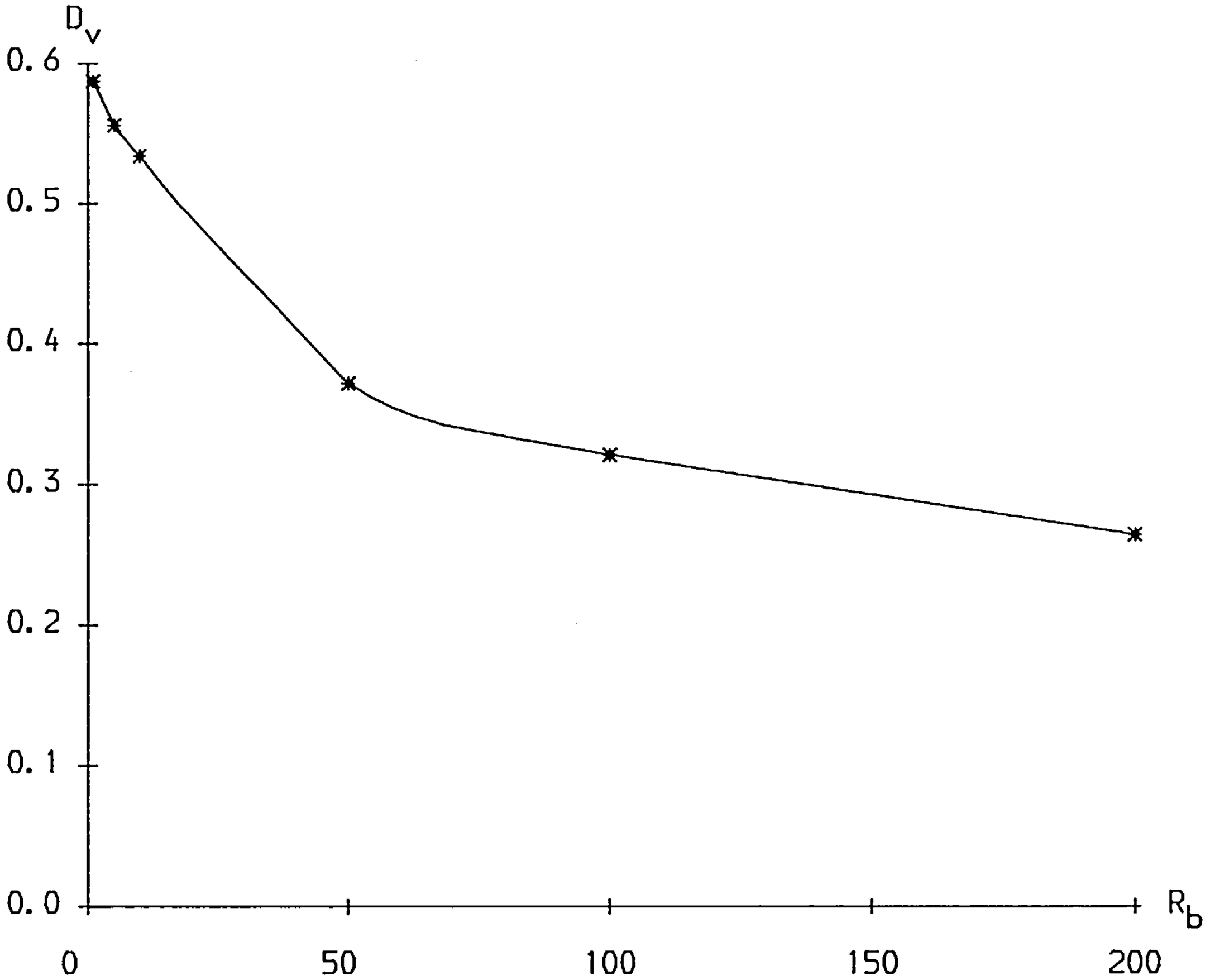

Fig.3.6 The X-component of the centre of the vortex as a function of R_b.

Fig.3.7 shows the steady streamline patterns for R_b=1, 5, 10, 50 and 100 with $-X_L=X_R=15$. Mesh sizes are again the same as those used for the cascade of normal flat plates and the results from different mesh sizes show very good consistency as the mesh size is reduced. It is observed from **Fig.3.7** that there are now eight vortices arranged around each cylinder (due to the symmetry of the problem only 4 vortices are shown). At small values of R_b the two vortices between the square cylinders are very weak and small in

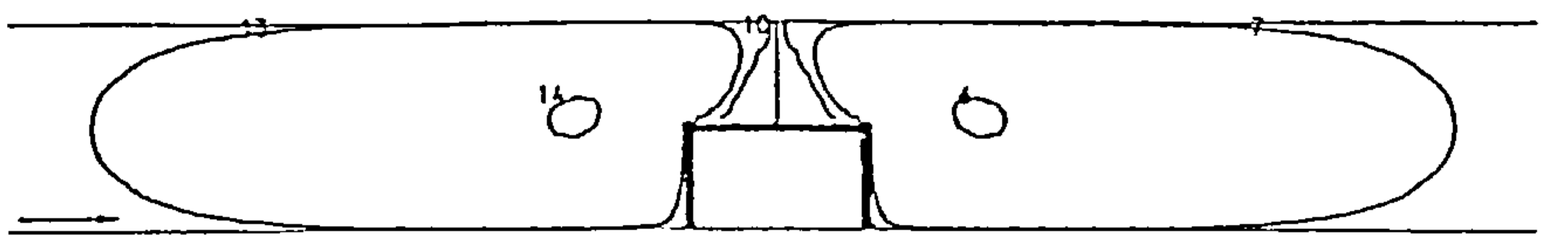

(a)

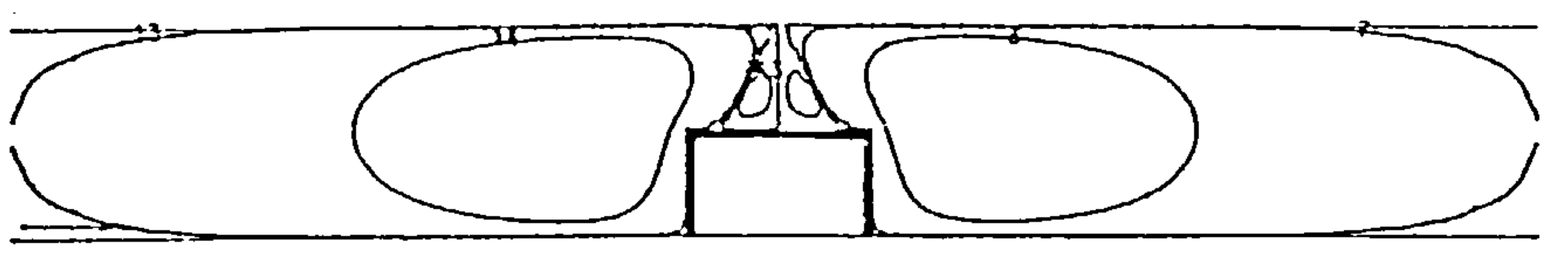

(b)

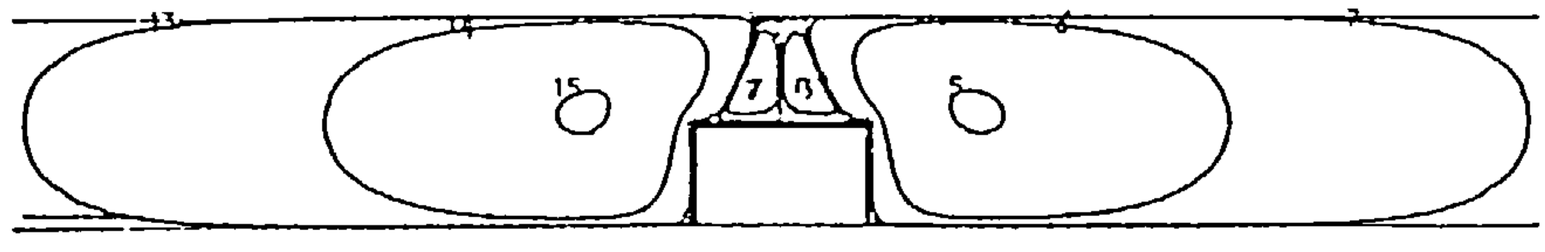

(c)

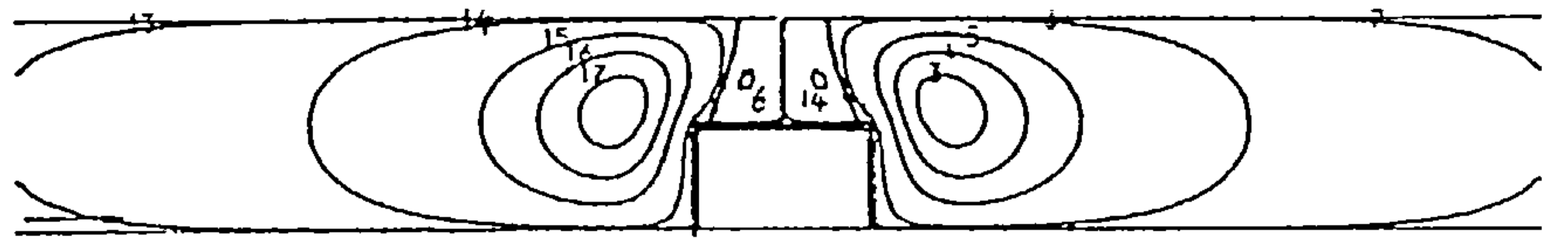

(d)

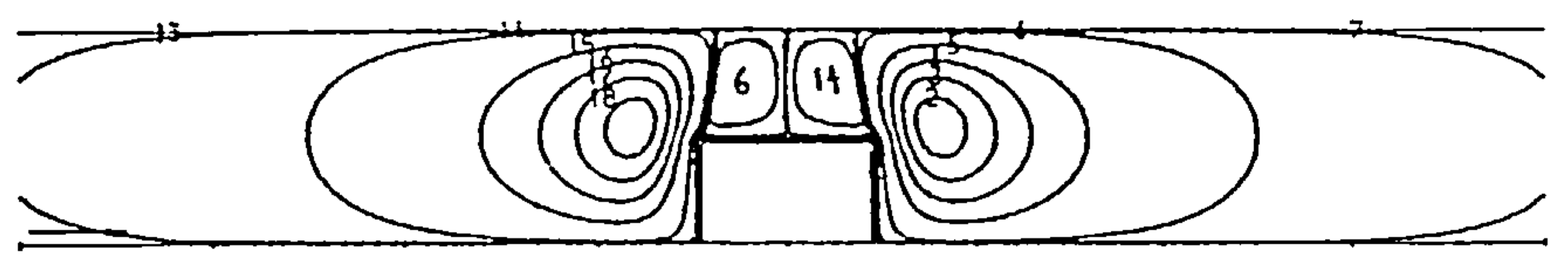

(e)

Fig.3.7 The steady streamlines for various values of R_b with the cascade of square cylinders. (a) R_b=1, (b) R_b=5, (c) R_b=10, (d) R_b=50, (e) R_b=100. The values of the streamfunction are the same as those given in the caption to **Fig.3.2a.**

size. However, as the frequency of the oscillations increase all the vortices become much stronger and those between the cylinders increase in size. This effect is again to be expected as increasing R_b effectively increases the energy being pumped into the system. As in the case of the cascade of normal flat plates, as the value of R_b increases then the centre of vortices at the side of the cascade also becomes closer to the cascade.

CHAPTER 4 STREAMING FLOWS INDUCED BY A CASCADE OF BODIES WHICH IS OSCILLATING WITH A SMALL-AMPLITUDE AT A HIGH-FREQUENCY

4.1 Introduction

In chapter 2 numerical solutions were obtained for the fluid flow induced by a harmonically oscillating cascade of normal flat plates with relatively large amplitude and low frequency, i.e. ε, R_e, R_b and R_s were all *O(1)*, whilst in chapter 3 we assumed that $\varepsilon \ll 1$ and $R_b = O(1)$ and as a result the streaming Reynolds number, R_s, was much smaller than unity. When ε remains very small and R_b increases then the streaming Reynolds number, R_s, will increase. When $R_s = O(1)$ the streaming flow outside the Stokes-layer induced by the oscillating body is governed by the full Navier-Stokes equations which is characterised by the Reynolds number R_s, see, for example, Riley (1967). Taking advantage of the conformal mapping technique Kim and Troesch (1989) were able to solve, using a *finite-difference method, the streaming flow between two cylinders* of which the inner square cylinder performs a harmonic oscillation with $R_s = O(1)$ and the outer cylindrical cylinder is at rest.

In this chapter we investigate, numerically, the flow induced by a cascade of normal flat plates and a cascade of square bars which perform harmonic oscillations with $\varepsilon \ll 1$ and $R_s \geq O(1)$ in an unbounded, incompressible fluid which is otherwise at rest.

Consistent with the early theories, the leading-order unsteady outer flow is given by the unsteady velocity potential. This flow is determined using both a conformal mapping technique and a standard finite-difference method, which takes into account the corner singularities, and these results are shown to be in good agreement. It is assumed, as Kim and Troesch (1989) did, that the flow does not separate and that in the corner region the standard boundary-layer assumption holds. Given the tangential velocity next to the body these inner boundary-layer equations may be solved. The $O(\varepsilon)$ outer flow may be determined and this consists of an unsteady component and a steady streaming flow. In this chapter we use a specialised finite-difference scheme to solve for the steady streaming flow and great care has to be taken near the corner singularities. In the case of the cascade of square bars the steady streaming flow has eight recirculating flows close to each bar whereas for the cascade of flat plates there are four such recirculations. When dealing with a single square bar Kim and Troesch (1989) observed very similar flows.

4.2 Formulation

Mathematically the fluid flows induced by the oscillation of two infinite cascades of bodies have been investigated, namely, (i) a cascade of normal flat plates and (ii) a cascade of square cylinders as described in chapter 1, see **Fig.1.5** and **Fig.1.6**. The cascade oscillates harmonically and perpendicular to the plane of the cascade such that the displacement of the cascade is only in the x^*-direction and given by equation (1.1.1). The governing equations,

with the co-ordinate system fixed in the cascade and in terms of the streamfunction and vorticity can be written as (2.2.3)-(2.2.4), or alternatively, as

$$\frac{\partial\omega}{\partial t} - \varepsilon\frac{\partial(\Psi,\omega)}{\partial(X,Y)} = \frac{\varepsilon^2}{R_s}\nabla^2\omega \qquad (4.2.1)$$

$$\nabla^2\Psi = -\omega \qquad (4.2.2)$$

Due to the symmetry of the problem we need only consider the flow in the region $-\infty< X <\infty$ and $0 \leq Y \leq L$, where $L = \mathcal{L}/d$.

Equations (4.2.1) and (4.2.2) have now to be solved subject to the boundary conditions (2.2.7) with boundary condition (2.2.7a) being replaced by

$$\Psi = \frac{\partial\Psi}{\partial n} = 0 \qquad \text{on the body surface} \qquad (4.2.3)$$

where n is the outwards normal to the body surface.

As we have assumed that $\varepsilon\ll1$ and $R_s = O(1)$ we therefore write the streamfunction in the form,

$$\Psi = \Psi_0(X,Y,t) + \frac{1}{R_s^{1/2}/\varepsilon}\Psi_{01}(X,Y,t)$$

$$+ \varepsilon\left\{\left(\Psi_{10}^{(u)}(X,Y,t) + \frac{1}{R_s^{1/2}/\varepsilon}\Psi_{11}^{(u)}(X,Y,t)\right)\right.$$

$$\left. + \left(\Psi^{(s)}(X,Y) + \frac{1}{R_s^{1/2}/\varepsilon}\Psi_{11}^{(\zeta)}(X,Y,t)\right)\right\}$$

$$+ \varepsilon^2\Psi_2(X,Y,t) + \varepsilon^3\Psi_3(X,Y,t) + O(\varepsilon^4)... \qquad (4.2.4)$$

see Riley (1967). On substitution of expression (4.2.4) into the governing equations (4.2.1) and (4.2.2) gives, to the leading order (i.e. O(1)),

$$\frac{\partial}{\partial t}(\nabla^2\Psi_0)= 0 \qquad (4.2.5)$$

Subject to the no-slip boundary condition on the surface of the body equation (4.2.5) gives only the trivial solution $\Psi_0=0$. Therefore the no-slip boundary condition must be relaxed and we have to introduce a boundary-layer in which we write the streamfunction, Ψ, as

$$\begin{aligned}\bar{\Psi} = \bar{\Psi}_0(\xi,\eta,t)+ \frac{1}{R_s^{1/2}}\,\bar{\Psi}_{01}(\xi,\eta,t)\\ + \varepsilon\left\{\left(\bar{\Psi}_{10}^{(u)}(\xi,\eta,t) + \frac{1}{R_s^{1/2}/\varepsilon}\,\bar{\Psi}_{11}^{(u)}(\xi,\eta,t)\right)\right.\\ \left. + \left(\bar{\Psi}^{(s)}(\xi,\eta) + \frac{1}{R_s^{1/2}/\varepsilon}\,\bar{\Psi}_{11}^{(s)}(\xi,\eta,t)\right)\right\}\\ + O^2(\varepsilon) \qquad (4.2.6)\end{aligned}$$

where

$$\bar{\Psi} = \frac{R_s^{1/2}\Psi}{2^{1/2}\varepsilon} \qquad \xi = x' \qquad \eta = \frac{R_s^{1/2}y'}{2^{1/2}\varepsilon} \qquad (4.2.7)$$

and (x',y') are the unscaled boundary-layer variables along and normal to the surface of the body, respectively. The O(1) solution outside the boundary-layer, after relaxing the non-slip boundary condition, is then given by

$$\Psi_0=e^{it}\Psi_p \qquad (4.2.8)$$

where Ψ_p is the steady potential flow past the cascade and hence satisfies

$$\nabla^2\Psi_p = 0 \qquad (4.2.9)$$

In the boundary-layer the O(1) unsteady solution which satisfies the no-slip boundary condition on the surface of the body and matches the potential flow (4.2.8) at the outer edge of the boundary-layer can be shown, see for example, Riley (1967), to be given by

$$\bar{\Psi}_0 = U_p e^{it}\left\{1 - \frac{1}{2}(1-i)\left(1-e^{-(1+i)\eta}\right)\right\} \qquad (4.2.10)$$

The leading order of the O(ε) unsteady solution outside the boundary-layer, $\Psi_{10}^{(u)}$, is given by

$$\Psi_{10}^{(u)} \equiv 0 \qquad (4.2.11)$$

whilst the leading order of the O(ε) unsteady solution in the boundary-layer, $\bar{\Psi}_{10}^{(u)}$, is given by

$$\bar{\Psi}_{10}^{(u)}(\xi,\ \eta,\ t) = U_p \frac{dU_p}{d\xi} e^{2it}\left\{\frac{1+i}{4\sqrt{2}}\ e^{-(1+i)\sqrt{2}\eta} + \right.$$

$$\left. + \frac{i\eta}{2}\ e^{-(1+i)\eta} - \frac{1+i}{4\sqrt{2}}\right\} \qquad (4.2.12)$$

Expression (4.2.12) satisfies the no-slip boundary condition on the surface of the body and matches the outer solution (4.2.11) at the outer edge of the boundary-layer. For the O(ε) boundary-layer solution, $\bar{\Psi}^{(s)}(\xi,\eta)$, it is proven, see for example, Schlichting (1932), Stuart (1966), Riley (1967) and Wang (1968), that $\left.\frac{\partial \bar{\Psi}^{(s)}(\xi,\eta)}{\partial \eta}\right|_{\eta=\infty}$ must be finite (but non-zero) if the no-slip boundary condition on the surface of the body is to be satisfied. This O(ε) steady boundary-layer solution can be written as

$$\bar{\Psi}^{(s)} = U_p \frac{dU_p}{d\xi}\left(\frac{13}{8} - \frac{3}{4}\eta - \frac{1}{8}\ e^{-2\eta} - e^{-\eta}\sin(\eta) -\right.$$

$$- \frac{3}{2} e^{-\eta}\cos(\eta) - \frac{1}{2}\eta e^{-\eta}\sin(\eta)\Big) \qquad (4.2.13)$$

which gives the tangential velocity at the outer edge of the boundary-layer as

$$u_s \sim -\frac{3}{4}U_p(\xi)\frac{dU_p(\xi)}{d\xi} \qquad \text{as } \eta \longrightarrow \infty \qquad (4.2.14)$$

In this chapter we concentrate on the steady component of the $O(\varepsilon)$ solution outside the boundary-layer. On substitution of expression (4.2.4) into the governing equations (4.2.1) and (4.2.2) and equating the coefficients of the $O(\varepsilon^3)$ terms gives the following set of equations to be satisfied by the $O(\varepsilon)$ steady solution $\Psi^{(s)}$,

$$\frac{\partial(\Psi^{(s)},\omega^{(s)})}{\partial(X,Y)} + \frac{1}{R_s}\nabla^2\omega^{(s)} = 0 \qquad (4.2.15)$$

$$\nabla^2\Psi^{(s)} = -\omega^{(s)} \qquad (4.2.16)$$

and these equations have to be solved subject to the boundary conditions

$$\frac{\partial\Psi^{(s)}}{\partial Y} \longrightarrow 0, \quad \omega^{(s)} \longrightarrow 0 \qquad \text{as } X \longrightarrow \infty,\ 0 \le Y \le L \qquad (4.2.17)$$

$$\Psi^{(s)}(X,0) = \Psi^{(s)}(X,L) = \omega^{(s)}(X,0) = \omega^{(s)}(X,L) = 0 \qquad (4.2.18)$$

$$\left.\begin{aligned} \Psi^{(s)} &= 0 \\ \frac{\partial\Psi^{(s)}}{\partial n} &= u_s = -\frac{3}{4}U_p(\xi)\frac{dU_p(\xi)}{d\xi} \end{aligned}\right\} \quad \text{on the surface of the cascade} \qquad (4.2.19)$$

$$\Psi^{(s)}(0,Y) = 0 \qquad 0 \le Y \le L \qquad (4.2.20)$$

In order to solve equations (4.2.15)-(4.2.20) for $\Psi^{(s)}$ we need first obtain Ψ_p and hence u_s. Equation (4.2.9) has been solved using both the conformal mapping technique, a standard central

finite-difference discretisation and a direct inversion of the resulting equations. Singularities occur near the sharp corners of the body and in the finite-difference method they have been dealt with in a manner similar to that described by Motz (1946). In order to illustrate the conformal mapping technique we present the method, method *I*, for the cascade of normal flat plates only. The extension to other shaped bodies, such as a cascades of square bars, is trivial.

Using the Christoffel-Schwarz mapping

$$\frac{\partial z}{\partial \zeta} = k(\zeta-\zeta_b)^{-1/2}\zeta(\zeta-\zeta_d)^{-1/2}(\zeta-1)^{-1} \qquad (4.2.21)$$

then the region shown in **Fig.4.1a** in the z-plane, i.e. the X-Y plane, is conformally mapped onto the upper half ζ-plane as shown in **Fig.4.1b.**

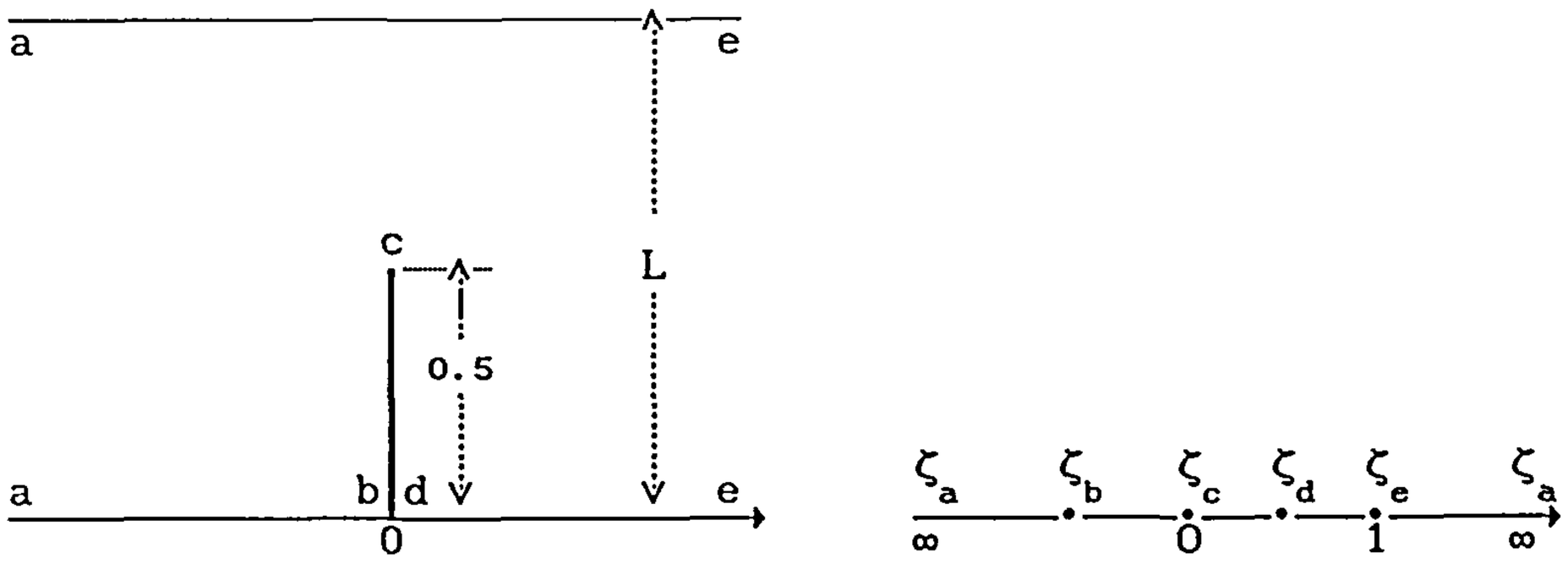

(a) z-plane (i.e. X-Y plane). (b) ζ-plane.

Fig.4.1 The conformal mapping given by (4.2.21).

The quantities k, ζ_b and ζ_d are constants to be determined and ζ_a, ζ_c and ζ_e are chosen to be $-\infty$, 0 and 1, respectively. The complex potential in the ζ-plane due to a sink of strength $u_\infty L\cos(t)$ at ζ_e

is $W= \frac{u_\infty L}{\pi} \ln(\zeta-1)\cos(t)$ and so the complex velocity potential is $U_p e^{it}$, where $u_\infty=1$ is the non-dimensional velocity at infinity and

$$U_p = \frac{u_\infty L(\zeta-\zeta_b)^{-1/2}(\zeta-\zeta_d)^{-1/2}}{k\pi\zeta} \qquad (4.2.22)$$

From the boundary conditions at infinity in the z-plane, i.e.

$$\left.\begin{aligned} U_p &\longrightarrow 1 \qquad \text{as } \zeta\longrightarrow \infty \\ U_p &\longrightarrow u_\infty \qquad \text{as } \zeta\longrightarrow -1 \end{aligned}\right\} \qquad (4.2.23)$$

then $k=L/\pi$ and $\zeta_b= -\zeta_d/(1-\zeta_d)$. Further, on integrating the differential equation (4.2.21) between z=c and z=d gives

$$-\frac{1}{2} = \frac{\pi}{L}\int_0^{\zeta_d} \frac{\zeta}{(\zeta+\zeta_d/(1-\zeta_d))^{1/2}(\zeta-\zeta_d)^{1/2}(\zeta-1)}\, d\zeta \qquad (4.2.24)$$

This equation is solved numerically in order to find ζ_d and then ζ_b is determined. It should be noted that in order to avoid the singularity which occurs at $\zeta=\zeta_d$ the following transformation

$$\zeta_1 = (\zeta_d-\zeta)^{1/2} \qquad (4.2.25)$$

was introduced when solving equation (4.2.24) for ζ_d numerically.

The relationship between a point z_0 in the z-plane and the point ζ_0 in the ζ-plane is obtained by integrating expression (4.2.21) to give

$$z_0-\frac{1}{2} = \frac{\pi}{L}\int_0^{\zeta_0} \frac{\zeta}{(\zeta-\zeta_b)^{1/2}(\zeta-\zeta_d)^{1/2}(\zeta-1)}\, d\zeta \qquad (4.2.26)$$

Thus in order to find the velocity on the plate of the cascade at the point z_0 we find the corresponding value of ζ_0 in the ζ-plane

from expression (4.2.26) by using a numerical integration method and then the velocity may be obtained from expression (4.2.22).

As an alternative, a central-difference discretisation and an iterative scheme, method *II*, is also used in order to solve equation (4.2.9) subject to the potential flow boundary conditions. The $O(\varepsilon)$ steady tangential velocity on the surface of the cascade (see expression (4.2.14)) is obtained by using both the conformal mapping technique and the finite-difference method and the results are compared in Fig.4.2. When using method *II* results have been obtained

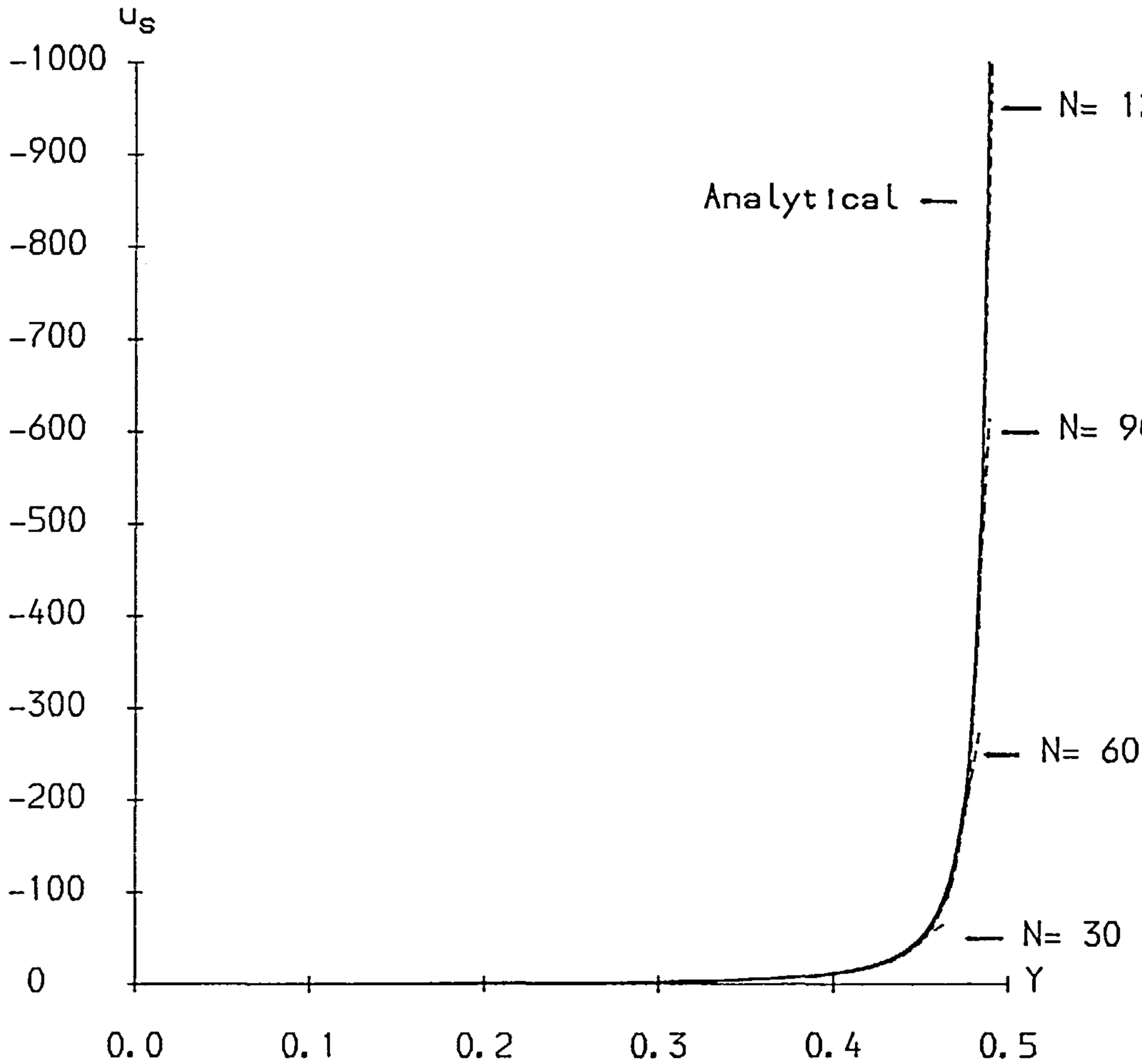

Fig.4.2 The steady vertical velocity u_s on the surface of the plate. ------- numerical, ——— analytical.

for different mesh sizes, namely 1/30, 1/60, 1/90 and 1/120 and these results are shown in **Fig.4.2.** It is clear that the results from these two methods are, in general, in very good agreement, and as the mesh size tends to zero the solution obtained from method *II* approaches that obtained using method *I*. As the conformal mapping technique is an analytical method it gives the results for u_s accurately and easily and therefore it has been used throughout the remainder of this chapter.

Thus we have determined the tangential velocity on the surface of the cascade and this forms the inner boundary condition when determining the outer steaming flow at the outer edge of the Stokes-layer.

4.3 The Outer Streaming Flow

In this section we consider the streaming flow due to a harmonically oscillating cascade of bodies which have sharp corners, i.e. cascades of square cylinders and flat plates, see **Fig.1.5** and Fig.1.6. The equations of motion are (4.2.15) and (4.2.16) and these have to be solved for the case of the cascade of square cylinders subject to the boundary conditions (4.2.17)-(4.2.20). A detailed description of the method used will be given for the cascade of square cylinders and as the technique is very similar for a cascade of flat plates only a brief description for this geometry will be presented.

To adequately deal with the more rapidly changing flow near to the cascade more mesh points are required in this vicinity. In order to achieve this we introduce the following co-ordinate

transformation

$$\begin{cases} \alpha = \ln(1 + D_x(X-0.5)) + 0.5 & 0.5 \le X < \infty \quad (4.3.1) \\ \beta = \ln(1 + D_y(Y-0.5)) + 0.5 & 0.5 \le Y \le L \quad (4.3.2) \\ \alpha = X & 0 < X < 0.5 \quad (4.3.3) \\ \beta = Y & 0 < Y < 0.5 \quad (4.3.4) \end{cases}$$

where D_x and D_y are constants which will be specified later. Thus if a constant mesh is set up in the (α, β) coordinate system then there will be more mesh points near the cascade than at large distances from the cascade. It is found convenient to use a mesh size, h, in both the α- and β-directions and for the mesh to be square in both the X- and Y-directions on X=1/2. Hence we choose $D_x = D_y \equiv D$, say, such that

$$h = \ln(1+Dh) \quad (4.3.5)$$

A typical grid system is shown in **Fig.4.3** with h=1/20 and L=1.

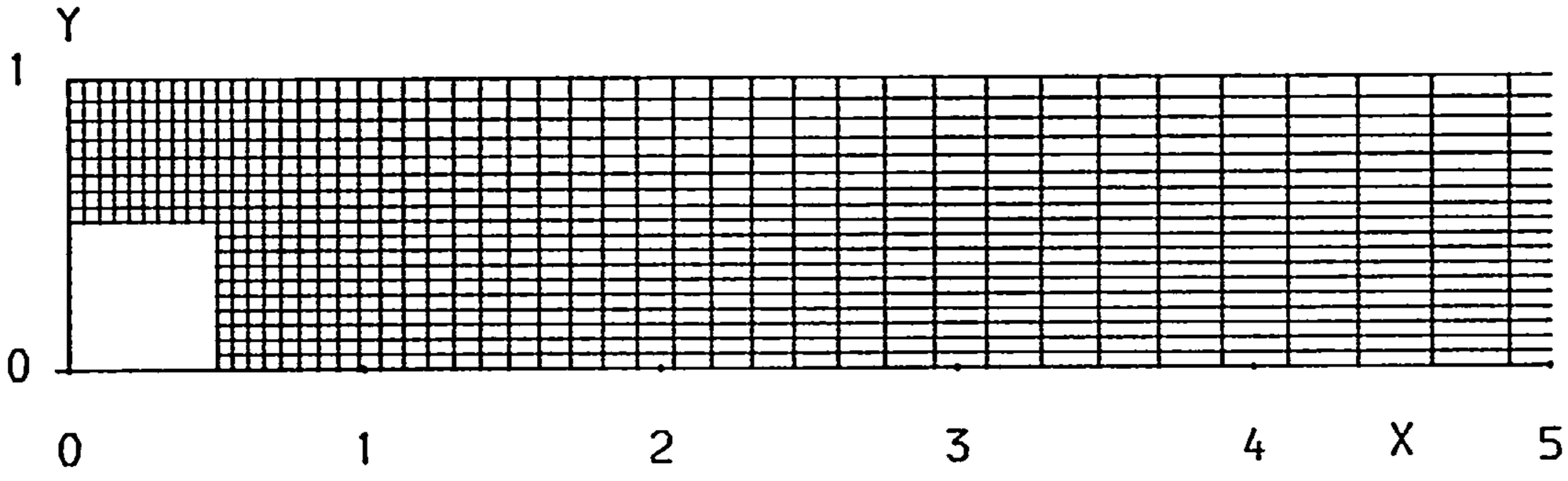

Fig.4.3 The grid system generated by the transformations (4.3.1)-(4.3.4) for the cascade of normal flat plates with h=1/20.

On using the transformation (4.3.1)-(4.3.4) the governing equations (4.2.15) and (4.2.16) may be written in the following form

in the region $0.5 \leq x < \infty$, $0.5 \leq y \leq y_L$:

$$\frac{E(x)^2}{R_s}\left(\frac{\partial^2 \omega^{(s)}}{\partial x^2} - \frac{\partial \omega^{(s)}}{\partial x}\right) + \frac{E(y)^2}{R_s}\left(\frac{\partial^2 \omega^{(s)}}{\partial y^2} - \frac{\partial \omega^{(s)}}{\partial y}\right) + E(x)E(y)\frac{\partial(\Psi^{(s)}, \omega^{(s)})}{\partial(x, y)} = 0 \qquad (4.3.6)$$

$$E(x)^2\left(\frac{\partial^2 \Psi^{(s)}}{\partial x^2} - \frac{\partial \Psi^{(s)}}{\partial x}\right) + E(y)^2\left(\frac{\partial^2 \Psi^{(s)}}{\partial y^2} - \frac{\partial \Psi^{(s)}}{\partial y}\right) = -\omega^{(s)} \qquad (4.3.7)$$

in the region $0 \leq x < 0.5$, $0.5 \leq y \leq y_L$:

$$\frac{1}{R_s}\frac{\partial^2 \omega^{(s)}}{\partial x^2} + \frac{E(y)^2}{R_s}\left(\frac{\partial^2 \omega^{(s)}}{\partial y^2} - \frac{\partial \omega^{(s)}}{\partial y}\right) + E(y)\frac{\partial(\Psi^{(s)}, \omega^{(s)})}{\partial(x, y)} = 0 \qquad (4.3.8)$$

$$\frac{\partial^2 \Psi^{(s)}}{\partial x^2} + E(y)^2\left(\frac{\partial^2 \Psi^{(s)}}{\partial y^2} - \frac{\partial \Psi^{(s)}}{\partial y}\right) = -\omega^{(s)} \qquad (4.3.9)$$

and in the region $0.5 \leq x < \infty$, $0 \leq y < 0.5$:

$$\frac{E(x)^2}{R_s}\left(\frac{\partial^2 \omega^{(s)}}{\partial x^2} - \frac{\partial \omega^{(s)}}{\partial x}\right) + \frac{1}{R_s}\frac{\partial^2 \omega^{(s)}}{\partial y^2} + E(x)\frac{\partial(\Psi^{(s)}, \omega^{(s)})}{\partial(x, y)} = 0 \qquad (4.3.10)$$

$$E(x)^2\left(\frac{\partial^2 \Psi^{(s)}}{\partial x^2} - \frac{\partial \Psi^{(s)}}{\partial x}\right) + \frac{\partial^2 \Psi^{(s)}}{\partial y^2} = -\omega^{(s)} \qquad (4.3.11)$$

where $y_L = \ln(1 + D_y(L - 0.5)) + 0.5$, $E(x) = D \exp(-x + 0.5)$ and $E(y) = D \exp(-y + 0.5)$.

Denoting the points with coordinates (ih, jh), ((i+1)h, jh), (ih, (j+1)h), ((i-1)h, jh) and (ih, (j-1)h) by 0, 1, 2, 3 and 4, respectively, then the standard 5 point central-difference discretised form of equation (4.3.6) can be written as

$$\tilde{c}_1 \omega_1^{(s)} + \tilde{c}_2 \omega_2^{(s)} + \tilde{c}_3 \omega_3^{(s)} + \tilde{c}_4 \omega_4^{(s)} - \tilde{c}_0 \omega_0^{(s)} = 0 \qquad (4.3.12)$$

where

$$\left.\begin{aligned}
\tilde{c}_1 &= \frac{1}{h^2}E_{XO}^2 - \frac{1}{2h}E_{XO}(E_{XO} + E_{YO}R_sU_O)\\
\tilde{c}_2 &= \frac{1}{h^2}E_{YO}^2 - \frac{1}{2h}E_{YO}(E_{YO} + E_{XO}R_sV_O),\\
\tilde{c}_3 &= \frac{1}{h^2}E_{XO}^2 + \frac{1}{2h}E_{XO}(E_{XO} + E_{YO}R_sU_O)\\
\tilde{c}_4 &= \frac{1}{h^2}E_{YO}^2 + \frac{1}{2h}E_{YO}(E_{YO} + E_{XO}R_sV_O)\\
\tilde{c}_O &= \tilde{c}_1 + \tilde{c}_2 + \tilde{c}_3 + \tilde{c}_4
\end{aligned}\right\} \qquad (4.3.13)$$

and

$$\left.\begin{aligned}
U_o &= \left(\frac{\partial\Psi^{(s)}}{\partial y}\right)_o\\
V_o &= -\left(\frac{\partial\Psi^{(s)}}{\partial x}\right)_o
\end{aligned}\right\} \qquad (4.3.14)$$

with $E_{XO}=E(x_o)$ and $E_{YO}=E(y_o)$. Similar discretisations can be written down for equations (4.3.8) and (4.3.10).

The matrix associated with the set of finite-difference equations (4.3.12) is not always diagonally dominant and therefore S.O.R. iterative methods may not always be convergent. In order to obtain a discretised system of equations which is diagonally dominant but still has an accuracy $O(h^2)$ we use a specialised central finite-difference scheme. The method is similar to that developed by Dennis and Hudson (1978) and was successfully used and extended by Ingham *et al.* (1990a) on a related problem and is that employed in chapter 2. Therefore the detailed derivation of the finite-difference equations is not presented and they are given by

$$c_1\omega_1^{(s)} + c_2\omega_2^{(s)} + c_3\omega_3^{(s)} + c_4\omega_4^{(s)} - c_o\omega_o^{(s)} = 0 \qquad (4.3.15)$$

$$b_1\Psi_1^{(s)} + b_2\Psi_2^{(s)} + b_3\Psi_3^{(s)} + b_4\Psi_4^{(s)} - b_o\Psi_o^{(s)} + h^2\omega_o^{(s)} = 0 \qquad (4.3.16)$$

where

$$c_1=\begin{cases} E_{xo}^2-\frac{h}{2}E_{xo}(E_{xo}+E_{yo}R_sU_o)+\frac{h^2}{8}(E_{xo}+E_{yo}R_sU_o)^2 & \frac{1}{2}\le x<\infty,\ \frac{1}{2}\le y\le y_L \\ 1-\frac{h}{2}E_{yo}R_sU_o+\frac{h^2}{8}E_{yo}^2R_s^2U_o^2 & 0\le x<\frac{1}{2},\ \frac{1}{2}\le y\le y_L \\ E_{xo}^2-\frac{h}{2}E_{xo}(E_{xo}+R_sU_o)+\frac{h^2}{8}(E_{xo}+R_sU_o)^2 & \frac{1}{2}\le x<\infty,\ 0\le y\le\frac{1}{2} \end{cases} \quad (4.3.17a)$$

$$c_2=\begin{cases} E_{yo}^2-\frac{h}{2}E_{yo}(E_{yo}+E_{xo}R_sV_o)+\frac{h^2}{8}(E_{yo}+E_{xo}R_sV_o)^2 & \frac{1}{2}\le x<\infty,\ \frac{1}{2}\le y\le y_L \\ E_{yo}^2-\frac{h}{2}E_{yo}(E_{yo}+R_sV_o)+\frac{h^2}{8}(E_{yo}+R_sV_o)^2 & 0\le x<\frac{1}{2},\ \frac{1}{2}\le y\le y_L \\ 1-\frac{h}{2}E_{xo}R_sV_o+\frac{h^2}{8}E_{xo}^2R_s^2V_o^2 & \frac{1}{2}\le x<\infty,\ 0\le y\le\frac{1}{2} \end{cases} \quad (4.3.17b)$$

$$c_3=\begin{cases} E_{xo}^2+\frac{h}{2}E_{xo}(E_{xo}+E_{yo}R_sU_o)+\frac{h^2}{8}(E_{xo}+E_{yo}R_sU_o)^2 & \frac{1}{2}\le x<\infty,\ \frac{1}{2}\le y\le y_L \\ 1+\frac{h}{2}E_{yo}R_sU_o+\frac{h^2}{8}E_{yo}^2R_s^2U_o^2 & 0\le x<\frac{1}{2},\ \frac{1}{2}\le y\le y_L \\ E_{xo}^2+\frac{h}{2}E_{xo}(E_{xo}+R_sU_o)+\frac{h^2}{8}(E_{xo}+R_sU_o)^2 & \frac{1}{2}\le x<\infty,\ 0\le y\le\frac{1}{2} \end{cases} \quad (4.3.17c)$$

$$c_4=\begin{cases} E_{yo}^2+\frac{h}{2}E_{yo}(E_{yo}+E_{xo}R_sV_o)+\frac{h^2}{8}(E_{yo}+E_{xo}R_sV_o)^2 & \frac{1}{2}\le x<\infty,\ \frac{1}{2}\le y\le y_L \\ E_{yo}^2+\frac{h}{2}E_{yo}(E_{yo}+R_sV_o)+\frac{h^2}{8}(E_{yo}+R_sV_o)^2 & 0\le x<\frac{1}{2},\ \frac{1}{2}\le y\le y_L \\ 1+\frac{h}{2}E_{xo}R_sV_o+\frac{h^2}{8}E_{xo}^2R_s^2V_o^2 & \frac{1}{2}\le x<\infty,\ 0\le y\le\frac{1}{2} \end{cases} \quad (4.3.17d)$$

$$b_1=\begin{cases} E_{xo}^2(1-\frac{h}{2}) & \frac{1}{2}\le x<\infty,\ 0\le y\le y_L \\ 1 & 0\le x<\frac{1}{2},\ \frac{1}{2}\le y\le y_L \end{cases} \quad (4.3.18a)$$

$$b_2=\begin{cases} E_{yo}^2(1-\frac{h}{2}) & 0\le x<\infty,\ \frac{1}{2}\le y\le y_L \\ 1 & \frac{1}{2}\le x<\infty,\ 0\le y\le\frac{1}{2} \end{cases} \quad (4.3.18b)$$

$$b_3=\begin{cases} E_{xo}^2(1+\frac{h}{2}) & \frac{1}{2}\le x<\infty,\ 0\le y\le y_L \\ 1 & 0\le x<\frac{1}{2},\ \frac{1}{2}\le y\le y_L \end{cases} \quad (4.3.18c)$$

$$b_4=\begin{cases} E_{yo}^2(1+\frac{h}{2}) & 0\le x<\infty,\ \frac{1}{2}\le y\le y_L \\ 1 & \frac{1}{2}\le x<\infty,\ 0\le y\le\frac{1}{2} \end{cases} \quad (4.3.18d)$$

$$\left.\begin{aligned} c_o &= c_1+c_2+c_3+c_4 \\ b_o &= b_1+b_2+b_3+b_4 \end{aligned}\right\} \qquad (4.3.19)$$

Although boundary condition (4.2.17) applies as $X\longrightarrow\infty$ for computational purposes we have to apply this condition at a finite, but large, value of X, say $X=X_R$. In order to choose X_R as small as possible we look for an asymptotic solution of equations (4.2.15) and (4.2.16) which is valid at large values of X. We assume, as is common in this type of flow, that

$$\Psi^{(s)} = e^{-\alpha X} f(Y) \qquad (4.3.20)$$

where α (>0) is an unknown constant and f(Y) is unknown function of Y. On substituting of expression (4.3.20) into the equations (4.2.15) and (4.2.16) we find that if the boundary condition (4.2.18) is satisfied then

$$\Psi^{(s)} = \sum_{n=1}^{\infty} d_n e^{-\frac{n\pi X}{L}} \sin\frac{n\pi Y}{L} \qquad \text{for large X} \qquad (4.3.21)$$

where d_n are unknown constants. Taking the leading-order in the expression (4.3.21) we obtain the following condition

$$\frac{\partial\Psi^{(s)}}{\partial X} = -\frac{\pi}{L}\Psi^{(s)} \qquad \text{on } 0 \le Y \le L, \text{ as } X \longrightarrow \infty \qquad (4.3.22)$$

and this is in a much more convenient form of boundary condition than condition (4.3.21) to be applied at $X=X_R$. For the boundary condition on the vorticity on the surface of the cascade we use the scheme which was derived by Woods (1954), as given in (2.2.14) in which U_B is the steady streaming velocity of the fluid at the point B and is given by expression (4.2.14).

The cascade has sharp corners. Therefore the potential flow is

singular at these points and hence the boundary condition (4.2.14) needs further discussion. In this chapter we use the method derived by Kim and Troesch (1989) to deal with this problem. They found that the flow around the corner is composed of three regions, namely at the corner the locally valid Stokes region, I, next to this is the unsteady boundary-layer, II, and outside is the potential flow region, III. For small values of the distance from the corner, r, the tangential velocity, u, will behave as $u \sim r^{0.54448}$ in region I and $u_p \sim r^{-1/2}$ in region III. In the intermediate boundary-layer region, II, the two velocities have to be matched. The maximum potential velocity in region II occurs at a point which is at a distance δ from the corner of the body and the choice of the value of δ is that as described by Kim and Troesch (1989).

In the case of a harmonically oscillating cascade of normal flat plates the analysis follows in a manner very similar to that described above for the cascade of square cylinders. For this case we use the following co-ordinate transformation,

$$\alpha = \ln(1+D_x X) \qquad 0 \le X < \infty,\ 0 \le Y \le L \qquad (4.3.23)$$

$$\psi = \ln(1+D_y (Y-0.5)) + 0.5 \qquad 0 \le X < \infty,\ \frac{1}{2} \le Y \le L \qquad (4.3.24)$$

$$\psi = Y \qquad 0 \le X < \infty,\ 0 \le Y \le \frac{1}{2} \qquad (4.3.25)$$

Again D_x and D_y are taken to be constants and determined from equation (4.3.5). The governing equations (4.2.15) and (4.2.16) now become:

in the region $0 \le \alpha < \infty,\ 0.5 \le \psi \le \psi_L$:

$$\frac{E(\alpha)^2}{R_s}\left(\frac{\partial^2\omega^{(s)}}{\partial\alpha^2}-\frac{\partial\omega^{(s)}}{\partial\alpha}\right)+\frac{E(\psi)^2}{R_s}\left(\frac{\partial^2\omega^{(s)}}{\partial\psi^2}-\frac{\partial\omega^{(s)}}{\partial\psi}\right)+E(\alpha)E(\psi)\frac{\partial(\Psi^{(s)},\omega^{(s)})}{\partial(\alpha,\psi)}=0 \qquad (4.3.26)$$

$$E(\alpha)^2\left(\frac{\partial^2\Psi^{(s)}}{\partial\alpha^2}-\frac{\partial\Psi^{(s)}}{\partial\alpha}\right)+E(\psi)^2\left(\frac{\partial^2\Psi^{(s)}}{\partial\psi^2}-\frac{\partial\Psi^{(s)}}{\partial\psi}\right)=-\omega^{(s)} \qquad (4.3.27)$$

and in the region $0\leq\alpha<\infty$, $0\leq\psi\leq0.5$:

$$\frac{E(\alpha)^2}{R_s}\left(\frac{\partial^2\omega^{(s)}}{\partial\alpha^2}-\frac{\partial\omega^{(s)}}{\partial\alpha}\right)+\frac{1}{R_s}\frac{\partial^2\omega^{(s)}}{\partial\psi^2}+E(\alpha)\frac{\partial(\Psi^{(s)},\omega^{(s)})}{\partial(\alpha,\psi)}=0 \qquad (4.3.28)$$

$$E(\alpha)^2\left(\frac{\partial^2\Psi^{(s)}}{\partial\alpha^2}-\frac{\partial\Psi^{(s)}}{\partial\alpha}\right)+\frac{\partial^2\Psi^{(s)}}{\partial\psi^2}=-\omega^{(s)} \qquad (4.3.29)$$

where $E(\alpha)=D\exp(-\alpha)$, $E(\psi)=D\exp(-\psi+0.5)$.

Equations (4.3.26)-(4.3.29) are put into finite-difference form using a specialised scheme which retains $O(h^2)$ accuracy but makes the associated matrix to the finite-difference equations diagonally dominant. The infinity boundary condition (4.3.22) is again applied at $X=X_R$ and the determination of the vorticity on the plates of the cascade are given by equation (2.2.14).

The flow structure near the corner of the plate is again assumed to be composed of the three regions, the locally valid Stokes region I, the unsteady boundary-layer II and the potential region III. In region I $u\sim O(r^{1/2})$ whilst in region III $u_p\sim r^{-1/2}$ and these two velocities are matched to region II using the method as described by Kim and Troesch (1989).

4.4 Results and Discussion

Numerical results have been obtained for values of the streaming Reynolds number R_s=1, 1.4, 5, 10, 20, 30, 40, 50, 60 and

70 with mesh sizes h=1/20, 1/40 and 1/60. All the results presented in this chapter are the h^2-extrapolation of these results. For small values of the streaming Reynolds number the results obtained with the coarsest grid gives reasonably accurate results but as the Reynolds numbers increase then a finer mesh sizes is required. However, even at R_s=70 the results obtained using h=1/60 and the h^2-extrapolated results are almost graphically indistinguishable. In order to illustrate the numerical method we present results only for L=1 although calculations have been performed over a wide range of values of L and all the results show the same general flow characteristics. Further, the experimental investigations that have been performed have also been restricted to L=1. Several values of X_R have been tried. It is found that as the streaming Reynolds number increases then the strength of the recirculating eddies that are formed increases both in magnitude and in physical size and therefore X_R must be increased as R_s increases. It has been found that for $R_s \leq 30$ a value of X_R=10 is sufficiently large but for $R_s \approx 70$ a value of X_R=15 is necessary. Computations were performed over a wide range of values of X_R and the results shown in this chapter are graphically indistinguishable if X_R is taken any larger than the values used in the figures presented.

4.4.1 The Cascade of Square Cylinders

The numerical results were first obtained for a cascade of square cylinders with L=1 and R_s=1.4 with h=1/20 and X_R=5. Using a point by point successive relaxation procedure with the relaxation parameter being 1.2 for the vorticity everywhere, except on the

boundary, 0.2 for the vorticity on the boundary and 1.2 for the streamfunction a converged solution was obtained in about 30 CPU seconds on an Amdhal-5860 computer at Leeds University. In order to find a first approximation to the solution with h=1/30 the results obtained using h=1/20 were extrapolated to the new mesh system and again an S.O.R. technique was used to obtain a convergent solution. The same process was used to obtain the solution for h=1/40. Using the solutions obtained with R_s=1.4 as a first guess the solutions with R_s=5 were obtained using S.O.R. and with h=1/20, 1/30 and 1/40. This whole process was continued until results were obtained for values of R_s up to 70. Then the value of X_R was increased for each value of h and R_s until any further increase in X_R resulted in only negligible changes in the solutions obtained. The smallest value of the relaxation factors used was when R_s=70 and h=1/60 and in this case the relaxation factor on the vorticity was 1.1 at all points other than on the boundary, 0.1 for points on the boundary and 1.1 for the streamfunction. The whole process was repeated for the cascade of normal flat plates, see section **4.4.2.**

Fig.4.4 shows the outer streaming streamlines for R_s=1.4, 10, 30, 50 and 70 for the harmonically oscillating cascade of square bars with L=1 and $\varepsilon \ll 1$. It is observed that there are eight recirculating flows associated with each square bar of the cascade. The flow goes out along $|X|>\frac{1}{2}$ and $|Y|>\frac{1}{2}$ and towards each corner of the square and the flow never goes round the corners of the square. This phenomena has also been observed by Kim and Troesch (1989) who investigated the harmonic oscillation of a single square bar. As the value of R_s increases then the centre of each of the recirculating

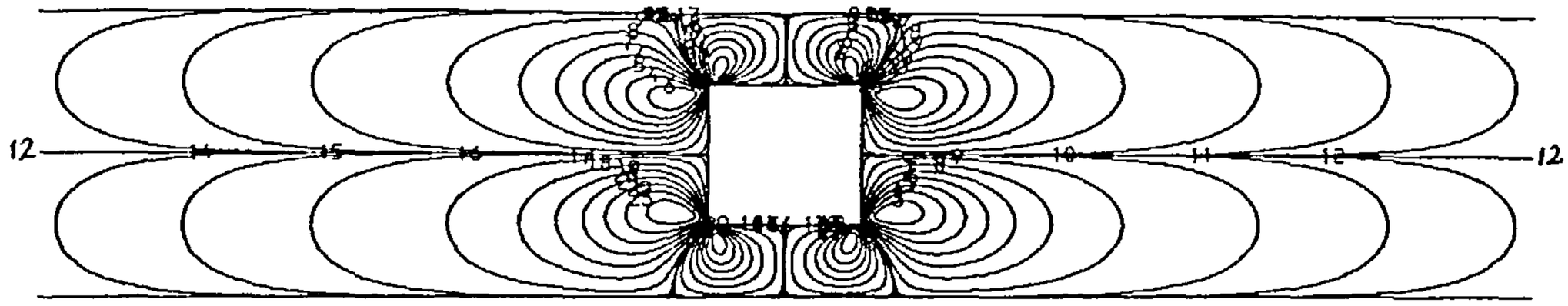

(a)

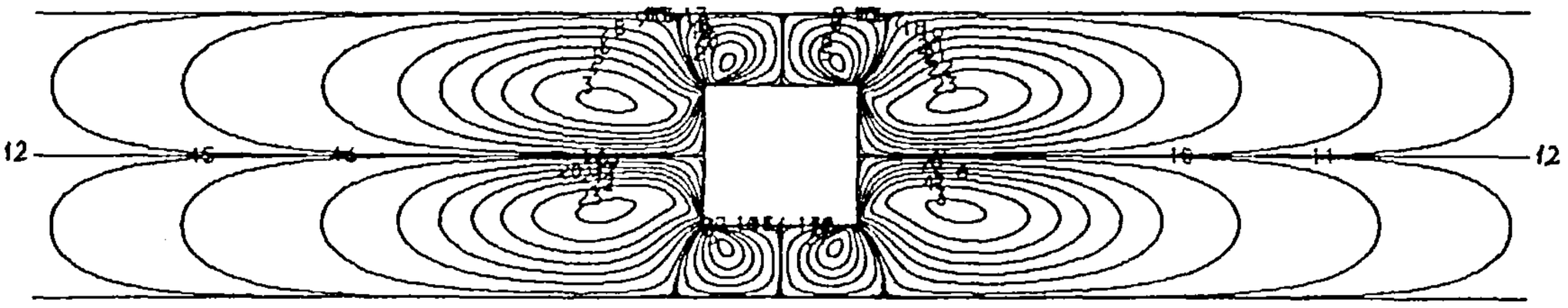

(b)

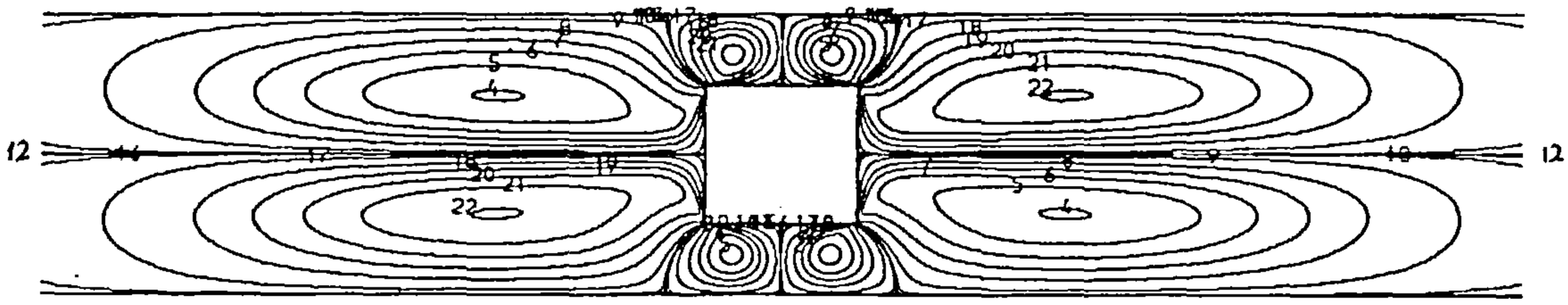

(c)

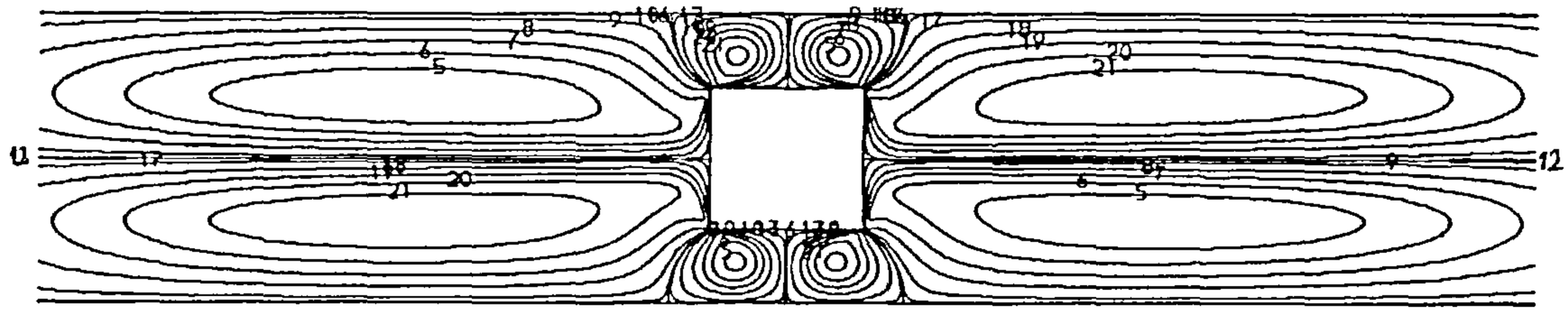

(d)

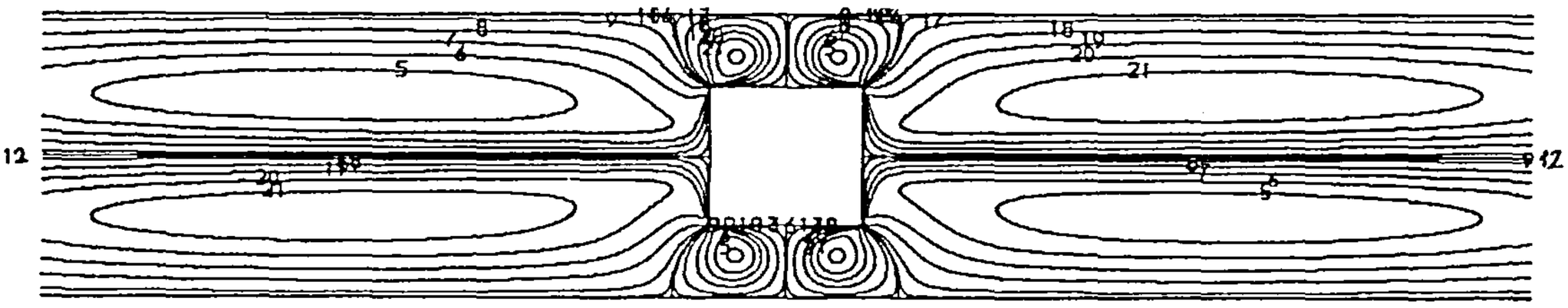

(e)

Fig.4.4 The outer streaming streamlines for the cascade of square cylinders obtained numerically for different values of the streaming Reynolds number R_s. The streamlines labelled 1-23 correspond to $\Psi^{(s)}$= -1.5, -1.3, -1.1, -0.9, -0.7, -0.5, -0.3, -0.1, -0.01, -0.001, -0.0001, 0, 0.0001, 0.001, 0.01, 0.1, 0.3, 0.5, 0.7, 0.9, 1.1, 1.3 and 1.5, respectively. (a) R_s=1.4, (b) R_s=10, (c) R_s=30, (d) R_s=50, (e) R_s=70.

regions in $|X|>\frac{1}{2}$ increases its $|X|$-component but the Y-component remains very close to $|Y|=\frac{1}{2}$. Also the strength of these recirculating regions increase as the streaming Reynolds number increases and this is not surprising since increasing R_s, for a given cascade and fluid, implies increasing the amplitude of the oscillatory motion of the cascade and hence increasing the amount of energy being put into the system.

4.4.2 The Cascade of Normal Flat Plates

Results for the outer streaming flow for R_s=1, 10, 30, 50 and 70 for the harmonically oscillating cascade of normal flat plates with L=1 and $\varepsilon \ll 1$ is given in **Fig.4.5**. Unlike the situation of the cascade of square bars there are only four recirculating flows associated with each plate much the same as is observed when a circular cylinder performs harmonic oscillatory motion. Again, as expected, as the streaming Reynolds number increases so does the strength of the recirculating region and the centres of the recirculating regions have a large X component.

4.5 Conclusion

Flows induced by the small-amplitude and high frequency harmonic oscillations of a cascade of bodies in an unbounded fluid which is otherwise at rest have been investigated theoretically. In this theoretical study we separate the flow into inner and outer regions with the inner flow being governed by the Stokes boundary-layer equation. The first-order outer flow is governed by the potential solution which is found by using both a conformal

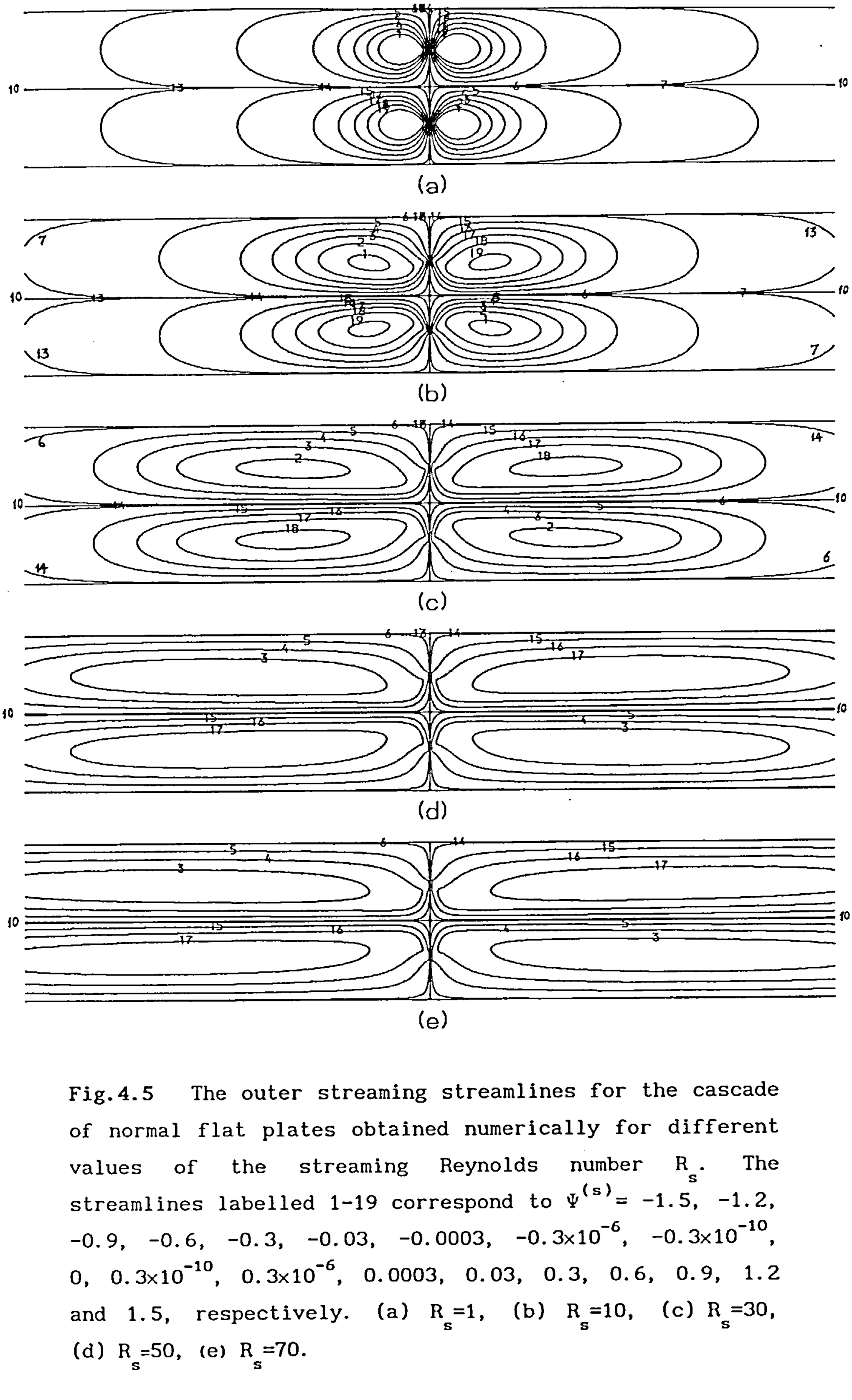

Fig.4.5 The outer streaming streamlines for the cascade of normal flat plates obtained numerically for different values of the streaming Reynolds number R_s. The streamlines labelled 1-19 correspond to $\Psi^{(s)}$= -1.5, -1.2, -0.9, -0.6, -0.3, -0.03, -0.0003, -0.3×10^{-6}, -0.3×10^{-10}, 0, 0.3×10^{-10}, 0.3×10^{-6}, 0.0003, 0.03, 0.3, 0.6, 0.9, 1.2 and 1.5, respectively. (a) R_s=1, (b) R_s=10, (c) R_s=30, (d) R_s=50, (e) R_s=70.

mapping technique and a finite-difference method. The second-order outer streaming flow ($O(\varepsilon)$) is governed by the full Navier-Stokes equations and which has been solved using a modified central-difference scheme for cascades with square cylinders and flat plates for values of the streaming Reynolds number, R_s, up to 70. The structure of the outer streaming flow is complicated but it is quite similar to those observed when there is only one oscillating cylinder, see for example the results obtained by Kim and Troesch (1989) for an oscillating single square cylinder.

CHAPTER 5 STREAMING FLOWS INDUCED BY AN OSCILLATING CASCADE OF CYLINDERS

5.1 Introduction

Similar to those investigated in chapter 4, in this chapter we numerically investigate the flow induced by a cascade of circular cylinders which performs harmonic oscillations with very small amplitude ($\varepsilon \ll 1$) and have a large frequency (i.e. $R_s \geq O(1)$) in an unbounded, incompressible fluid which is otherwise at rest. Consistent with the early theories, the leading-order unsteady outer flow is given by the unsteady velocity potential and this flow is determined using a conformal mapping technique. It is assumed, as Kim and Troesch (1989) did when investigating the harmonic oscillations of a single square cylinder, that the flow does not separate. Given the tangential velocity next to the body then these inner boundary-layer equations may be solved. The $O(\varepsilon)$ outer flow may be determined and this consists of an unsteady component and a steady streaming flow. In this chapter we use a finite-difference scheme, which is similar to that used in chapter 4, to solve for the steady streaming flow and different kinds of boundary conditions are employed to see their influence on the solution. It is observed that when the streaming Reynolds number is small then the outer streaming flow around each cylinder of the cascade is similar to that in the case of one oscillating circular cylinder whilst different

phenomena are observed when this Reynolds number is increased. As the Reynolds number increases then the symmetry of the streaming flow breaks down, i.e. a bifurcation occurs at a critical value of R_s, R_{s0} say, and we have shown, numerically, that $8<R_{s0}<9$. It is well known that this kind of break-down of symmetry may be due to the instability of the flow at high values of the Reynolds number (see for example Fearn *et al.* (1990)). In order to investigate why the break-down occurs at small values of R_s a stability analysis of the streaming cascade flow is presented. The numerical results compare well with some related experimental data. At small values of the streaming Reynolds number the steady streaming flow is symmetrical whilst at large values of R_s the flow becomes asymmetrical and the experimental results compare well with the present numerical calculations. Finally, the experimental results of the streaming flow induced by oscillating cascade of square and rectangular cylinders are also discussed.

5.2 Governing Equations and Boundary Conditions

Mathematically the fluid flow induced by the harmonic oscillation of an infinite cascade of circular cylinders has been investigated. This cascade of circular cylinder is as described in chapter 1 (see **Fig.1.7**) and oscillates harmonically and perpendicular to the plane of the cascade in an unbounded, incompressible fluid which is otherwise at rest. The displacement of the cascade is in the x^*-direction and is given by equation (1.1.1). The governing non-dimensional equations for the $O(\varepsilon)$ outer streaming flow, with the co-ordinate system fixed in the cascade and in terms of the streamfunction and vorticity, are equations (4.2.15) and

(4.2.16), namely,

$$\frac{\partial(\omega^{(s)},\ \Psi^{(s)})}{\partial(X,\ Y)} = \frac{1}{R_s}\nabla^2\omega^{(s)} \qquad (5.2.1)$$

$$\nabla^2\Psi^{(s)} = -\omega^{(s)} \qquad (5.2.2)$$

Equations (5.2.1) and (5.2.2) must be solved subject to the following boundary conditions

$$u_s \equiv \left.\frac{\partial\Psi^{(s)}}{\partial n}\right|_{X^2+(Y\pm 2k\mathcal{L})^2=0.5^2} = -\frac{3}{4}\,u_p\frac{du_p}{ds} \qquad (5.2.3)$$

$$\Psi^{(s)}(X,\ Y:\ X^2+(Y\pm 2k\mathcal{L})^2=0.5^2) = 0 \qquad (5.2.4)$$

$$\frac{\partial\Psi^{(s)}}{\partial Y} \longrightarrow 0,\quad \omega^{(s)} \longrightarrow 0,$$

for all values of Y as $X\longrightarrow 0$ (5.2.5)

where k is an integer, s and n are the variables along and normal to the surface of the body, u_s is the tangential velocity along the surface of the body and u_p is the potential tangential velocity along the surface of the body due to the cascade of the circular cylinders, see Riley (1967).

Mathematically one would expect the flow to have several symmetries and hence a numerical solution should only be sought in the region $0 \le X < +\infty$, $0 \le Y \le L$, see **Fig.5.1a**. However, experimentally we observe that above a critical value of the Reynolds number the fluid flow breaks these symmetries and hence numerical results have been obtained in solution domains which invoke other symmetries and we will return to these flows in section 5.4.

In order to solve the problem described by equations

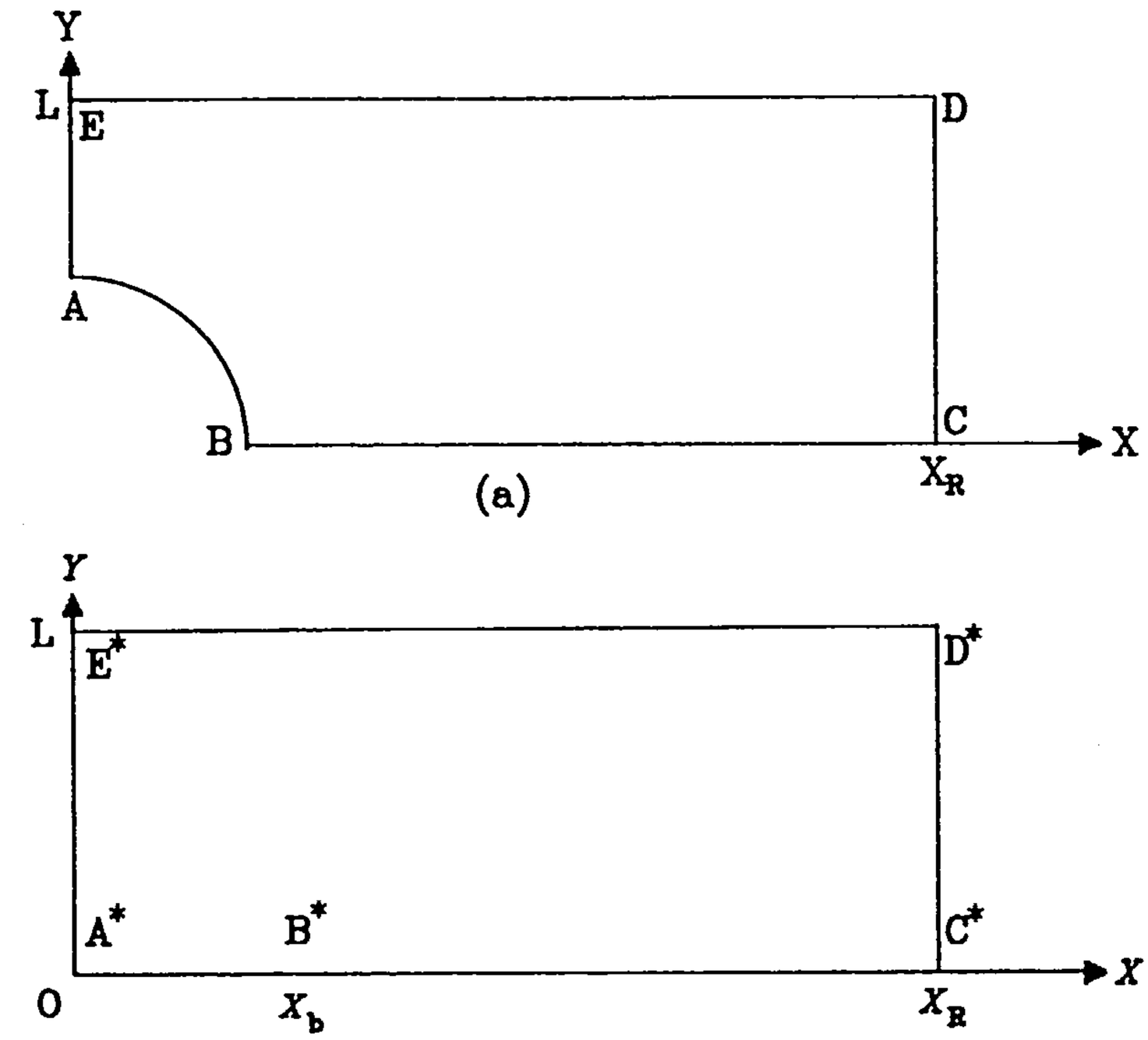

Fig.5.1 Different solution domains. (a) DM0 domain, (b) transformed DM0 domain, (c) DM1 and DM4 domain, (d) transformed DM1 and DM4 domain, (to be continued).

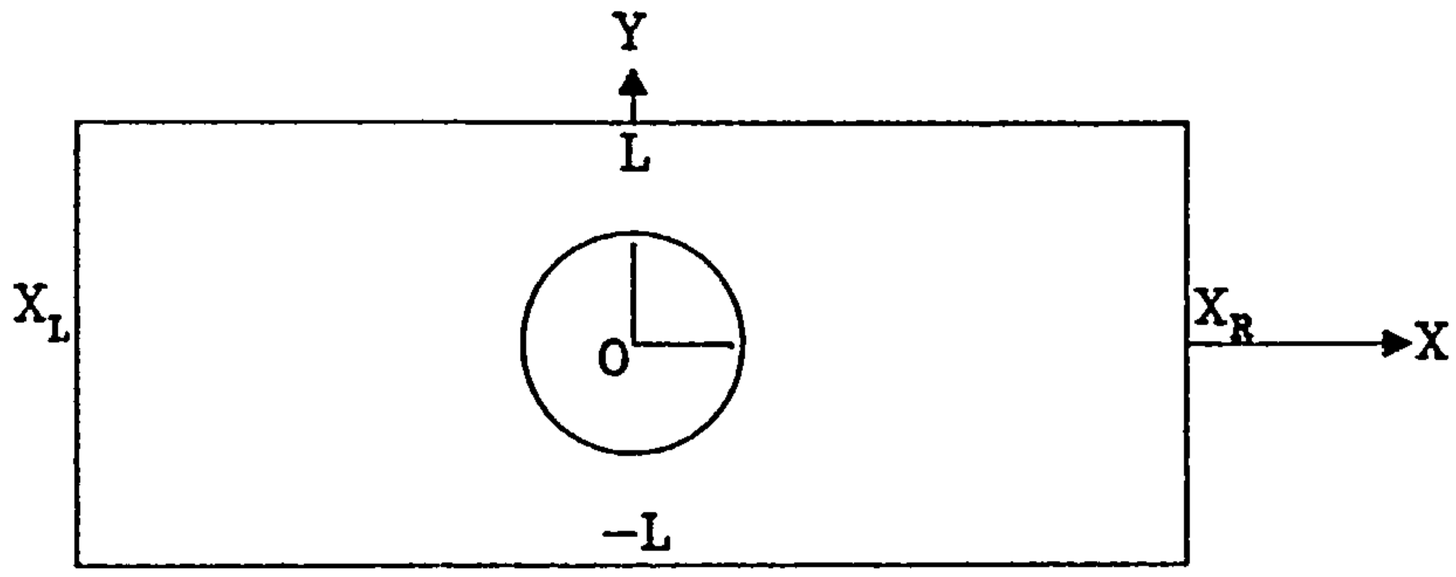

(e)

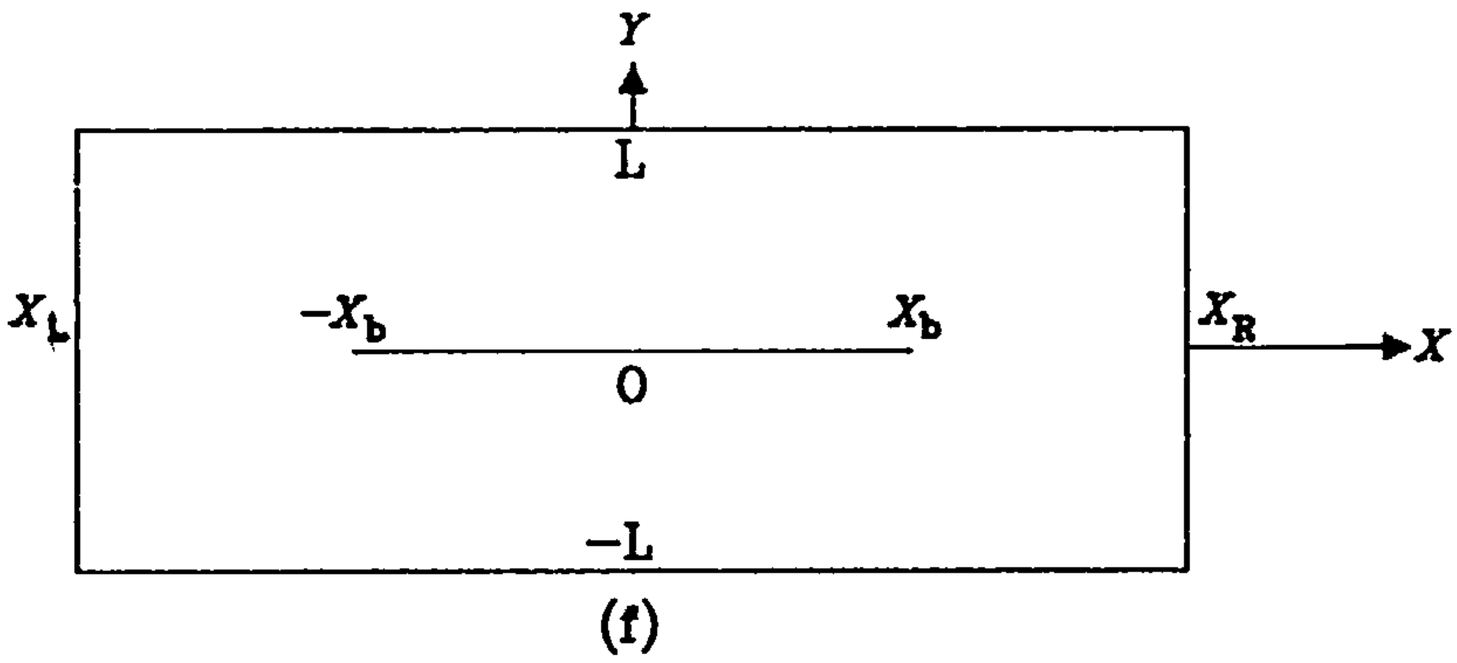

(f)

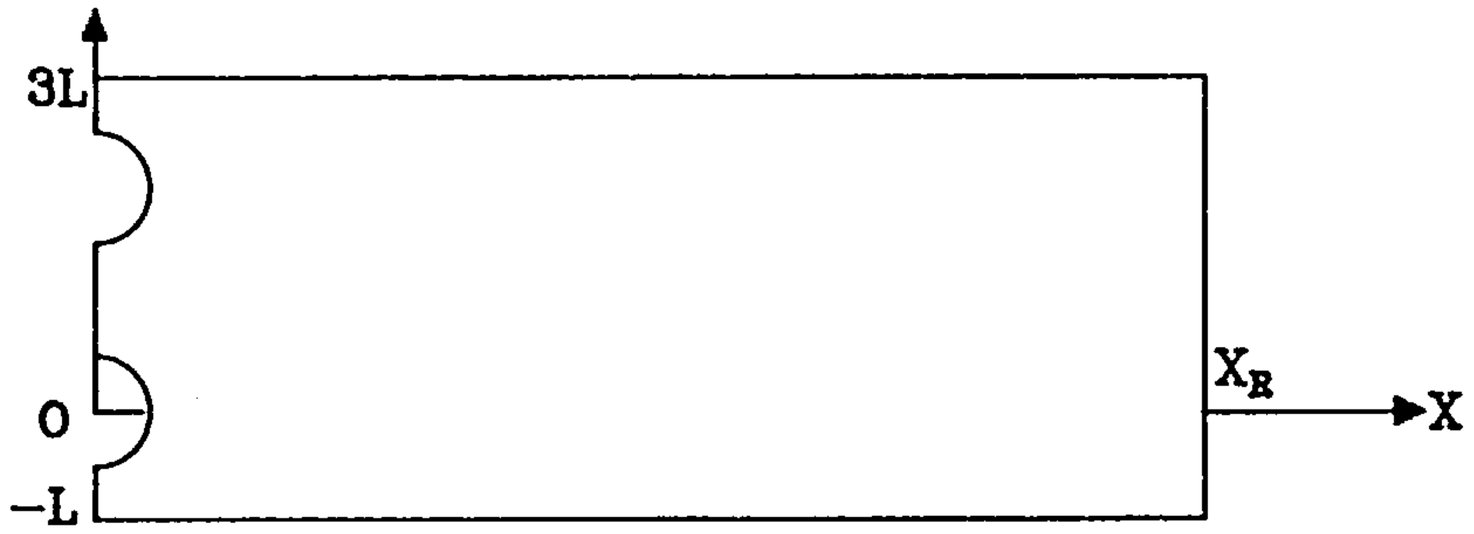

(g)

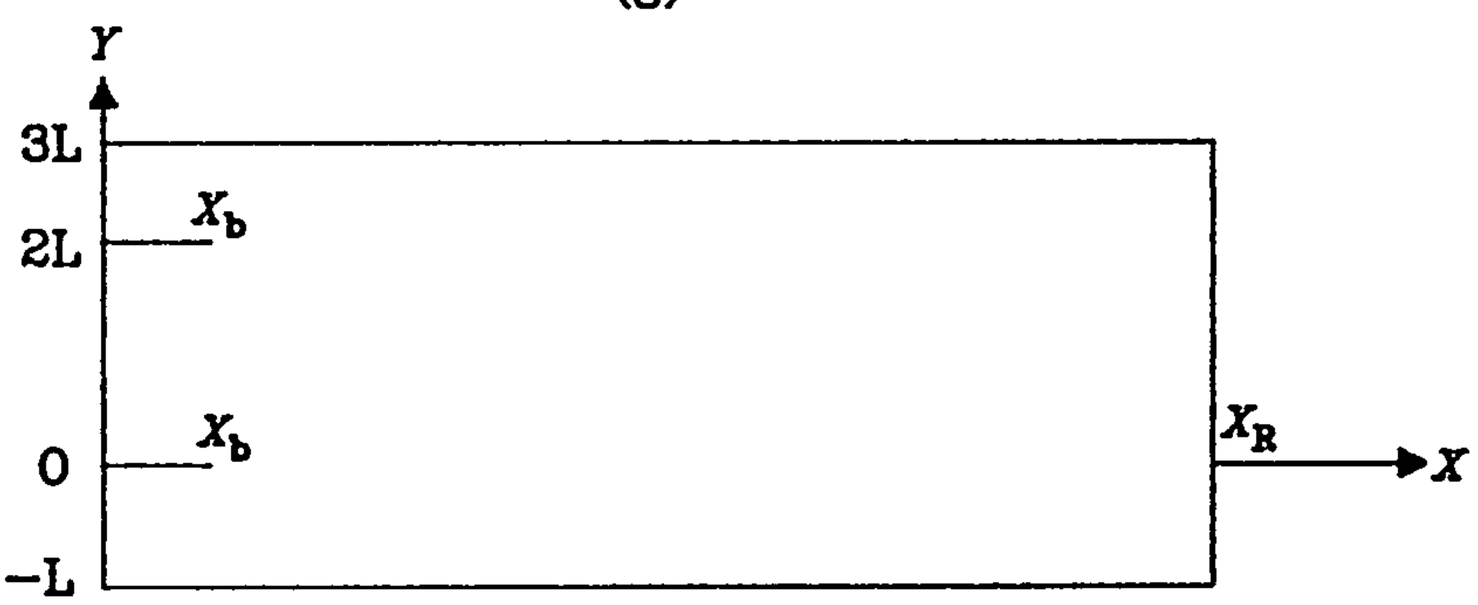

(h)

Fig.5.1 (Cont.) Different solution domains. (e) DM2 domain, (f) transformed DM2 domian, (g) DM3 domain, (h) transformed DM3 domain.

(5.2.1)-(5.2.5) we first transform the solution domain of the problem in the (X, Y) plane onto a simple domain in a new computational plane and then determine u_p.

5.3 Grid Generation and Potential Velocity u_p

Due to the complexity of the physical domain of the problem, we transform it onto a simpler one. In general one can use the following transformation (see Thompson *et al.* (1974))

$$\nabla^2 x = P(x, y) \tag{5.3.1}$$

$$\nabla^2 y = Q(x, y) \tag{5.3.2}$$

to transform the domain Ω_p in the (X, Y) plane onto domain Ω_P in the new (x, y) plane (where the functions P and Q are arbitrary functions which can be used to control the density of the grid lines). The problem is that, in general, transformations (5.3.1) and (5.3.2) are not conformal so some substantial changes will be introduced into the governing equations and the potential surface velocity may be difficult to obtain. However, if we take P=Q=0 then equations (5.3.1) and (5.3.2) reduce to

$$\nabla^2 x = 0 \tag{5.3.3}$$

$$\nabla^2 y = 0 \tag{5.3.4}$$

and, subject to some appropriate boundary conditions, equations (5.3.3) and (5.3.4) may become a conformal transformation and the velocity u_p on the surface of the body may be obtained.

Clearly the physical domain of the problem described by equations (5.2.1)-(5.2.5) is infinite in both the X- and

Y-directions. Because the solution domain is periodic in the Y-direction we would expect to have to solve the problem in the domain as shown in **Fig.5.1a**, as explained earlier. Thus the equations (5.3.3) and (5.3.4) have to be solved subject to the following boundary conditions:

$\frac{\partial x}{\partial n} = 0$, when $X^2 + Y^2 = 0.5^2$;

$0.5 \leq X < +\infty$, $Y = 0$; $0 \leq X < +\infty$, $Y = L$ (5.3.5a)

$\frac{\partial x}{\partial n} = 1$, when $X = +\infty$, $0 \leq Y \leq L$ (5.3.5b)

$x=0$, when $X = 0$, $0.5 \leq Y \leq L$ (5.3.5c)

$y=0$, when $X^2 + Y^2 = 0.5^2$; $0.5 \leq X < +\infty$, $Y = 0$ (5.3.6a)

$y=Y$, when $X = +\infty$, $0 \leq Y \leq L$ (5.3.6b)

$y=L$, when $0 \leq X < +\infty$, $Y = L$ (5.3.6c)

$\frac{\partial y}{\partial n} = 0$, when $X = 0$, $0.5 \leq Y \leq L$ (5.3.6d)

where $L=\mathcal{L}/d$. Equations (5.3.3)-(5.3.6) now define a conformal transformation from the (X,Y)-plane to the (x,y)-plane. The governing equations (5.2.1) and (5.2.2) become

$$\frac{\partial(\omega^{(s)}, \Psi^{(s)})}{\partial(x, y)} = \frac{1}{R_s}\nabla^2\omega^{(s)} \qquad (5.3.7)$$

$$\nabla^2\Psi^{(s)} = -\omega^{(s)}/J(x, y) \qquad (5.3.8)$$

where $J(x,y)$ is the inverse Jacobian of the transformation.

We now solve equations (5.3.3)-(5.3.6) to obtain x, y, $\frac{\partial x}{\partial n}$ and $\frac{\partial y}{\partial n}$ on $\partial\Omega_p$ and u_p on the surface of the body using the Boundary Element Method (BEM). The corresponding inverse problem is solved in

the (x, y) plane to obtain $X(x, y)$ and $Y(x, y)$ and hence $J(x, y)$ $(\equiv 1/(J(X, Y))$. In this way we can obtain the value of $J(X, Y)$ at any given point (x, y).

5.3.1 The Boundary Element Method

The basis of the BEM is Green's integral formula. For any sufficiently smooth function u which satisfies the Laplace equation in $\Omega \in \mathbb{R}^2$ with a piecewise smooth boundary $\partial\Omega$, we may write

$$\eta(p)u(p) = \int_{\partial\Omega} u(q)\frac{\partial G(p,q)}{\partial n_q}dq - \int_{\partial\Omega} \frac{\partial u(p,q)}{\partial n_q}G(p,q)dq \qquad (5.3.9)$$

where $p=(p_1, p_2)\in\bar{\Omega}$, $q=(q_1, q_2)\in\partial\Omega$, $G(p, q)=\ln|p-q|$ is the fundamental solution of the Laplace equation, n_q is the outward normal to $\partial\Omega$ at q and

$$\eta(p) = \begin{cases} 2\pi & \text{when } p\in\Omega \\ \theta & \text{when } p\in\partial\Omega,\ \theta \text{ is the angle between the tangents to } \partial\Omega \text{ on either sides of p.} \end{cases} \qquad (5.3.10)$$

Taking the prime (′) to denote the derivative in the direction of the outward normal and the boundary values of u(p) to be $\phi(p)$, then for any p, $q\in\partial\Omega$ we have

$$\int_{\partial\Omega} \phi(q)\ln'|p-q|dq - \int_{\partial\Omega} \phi'(q)\ln|p-q|dq = \eta(p)\phi(p) \qquad (5.3.11)$$

If we now know either $\phi(p)$ or $\phi'(p)$ on $\partial\Omega$, we can obtain the unknown function by using equation (5.3.11). We may then substitute both these values into equation (5.3.9) in order to obtain the solution of the Laplace equation in Ω.

In order to obtain the numerical solution of the Laplace

equation from the integral equations (5.3.9) and (5.3.11) then the linear BEM is used. This is achieved by first subdividing the boundary $\partial\Omega$ into N segments $\partial\Omega_j$, j=1, 2,...,N. On each segment ϕ and ϕ' are approximated by a linear function, i.e. on each segment $\partial\Omega_j$, we use

$$\phi = (1-\zeta)\phi(p_j) + \zeta\phi(p_{j+1}) \qquad (5.3.12)$$

$$\phi' = (1-\zeta)\phi'(p_j) + \zeta\phi'(p_{j+1}) \qquad (5.3.13)$$

to represent ϕ and ϕ' in the jth segment $[p_j, p_{j+1}]$ on $\partial\Omega_j$, where ζ is a linear function which increases from zero at p_j to unity at p_{j+1}. Substituting (5.3.12) and (5.3.13) into equations (5.3.9) and (5.3.11) gives

$$\sum_{j=1}^{N} \mathbb{E}^*_{ij}\phi_j - \sum_{j=1}^{N} \mathbb{G}^*_{ij}\phi'_j = 0 \qquad i=1, 2,..., N \qquad (5.3.14)$$

where ϕ_j and ϕ'_j denote $\phi(p_j)$ and $\phi'(p_j)$, respectively, and

$$\mathbb{E}^*_{ij}=\int_{\partial\Omega_j}(1-\zeta)\ln'|p_i-q|dq+\int_{\partial\Omega_{j-1}}\zeta\ln'|p_i-q|dq\ -\eta_i\delta_{ij}$$

$$j=2,..., N \qquad (5.3.15)$$

$$\mathbb{G}^*_{ij}=\int_{\partial\Omega_j}(1-\zeta)\ln|p_i-q|dq\ +\int_{\partial\Omega_{j-1}}\zeta\ln|p_i-q|dq \qquad j= 2,..., N \qquad (5.3.16)$$

$$\mathbb{E}^*_{i1}= \int_{\partial\Omega_N}(1-\zeta)\ln'|p_i-q|dq + \int_{\partial\Omega_1}\zeta\ln'|p_i-q|dq\ -\eta_i\delta_{i1} \qquad (5.3.17)$$

$$\mathbb{G}^*_{i1}= \int_{\partial\Omega_N}(1-\zeta)\ln|p_i-q|dq + \int_{\partial\Omega_1}\zeta\ln|p_i-q|dq \qquad (5.3.18)$$

If the segment $\partial\Omega_j$ is a straight line, then the integrals

occurring in equations (5.3.15)-(5.3.18) may be written as

$$\int_{\partial\Omega_j} \ln'|p-q|dq = I_1, \qquad \int_{\partial\Omega_j} \ln|p-q|dq = J_1 \tag{5.3.19}$$

$$\int_{\partial\Omega_j} \zeta \ln'|p-q|dq = \frac{1}{h_{ab}}(h_a \cos\beta\ I_1 + I_2) \tag{5.3.20}$$

$$\int_{\partial\Omega_j} \zeta \ln|p-q|dq = \frac{1}{h_{ab}}(h_a \cos\beta\ J_1 + J_2) \tag{5.3.21}$$

where, see Manzoor (1984),

$$I_1 = \gamma, \qquad J_1 = h_a \cos\beta\ (\ln h_a - \ln h_b) + h_{ab}(\ln h_b - 1) + h_a \gamma \sin\beta$$

$$I_2 = h_a \sin\beta(\ln h_b - \ln h_a) \qquad J_2 = (h_b^2 \ln h_b - h_a^2 \ln h_a)/2 - (h_b^2 - h_a^2)/4$$

and if p_{aj} and p_{bj} denote the endpoints of $\partial\Omega_j$ then h_a, h_b and h_{ab} are the lengths of the straight lines pp_{aj}, pp_{bj} and $p_{aj}p_{bj}$, respectively. Further β and γ are the angles $p_{bj}p_{aj}p$ and $p_{aj}pp_{bj}$, respectively, see Fig.5.2.

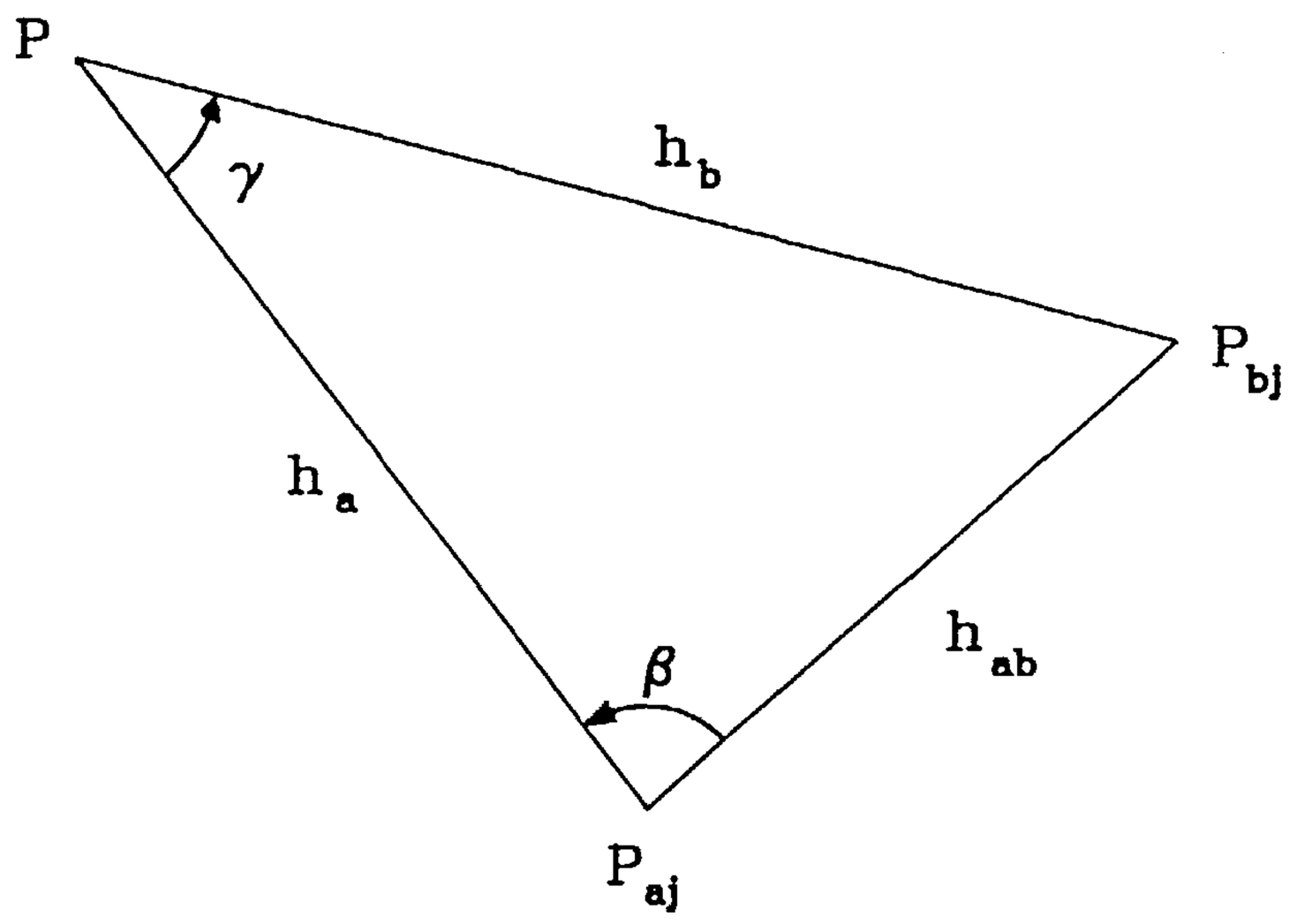

Fig.5.2 The notation for the analytic evalution of integrals on straight-line segment geometry.

5.3.2 The Direct Problem

It is noted that equations (5.3.3) and (5.3.4) are actually two Laplace equations and only one of them has to be solved and the solution of the other equation may then be obtained by using the Cauchy-Riemann equations. Here we solve equation (5.3.4) subject to the boundary conditions (5.3.6) and at the same time obtain the tangential velocity on the cylinder due to the potential flow induced by the motion of the cascade.

For viable computation we must limit the length of the computational region (say $0 \le X \le X_R$) without introducing significant errors into the results obtained numerically in this region. So the finite value $X = X_R$ at which boundary condition (5.3.6b) (also (5.2.5)) must be applied should be very large.

Given the value X_R and the mesh size h, the boundary $\partial\Omega_p$ is divided into N segments: $N=N_1+N_2+N_3+N_4+N_5$, with $N_1=\text{int}((\pi/4)/N_3)$, $N_2=\text{int}((X_R-0.5)/h)$, $N_3=\text{int}(L/h)$, $N_4=\text{int}(X_R/h)$ and $N_5=\text{int}((L-0.5)/h)$ being the number of segments on AB, BC, CD, DE and EA (see Fig.5.1a), respectively, then the counterpart of the algebraic system (5.3.14) which corresponds to the problem (5.3.4) and (5.3.6) may be written as

$$\sum_{j=1}^{N} \mathbb{E}_{ij} Z_j = B(i) \qquad i=1, 2, \ldots, N \tag{5.3.22}$$

where $B(i)=\sum_{j=1}^{N} \mathbb{G}_{ij} \bar{Z}_j$, $\{Z_j\}_1^N=\{y_1, \ldots, y_{N-N_5}, y'_{N-N_5+1}, \ldots, y'_N\}$, $\{\bar{Z}_j\}_1^N=\{y_j\}_1^N \cup \{y'_j\}_1^N$ and all of the elements of $\mathbb{E}$ and $\mathbb{G}$ are known. The system of equations (5.3.22) can now be solved by the standard Gaussian-elimination method.

The values of x_j and x'_j on $\partial\Omega_p$ can now be calculated by using the Cauchy-Riemann equations

$$\frac{\partial x}{\partial Y} = \frac{\partial y}{\partial X} \qquad \frac{\partial x}{\partial X} = -\frac{\partial y}{\partial Y} \tag{5.3.23}$$

5.3.3 Tangential Velocity on the Surface of the Body

If the solution y represents the potential flow due to the cascade then u_p can be obtained from

$$u_p = -\frac{\partial y}{\partial n} \tag{5.3.24}$$

The problem now is to find an appropriate value of X_R such that the BEM gives a solution of (5.3.4) and (5.3.6) to a high degree of accuracy. In all the calculations presented in this chapter it is found that X_R= 15 is sufficiently large since any further increase in this value only results in changes in the value of u_p of less than one percent.

5.3.4 The Inverse Boundary Element Problem

On knowing all the values of x, x', y and y' we can now use them to calculate the corresponding values of X, X′, Y and Y′ on $\partial\Omega_p$ in the (x, y) plane and then calculate X=X(x, y) and Y=Y(x, y) in the domain as shown in **Fig.5.1b** using the Green's integral formula. Hence J(X, Y)= 1/J(x, y) may be obtained and X(x, y) and Y(x, y) satisfy the Laplace equations

$$\nabla^2 X = 0 \tag{5.3.25}$$

$$\nabla^2 Y = 0 \tag{5.3.26}$$

Knowing the values of X, X′, Y and Y′ on $\partial\Omega_p$, the solutions of the

equations (5.3.25) and (5.3.26) may be obtained by using the Green's integral formulae:

$$\eta(P)X(P) = \int_{\partial\Omega_P} X(Q)\ln'|P-Q|dQ - \int_{\partial\Omega_P} X'(Q)\ln|P-Q|dQ \qquad (5.3.27)$$

$$\eta(P)Y(P) = \int_{\partial\Omega_P} Y(Q)\ln'|P-Q|dQ - \int_{\partial\Omega_P} Y'(Q)\ln|P-Q|dQ \qquad (5.3.28)$$

where $P=(P_1, P_2)\in\bar{\Omega}_P$, $Q=(Q_1, Q_2)\in\partial\Omega_P$, $G(P, Q)=\ln|P-Q|$ is the fundamental solution of Laplace equation, n_Q is the outwards normal to $\partial\Omega_P$ at Q and

$$\eta(p) = \begin{cases} 2\pi & \text{when } P\in\Omega_P \\ \Theta & \text{when } P\in\partial\Omega_P, \ \Theta \text{ is the angle between the tangents to } \partial\Omega_P \text{ on either sides of P.} \end{cases} \qquad (5.3.29)$$

On knowing $X=X(x, y)$ and $Y=Y(x, y)$ the Jacobian of the transformations (5.3.3) and (5.3.4) can be obtained by numerical means at any required point $(x, y)\in\bar{\Omega}_P$.

5.4 Numerical Procedure

5.4.1 Boundary Conditions

Apart from the boundary conditions (5.2.3) and (5.2.4) we require to determine the vorticity on the surface of the body, i.e. for $|x|\leq x_b$, $y=0+$ in the (x, y) plane, see **Fig.5.1b**. Using the Taylor expansion method at a boundary point B then for the first internal point from B, say I, it can be shown that:

$$\omega_B^{(s)} = \frac{6\Psi_B^{(s)} - 6\Psi_I^{(s)} - 6h_Y u_s \Big/ \left(\frac{\partial y}{\partial n}\right)_B - h_Y^2 J(X_B, Y_B)\omega_I^{(s)}}{h_Y^2\left[h_Y\left(\frac{\partial J(X, Y)}{\partial y}\right)_B + 2J(X_B, Y_B)\right]} \qquad (5.4.1)$$

It should be noted that expression (5.4.1) can not be used at the points $(X_B, Y_B)=(0.5, 1)$ and $(-0.5, 1)$ due to the singularity of the transformation (5.3.4)-(5.3.6). However, bearing in mind that both the streamfunction and the vorticity are not singular at these points, then the values of the vorticity at these points may be obtained using an (r, θ) co-ordinate system. Thus at $(r_B, \theta_B)=(0.5, 0)$ and $(0.5, \pi)$, which correspond to $(X_B, Y_B)=(0.5, 1)$ and $(-0.5, 1)$ in the (X, Y)-plane, respectively, the vorticity is given by

$$\omega_B^{(s)}=\frac{6\Psi_B^{(s)}-6\Psi_I^{(s)}+2\delta r(3-3\delta r+4\delta r^2)u_s+\dfrac{\delta r^2\omega_{I1}^{(s)}}{k(k+1)}-\dfrac{\delta r^2(1+k)\omega_I^{(s)}}{k}}{\delta r^2\left(3+2\delta r-\dfrac{2+k}{1+k}\right)} \qquad (5.4.1a)$$

where I1 is the second internal point from the boundary point B, $(r_B, \theta_B)=(0.5, 0)$ or $(0.5, \pi))$, $\delta r=r_I-r_B$ and $k=(r_{I1}-r_B)/\delta r$.

Due to the symmetry of the problem, in addition to the boundary conditions (5.2.3)-(5.2.5) and (5.4.1) the following symmetrical boundary conditions are applied:

DM0: Mathematically we can enforce a set of symmetrical boundary conditions about both $X = 0$ and $Y = 0$ and then take the solution domain as shown in **Fig.5.1a** due to the symmetry of the physical domain, i.e.

$$\Psi^{(s)} = \omega^{(s)} = 0 \qquad \left.\begin{array}{l}\text{when } X\geq 0.5,\ Y=0,\\ \text{and when } 0\leq X\leq X_R,\ Y=L\end{array}\right\} \qquad (5.4.2a)$$

$$\Psi^{(s)} = 0 \qquad \text{when } X=0,\ 0.5\leq Y\leq L \qquad (5.4.2b)$$

However, the physical solution of the problem may not be symmetrical for large values of R_s. Indeed, as will be shown in the

experimental results (see section 5.7), the streaming flow is symmetrical when the streaming Reynolds number R_s is small and asymmetrical when R_s is large. This break-down in symmetry of the flow is similar to that observed in the two-dimensional sudden expansion channel flow which becomes asymmetrical at about R_e=40, see Fearn *et al.* (1990). In order to predict the experimentally observed solutions then the boundary condition (5.4.2) must be relaxed. Therefore some further different asymmetrical boundary conditions for the possible solution domains as shown in Fig.5.1 have been considered, namely:

DM1: We relax the symmetrical boundary conditions about Y=0 and solve the problem in the solution domain DM1 (see Fig.5.1c) subject to the following boundary conditions:

$$\Psi^{(s)}\big|_{Y=L} = \Psi^{(s)}\big|_{Y=-L} \qquad \text{when } 0 \le X \le X_R \qquad (5.4.3a)$$

$$\omega^{(s)}\big|_{Y=L} = \omega^{(s)}\big|_{Y=-L} \qquad \text{when } 0 \le X \le X_R \qquad (5.4.3b)$$

$$\left.\frac{\partial \Psi^{(s)}}{\partial X}\right|_{(0,Y)} = -\left.\frac{\partial \Psi^{(s)}}{\partial X}\right|_{(0,-Y)} \qquad \text{when } 0.5 \le Y \le L \qquad (5.4.3c)$$

$$\left.\frac{\partial \omega^{(s)}}{\partial X}\right|_{(0,Y)} = -\left.\frac{\partial \omega^{(s)}}{\partial X}\right|_{(0,-Y)} \qquad \text{when } 0.5 \le Y \le L \qquad (5.4.3d)$$

The vorticity on $0 \le x < x_b$ and $y=0+$ is given by expression (5.4.1) whilst on $0 \le x < x_b$ and $y=0-$, see Fig.5.1d, the vorticity is given by

$$\omega_B^{(s)} = \frac{6\Psi_B^{(s)} - 6\Psi_I^{(s)} + 6h_Y u_s \Big/ \left(\frac{\partial y}{\partial n}\right)_B - h_Y^2 J(X_B,\ Y_B)\omega_I^{(s)}}{h_Y^2\left[h_Y\left(\frac{\partial J(X,\ Y)}{\partial y}\right)_B + 2J(X_B,\ Y_B)\right]} \qquad (5.4.3e)$$

DM2: We now relax the symmetry conditions about X=0 and Y=0 and therefore we have to solve the governing equations (5.2.1) and

(5.2.2) in the solution domain as shown in Fig.5.1e. Hence the boundary conditions (5.4.3a) and (5.4.3b) must be supplemented by the boundary conditions

$$\Psi^{(s)}\big|_{Y=L} = \Psi^{(s)}\big|_{Y=-L} \qquad \text{when } X_L \le X \le X_R \qquad (5.4.4a)$$

$$\omega^{(s)}\big|_{Y=L} = \omega^{(s)}\big|_{Y=-L} \qquad \text{when } X_L \le X \le X_R \qquad (5.4.4b)$$

The boundary condition for the vorticity on the surface of the body, i.e. on $-x_b<x<x_b$ and $y=0+$ in the (x, y) plane, see Fig.5.1f, is given by expression (5.4.1) whilst on $-x_b<x<x_b$ and $y=0-$ the vorticity is given by expression (5.4.3e).

DM3: In this case we assume, again, that the flow is periodic in the y-direction but with the period of symmetry being four times that of the fundamental solution. Hence we solve the governing equation (5.2.1) and (5.2.2) in the region described by Fig.5.1g. Hence the boundary conditions (5.4.2) have to be supplemented by the following boundary conditions

$$\Psi^{(s)}\big|_{Y=3L} = \Psi^{(s)}\big|_{Y=-L} \qquad \text{when } 0 \le X \le X_R \qquad (5.4.5a)$$

$$\omega^{(s)}\big|_{Y=3L} = \omega^{(s)}\big|_{Y=-L} \qquad \text{when } 0 \le X \le X_R \qquad (5.4.5b)$$

$$\left.\frac{\partial \Psi^{(s)}}{\partial X}\right|_{(0,Y)} = -\left.\frac{\partial \Psi^{(s)}}{\partial X}\right|_{(0,2L-Y)} \qquad \begin{matrix}\text{when } -L\le Y\le -0.5 \\ \text{or } 0.5\le Y\le L\end{matrix} \qquad (5.4.5c)$$

$$\left.\frac{\partial \omega^{(s)}}{\partial X}\right|_{(0,Y)} = -\left.\frac{\partial \omega^{(s)}}{\partial X}\right|_{(0,2L-Y)} \qquad \begin{matrix}\text{when } -L\le Y\le -0.5 \\ \text{or } 0.5\le Y\le L\end{matrix} \qquad (5.4.5d)$$

The boundary conditions for the vorticity on the surface of the bodies, i.e. on $0\le x<x_b$ and $y=0+$, $y=2L+$ are given by expression (5.4.1) whilst on $0\le x<x_b$ and $y=0-$, $y=2L-$, see Fig.5.1h, the vorticity is given by (5.4.3e).

DM4: In DM1 we have used antisymmetrical boundary conditions about X=0 and periodic boundary conditions on Y=-L and Y=L. In this section we apply the following boundary conditions to the solution domain DM1, see Fig.5.1c:

$$\Psi^{(s)}\big|_{Y=L} = \Psi^{(s)}\big|_{Y=-L} \qquad \text{when } 0 \le X \le X_R \qquad (5.4.6a)$$

$$\omega^{(s)}\big|_{Y=L} = \omega^{(s)}\big|_{Y=-L} \qquad \text{when } 0 \le X \le X_R \qquad (5.4.6b)$$

$$\Psi^{(s)}\Big|_{(X,Y)} = -\Psi^{(s)}\Big|_{(-X,Y)} \qquad \begin{matrix}\text{when } -L \le Y \le -0.5,\\ 0.5 \le Y \le L\end{matrix} \qquad (5.4.6c)$$

$$\omega^{(s)}\Big|_{(X,Y)} = -\omega^{(s)}\Big|_{(-X,Y)} \qquad \begin{matrix}\text{when } -L \le Y \le -0.5,\\ 0.5 \le Y \le L\end{matrix} \qquad (5.4.6d)$$

and the boundary conditions for the vorticity on the surface of the cylinder are those used in DM1 and are given by expressions (5.4.1) and (5.4.3e).

Other less severe symmetries can be considered but this will increase the size of the computational domain and hence the computational time. Hence such flows have not been investigated.

If the solution at a given value of R_s is symmetrical about X=0 then the solution obtained by solving in domain DM1 will be the same as that obtained when using domain DM4.

5.4.2 Numerical Procedure

The numerical procedure used in this chapter is as follows:

(a) Take X_R=15 and obtain u_s (see section 5.3.3),

(b) Solve equations (5.3.3) and (5.3.4) subject to the boundary conditions (5.3.5)-(5.3.6) on $\partial\Omega_p$ and then solve the inverse problem (5.3.25) and (5.3.26) on $\partial\Omega_p$ by using the BEM (see sections 5.3.1-5.3.4),

(c) Use Green's integral formula to calculate $X=X(x, y)$ and $Y=Y(x, y)$ and then obtain $J(X, Y)$ in the (x, y) plane, and

(d) Solve the equations (5.3.7) and (5.3.8) according to the numerical scheme as follows:

Following Ingham and Yan (1989), in order to reduce the number of grid points in the x-direction and at the same time maintaining the number of grid points near $x=0$ (i.e. near the cylinder) we introduce the following transformation,

$$\alpha = \begin{cases} x & \text{when } |x| \le x_b \\ x_b + \ln[1 + A_d(x - x_b)] & \text{when } x > x_b \\ -x_b - \ln[1 + A_d(x_b - x)] & \text{when } x < -x_b \end{cases} \qquad (5.4.7a)$$

$$\eta = y \qquad (5.4.7b)$$

where x_b is the x component of the image of B (see **Fig.5.1**) in the (x, y) plane and A_d is a constant such that the mesh sizes in the x-direction on both sides of $x=x_b$ are the same for a given mesh size in the α-direction of the (α, η) plane.

The governing equations (5.3.7) and (5.3.8) now become:

When $|\alpha| > x_b$

$$E(\alpha)\frac{\partial(\omega^{(s)}, \Psi^{(s)})}{\partial(\alpha, \eta)} \pm \frac{E^2(\alpha)}{R_s}\frac{\partial\omega^{(s)}}{\partial\alpha} = \frac{1}{R_s}\left[E^2(\alpha)\frac{\partial^2\omega^{(s)}}{\partial\alpha^2} + \frac{\partial^2\omega^{(s)}}{\partial\eta^2}\right] \qquad (5.4.8)$$

$$E^2(\alpha)\left[\frac{\partial^2\Psi^{(s)}}{\partial\alpha^2} \mp \frac{\partial\Psi^{(s)}}{\partial\alpha}\right] + \frac{\partial^2\Psi^{(s)}}{\partial\eta^2} = -\omega^{(s)}/J(x(\alpha), \eta) \qquad (5.4.9)$$

When $|\alpha| \le x_b$

$$\frac{\partial(\omega^{(s)}, \Psi^{(s)})}{\partial(\alpha, \eta)} = \frac{1}{R_s}\left[\frac{\partial^2\omega^{(s)}}{\partial\alpha^2} + \frac{\partial^2\omega^{(s)}}{\partial\eta^2}\right] \qquad (5.4.10)$$

$$\frac{\partial^2\psi^{(s)}}{\partial\alpha^2} + \frac{\partial^2\psi^{(s)}}{\partial\gamma^2} = -\omega^{(s)}/J(x(\alpha),\ \gamma) \qquad (5.4.11)$$

where $x(\alpha)$ is the inverse function of (5.4.7a) and

$$E(\alpha) = \exp(-(\alpha - x_b)) \qquad (5.4.12)$$

or $$E(\alpha) = \exp(\alpha + x_b) \qquad (5.4.13)$$

depending on whether $\alpha > x_b$ or $\alpha < -x_b$, respectively, and the upper sign in the equations (5.4.8) and (5.4.9) occurs when $\alpha > x_b$ whilst the lower sign occurs when $\alpha < -x_b$.

A modified central-difference scheme (see Dennis and Hudson (1978)) which is similar to that used in chapter 2 is used to discretise equations (5.4.8) and (5.4.10). Taking h_α and h_γ to be the mesh sizes in the α- and γ-directions, respectively, and using the subscripts 0, 1, 2, 3 and 4 to denote typical grid points $(ih_\alpha,\ jh_\gamma)$, $((i+1)h_\alpha,\ jh_\gamma)$, $(ih_\alpha,\ (j+1)h_\gamma)$, $((i-1)h_\alpha,\ jh_\gamma)$, $(ih_\alpha,\ (j-1)h_\gamma)$, respectively, then the finite-difference representation of the equations (5.4.8)-(5.4.11) can be written as

$$c_1\omega_1^{(s)} + c_2\omega_2^{(s)} + c_3\omega_3^{(s)} + c_4\omega_4^{(s)} - c_0\omega_0^{(s)} = 0 \qquad (5.4.14)$$

$$b_1\psi_1^{(s)} + b_2\psi_2^{(s)} + b_3\psi_3^{(s)} + b_4\psi_4^{(s)} - b_0\psi_0^{(s)} + h_\alpha^2 h_\gamma^2\omega_0^{(s)}/J(x(\alpha_0),\gamma_0) = 0 \qquad (5.4.15)$$

where

$$c_1 = \begin{cases} E_0 h_\gamma^2\left\{1 \mp \frac{h_\alpha}{2}\left[E_0 \pm R_s U_0\right] + \frac{h_\alpha^2}{8}\left[E_0 \pm R_s U_0\right]^2\right\} & |\alpha| > x_b \\ h_\gamma^2\left\{1 - \frac{h_\alpha}{2}R_s U_0 + \frac{h_\alpha^2}{8}R_s^2 U_0^2\right\} & |\alpha| \le x_b \end{cases}$$

$$c_2=\begin{cases} h_x^2\left\{1 - \frac{h_y}{2}R_s E_0 V_0 + \frac{h_y^2}{8}R_s^2 E_0^2 V_0^2\right\} & |x|>x_b \\ h_x^2\left\{1 - \frac{h_y}{2}R_s V_0 + \frac{h_y^2}{8}R_s^2 V_0^2\right\} & |x|\le x_b \end{cases}$$

$$c_3=\begin{cases} E_0 h_y^2\left\{1 \pm \frac{h_x}{2}\left[E_0 \pm R_s U_0\right] + \frac{h_x^2}{8}\left[E_0 \pm R_s U_0\right]^2\right\} & |x|>x_b \\ h_y^2\left\{1 + \frac{h_x}{2}R_s U_0 + \frac{h_x^2}{8}R_s^2 U_0^2\right\} & |x|\le x_b \end{cases}$$

$$c_4=\begin{cases} h_x^2\left\{1 + \frac{h_y}{2}R_s E_0 V_0 + \frac{h_y^2}{8}R_s^2 E_0^2 V_0\right\} & |x|>x_b \\ h_x^2\left\{1 + \frac{h_y}{2}R_s V_0 + \frac{h_y^2}{8}R_s^2 V_0\right\} & |x|\le x_b \end{cases}$$

$$c_0 = c_1 + c_2 + c_3 + c_4$$

and

$$b_1=\begin{cases} h_y^2 E_0^2 (1\mp h_x/2) \\ h_y^2 \end{cases}$$

$$b_3=\begin{cases} h_y^2 E_0^2 (1\pm h_x/2) \\ h_y^2 \end{cases}$$

$$b_2 = b_4 = h_x^2$$

$$b_0 = b_1 + b_2 + b_3 + b_4$$

$$U_0 = \left(\frac{\partial \Psi^{(s)}}{\partial y}\right)_0 \qquad V_0 = -\left(\frac{\partial \Psi^{(s)}}{\partial x}\right)$$

The matrices associated with the set of finite-difference equations (5.4.14) and (5.4.15) are diagonally dominant under all circumstances and therefore an over relaxation iterative scheme may be employed in order to reduce the number of iterations required for

convergence.

5.5 Numerical Results

Calculations have been obtained for several values of the blockage ratio, $d/2\ell$, from 0.25 to 0.75, which are O(1) and they all show very similar trends. In order to be able to compare with the experimental data and the available steady state calculations of Ingham *et al.* (1990a) and the streaming flow calculations of Ingham and Yan (1991) we have concentrated in this chapter on producing detailed results only for L=1. It has been found that $X_R=10$ is sufficiently large for $R_s \leq 15$ whilst $X_R=15$ has to be used for $R_s>15$ and $X_L=-X_R$ has been taken when a solution is required in X<0. Mesh sizes $h_y=1/20$ and $h_x=x_b/25$ or $h_y=1/40$ and $h_x=x_b/50$ have been used depending on the value of the streaming Reynolds number. In order to reduce the complexity of the computer program it is convenient to take the mesh size on both sides of the lines $x=\pm x_b$ to have the same magnitude and hence the constant A_d in expression (5.4.7) is determined according to

$$h_x = \ln(1+A_d h_x) \qquad (5.5.1)$$

For $R_s \leq 15$ it is found that the results obtained with $h_x=x_b/25$ and $h_y=1/20$ are not significantly different from those obtained with $h_x=x_b/50$ and $h_y=1/40$. So the results shown here for $R_s \leq 15$ have been obtained with the larger mesh whilst the results for $R_s>15$ have been obtained using the finer mesh. It has been found that further decreasing the mesh size for $R_s>15$ results in graphically indistinguishable solutions from those obtained with $h_x=x_b/50$ and $h_y=1/40$.

5.5.1 Boundary Conditions——DM0

Numerical results have been obtained for values of R_s up to 100. Fig.5.3 shows the outer steady streamlines for R_s=0.636, 10, 35 and 70, respectively, using the solution domain and boundary condition described as DM0. The value of R_s=0.636 was chosen as experimental results have been obtained for this value of the Reynolds number, see section 5.7 (experimental data has also been obtained for values of R_s=2.54 and 8.9). It is found from Fig.5.3 that there are 4 recirculating regions between each successive cylinders with the directions of the flow being along the direction of the oscillations away from each cylinder (i.e. along Y=2kL, where k is an integer) at a distance O(1) from the body and towards X=0 along Y=(2k+1)L. The magnitudes of all the recirculations are very weak at large distances from the cascade and the general flow structure is very similar for all values of R_s. However, as the value of R_s increases then the centres of these 4 recirculating regions occur at increasing distances from the plane of the axes of the cylinders and the strengths of the recirculations increase, see Figs.5.3b, 5.3c and 5.3d. This is because more energy is being put into the system as the value of R_s increases.

Fig.5.4 shows the variation of the minimum distance between the centre of each of the recirculating regions and the axis of the nearest cylinder, d_c, and the streaming Reynolds number, R_s. It is observed that for $R_{s\sim}>25$ then d_c is almost directly proportional to R_s and we find that $d_c \approx 0.037R_s + 0.5$.

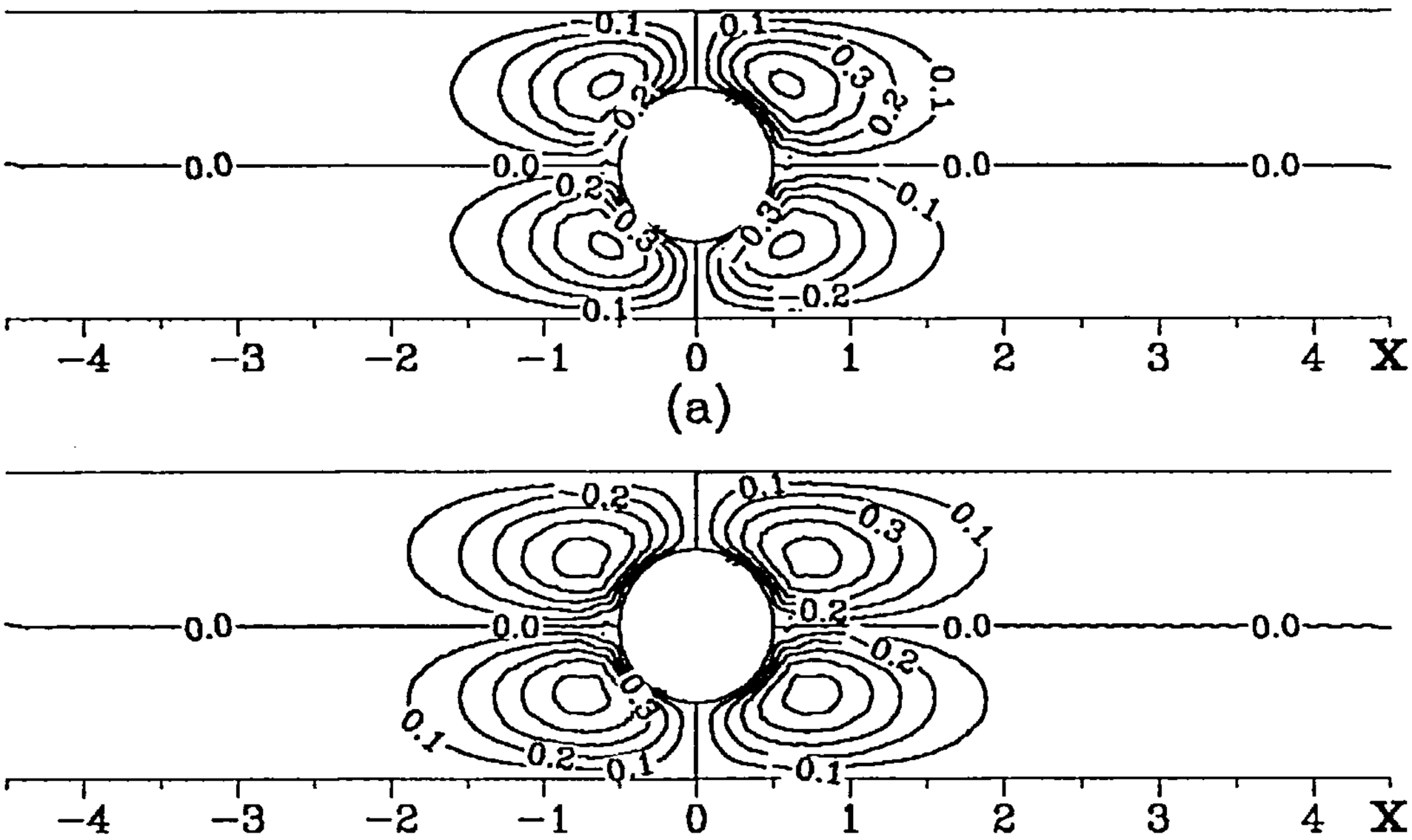

Fig.5.3 The streamlines for the outer streaming flow obtained by using DMO. (a) R_s=0.636, (b) R_s=10, (c) R_s=35, (d) R_s=70.

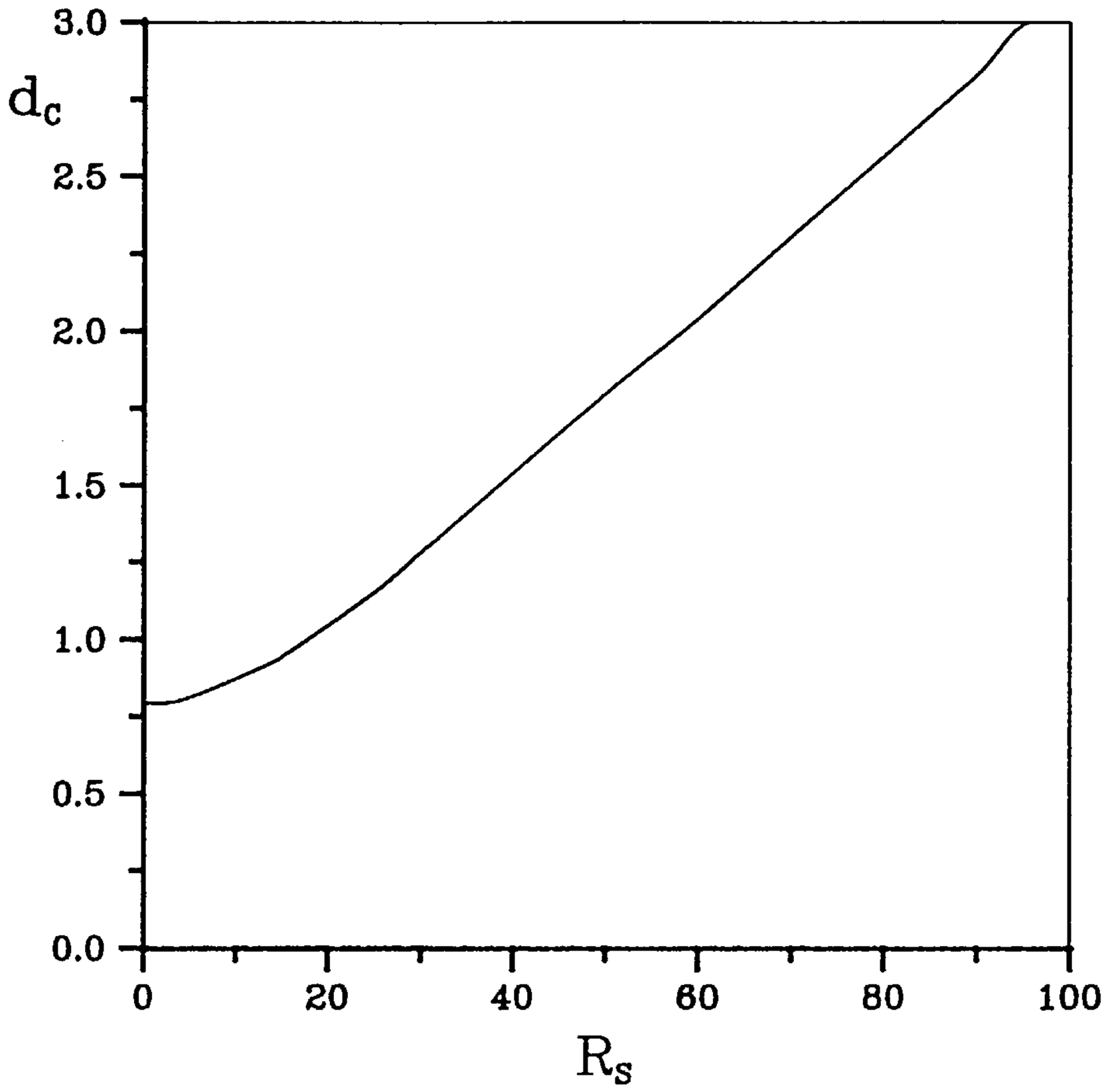

Fig.5.4 Distance between the centres of the recirculations and the axis of the cylinder.

5.5.2 Boundary Conditions——DM1

Numerical results for the outer streaming flow have been obtained for R_s=0.636, 2.54, 5, 6, 7, 8, 9, 10, 10.9, 15, 20, ..., 60. Fig.5.5 shows the streamlines of the outer streaming flow with R_s=0.636, 2.54 and 10.9 and it is clear that at the smaller values of R_s the streaming flow is almost symmetrical about both the axes X=0 and Y=0, and the values of streamfunction on Y=L and Y=-L for any value of X are very small. Further, the results at the smaller values of R_s are almost identical to those obtained by using the

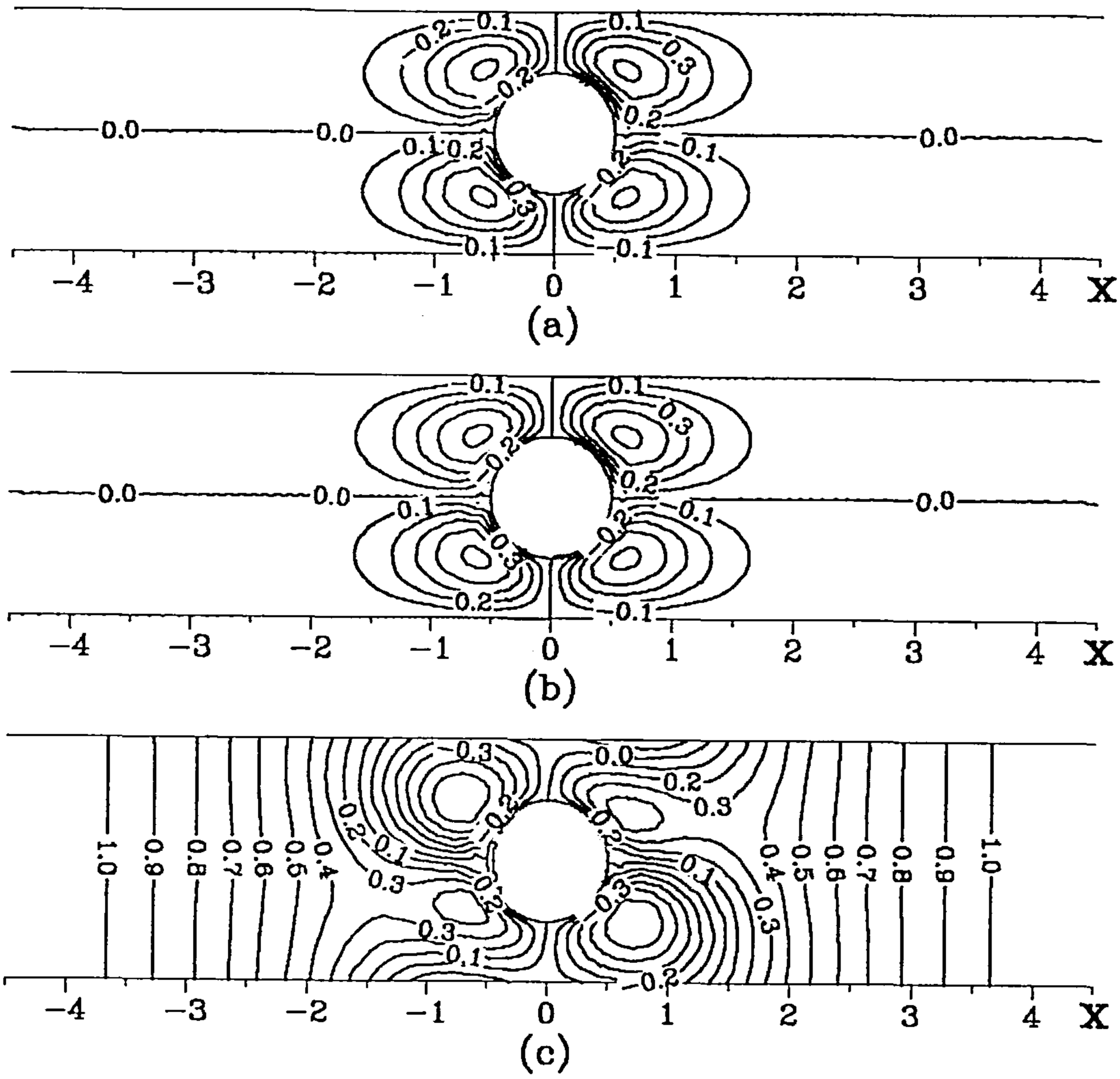

Fig.5.5 The streamlines for the outer streaming flow obtained by using DM1. (a) R_s=0.636, (b) R_s=2.54, (c) R_s=10.9.

boundary conditions described in DM0.

As the value of R_s increases the symmetry of the numerical results begin to break down and the flow becomes asymmetrical. Instead of four recirculations of equal strength occurring between any two successive cylinders of the cascade, as there are at smaller values of R_s, two of the recirculations become stronger than the

other two (see **Fig.5.5**). As a result fluid flows in the Y-direction are generated at distances of just over 1 diameter from the cylinders, and the strength of this flow becomes stronger, at a given distance from the body, as the value of R_s increases but decreases in strength as $|X|$ increases.

The results indicate that there exists a critical value of R_s, R_{s0} say, such that $8 \lesssim R_{s0} \lesssim 9$ for which the flow is symmetrical about both the axes X=0 and y=0 for $R_s < R_{s0}$ and antisymmetrical for $R_s > R_{s0}$ (see **Fig.5.5**). The induced velocity on Y=L in the Y-direction for R_s=10, 15, 20 and 25 as a function of X is shown in **Fig.5.6**. It has

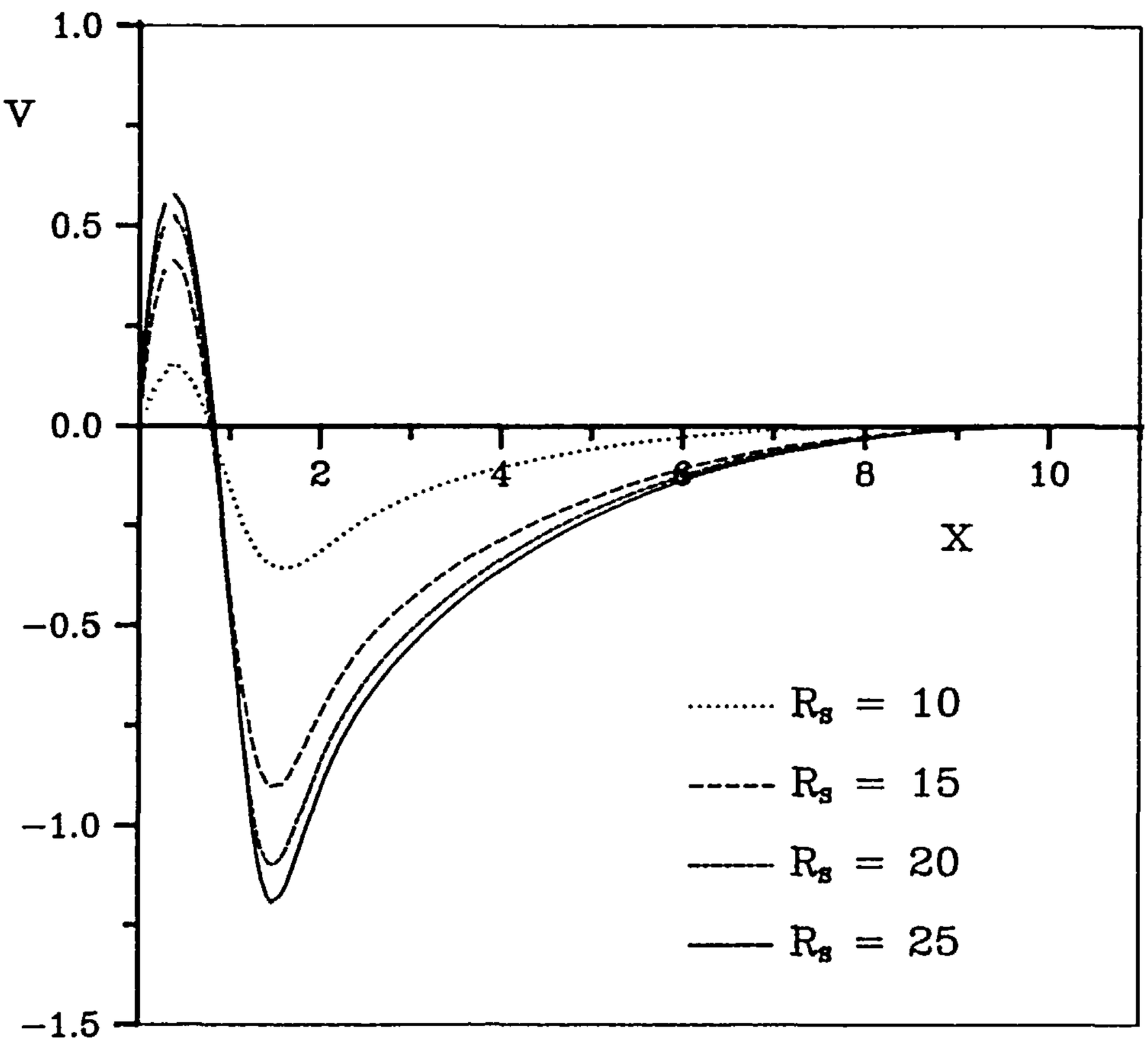

Fig.5.6 The vertical velocity at Y=1 as a function of X for R_s=15.

been found that there exists a non-zero Y component of negative vertical velocity for all values of R_s and this contrasts with the results obtained for $R_s<R_{s0}$ where the vertical velocity at Y=L is always zero.

In order to measure the asymmetry of the flow we define the quantities σ_u and σ_v such that

$$\sigma_u^2 = \int_{-L}^{L} |u|_{X=0} dY \qquad (5.5.2)$$

and

$$\sigma_v^2 = \int_{X_L}^{X_R} |v|_{Y=L} dX \qquad (5.5.3)$$

Physically, σ_u^2 represents the mass exchange across X=0 in any interval [2kL-L, 2kL+L] (k=1, 2,....) and σ_v^2 the mass exchange across any line Y=(2k+1)L in the interval [X_L, X_R]. As X_L and X_R tends to $-\infty$ and $+\infty$, respectively, σ_v^2 becomes the total mass exchange across Y=(2k+1)L.

The variations of σ_u and σ_v as a function of R_s as obtained using the **DM1** conditions are shown in **Fig.5.7** and **Fig.5.8**, respectively. It is clear that both σ_u and σ_v are identically zero when $R_{s\sim}<8$ whilst they become non-zero when $R_{s\sim}>9$, i.e. a bifurcation via the break-down of symmetry occurs when the streaming Reynolds number lies somewhere between 8 and 9.

5.5.3 Boundary Conditions——DM2

Again, numerical results for the outer streaming flow have been obtained for R_s=0.636, 2.54, 5, 6, 7, 8, 9, 10, 10.9, 15, 20, ..., 60. **Fig.5.9** shows the streamlines for the outer streaming flow with

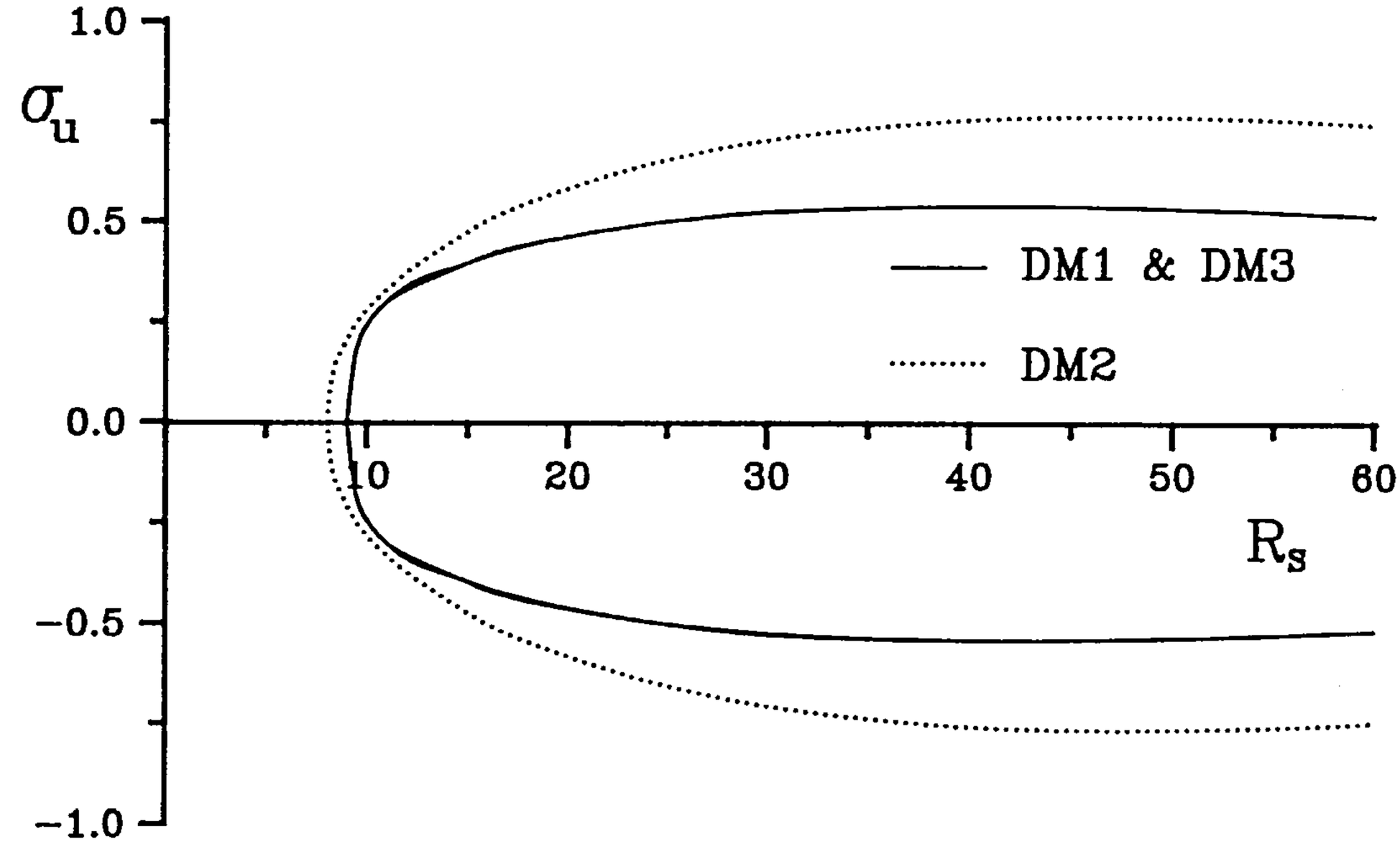

Fig.5.7 Bifurcation diagram of the streaming cascade flow (σ_u).

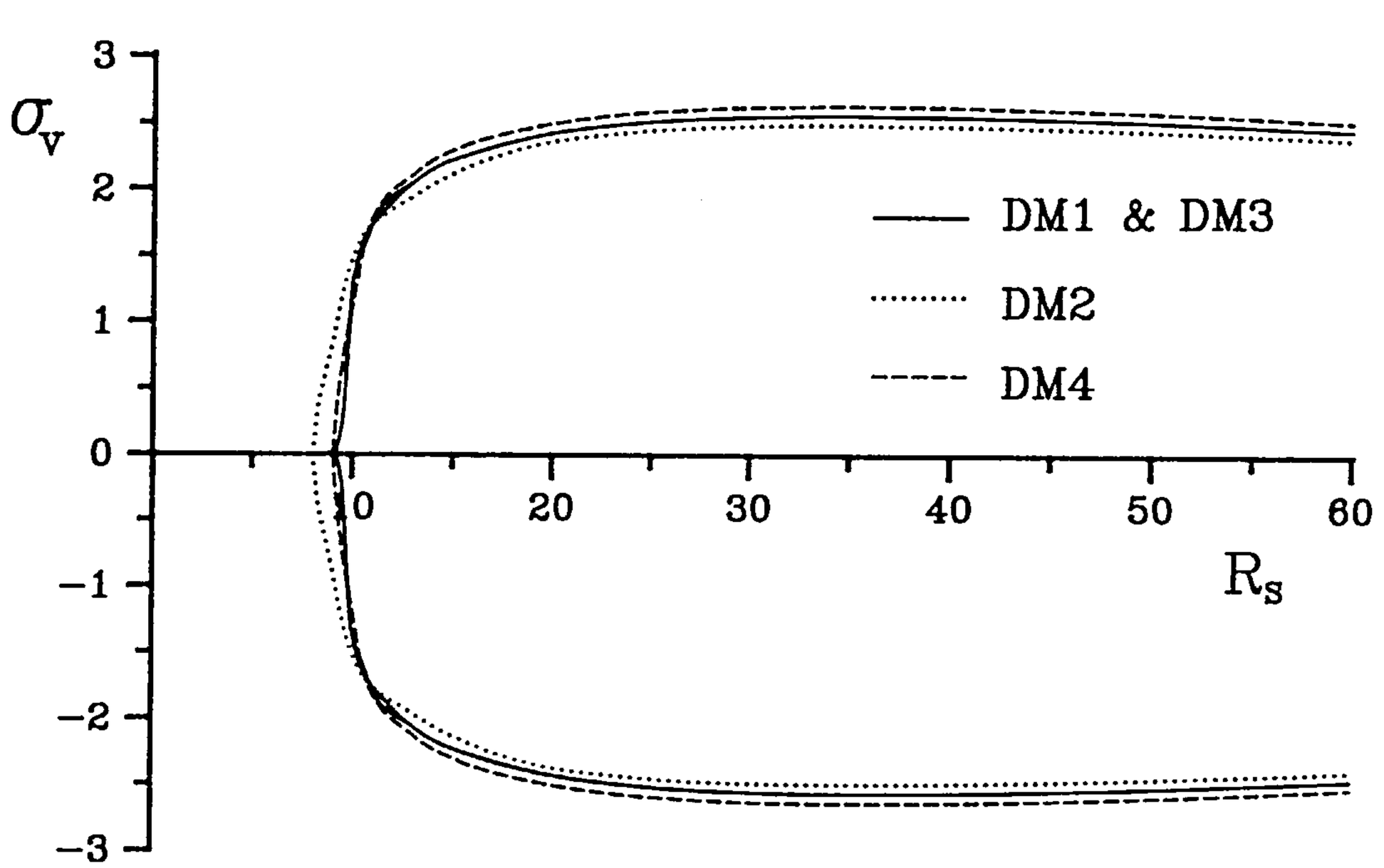

Fig.5.8 Bifurcation diagram of the streaming cascade flow (σ_v).

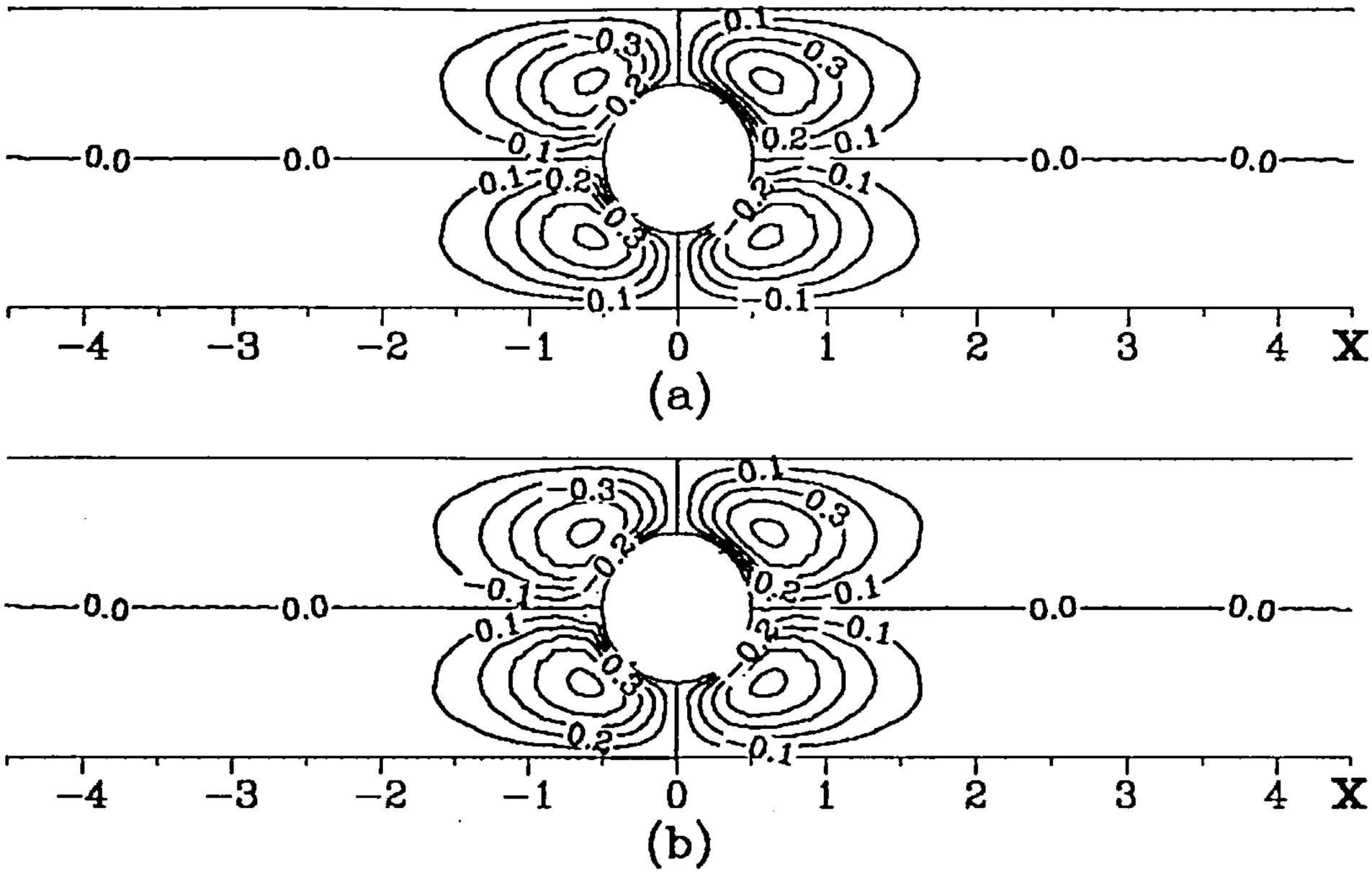

Fig.5.9 The streamlines for the outer streaming flow obtained by using DM2. (a) R_s=0.636, (b) R_s=2.54, (c) R_s=10.9.

R_s= 0.636, 2.54 and 10.9. It is again clear that the flow is almost symmetrical about both the axes X=0 and Y=0 at the smaller values of R_s but the flow becomes more asymmetrical as the value of R_s increases. The critical value for the streaming Reynolds number R_s was found to lie somewhere between 8 and 9 as was the case for the boundary conditions DM1.

Further the bifurcation diagrams according to the values of σ_u and σ_v for the different values of R_s that we have investigated are

shown in Fig.5.7 and Fig.5.8, respectively. It is observed that both the values of σ_u and σ_v are almost zero when $R_s \lesssim 8$ whilst both of them are non-zero when $R_s \gtrsim 9$, i.e. the bifurcation via the break-down of symmetry about both the X- and Y-axes occurs at about the same value of R_s as they did for the boundary conditions DM1.

5.5.4 Boundary Conditions——DM3

Numerical results have been obtained for R_s=0.636, 2.54,...,10.9,..., 60 and it is found that all of the results obtained are similar to those obtained when using DM1 and DM2. The critical value for R_s was, again, found to be between 8 and 9, and no further period doubling solutions have been found for the values of R_s that we have investigated.

The values of quantities σ_u and σ_v as functions of R_s are plotted in Fig.5.7 and Fig.5.8 and it is observed the results show very similar tendency to those obtained using DM1 and DM2. In particular, both σ_u and σ_v are almost identical to those obtained using the boundary conditions DM1. This is not surprising since the solutions here are periodic in the Y-direction with a period of 2L and in this case the boundary conditions (5.4.3) are included in the boundary conditions (5.4.5) and therefore the solutions obtained here should be identical to those obtained when using the boundary conditions DM1.

5.5.5 Boundary Conditions——DM4

Numerical results have been obtained for R_s=0.636, 2.54, 5, 6, 7, 8, 9, 10, 10.9, 15,..., 55 and 60. It is found from these results that the streaming flow is symmetrical about both the axes X=0 and

Y=0 when $R_s \lesssim 8$ and this is consistent with the numerical results obtained when using the solution domains DM0, DM1, DM2 and DM3 subject to the corresponding boundary conditions. When $R_s \gtrsim 9$ the streaming flow is no longer symmetrical about the axis Y=0 and two of the four recirculations around each cylinder become stronger than the other two. In order to show the flow structure in this case the streamlines are plotted for R_s=8, 15 and 25 in Fig.5.10 where a

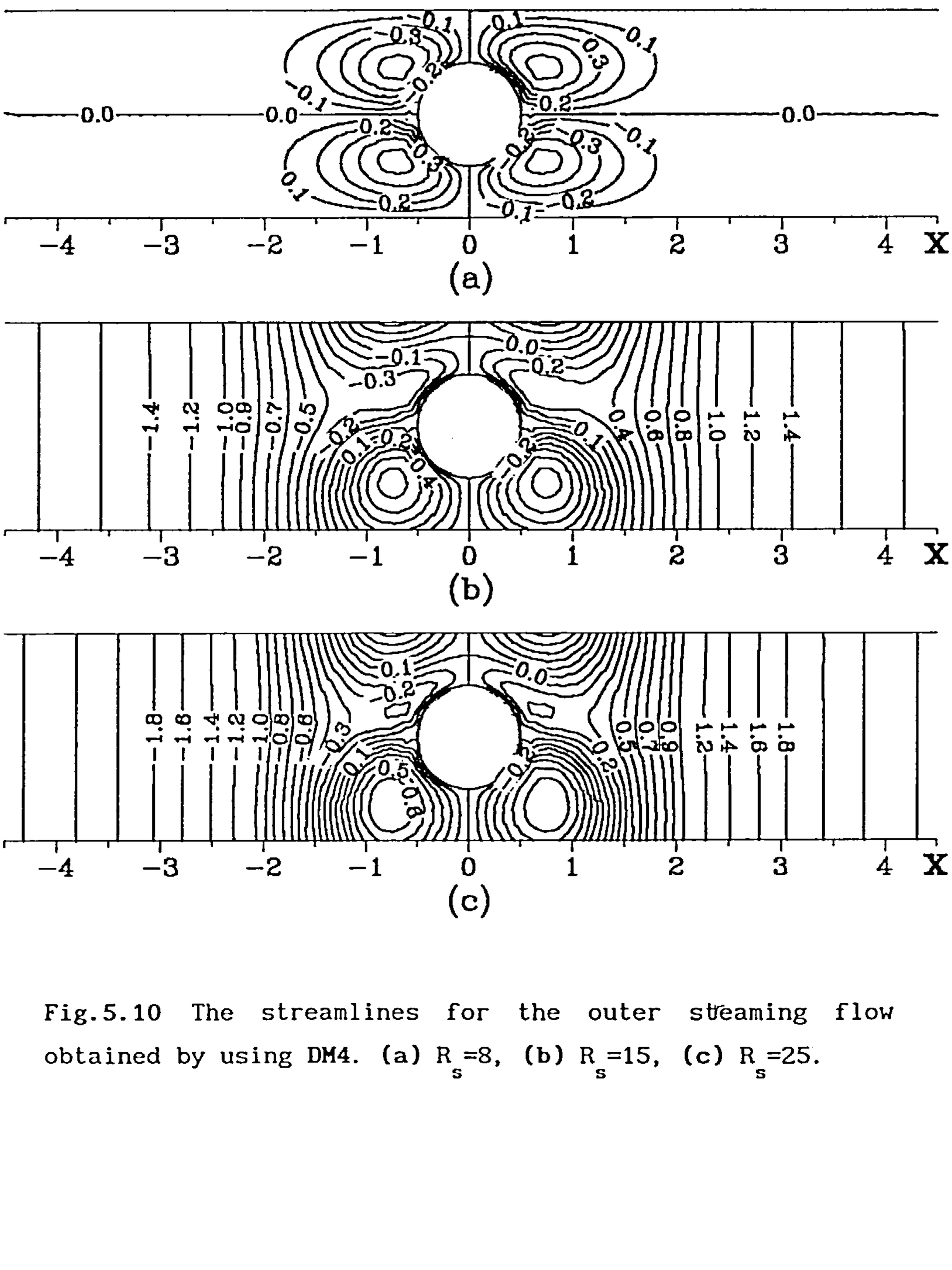

Fig.5.10 The streamlines for the outer streaming flow obtained by using DM4. (a) R_s=8, (b) R_s=15, (c) R_s=25.

clear tendency of how the flow structure changes with R_s can be observed.

The bifurcation diagrams according to the functions σ_u and σ_v as a function of R_s are plotted in **Figs.5.7** and **5.8**. The values of σ_u are always zero as symmetrical boundary conditions have been used on X=0 and clearly the tendency of σ_v is similar to those obtained when using the boundary conditions **DM1, DM2** and **DM3**.

It is obvious from **Figs.5.7** and **5.8** that unless symmetry is enforced by the use of the boundary conditions **DM0** then the streaming flow becomes asymmetrical either about X=0 or Y=0 when $R_s \gtrsim 9$. This suggests that a bifurcation has occurred via the break-down of symmetry.

5.6 Stability of the Streaming Flow

In order to understand the mechanism of the break-down in the symmetry of the flow we now study the stability of the streaming cascade flow. Stability and bifurcation of parallel flows have been of interest to researchers for a long time and much work has been reported, see for example Betchov and Criminale (1967), Sobey and Drazin (1986) and John (1984). If the main flow can be assumed to be parallel and the disturbance to the main flow is to be infinitesimally small then the linear stability analysis of the problem may be reduced to finding the solution of the well known Orr-Sommerfeld equation. Thomas (1953), Osborne (1967) and Gary and Helgason (1969) have solved the Orr-Sommerfeld equation for Poiseuille flow using several different numerical techniques. Sobey and Drazin (1986) used a stability analysis to study the two-dimensional sudden expansion symmetrical channel flow and showed

that symmetrical flow about the central line of the channel breaks down at a critical value of the Reynolds number, i.e. a bifurcation occurs. In order to test if this kind of break-down is due to the asymmetry of the sudden-expansion channel flows Fearn *et al.* (1990) performed an experimental investigation for a slightly asymmetrical geometry and found that the break-down is in fact due to the flow rather than the imperfection in the symmetry of the channel.

In this chapter we follow the analysis of John (1984) and assume that we have an undisturbed two-dimensional parallel flow and then introduce a linearised disturbance to the parallel flow. Then the streamfunction may be written in the form

$$\Psi^{(s)}(X,Y,t)=\Psi_0^{(s)}(X,Y)+\Psi_1^{(s)}(X,Y,t)=\Psi_0^{(s)}(X,Y)+\phi(Y)e^{i(\alpha X-\beta t)} \qquad (5.6.1)$$

where $\Psi_0^{(s)}$ is the main flow and $\Psi_1^{(s)}$ is the disturbance component to $\Psi^{(s)}$. Here $\phi(Y)$ determines the shape of $\Psi_1^{(s)}$ in the cross-stream direction whilst $\alpha\equiv\alpha_r+i\alpha_i$ and $\beta\equiv\beta_r+i\beta_i$ determine the growth or decay of the disturbance in space and time, respectively.

The simplified equation for the disturbance, i.e. the equation for the perturbation function ϕ, i.e. the eigenfunction, then satisfies the Orr-Sommerfeld equation (see for example Betchov and Criminale (1967))

$$(u-c)(\phi''-\alpha^2\phi)-u''\phi = -\frac{i}{\alpha R}(\phi^{IV}-2\alpha^2\phi''+\alpha^4\phi) \qquad (5.6.2)$$

where the derivatives are with respect to Y and $c\equiv\beta/\alpha$. This equation may now be solved numerically for both the eigenvalue c (or α) and the eigenfunction ϕ if α (or β) is specified and the appropriate boundary conditions for ϕ specified. For temporal instability one needs to solve for c for a specified real value of α and for spatial

stability one needs to solve for α provided a real value of c (or β) is given.

Using a central-difference scheme, equation (5.6.2) along with the appropriate boundary conditions may be approximated by the solution of the following set of linear equations in the form

$$A(\alpha,\ c)\underline{\phi} = 0 \qquad (5.6.3)$$

where $A(\alpha,\ c)$ is a matrix which is a function of both α and c. In order to obtain the non-trivial solution for ϕ then we must have

$$\det(A(\alpha,\ c))=0 \qquad (5.6.4)$$

For temporal stability the eigenvalue c (or α) can be obtained for a given (real) wave number α (or β). Full details of the numerical methods for solving equation (5.6.4) are similar to those described by John (1984) and therefore are not presented in this chapter.

5.6.1 A Model Problem

As already shown in section 5.5, the velocity of the streaming flow induced by an oscillating cascade of circular cylinders is dominated, for L=1, by the u-velocity component in the majority of the flow. This is particularly true when X>0.5. Thus as a first approximation the streaming flow may simply be approximated by a parallel flow in the X-direction at any station, say $X=X_0$, and therefore in this model we specify a u-velocity profile for the main flow as

$$u = \cos(\pi Y/L) \qquad (5.6.5)$$

and set v≡0. This has the simple property that the flow is periodic

in the Y-direction and the fluid speed has a maximum and a minimum as one would expect physically, when Y=2kL and Y=(2k-1)L, respectively, where k is an integer. Here (u, v) are the velocity components in the (X, Y) directions. It may be expected that the most unstable region will be close to the body since the flow is driven by the tangential component of the velocity. In section 5.5 we have shown that the numerical results obtained using DM1, DM2, DM3 and DM4 are all periodic in the Y-direction with a period of 2L. In order that the stability analysis here may predict the asymmetrical phenomena we now solve equation (5.6.2) in this model problem subject to the following periodic boundary conditions in ϕ (with period 2L in the Y-direction),

$$\phi|_{Y=L}=\phi|_{Y=-L} \tag{5.6.6}$$

$$\phi'|_{Y=L}=\phi'|_{Y=-L} \tag{5.6.7}$$

for the perturbation function ϕ. For a given value of α we are interested in the eigenvalue which has the largest imaginary part since this, physically, corresponds to the most unstable solution of the flow. Eigenvalues of the most unstable solutions have been obtained for $0 < \alpha \leq 15$ and for streaming Reynolds numbers up to 100. The imaginary part of c, i.e. c_i (the flow is stable when $c_i<0$ and unstable when $c_i>0$), as a function of the streaming Reynolds number R_s and α is plotted in **Fig.5.11**.

It is observed from **Fig.5.11** that for values of $\alpha\in(0.4, 3.5)$, approximately, there exists a critical value of R_s, say R_{sm}, such that for $R_s<R_{sm}$ the flow is stable whilst for $R_s>R_{sm}$ the flow is unstable. As α increases from 0.4 the value of R_{sm} decreases from

about 7 and reaches its minimum value of $R_{sm} \approx 6$ when $\alpha \approx 1.1$ and then increases again to about 25 when $\alpha \approx 3$. This suggests that, for $0 < \alpha \leq 15$, the wave number $\alpha \approx 1.1$ is the most unstable solution for $0 \leq R_s \leq 100$.

It is also observed from **Fig.5.11** that for $\alpha \lesssim 0.4$ and $\alpha \gtrsim 3.5$ that the value of c_i is negative for all values of $R_s \leq 100$, i.e. for these initial disturbances which correspond to a wave number $\alpha \lesssim 0.4$ or $3.5 \lesssim \alpha \lesssim 15$ the flow is always stable for $0 \leq R_s \leq 100$. As α increases from 0.4 to about 1.1 then c_i increases for all values of R_s, i.e. the flow becomes more unstable as R_s increases. As α increases further from 1.1 to 3.5, then c_i decreases for all values of R_s considered

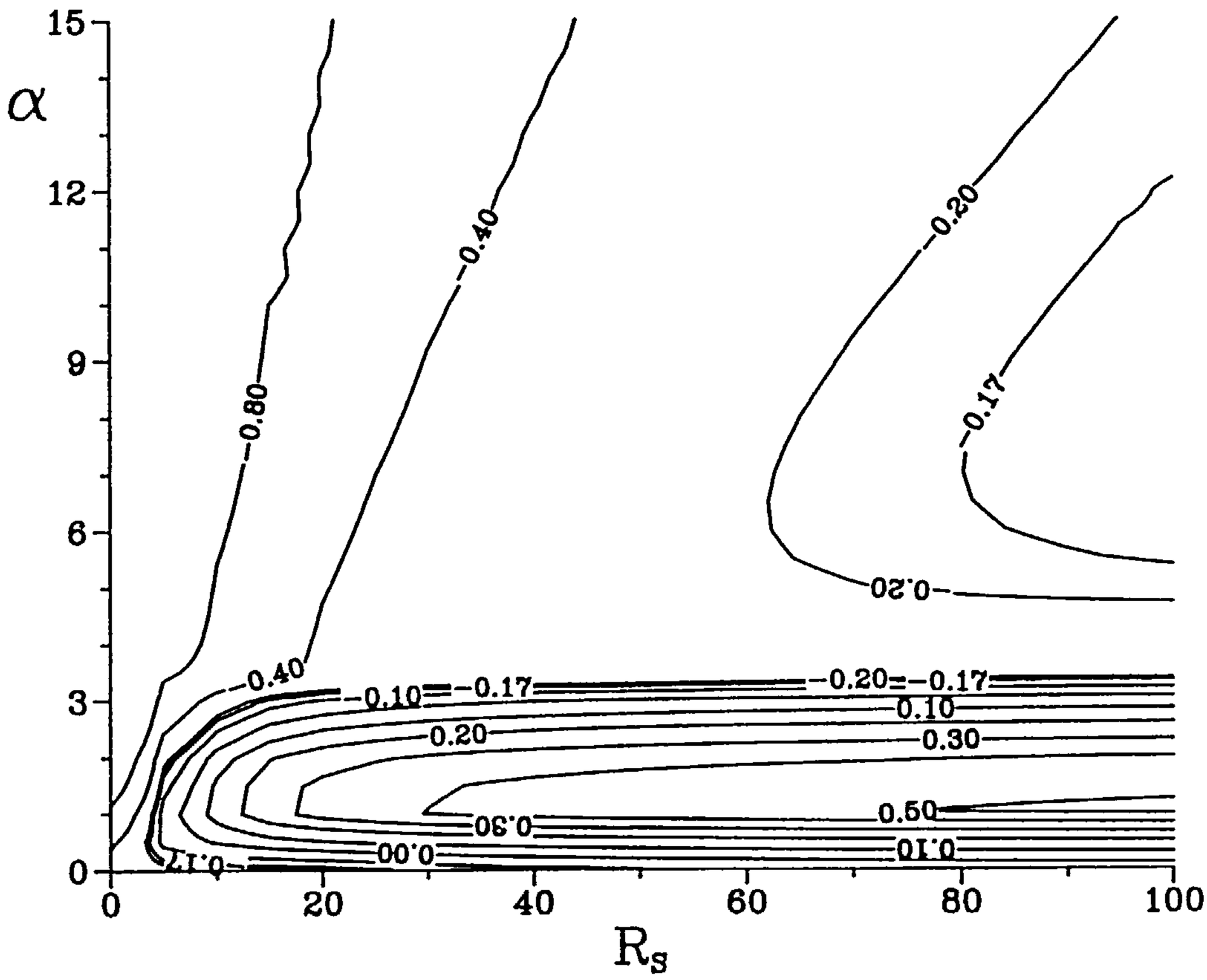

Fig.5.11 Stability diagram of the model problem.

here, and this suggests that the unstable flow becomes more stable as α increases in the range from 1.1 to 3.5 for any given value of $R_s \in (0,\ 100)$.

It is also clear from **Fig.5.11** that there exists another local unstable region in the stable region $[60<R_s\leq 100,\ 4.0<\alpha\leq 15]$. For any given value of $R_s \gtrsim 60$ then $\alpha \approx 7$ gives the most unstable solution region.

5.6.2 Stability for the Streaming Cascade Flow

Having developed the mathematical technique to investigate the stability of the flow in the model problem we now investigate the stability of a more realistic model for the streaming flow induced by an oscillating cascade of circular cylinders. Instead of specifying the velocity profile as given by expression (5.6.5) we use the u-component of the velocity profile obtained according to the mathematical model **DM0** at $X=X_0$ and assume that the v-component of the velocity is zero since the streaming is dominated by the u-velocity. We then investigate the effects on stability of changing the value of X_0. The equation (5.6.2) for ϕ must now be solved subject to the boundary conditions (5.6.6) and (5.6.7) since we still assume that the flow is periodic with a period 2L in the Y-direction.

Again the eigenvalues for the most unstable solutions for $0.01\leq\alpha\leq 15.0$ are obtained. The stability diagrams in the $(R_s,\ \alpha)$ plane for $X_0=1$, 2 and 3 are given in **Fig.5.12**. It is found that for any value of α the flow becomes more unstable as the value of R_s increases for all values of X_0 investigated ($X_0 \in (0,\ 15)$). This indicates that the most unstable region of the flow occurs close to

the cascade. For all values of X_0 that we have investigated it has been observed that as R_s increases the flow changes from being stable to unstable, for a given value of α, at a critical value of R_s, $R_{s\alpha}$ say, i.e. the flow is stable when $R_s < R_{s\alpha}$ whilst it is unstable when $R_s > R_{s\alpha}$.

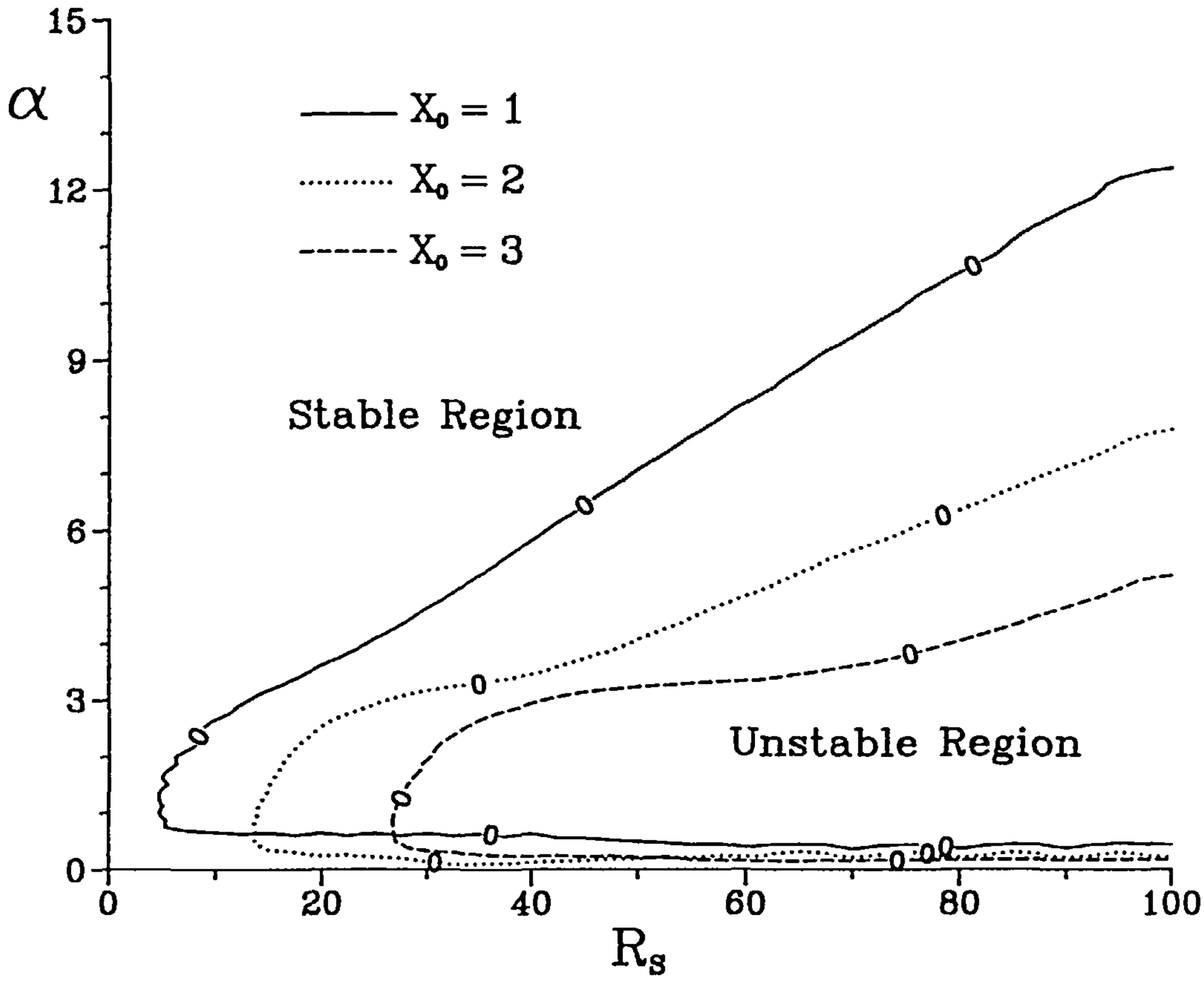

Fig.5.12 Stability diagram of the streaming cascade flow.

For a given value of X_0 then $R_{s\alpha}$ depends on α and it is found that there exists a minimum value of $R_{s\alpha}$, $R_{s\alpha m}$ say, which occurs at a certain value of α, α_{mi} say, for different values of X_0. The values of $R_{s\alpha m}$ and α_{mi} as a function of X_0 is given Table 5.1. As

the value X_0 increases then the value of $R_{s\alpha m}$ increases and the variation of $R_{s\alpha m}$ as a function of X_0 is presented in Fig.5.13 where

X_0	1	2	3	4	5	6	7
$R_{s\alpha m}$	5	14	27	42	57	73	91
α_{ml}	1.1	0.95	0.95	0.8	0.77	0.75	0.75

Table 5.1 Variation of $R_{s\alpha m}$ with α_{ml} for various values of X_0.

we can see that for $X_0 \gtrsim 7.5$ the value $R_{s\alpha m}$ is beyond the range of values of R_s that we have investigated here.

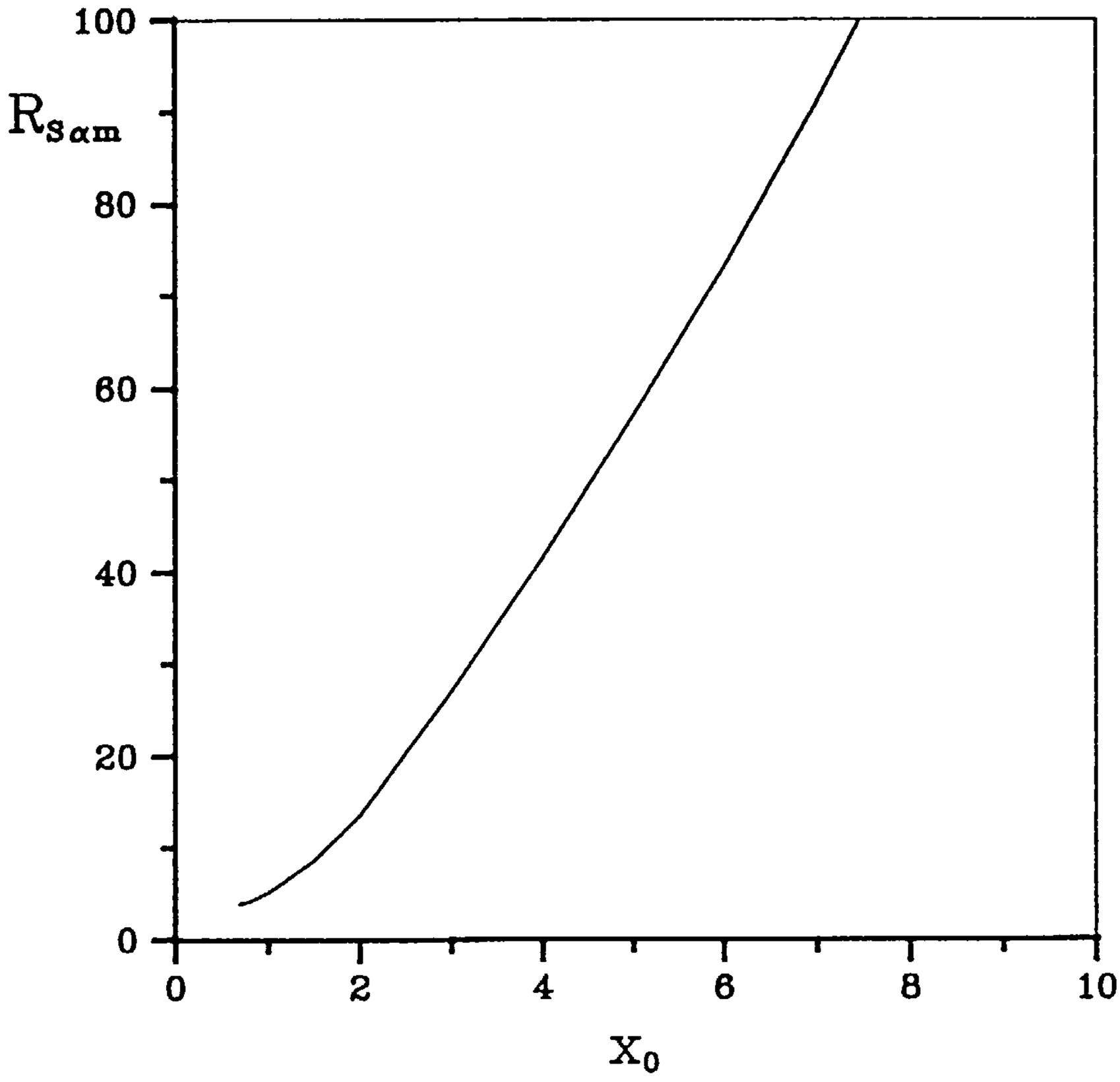

Fig.5.13 Critical streaming Reynolds number as a function of X_0.

It is also demonstrated in **Fig.5.12** that the most unstable region is when $\alpha \lesssim 13$ for $X_0=1$ and $\alpha \lesssim 6$ for $X_0=3$, and as X_0 increases this region becomes smaller and smaller and eventually at $X_0 \gtrsim 7.5$ the flow becomes stable for all the values of α and R_s that we have investigated.

5.7 Comparison with Experiments

As we observed in section 5.5 the numerical results obtained using the boundary conditions **DM1**, **DM2**, **DM3** and **DM4** are similar to each other for all the values of R_s that we have investigated. The numerical results for the streaming flow when $R_s=0.636$, 9 and 15 are shown in **Fig.5.14** whilst the experimental results for $R_s=0.636$, 2.54 and 8.9 are shown in **Fig.5.15** where the values of ε for the experimental data are 1/40, 1/20 and 1/20, respectively. Clearly the tendency of the numerical results show good agreement with the experimental investigations. It can be observed that the symmetry of the experimental result for $R_s=0.636$ is good whilst for $R_s=2.54$ the flow is starting to show signs of symmetry breaking. For $R_s=8.9$ a break-down in the symmetry is clearly observed from the experimental results and a comparison with the numerical results show qualitative agreement.

It should be noted that it is very hard to obtain exactly symmetrical experimental pictures even for very small values of R_s and in order to determine exactly the critical value of R_{s0} from the experimental work is extremely difficult. The discrepancy between the experimental and numerical solutions is probably due to (i) the axes of the cylinders are not exactly in a plane; (ii) the use of a

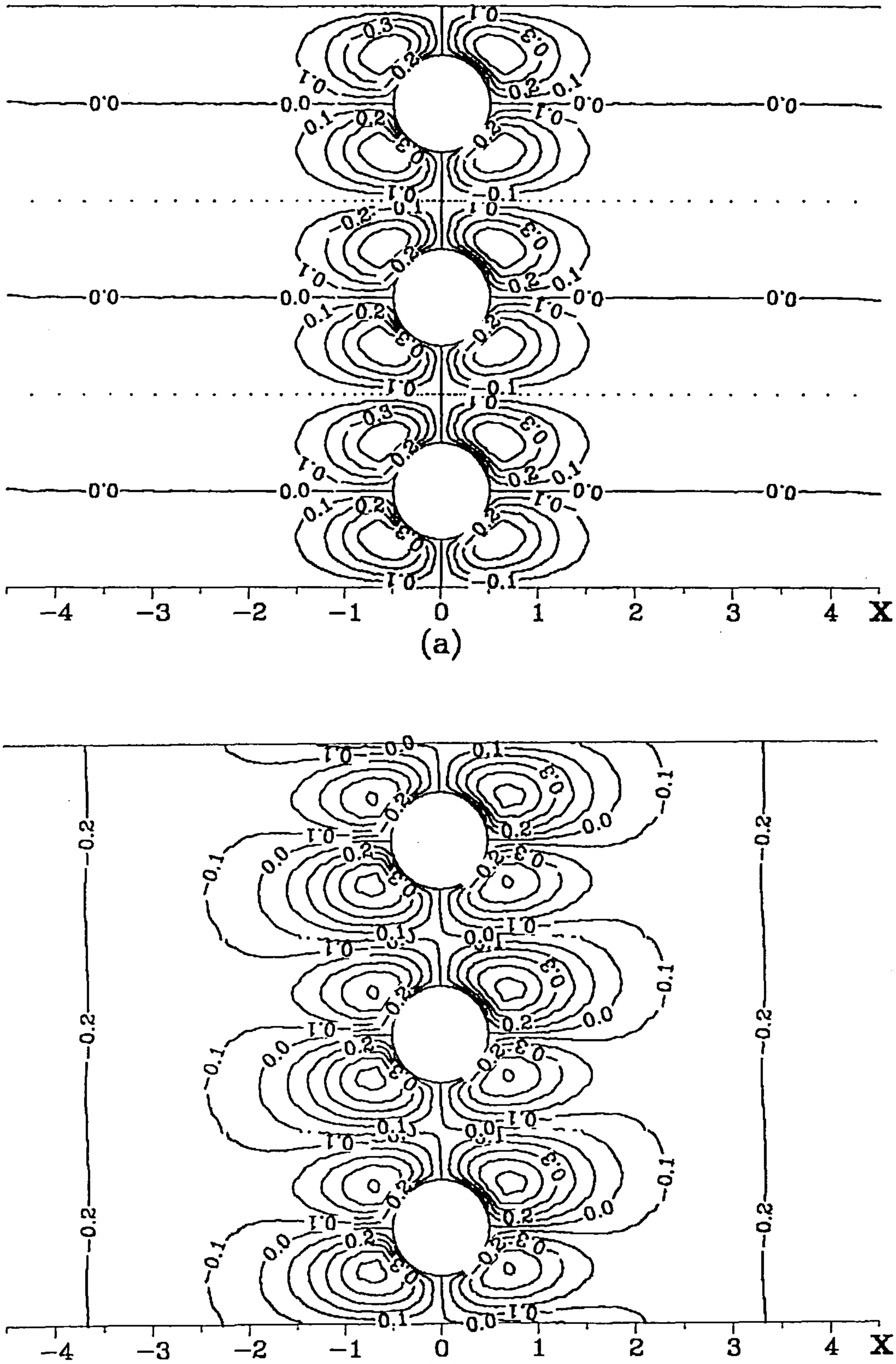

Fig.5.14 (to be continued in next page).

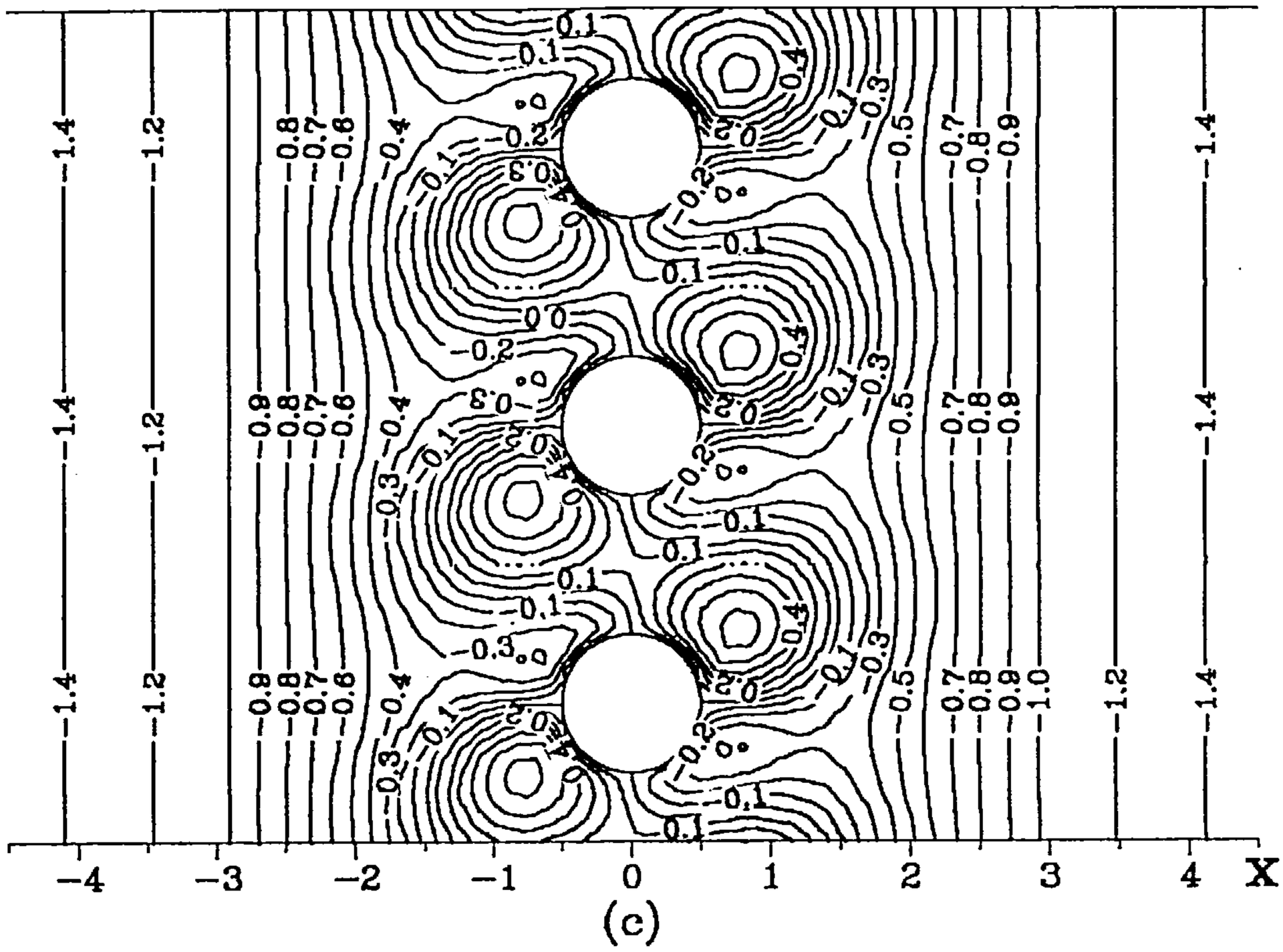

Fig.5.14 The streamlines from the numerical results for the outer streaming flow. (a) R_s=0.636, (b) R_s=9, (c) R_s=15.

finite number of the cylinders in the experimental work; (iii) the effects of the free surface and the bottom of the tank being at a finite distance from where the experimental results were obtained and (iv) the value of ε is finite in the experiments.

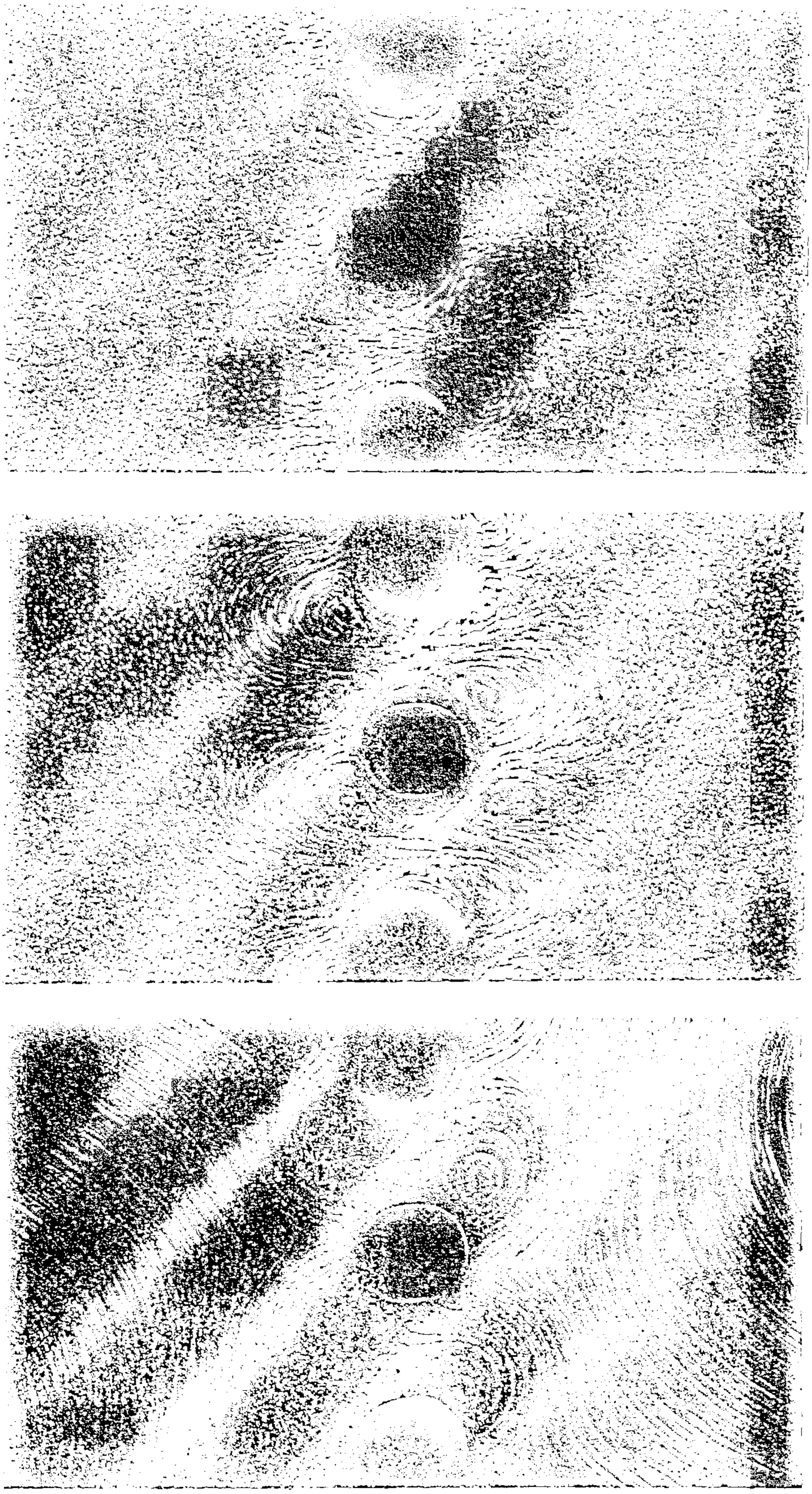

(a)

(b)

(c)

Fig.5.15 The experimental results for the cascade of circular cylinders. (a) R_s=0.636, (b) R_s=2.54, (c) R_s=8.9.

Experimental results for streaming flows have also been obtained for cascades of square and rectangular cylinders which oscillate harmonically in an unbounded, incompressible viscous fluid which is otherwise at rest. The cascade of rectangular cylinders is assumed to consist of an infinite number of rectangular cylinders which have sides of length d_1 and d in the x^*- and y^*-directions, respectively, and of infinite extent in the z^*-direction (for the co-ordinate system see Fig.1.7). The cylinders occupy the space between the planes $x^* = -\frac{d_1}{2}$, $x^* = \frac{d_1}{2}$, $y^* = -\frac{d}{2}+2k\mathcal{L}$ and $y^* = \frac{d}{2}+2k\mathcal{L}$ at time $t^*=0$, where k=0, ±1, ±2,.... In the case when $d_1=d$ this rectangular cascade becomes a square cascade, see Fig.1.6. The experimental setup for the cascades of square and rectangular cylinders are exactly the same as those used for the cascade of circular cylinders, see chapter 2 for detailed experimental methods. In the experiments the values of d, d_1 and $\mathcal{L}$ are chosen to be 0.01m, 0.02m and 0.02m, respectively.

Fig.5.16 shows the streaming flow induced by a harmonically oscillating cascade of square cylinders in a fluid at rest for ε=1/40. At R_s=0.318 the flow is almost symmetrical about both the X- and Y-directions (see Fig.5.16a) whilst at R_s=0.636 the streaming flow has started to show signs of being asymmetric (see Fig.5.16b), and finally at R_s=2.23 the streaming flow has developed a very asymmetrical structure with a strong vertical flow on both sides of the cascade at a distance of the order of the size of the cylinder. Fig.5.17 shows similar flow structures to those observed in Fig.5.16 for the streaming flow induced by an oscillating cascade of rectangular cylinders where the values of R_s and ε are the same as

those in the case of the cascade of square cylinders. It can be seen that these results for the cascades of square and rectangular cylinders show very similar tendencies to those obtained for the cascade of circular cylinders, i.e. for small values of the streaming Reynolds number the streaming flow is symmetrical about both the X- and Y-axes whilst it becomes asymmetrical as the value of R_s increases. Generally, for both of these cascades considered when R_s is small there are eight recirculating vortices around each of the bar with two vortices in each quadrant of the flow.

It should be noted that on the photographs shown in Figs.5.15-5.17 there is a diagonal pattern. This is caused by the use of light sources slanting rearwards to the left and forwards to the right; these produce bright diagonal bands where the marker particles are illuminated by both sources and darker bands of roughly half the intensity where one beam is obstructed by a tooth of the cascade.

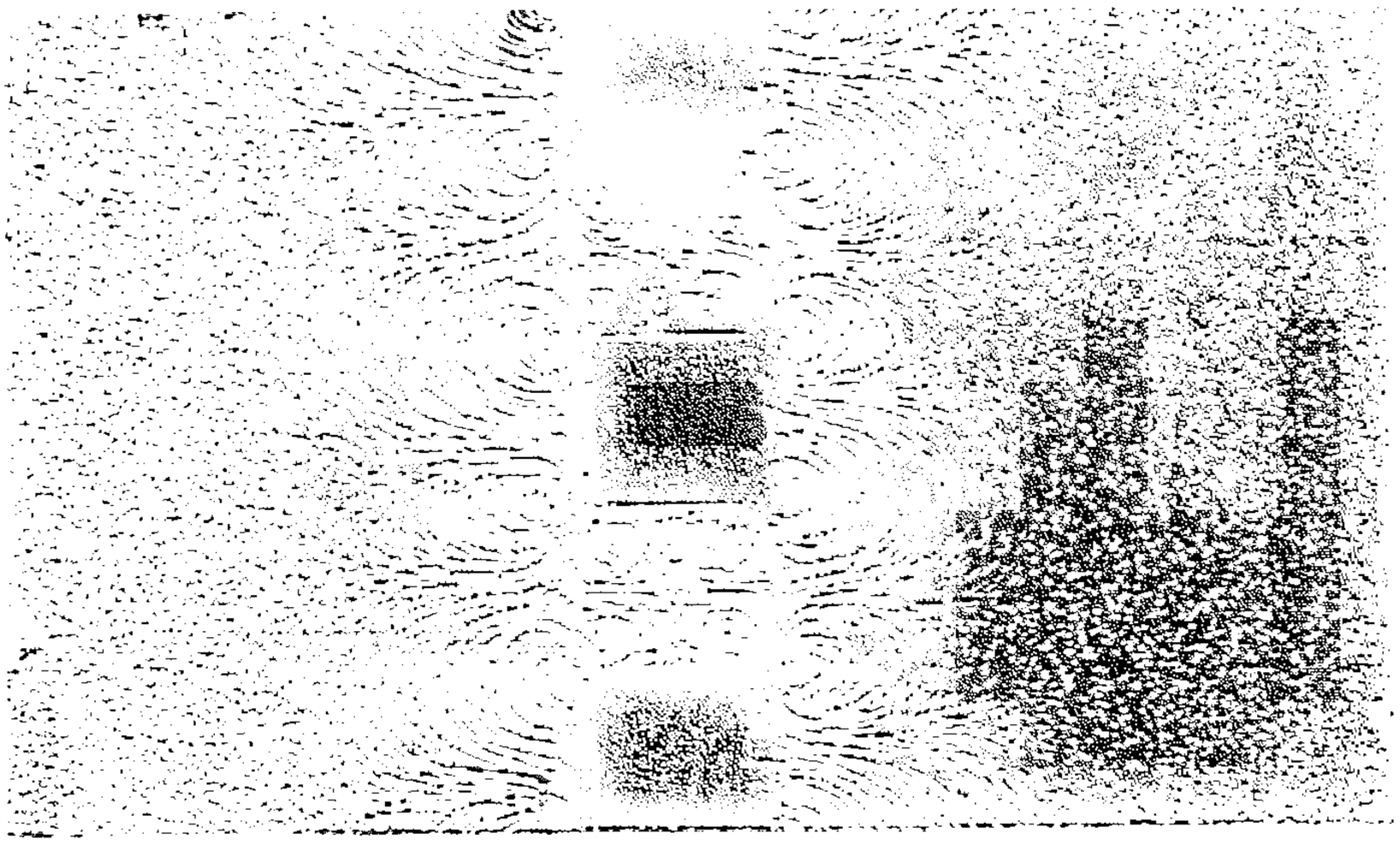

(a)

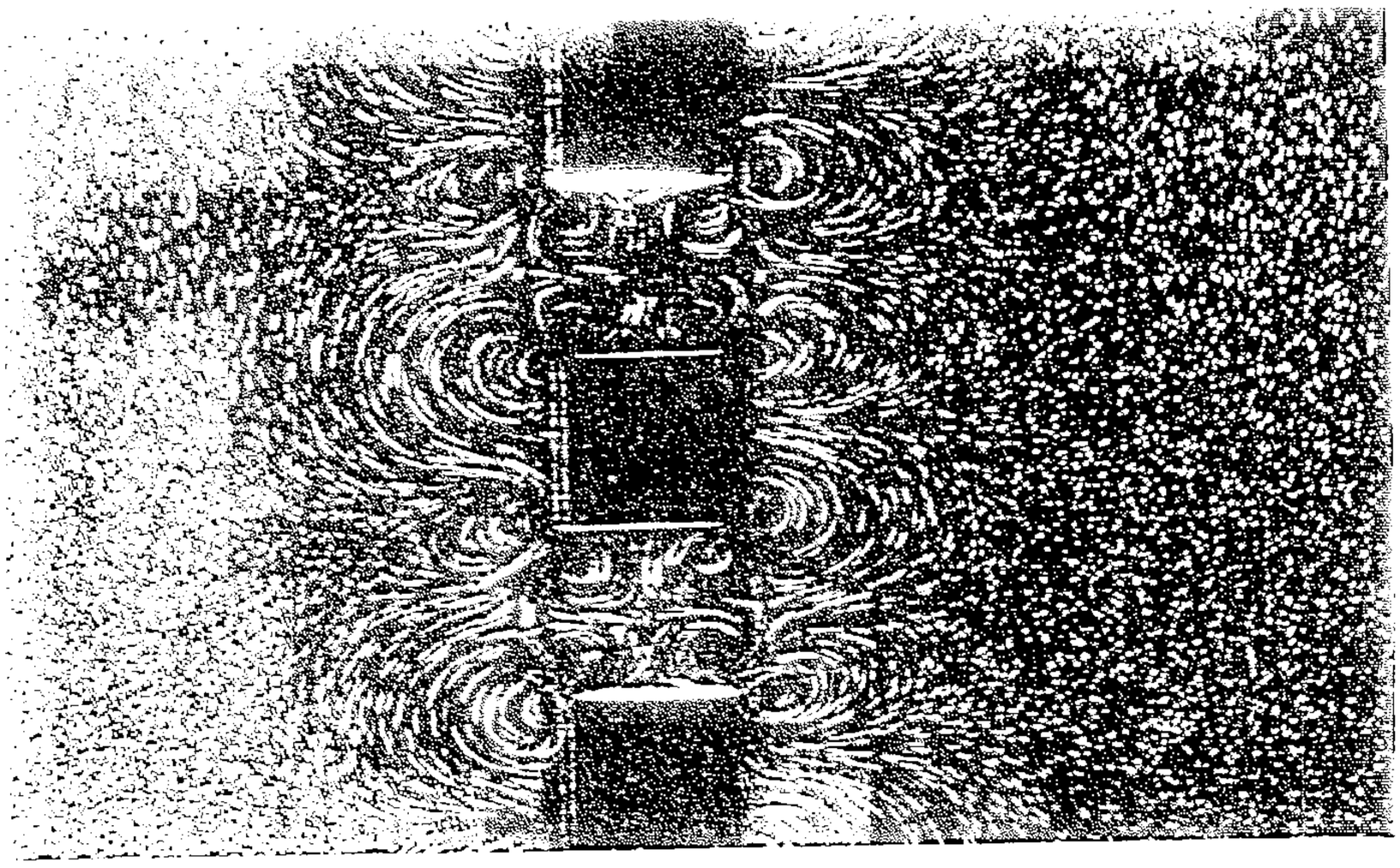

(b)

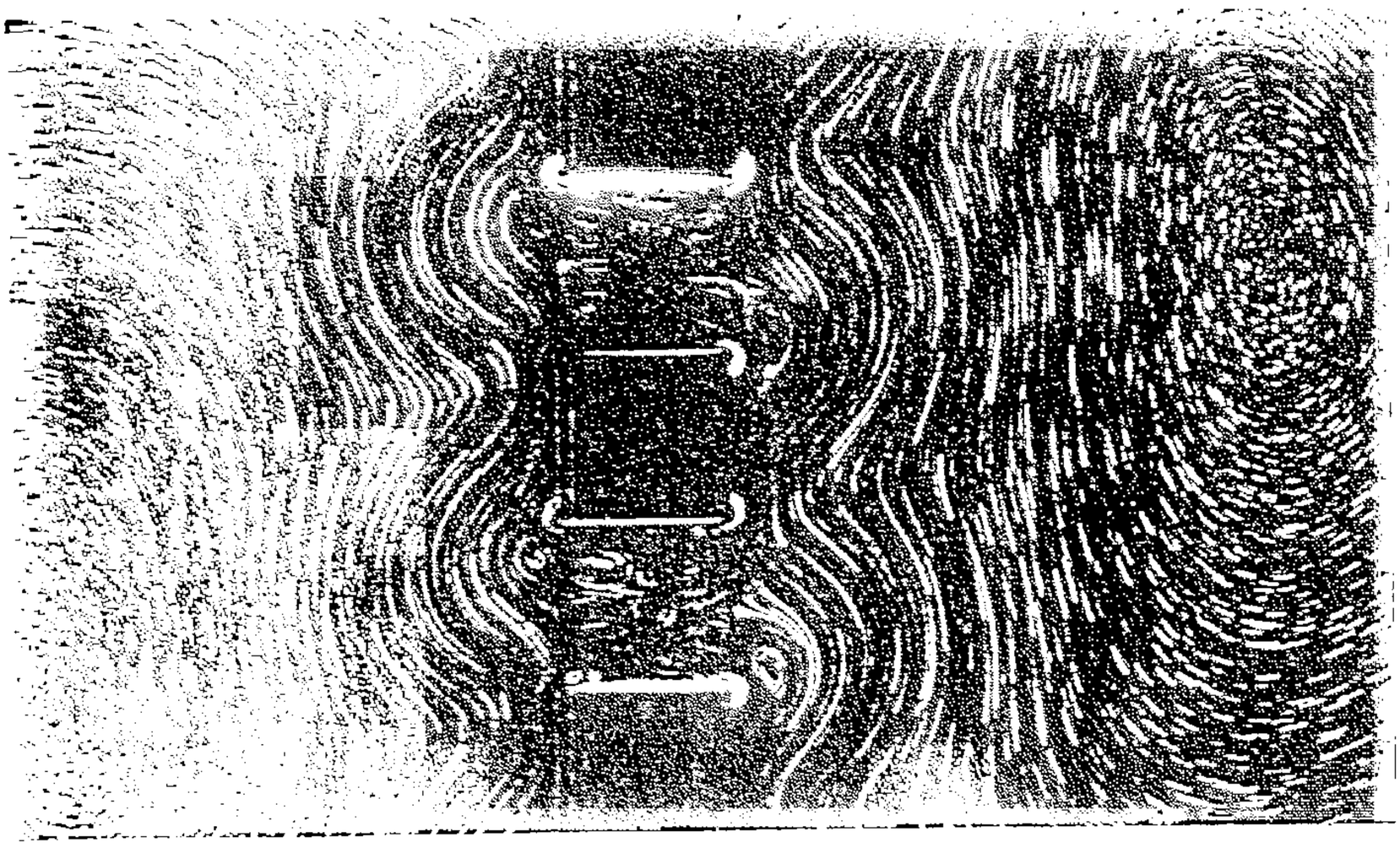

(c)

Fig.5.16 The experimental results for the cascade of square cylinders. (a) R_s=0.316, (b) R_s=0.636, (c) R_s=2.23.

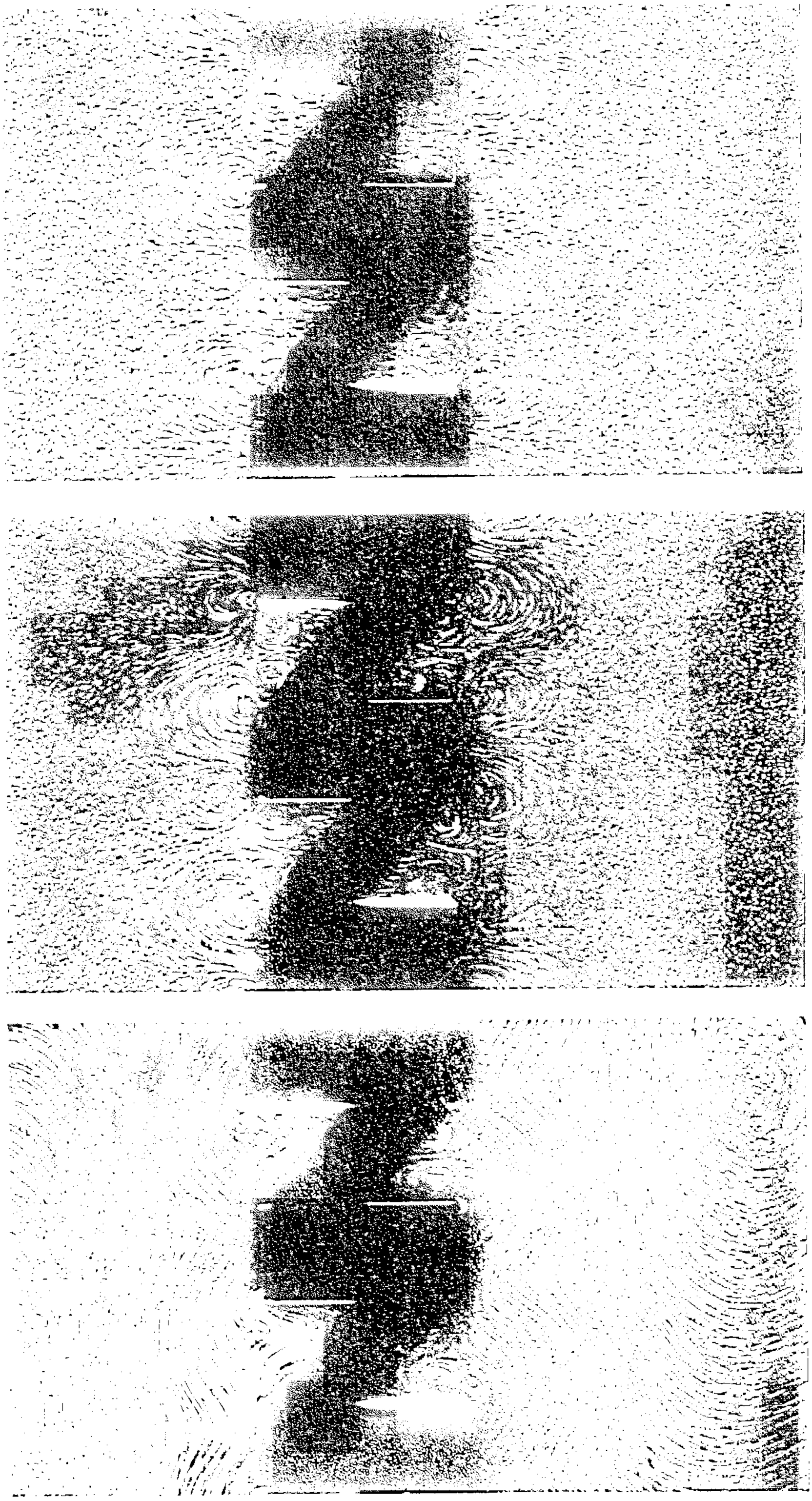

(a)

(b)

(c)

Fig.5.17 The experimental results for the cascade of rectangular cylinders. (a) R_s=0.318, (b) R_s=0.636, (c) R_s=2.23.

5.8 Conclusions

The outer streaming flow induced by a harmonically oscillating cascade of circular cylinders has been investigated both numerically and experimentally. The complex physical domain has been conformally transformed onto an rectangular solution domain and then the Navier-Stokes equations are solved using a specialised finite- difference technique. Various solution domains and boundary conditions have been applied in order to solve the problem and it is found that it is not always possible to obtain symmetrical flows for all values of the streaming Reynolds number R_s although, mathematically, symmetrical flows can always be predicted. The numerical results indicate that the boundary conditions on Y=kL (k an integer) are very important in predicting the observed flow. Numerical results for the flow field show a reasonable agreement with those obtained experimentally. A stability analysis for the streaming flow induced by an oscillating cascade of circular cylinders has been investigated numerically and the results show that the flow is stable for small values of R_s but unstable for large values of R_s, the regimes of R_s within which the flow is stable (unstable) predicted by the stability analysis are typically the same as those predicted by the full numerical calculations and the experimental work. Experimental results for cascades of both square and rectangular cylinders have also been obtained and they show a similar tendency for the structure as for the cascade of circular cylinders. The numerical results and stability analysis have not been presented here for the streaming flow induced by an

oscillating cascade of square and rectangular cylinders, however we believe that, in principle, the numerical methods in this chapter may be applied to these types of cascades.

CHAPTER 6 A NUMERICAL INVESTIGATION INTO FLUID DYNAMICS OF THE INDUSTRIAL CYCLONES

6.1 Introduction

There has been much work performed on the design and operation of cyclones, most of it being experimental and empirical, see for example Kelsall (1952), Bradley and Pulling (1959) and Rietema (1961). Kelsall's (1952) fundamental experimental investigation provides very detailed velocity distributions within the cyclone and has been used to test subsequent theoretical studies. Theoretical workers, for example Bradley and Pulling (1959), Rietema (1961) and Bloor and Ingham (1983), have concentrated on both the velocity distributions and the relationship between the separation efficiency and other physical quantities such as the pressure drop, the flow rate, the geometry of the cyclone, the particle characteristics, etc. Ferguson (1989) improved the inviscid fluid flow model of Bloor and Ingham (1987), which accurately predicts the flow field below the level of the vortex finder, by including the details of the recirculating flow which occurs above the level of the vortex finder.

In this chapter, we describe an inviscid mathematical model for the fluid flow in the cyclone and simulate, numerically, the fluid flow inside the cyclone. The velocity distributions, the particle trajectories and the separation efficiency have been investigated

numerically for cyclones whose geometry is that as shown in **Fig.1.4.** The influence of a small perturbation to the angular momentum on the separation efficiency of the cyclone has also been studied. Finally, based on the theories of Batchelor (1956) and Riley (1981), the influence of different estimates for the vorticity in the recirculating region, which occurs in the upper part of the cyclone, on the flow field and the separation efficiency is also studied. The numerical results have been compared with the experimental data of Kelsall (1952).

6.2 Equations of Motion and Boundary Conditions

Using cylindrical polar co-ordinates (z, R, λ), see **Fig.6.1,** the continuity equation for an incompressible fluid is:

$$\frac{\partial v}{\partial z} + \frac{1}{R}\frac{\partial}{\partial R}(Ru) = 0 \qquad (6.2.1)$$

where u and v are the velocity components in the R- and z-directions, respectively, and the assumption of axially symmetric flow in the cyclone ensures that all derivatives with respect to λ are identically zero.

In many cyclones the inlet Reynolds number based on the spin velocity and the typical diameter of the inlet tube is of the order of tens of thousands and it is reasonable to assume that the main flow in the cyclone is inviscid, i.e. everywhere outside the boundary-layers that exist near solid surfaces and the air core. Therefore the momentum equation, in vector form, may be written as:

$$\nabla\left(\frac{p}{\rho} + \frac{1}{2}q^2\right) - \underline{u}\wedge\underline{\omega} = 0 \qquad (6.2.2)$$

in the main body of the cyclone, where p is the modified pressure,

$\underline{\omega} = (\omega_z, \omega_R, \omega_\lambda)$ is the vorticity, q is the magnitude of the velocity $\underline{u} = (v, u, w)$ and ρ is the density of the fluid.

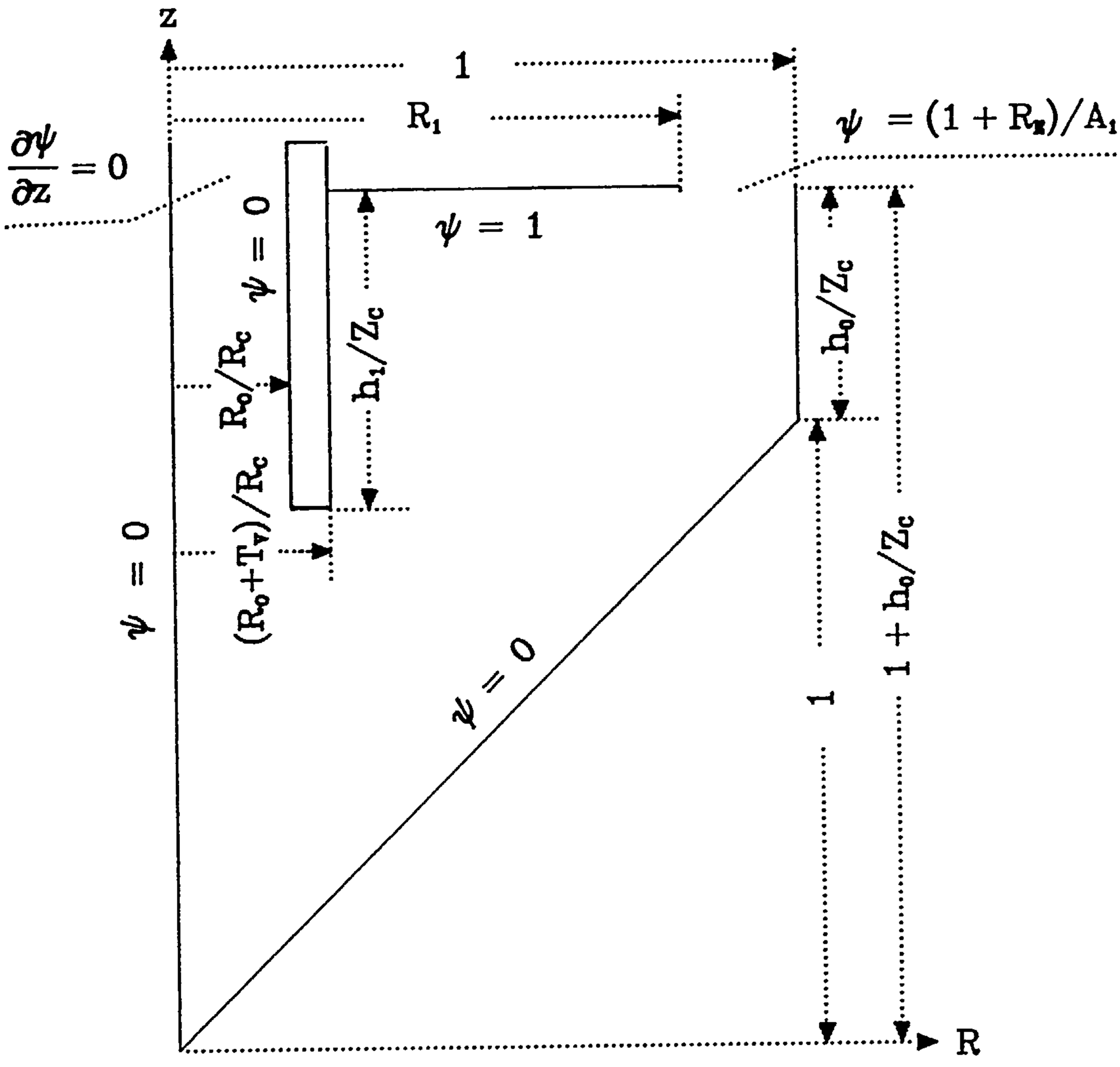

Fig.6.1 The computational Geometry of the cyclone.

In the polar coordinate system (z, R, λ) (see Fig.6.1) the vorticity components are defined by:

$$\omega_z = \frac{1}{R}\frac{\partial}{\partial R}(Rw) \qquad (6.2.3a)$$

$$\omega_R = -\frac{1}{R}\frac{\partial}{\partial z}(Rw) \qquad (6.2.3b)$$

$$\omega_\lambda = \frac{\partial u}{\partial z} - \frac{\partial v}{\partial R} \qquad (6.2.3c)$$

In order to satisfy the continuity equation (6.2.1) a streamfunction ψ is also introduced such that

$$u = -\frac{1}{R}\frac{\partial \psi}{\partial z} \qquad (6.2.4a)$$

$$v = \frac{1}{R}\frac{\partial \psi}{\partial R} \qquad (6.2.4b)$$

Following Batchelor (1967), it is convenient to introduce the quantity H, the total head of the fluid, defined by:

$$H = \frac{p}{\rho} + \frac{1}{2}q^2 \qquad (6.2.5)$$

Taking the scalar product of equation (6.2.2) with a line element parallel to $\underline{u}$, it can be shown that the term in $\underline{\omega}$ is eliminated and using equations (6.2.4) and (6.2.5) then Bernoulli's equation is obtained in the form

$$H(\psi) = \frac{p}{\rho} + \frac{1}{2}q^2 \qquad (6.2.6)$$

Writing equation (6.2.2) in its components, we have:

in the R-direction:

$$\frac{1}{\rho}\frac{\partial p}{\partial R} + u\frac{\partial u}{\partial R} + v\frac{\partial v}{\partial R} + w\frac{\partial w}{\partial R} - w\omega_z + v\omega_\lambda = 0 \qquad (6.2.2a)$$

in the λ-direction:

$$\frac{1}{\rho}\frac{\partial p}{\partial \lambda} + \frac{1}{R}\left(u\frac{\partial u}{\partial \lambda} + v\frac{\partial v}{\partial \lambda} + w\frac{\partial w}{\partial \lambda}\right) - v\omega_R + u\omega_z = 0 \qquad (6.2.2b)$$

in the z-direction:

$$\frac{1}{\rho}\frac{\partial p}{\partial z} + u\frac{\partial u}{\partial z} + v\frac{\partial v}{\partial z} + w\frac{\partial w}{\partial z} - u\omega_\lambda + w\omega_R = 0 \qquad (6.2.2c)$$

Using the assumption of axially symmetric flow in the cyclone

and equation (6.2.3), equation (6.2.2b) can be written as

$$\left(v \frac{1}{R} \frac{\partial}{\partial z} + u \frac{1}{R} \frac{\partial}{\partial R} \right) (Rw) = 0 \qquad (6.2.7)$$

Since $v \frac{1}{R} \frac{\partial}{\partial z} + u \frac{1}{R} \frac{\partial}{\partial R}$ represents differentiation along a streamline equation (6.2.7) can be integrated to give

$$wR = C(\psi) \qquad (6.2.8)$$

where $C(\psi)$ is the angular momentum of the flow. This implies that the angular momentum of the fluid is conserved along each streamline.

On substituting equation (6.2.8) into equation (6.2.3a) we have

$$\omega_z = \frac{1}{R} \frac{dC}{d\psi} \frac{\partial \psi}{\partial R} \qquad (6.2.9)$$

and using equations (6.2.4), (6.2.6), (6.2.8) and (6.2.9) then equation (6.2.2a) becomes

$$\frac{dH}{d\psi} \frac{\partial \psi}{\partial R} + \left[\frac{1}{R} \frac{\partial \psi}{\partial R} \omega_\lambda - \frac{C(\psi)}{R} \frac{1}{R} \frac{dC}{d\psi} \frac{\partial \psi}{\partial R} \right] = 0$$

$$\text{i.e. } \frac{\omega_\lambda}{R} = \frac{1}{R^2} C \frac{dC}{d\psi} - \frac{dH}{d\psi} \qquad (6.2.10)$$

Since we assume that the fluid flow in the cyclone is axially symmetric we would expect that the boundary conditions on the entry to the cyclone can be modelled as if it is two-dimensional. The three - dimensional entry is taken account by assuming that the fluid enters the cyclone vertically through the lid of the cyclone within the region $R_1 < R_E < R_c$ (where R_c is the radius of the cyclone) with uniform speed V_0 and angular momentum C. The value of R_1 is a quantity which has to be determined and this will be discussed later. Thus the boundary conditions at the entry of the cyclone are

$$v = V_0, \qquad u = 0, \qquad w = w(R_E), \qquad R_1 \leq R_E \leq R_c \tag{6.2.11}$$

$$C = R_E w(R_E) \qquad R_1 \leq R_E \leq R_c \tag{6.2.12}$$

$$\psi = \frac{1}{2} V_0 (R_c^2 - R_E^2) \qquad R_1 \leq R_E \leq R_c \tag{6.2.13}$$

Further it is assumed that at the entry the fluid has zero azimuthal vorticity so equation (6.2.2a) reduces to

$$\frac{1}{\rho} \frac{dp}{dR_E} = \frac{w^2}{R_E} \tag{6.2.14}$$

Using equations (6.2.6), (6.2.12), (6.2.13) and (6.2.14) it can be shown from equation (6.2.10) that in the main flow region (see Ferguson (1989))

$$\frac{\omega_\lambda}{R} = -\frac{1}{R^2 V_0 R_E^3} C \frac{dC}{dR_E} (R_E^2 - R^2) \tag{6.2.15}$$

Using equations (6.2.3c) and (6.2.4) equation (6.2.15) can be written as

$$\frac{\partial^2 \psi}{\partial R^2} - \frac{1}{R} \frac{\partial \psi}{\partial R} + \frac{\partial^2 \psi}{\partial z^2} = \frac{1}{V_0 R^3} C \frac{dC}{dR_E} (R_E^2 - R^2) \qquad \text{for } \psi \leq 1 \tag{6.2.16}$$

It is this equation which governs the main flow in the cyclone. It is clear from equation (6.2.16) that the main flow is influenced by the angular momentum at the entry to the cyclone and we will investigate in section 6.6.2 how different estimates of $C(\psi)$ at the entry to the cyclone affect the flow in the cyclone and the separation efficiency of the cyclone.

It is expected that in the cylindrical section of the cyclone a circulation region will develop due to the viscous action of the

main flow forcing the fluid into the annular region between the vortex finder and the cyclone wall and hence into a closed region which is similar to that discussed by Batchelor (1956) and Riley (1981). Batchelor (1956) showed that at high values of the Reynolds number, for a steady laminar flow with closed streamlines, the azimuthal vorticity component is as follows:

$$\frac{\omega_\lambda}{R} = \frac{dH}{d\psi} = \text{constant} = D1, \text{ say} \qquad (6.2.17)$$

which governs the flow in the recirculation region in the upper part of the cyclone. It is difficult to solve equation (6.2.17) since the value of the constant D1 in the recirculation region is not known. By using Stokes' theorem it is, however, possible to find an estimate of the area of the recirculation region as follows:

By using Stokes' theorem we have:

$$\iint_S RD1 \; dS = \int_s \underline{u} \cdot \underline{ds} \qquad (6.2.18)$$

where S is the recirculation region and s a closed contour which defines the surface S. Using the mean value theorem and equation (6.2.17) we have

$$R_\xi \frac{\omega_\lambda}{R} S_v = V_\xi \int_s ds \qquad (6.2.19)$$

where S_v is the area of the recirculation region, $R_\xi \in (R_o, R_c)$ with R_o being the overflow radius, and V_ξ the magnitude of the velocity somewhere on the curve s.

Although we do not know the exact bounds of the recirculation region, a crude, but reasonable, assumption is available, see Ferguson (1989). He assumed that the recirculation region is

equivalent to a circle of radius $R_c/2$, with half the circumference representing the solid boundary, where the velocity is zero, and the other half representing the shear layer of the main flow, where the magnitude of the velocity is a constant and equal to V_0. In other words, by taking $R_\xi=R_c$, $V_\xi=V_0$, $S_v=\pi\left(\frac{R_c}{2}\right)^2$ and $\int_s ds=\pi R_c/2$, Ferguson (1989) obtained in the recirculation region

$$\frac{\omega_\lambda}{R} \approx 2V_0/R_c^2, \tag{6.2.20}$$

and using equations (6.2.3c) and (6.2.4), equation (6.2.20) becomes

$$\frac{\partial^2\psi}{\partial R^2} - \frac{1}{R}\frac{\partial\psi}{\partial R} + \frac{\partial^2\psi}{\partial z^2} \approx -2V_0R^2/R_c^2 \qquad \text{for } \psi > 1 \tag{6.2.21}$$

It is this equation which governs the flow in the recirculation region in the upper part of the cyclone. Further, it is found that this assumption, as Ferguson pointed out, works well for the experimental data of Kelsall (1952) since the cyclone that Kelsall used had an extra long vortex finder and a very high spin velocity at the entry to the cyclone. As a result, the recirculation region was well established in the upper part of the cyclone. However, other approaches in choosing values of R_ξ, V_ξ, S_v and $\int_s ds$ are available, and we will return to this in section 6.6.3.

Now we have seen from (6.2.16) and (6.2.21) that the governing equation for the flow in the cross plane of the cyclone is as follows

$$\frac{\partial^2\psi}{\partial R^2} - \frac{1}{R}\frac{\partial\psi}{\partial R} + \frac{\partial^2\psi}{\partial z^2} = \begin{cases} \dfrac{1}{V_0R_E^3}C\dfrac{dC}{dR_E}(R_E^2-R^2) & \text{for } \psi \le 1 \\ -2V_0R^2/R_c^2 & \text{for } \psi > 1 \end{cases} \tag{6.2.22}$$

At this stage it is useful to introduce the following non - dimensional quantities:

$$R = R_c \hat{R} \qquad R_E = R_c \hat{R}_E \qquad R_1 = R_c \hat{R}_1$$

$$z = Z_c \hat{z} \qquad \psi = \psi_Q \hat{\psi} \qquad C = W_0 R_c \hat{C}$$

$$U_{sc} = \frac{Q}{2\pi R_c Z_c} \qquad V_{sc} = \frac{Q}{2\pi R_c^2} \qquad W_{sc} = W_0$$

where R_c and Z_c are the radius and the length of the conical portion of the cyclone, respectively, Q is the total flux of fluid through the cyclone and $\psi_Q = Q/2\pi$. Also W_0 is the average spin velocity at the entry of the cyclone and R_1 is the inner radius of the annulus in the lid of the cyclone and is determined by the flux of the fluid through the cyclone. In fact $Q = \pi V_0 (R_c^2 - R_1^2)$ where $R_1 \leq R_E \leq R_c$.

It is then shown that the governing equations of motion for the cross plane flow field, equation (6.2.16) and (6.2.21), can be written as:

$$\frac{\partial^2 \psi}{\partial R^2} - \frac{1}{R}\frac{\partial \psi}{\partial R} + t_{Rz}^2 \frac{\partial^2 \psi}{\partial z^2} = \begin{cases} A_2 \frac{1}{R_E^3} C \frac{dC}{dR_E}(R_E^2 - R^2) & \text{for } \psi \leq 1 \\ -4R^2/A_1 & \text{for } \psi > 1 \end{cases} \qquad (6.2.23)$$

where the non - dimensional notation, ^, has been dropped for convenience. Also:

$$t_{Rz} = R_c/Z_c, \qquad A_1 = 1 - R_1^2,$$

$$A_2 = 2R_c^2 A_1 \left\{\frac{\pi R_c W_0}{Q}\right\}^2, \qquad R_E^2 = 1 - A_1 \psi.$$

Equations (6.2.23) have now to be solved subject to the following boundary conditions (see **Fig.6.1**),

$$\psi = (1-R_E)/A_1 \quad \text{when } R_1 \le R_E \le 1,\ z = 1+h_0/Z_c \tag{6.2.24}$$

$$\psi = 0 \quad \begin{cases} \text{when } R = 0,\ 0 \le z \le 1+h_0/Z_c \\ \text{when } R = z,\ 0 \le R \le 1 \\ \text{when } R = 1,\ 1 \le z \le 1+h_0/Z_c \end{cases} \tag{6.2.25}$$

$$\psi = 1 \quad \begin{cases} \text{when } R = R_0/R_c,\ 1+(h_0-h_1)/Z_c \le z \le 1+h_0/Z_c \\ \text{when } R_o/R_c \le R \le (R_o+T_v)/R_c,\ z = 1+(h_0-h_1)/Z_c \\ \text{when } R = (R_0+T_v)/R_c,\ 1+(h_0-h_1)/Z_c \le z \le 1+h_0/Z_c \\ \text{when } (R_o+T_v)/R_c \le R \le R_1/R_c \end{cases} \tag{6.2.26}$$

$$\frac{\partial \psi}{\partial z} = 0 \qquad \text{when } 0 \le R \le R_o/R_c,\ z = 1 + h_0/Z_c. \tag{6.2.27}$$

Another boundary condition that is required is the angular momentum at the entry to the cyclone, i.e $C(R_E)$ for $R_1 \le R_E \le 1$. Ferguson (1989) showed that in order to obtain the correct form of the cross plane flow, including the jetting of the fluid down the side wall of the cyclone and a recirculating zone in an annular region outside the vortex finder, it is necessary to choose $C(R_E)$ such that the value of $C(R_E)\frac{dC}{dR_E}$ is negative. More details of the influence of the choice of the form of $C(R_E)$ will be given in section 6.6.

Given the cyclones geometry and operating conditions the only unknown parameter is the value of R_1. This parameter is fixed by ensuring that the streamline $\psi = 1$ joins the vortex finder tangentially, see Bloor and Ingham (1987).

6.3 The Spin Velocity

The assumption of inviscid flow implies that the spin velocity

in the cyclone is dependent on R and the angular momentum at the entry to the cyclone, see equation (6.2.8). In non-dimensional form equation (6.2.8) can be written in the form

$$w = C(\psi)/R \qquad (6.3.1)$$

where $C(\psi)$ is the non-dimensional angular momentum which is conserved on any streamline.

Equation (6.3.1) predicts that the spin velocity will become infinite at R = 0 which is clearly inappropriate as viscous effects become important near the axis of the cyclone where the spin velocity will be solid body rotation. Nevertheless, equation (6.3.1) accurately predicts the spin velocity in the main body of the cyclone where viscous effects are unimportant, see for example Bloor and Ingham (1983) and Ferguson (1989). For the purpose of calculating the separation efficiency of the cyclone, this is adequate as most of the separation processes occur in the main body rather than near the axis of the cyclone.

6.4 Efficiency of the Cyclone

Theoretically, a cyclone can separate particles with different shapes from the fluid which carries them into the cyclone providing that the density of the particles is greater than that of the fluid. The separation efficiencies for particles with different shapes are usually different even when the densities and the volumes are the same. However, in this chapter we will not study the influence of the shape of the particle on the separation efficiency of the cyclone and assume that all particles have their Stokes diameters. (The Stokes diameter of a particle is the diameter of a sphere of

equal volume to that of the particle. In the following description, diameter or size relating to a particle will be taken to mean the Stokes diameter).

By assuming that the particle Reynolds number is small, the drag on the particle can be accurately described by the Stokes drag law. The drag force on the particle with a diameter d is

$$3\pi\mu U_p d \tag{6.4.1}$$

where μ is the viscosity of the fluid, U_p is the drift velocity for the particle. Equating this force to the applied centrifugal force gives

$$3\pi\mu U_p d = \frac{\pi d^3}{6} (\rho_p - \rho) (W_0 w)^2/(R_c R) \tag{6.4.2}$$

from which we have the drift velocity for the particle

$$U_p = \frac{1}{18\mu} \frac{d^2 (W_0 w)^2}{R_c R} (\rho_p - \rho) \tag{6.4.3}$$

where ρ_p and ρ are the densities of the particle and the fluid, respectively. Neglecting gravitational effects, the trajectory of the particle is then given by the following non - dimensional ordinary differential equation:

$$U_{sc} \frac{dR}{dt} \Big/ \left(V_{sc} \frac{dz}{dt} \right) = \frac{U_{sc} u + U_p}{V_{sc} v} \tag{6.4.4}$$

which can be written in the following easily integrable form as

$$\frac{dR}{dz} = \frac{u + cw^2/R}{v} \tag{6.4.5}$$

where

$$c = \frac{2\pi W_0^2 R_c (\rho_p - \rho) d^2}{18\mu t_{Rz} Q} . \tag{6.4.6}$$

By assuming that the particle distribution in the fluid at the entry to the cyclone is homogeneous, the trajectory of a particle of size d may be found by integrating equation (6.4.5) as an initial value problem starting from the particles radial position at the entry to the cyclone. This integration can be repeated for a large number of entry positions and therefore an accurate estimate of the efficiency for a particle of diameter d may be found. If $(1+h_0/Z_c, R_d)$, where $R_1 \leq R_d \leq 1$, is a position at the entry to the cyclone such that a particle of diameter d which enters the cyclone from there is separated, whilst the particle of the same diameter which enters the cyclone from any position $(1+h_0/Z_c, R)$, in which $R_1 \leq R < R_d$, at the entry is not separated and discharged to the overflow, then $\psi(1+h_0/Z_c, R_d)$ is the efficiency for particle of the diameter d.

6.5 Numerical Methods

Equation (6.2.23) is discretised using central-difference techniques. Using subscripts 0, 1, 2, 3 and 4 to denote typical grid points (ih, jh), ((i+1)h, jh), (ih, (j+1)h), ((i-1)h, jh) and (ih, (j-1)h), where h is the mesh size in both the R- and z-directions, then the discretised form of equation (6.2.23) at the point 0 may be written as

$$a_1\psi_1+a_2\psi_2+a_3\psi_3+a_4\psi_4-a_0\psi_0-RIT_0=0 \qquad (6.5.1)$$

where

$$a_1=1-1/(2(i-1))$$

$$a_2=a_4=t_{Rz}^2$$

$$a_3=1+1/(2(i-1))$$

$$a_0=a_1+a_2+a_3+a_4$$

$$RIT_0=\left[A_2\frac{1}{R_E^3}C\frac{dC}{dR_E}(R_E^2-R^2)\right]_0$$

A numerical solution of equation (6.5.1) is obtained using the Gauss - Seidel Relaxation technique. Convergence is achieved when the norm of the local error in the numerical solution between two successive iterations is less than a given tolerance, say ε.

Equation (6.4.5) is solved using the improved Euler method, coupled with bi-linear, or bi-cubic B-spline surface interpolation, (see Hayes and Halliday (1974)), in which the information at some grid points (4 for the bi-linear surface interpolation and 16, or 36, or 64 for the spline) around a typical non-grid point P is used to estimate the right hand side of equation (6.4.5) at the point P, where the numerical solution of equation (6.2.23) is not available. It is found that the splines obtained by using information at 16 points are sufficiently accurate for assessing the separation efficiency of the cyclone so they are used throughout all the calculations presented in this thesis.

6.6 Results and discussion

In this section we first test the numerical model developed here with the experimental work of Kelsall (1952). The influence of different choices of $C(R_E)$ at the entry to the cyclone on the velocity distributions and the separation efficiency of the cyclone is then investigated. Finally, effects of the different ways of

estimating the vorticity in the recirculation region of the cyclone on the separation efficiency are studied.

6.6.1 Kelsall's Work

We test the numerical model developed here with the experimental results of Kelsall (1952) where a long vortex finder was used in order to ensure that the flow was axially symmetric in the main body of the cyclone. The inlet Reynolds number for the flow was of the order of tens of thousands, typically 50,000, and hence the assumption of inviscid flow in the main body of the cyclone is valid. It is therefore appropriate to test the numerical model using the operating conditions and geometry given in Kelsall's series I experiments (KEL-I). One reason for this is that although a number of experimental investigations (see for example, ter Linden (1949), Kelsall (1952), Ohsai and Maeda (1958) and Knowles and Woods (1973)) have been performed on water cyclones, Kelsall's work on the velocity distribution within the cyclone is probably the most comprehensive. A more important reason is that the typical spin velocity in the cyclone is not high enough in some of the other experimental work and as a result the flow in the main body of the cyclone can not be modelled as an inviscid flow. Also, even though the inlet Reynolds number was large enough in Kelsall's series II and III experiments, the flux of fluid to the underflow was greater than that in the KEL-I, so a comparison was not made as the numerical model here does not include the treatment of the fluid flow to the underflow.

We first choose the angular momentum at the entry to the cyclone as

$$C(R_E) = \frac{1}{R_E}. \qquad (6.6.1)$$

This choice ensures that C(1)=1 (required by equation (6.3.1)), and the product of $C(R_E)$ and $\frac{dC}{dR_E}$ is less than zero, as suggested by Ferguson (1989) for the flow field to be in good agreement with the experimental data. Neglecting the leakage to the overflow and the fluid discharged to the underflow, solving equation (6.2.23) gives the stream-function and the velocity distribution and these are shown in **Figs.6.2** and **6.3**, respectively. It is seen from **Fig.6.2** that a jetting flow exists down the side wall of the cyclone from the entry to the lower part the cyclone and this flow is then discharged to the overflow with the flow being almost axial. Between this flow and the top of the cyclone there develops a recirculation region which has been observed by many experimental investigators, e.g. ter Linden (1949), Kelsall (1952), Bradley and Pulling (1959), Ohsai and Maeda (1959) and Knowles and Woods (1973).

Fig.6.3 shows the axial velocity component of the flow at seven levels in the main body of the cyclone and it can be seen that there is excellent agreement between the numerical solution and the experimental data of Kelsall (1952). Even the region where the flow is recirculating has been well modelled, as is shown at levels 6 and 7.

The free vortex flow, as given by equation (6.3.1), accurately predicts the form of the spin velocity profile given in Kelsall's experiments in the main flow (away from the axis of the cyclone) in the cyclone, see for example Bloor and Ingham (1983). It was found though, that in order to estimate the magnitude of the spin velocity

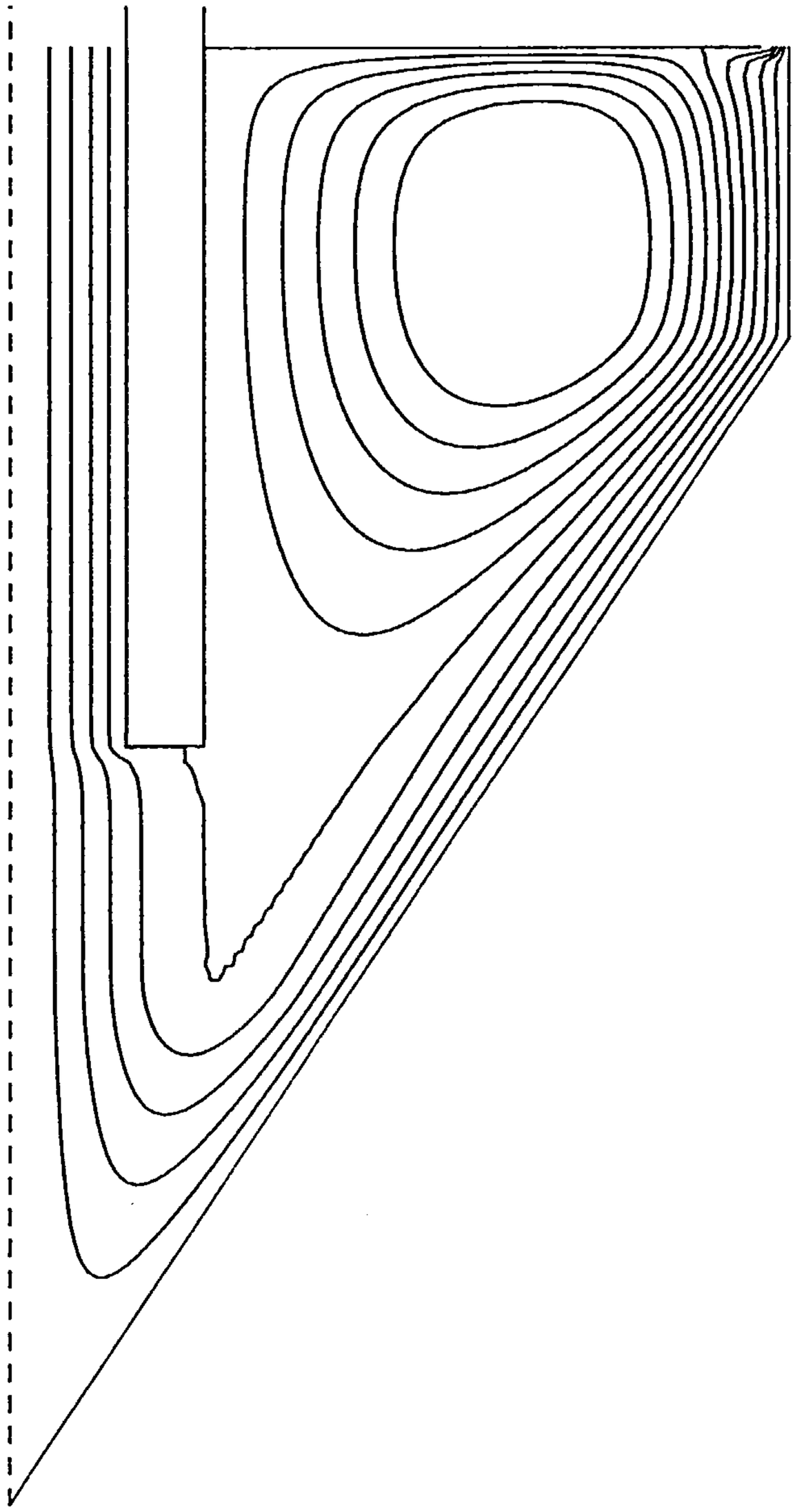

Fig.6.2 The streamlines for Kelsall's work. The values of the lines (from side wall to the axis) are 0.2, 0.4, 0.6,..., respectively.

at the periphery of the cyclone, in relation to the mean spin velocity at entry, a loss factor of about 0.6 must be introduced. This loss factor is a well known parameter, as we mentioned in

chapter 1, and is primarily associated with the sudden expansion of the flow at the inlet to the cyclone and the friction at the solid walls of the cyclone. An accurate estimate of this loss factor is clearly extremely important if the flow model is to accurately predict the separation efficiency of the cyclone.

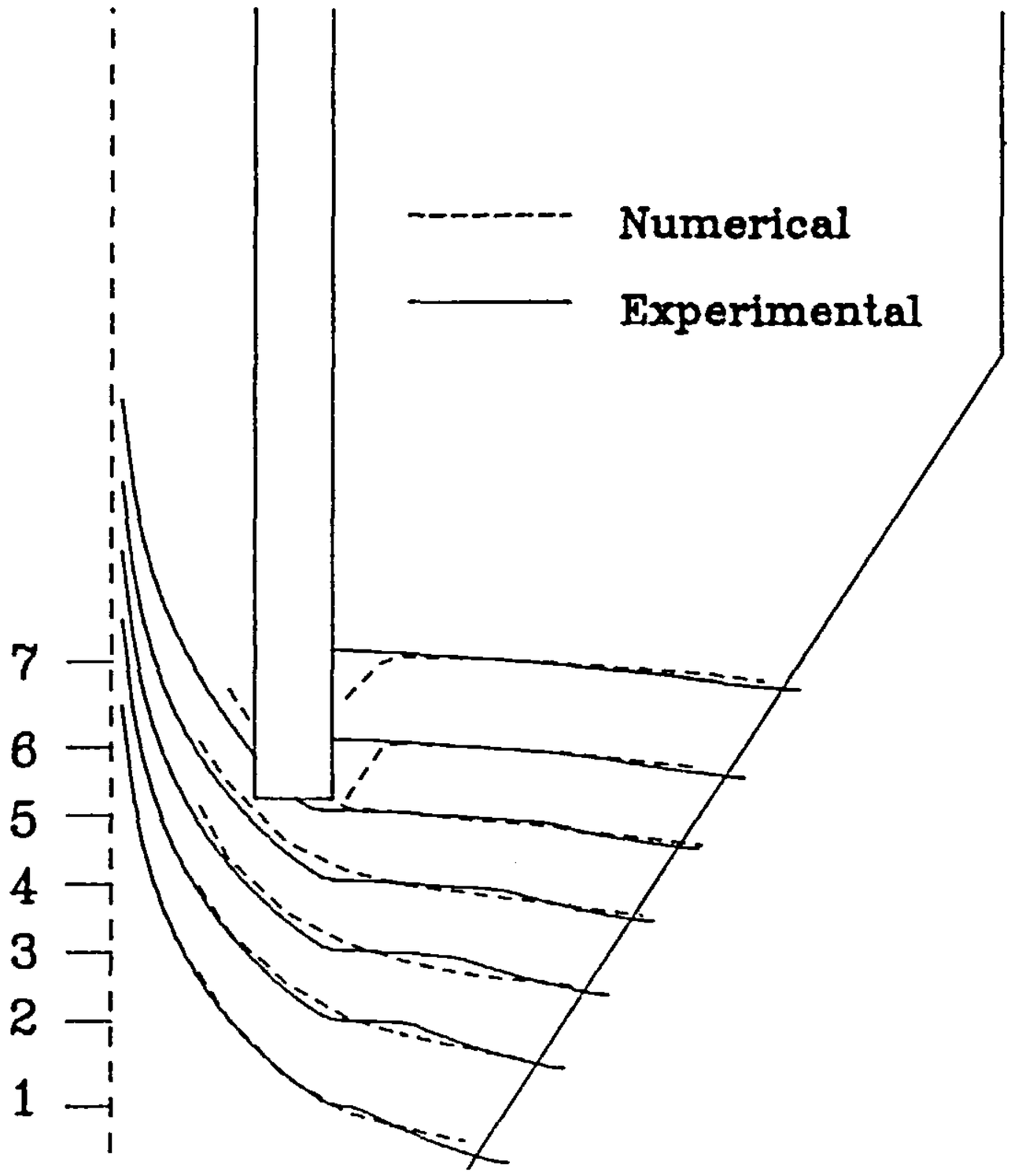

Fig.6.3 The vertical velocity of Kelsall's work.

Fig.6.4 gives the numerically predicted variation of the separation efficiency of the cyclone as a function of the particle size for Kelsall's operating conditions and geometry with a loss factor of α=0.6. It is found that $d_{50}\approx 7.0\mu$, and this compares reasonable well with the experimentally predicted value of about 10μ

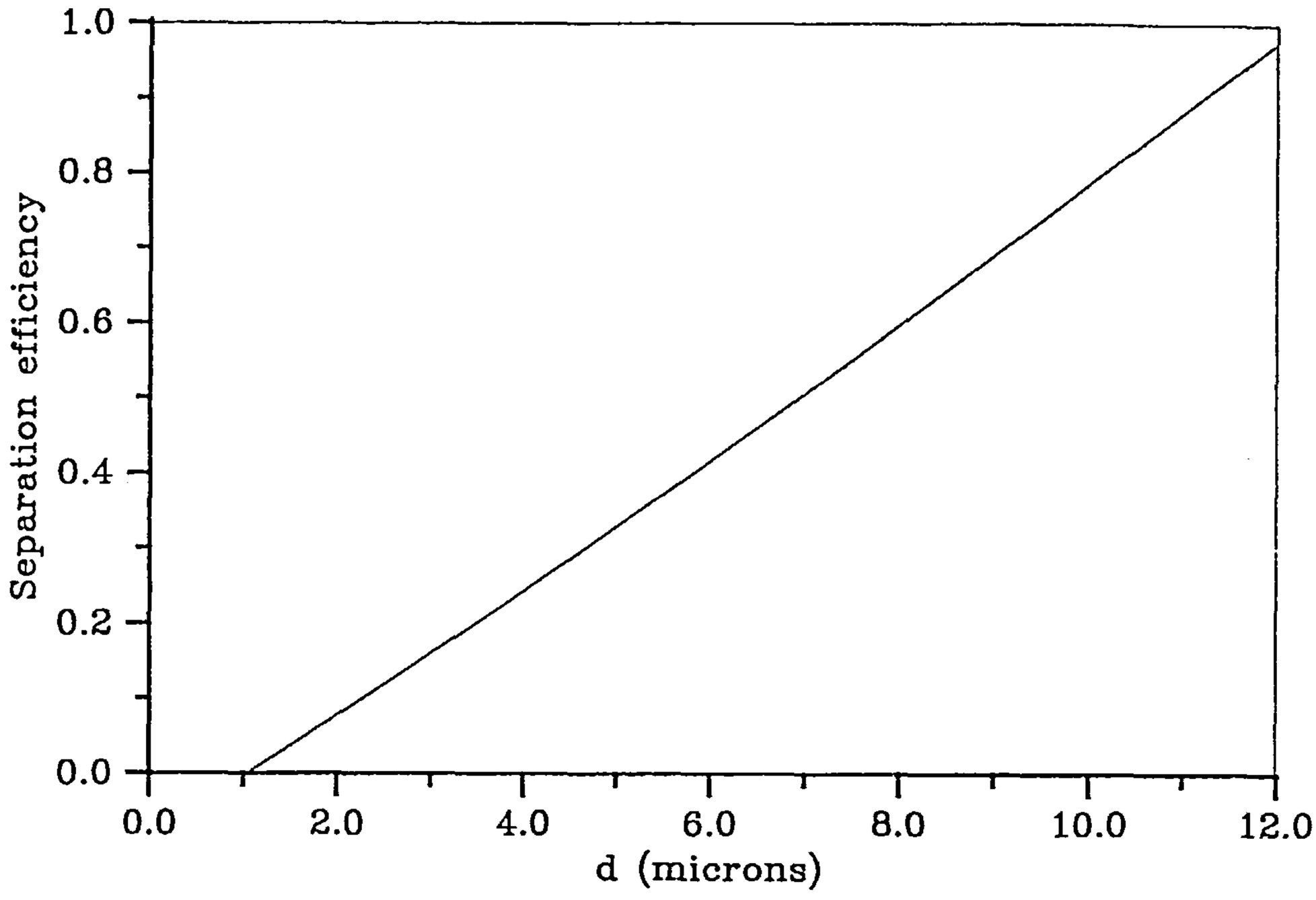

Fig.6.4 The efficiency curve for Kelsall's work with n=1.0.

and the difference between the these values is probably due to the exclusion of the boundary layers in this model. A consequence of this is an absence of the leakage effect, as we assumed earlier, and this will result in a smaller value of d_{50}. Another important factor is the assumption of the free vortex flow, as given by equation (6.3.1), which, although being a reasonable assumption for the flow where the separation is taking place, will result in a slightly improved separation efficiency when viscous effects are taken into account. Physically, the spin velocity profile near the axis of the cyclone is no longer given by equation (6.3.1) but tends to be solid body rotation.

6.6.2 The Influence of Different Choices of $C(R_E)$

As stated in section 6.2, all the boundary conditions except the choice of $C(R_E)$ can be easily determined by either the geometry of the cyclone or the property of the flow. Although the choice of $C(R_E) = \frac{1}{R_E}$ gives reasonable agreement with Kelsall's experiments it is still necessary to see how much influence different choices of $C(R_E)$ have on both the flow structure and the separation efficiency.

Since we require $C(R_E) > 0$, in order that $C\frac{dC}{dR_E} < 0$ then $C(R_E)$ must increase as R_E decreases. Hence we solve equation (6.2.23) with $C(R_E)=\left(\frac{1}{R_E}\right)^n$ and n=0.5, 1.0 and 2.0.

Figs.6.5, 6.2 and 6.6 show the streamlines for n=0.5, 1.0 and 2.0, respectively. It can be seen that the larger the value of the index n then the higher is the density of streamlines near the side wall of the cyclone. This is because the larger the value of n, then the higher is the value of $C\frac{dC}{dR_E}$, i.e. the larger the value of the vorticity present at the entry of the cyclone leading to a thinner jetting flow. Furthermore, the value of A_1 is smaller and a stronger recirculation region develops.

As a result of the different flow structures for different values of n, different separation efficiencies result. Fig.6.7 shows the efficiency curves for n=0.5, 1.0 and 2.0 with a loss factor 0.6. The value of d_{50} for n=0.5, 1.0 and 2.0 are found to be 7.3μ, 7.0μ and 6.1μ respectively. It is clear that a small perturbation in the angular momentum at entry does not affect the separation efficiency significantly but the efficiency is better the larger the value of n. However, a further increase in the value of n gives a significant change in the flow field because of the large amount of vorticity

present at the entry to the cyclone, therefore a large value of n may not be suitable.

Physically, from the few experimental investigations available, see for example ter Linden (1949), Kelsall (1952), Ohsai and Maeda

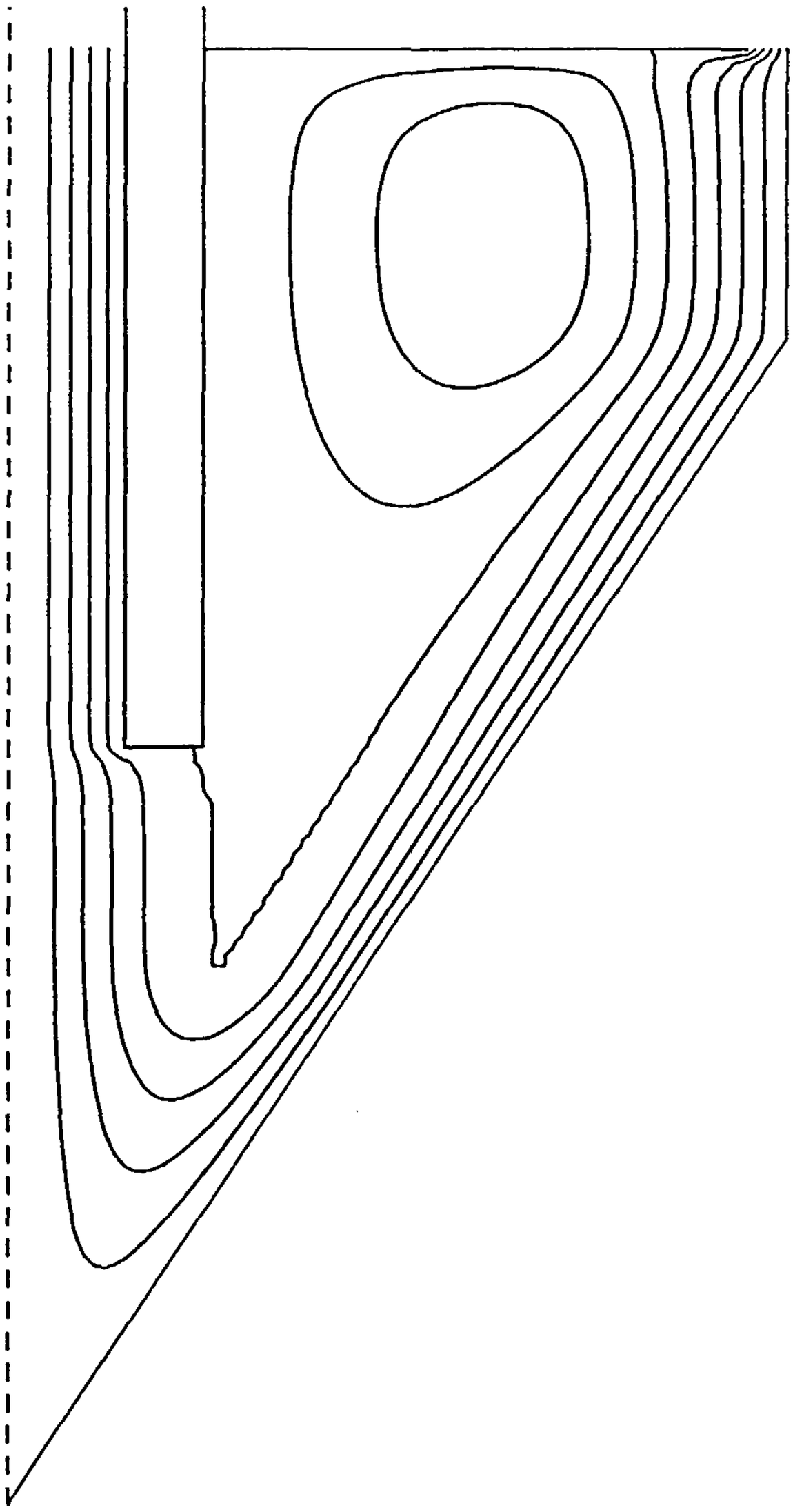

Fig.6.5 The streamlines for Kelsall's work with n=0.5. The values of the lines (from side wall to the axis) are 0.2, 0.4, 0.6,..., respectively.

(1959) and Knowles and Woods (1973), in which the velocity distributions are shown, it is unlikely that the vertical velocity near the side wall in the cylindrical portion of the cyclone is very large and this therefore suggests that a smaller value of n should be used than that used in **Fig.6.6.**

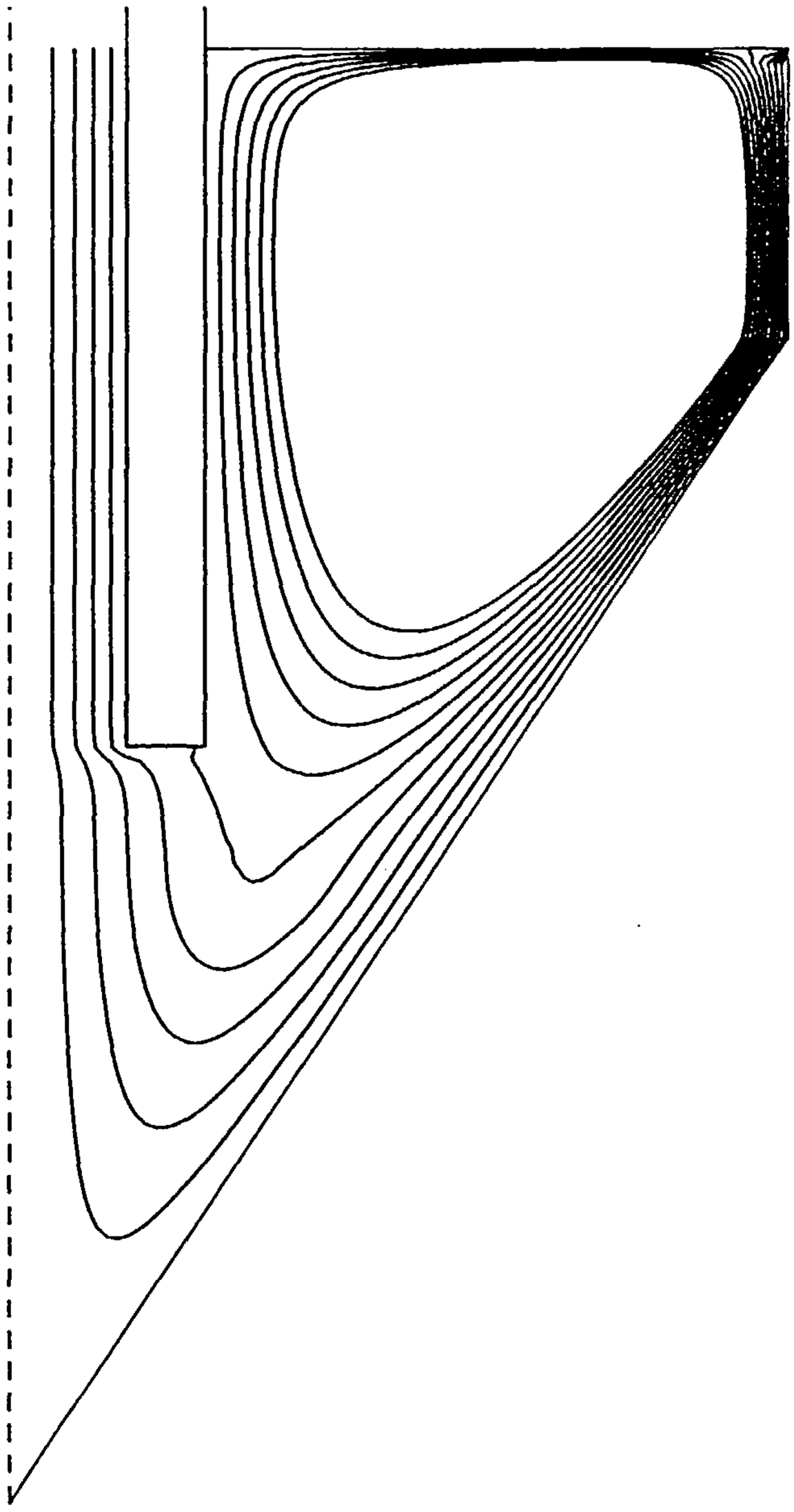

Fig.6.6 The streamlines for Kelsall's work with n=2.0. The values of the lines (from side wall to the axis) are 0.2, 0.4, 0.6,..., respectively.

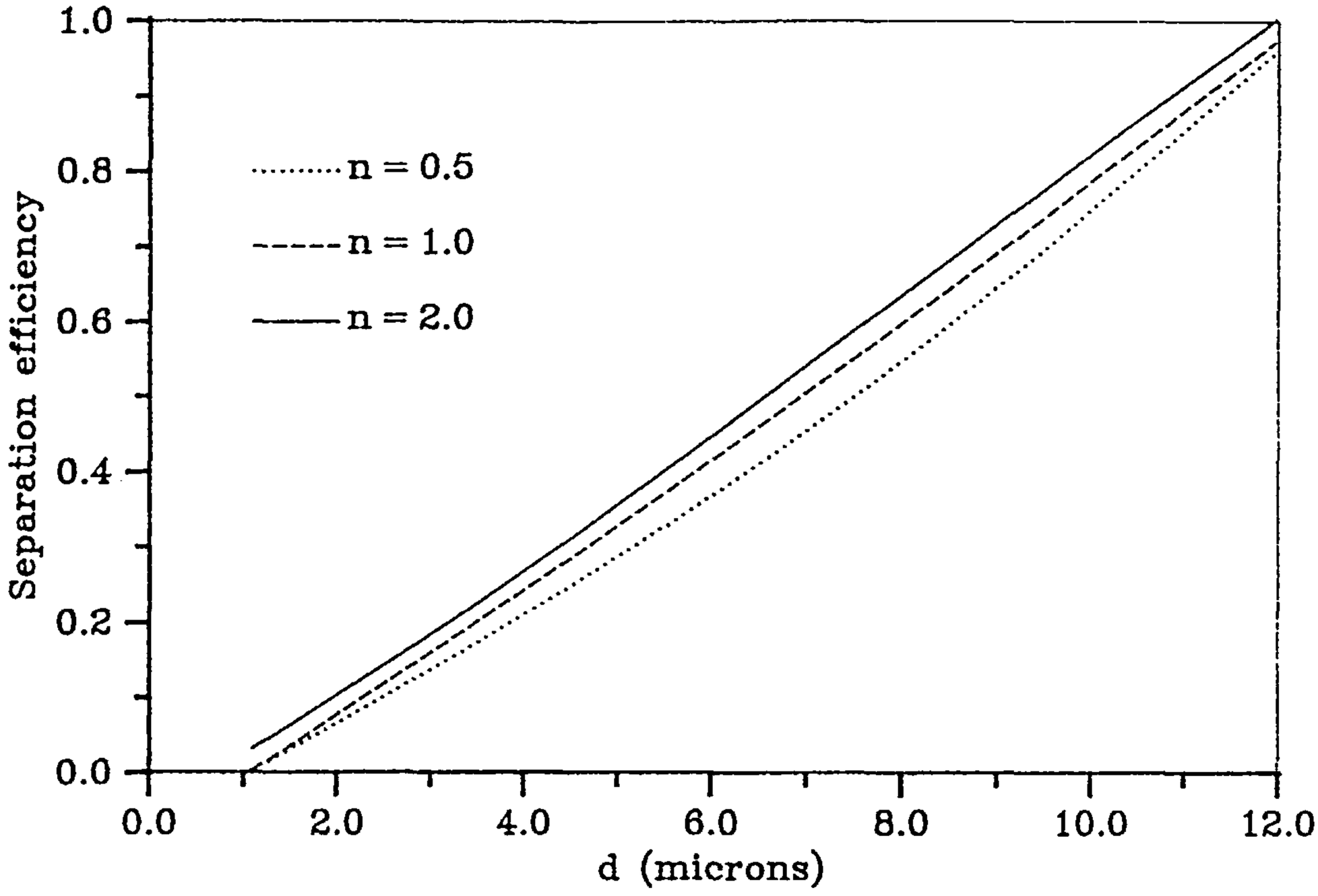

Fig.6.7 The efficiency curves for Kelsall's work with n=0.5, 1.0 and 2.0

We conclude that although the different values of n in the angular momentum result in some changes in the flow structure, their influence on the separation efficiency remains small. At this stage one may ask how much influence do the different estimates of vorticity in the recirculation region have on the flow structure and the separation efficiency of the cyclone.

6.6.3 The Estimation of the Vorticity in the Recirculation Region

Here we investigate the influence of different estimates of the vorticity in the recirculation region on the flow field and the separation efficiency. Three methods have been employed to estimate the vorticity in the recirculation region. First, similar to that

described by Ferguson (1989) we take $R_\xi=R_c/2$, $S_v=\pi(R_c/2)^2$, $V_\xi=V_0$ and $\int_s ds=\pi R_c/2$ in equation (6.2.19), and secondly we estimate the integration on the right hand side of equation (6.2.18) by numerical integration and use this value when equation (6.2.23) is being solved. The flow streamlines for the two methods are shown in Figs.6.8 and 6.9, respectively.

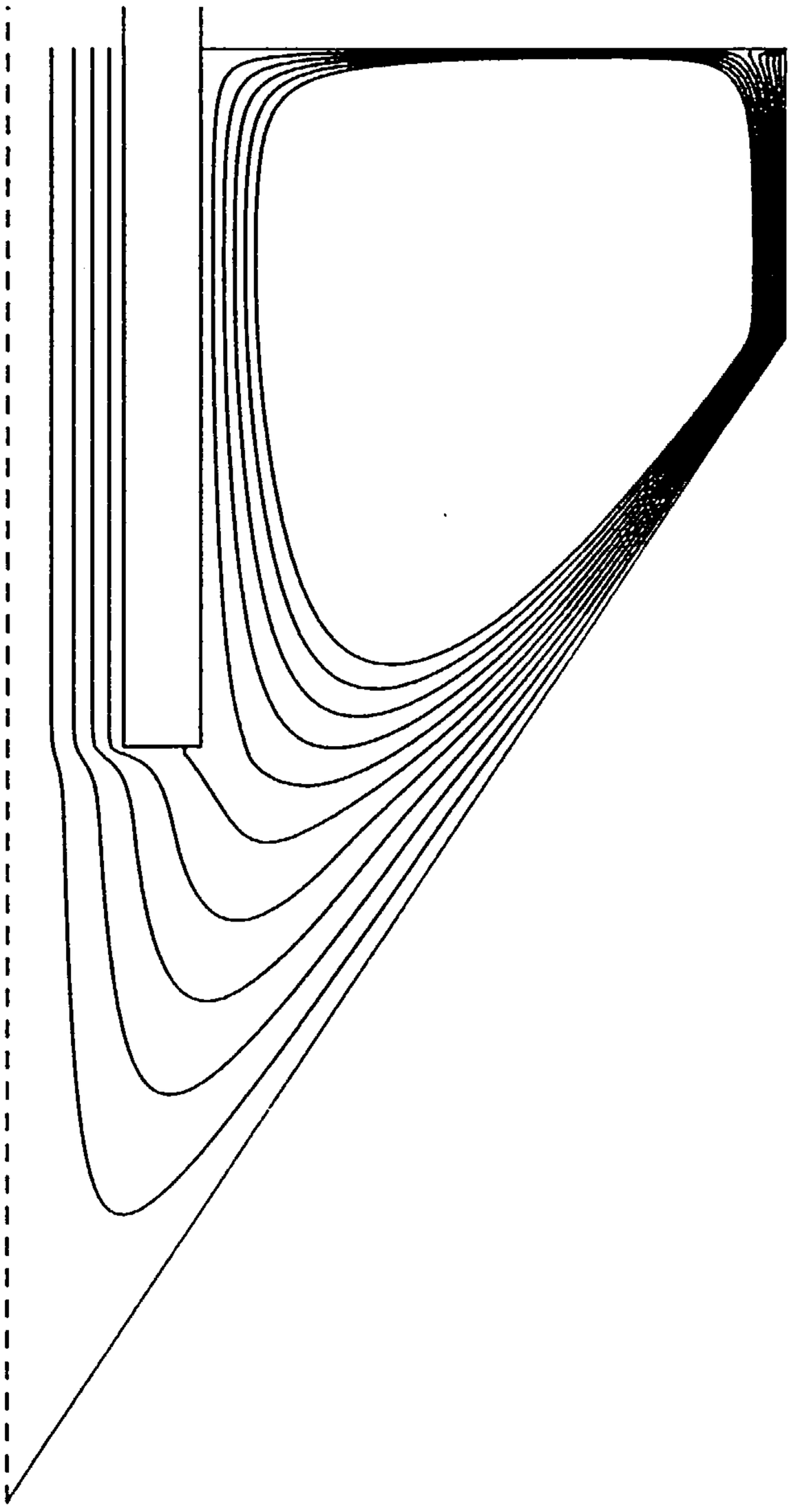

Fig.6.8 The streamlines for Kelsall's work with n=1.0 and $R_\xi=R_c/2$. The values of the lines (from side wall to the axis) are 0.2, 0.4, 0.6,..., respectively.

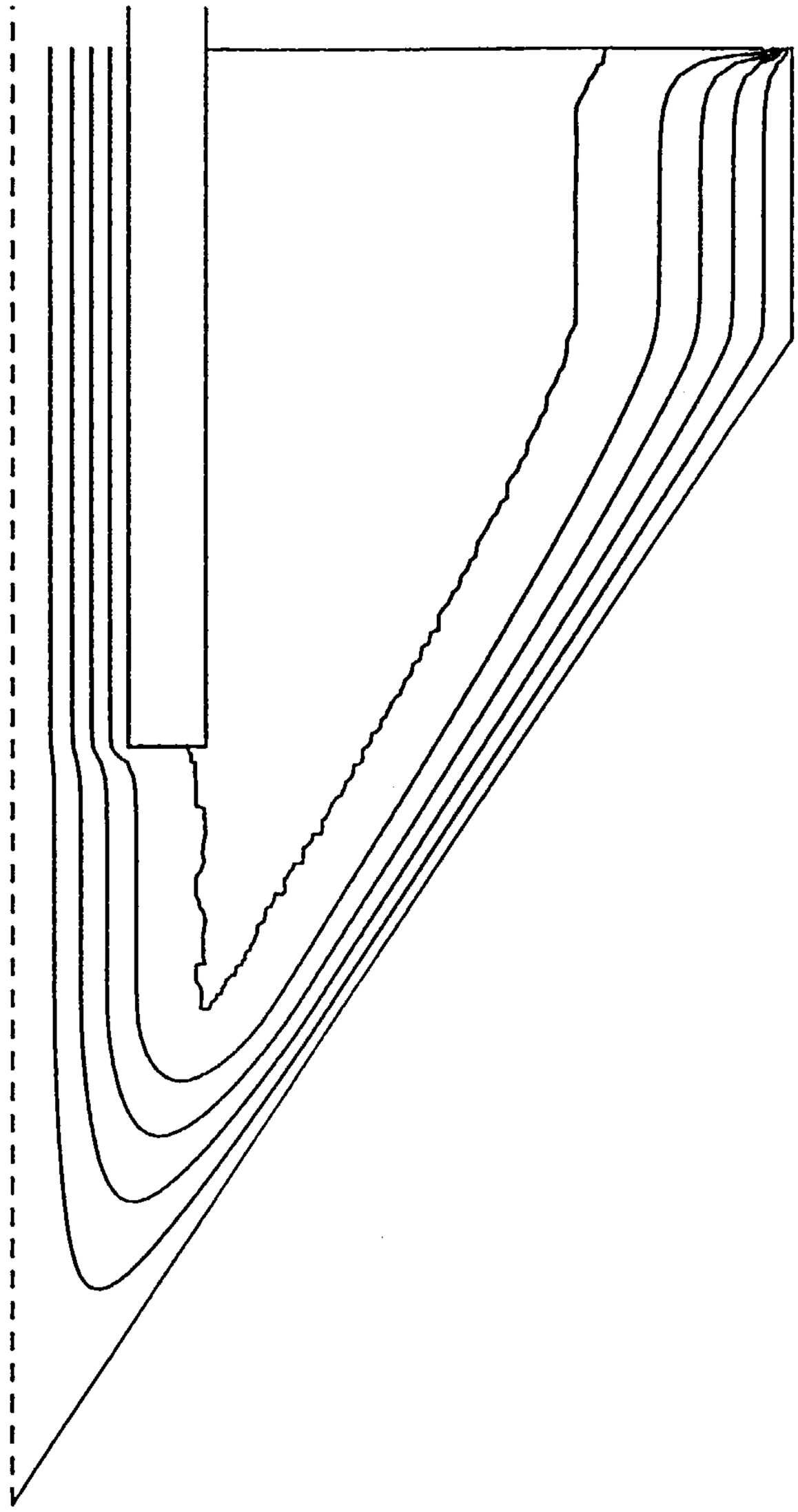

Fig.6.9 The streamlines for Kelsall's work with n=1.0 and the vorticity in the recirculation region determined by computer. The values of the lines (from side wall to the axis) are 0.2, 0.4, 0.6,..., respectively.

It is clear that the first estimate gives a stronger recirculation region than that obtained by the second method. The result obtained using the method described by Ferguson (1989), i.e.

the third method, shown in **Fig.6.2**, lies between these two solutions. In comparison with the experimental data (see Kelsall (1952)) it is postulated that the first and the third estimates overestimate the level of the vorticity and that the second method is more appropriate. **Fig.6.10** shows the efficiency curves corresponding to all the three estimates for the vorticity and it is observed that there is very little difference in the resulting separation efficiencies. So at this stage we may postulate, without considering the other operating conditions, that the separation efficiency is unlikely to be very sensitive to the estimates of the vorticity in the recirculation region.

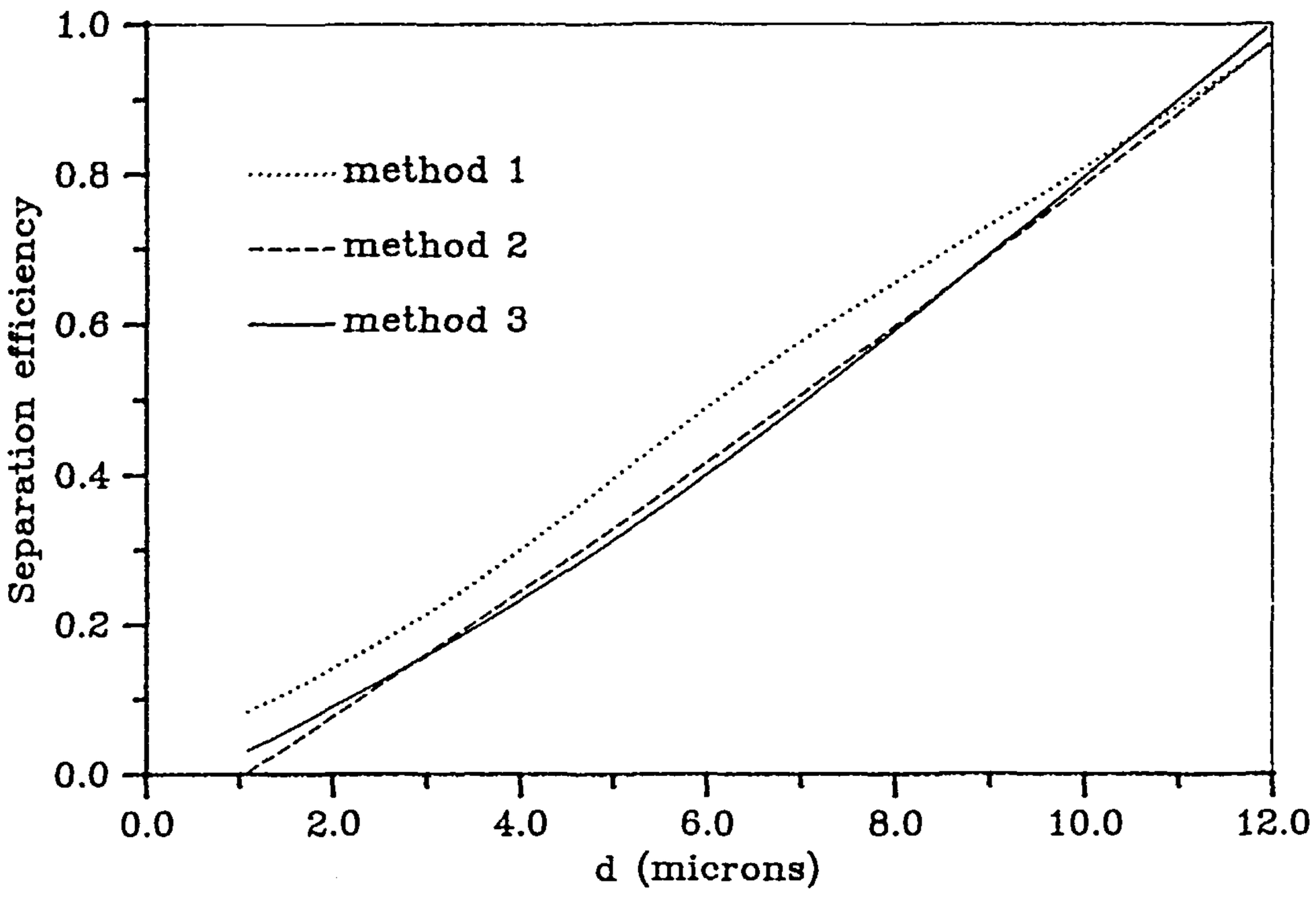

Fig.6.10 The efficiency curves for different estimations of vorticity in the recirculation region (n=1.0).

6.7 Conclusions

An accurate numerical model for the simulation of very high Reynolds number flow in the cyclone has been developed and theoretical efficiency curves have been given which are in good agreement with some experimental data. The influence of different estimates of the vorticity in the recirculation region on the velocity distributions and the separation efficiency has also been investigated numerically and it is found that there is very little difference in the separation efficiency among the results obtained with the 3 estimates we described in section 6.6.3. Furthermore, it has been found that the assumed functional form of the angular momentum given to the fluid at entry is well described in this model, as any small perturbation does not induce a dramatic change to the separation efficiency in the main body of the cyclone.

CHAPTER 7 A NUMERICAL INVESTIGATION OF THE CYCLONE EFFICIENCY

7.1 General Consideration

The main purpose of this chapter is to assess the separation efficiency of the cyclone so that the best design of cyclone may be predicted. Although cyclones may be regarded as one of the simplest pieces of equipment for separating solid from a liquid it has numerous geometrical parameters. Hence it may be very costly to perform a series of experiments in order to investigate the influence of the various parameters on the separation efficiency. To the best of our knowledge this kind of systematic test has not been reported but there are some individual reports on certain aspects of the design of the cyclone.

Knowing the influence of different choices of $C(R_E)$ and different estimates of the vorticity in the recirculation region on the velocity distribution and the separation efficiency of the cyclone, it is necessary for us to further numerically investigate how different parameters of the cyclone geometry affect the separation efficiency of the cyclone. So a basic understanding, at least for the model we have used here which is valid at high values of the Reynolds number, of these influences may be reached and hence suggest guidelines for the improvement of the design of the cyclone.

In this chapter we study numerically the influence of the cyclone geometry, operating conditions and similarities of the

cyclone configuration on the separation efficiency of the cyclone so some general parameters which affect the cyclone performance may be identified.

7.2 Effects of the Cyclone Geometry

Although the separation efficiency of the cyclone may be affected by both the cyclone geometry and the operating conditions, it may be wise to investigate the influence of the geometrical parameters on the efficiency first since the influence of the operating conditions can be studied for a given cyclone. So we begin with the influence of the geometrical parameters of the cyclone on the separation efficiency.

As has been observed in section 6.6.2, a higher value of the index n results in a flow structure which may be far from that which occurs in reality. Consequently, throughout this section, equation (6.2.23) is solved with either $C(R_E)=(1/R_E)^{0.5}$ or $C(R_E)=1/R_E$ and the parameters used are based on Kelsall's (1952) work with a high flow rate, i.e. series *I* of his experiments, unless stated otherwise. It will be seen that the two choices of $C(R_E)$ have only a small influence on the separation efficiency, but, as we have seen in section 6.6.2, the separation efficiency for $C(R_E)=1/R_E$ is higher than that for $C(R_E)=(1/R_E)^{0.5}$ in almost all situations for Kelsall's work (1952).

7.2.1 Influence of the Cyclone Diameter

Changing only the length of the vortex finder to two thirds of that in Kelsall's work, we use three values of R_c to test how the efficiency changes with the cyclone radius. We take R_c to have the

values $0.5R_{ck}$, $1.0R_{ck}$ and $1.5R_{ck}$, where R_{ck} is the radius of the cyclone used by Kelsall (1952). The resulting efficiency curves for $C=(1/R_E)^{0.5}$ are plotted in Fig.7.1. It is obvious that a cyclone

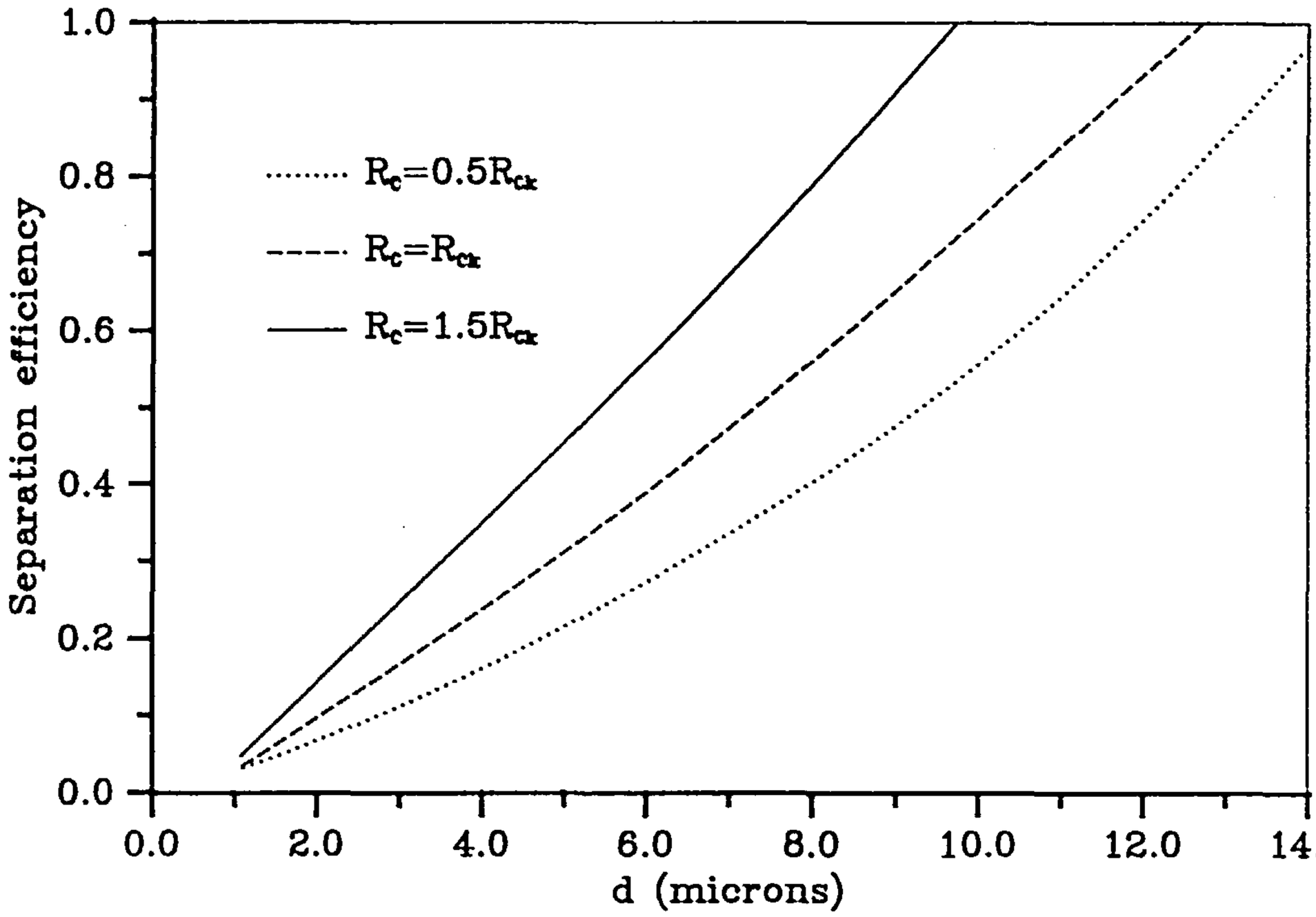

Fig.7.1 The efficiency curves for different R_c (with n=0.5 and all other parameters fixed).

with a smaller diameter gives a lower efficiency. The fifty percent cut size, d_{50}, for these three cyclones with $C=1/R_E$ are 9.4μ, 7.0μ and 5μ, respectively; and for $C=(1/R_E)^{0.5}$ are 9.3μ, 7.3μ and 5.6μ. Bradley (1958) gives the following empirical formula for d_{50}:

$$d_{50}=2.7\left[\frac{\tan(\alpha^*/2)\mu(1-R_f)}{2R_c Q(\rho_p-\rho)}\right]^{1/2}\frac{2.3D_o}{R_c}\frac{D_i^2}{\alpha} \qquad (7.2.1)$$

where α^*, D_i, μ and R_f are the full angle of the cyclone, inlet diameter, fluid viscosity and the ratio of the underflow to total flow rate, respectively. It can be shown from formula (7.2.1) that

$d_{50} \propto 1/R_c$. Our results here confirm this behaviour and any differences may be due to different loss factors, underflow rates and the neglect of any overflow leakage.

7.2.2 Influence of the Length of the Conical Portion

We now investigate the influence of the length of the conical portion of the cyclone on the separation efficiency. Again three values of the length of the conical portion, Z_c, were chosen, namely Z_c=0.15, 0.2161 (the value used by Kelsall) and 0.3. The resulting values of d_{50} are shown in Table 7.1.

Z_c		0.15	0.2161	0.3
$d_{50}(\mu)$	n=0.5	9	7.3	6.2
	n=1	8	7	6
	Eqn. (7.2.2) (m=0.8)	11.6	9.7	8.2

Table 7.1: d_{50} for different lengths of the conical portion of the cyclone.

In another attempt to find d_{50} empirically, Bradley and Pulling (1959) used the formula,

$$d_{50}=3.2(0.43)^m \frac{D_i}{\alpha}\left[\frac{\tan(\alpha^*/2)\mu(1-R_f)}{2R_c Q(\rho_p-\rho)}\right]^{1/2} \qquad (7.2.2)$$

where m is a constant which is to be determined by the performance of the cyclone.

It is noted that $R_c=Z_c\tan(\alpha^*/2)$, so expression (7.2.2) is in fact independent of R_c and α^* and hence $d_{50} \propto (1/Z_c)^{1/2}$. Hence a

longer conical portion gives a higher efficiency, and from Table 7.1, we observe that the change of d_{50}, with varying values of Z_c, is in reasonable agreement with that given by Bradley and Pulling (1959). The value of d_{50} as obtained using equation (7.2.2) with R_f=0, m=0.8 and α=0.6 is also shown in Table 7.1 where one can see that there is a reasonable agreement between the present numerical results and those obtained from the empirical formula (7.2.2). The differences may be due to the use of the wrong values of the loss factor and/or the parameter m. Another reason for the differences may be due to the exclusion of the influence of α^* and R_c. This may not be true since if one attempts to increase the efficiency of the cyclone by increasing Z_c only, and with R_c being very small, then the efficiency may not continue to increase as an over long conical portion increases the losses in energy.

7.2.3 Influence of the Angle of the Cyclone

It is now straightforward to discuss the influence of the cyclone angle, α^*, on the efficiency. Changes of the cyclone angle may be done in two ways: namely change R_c with Z_c fixed or change Z_c with R_c fixed. So what we require is to find the influence of the cyclone diameter and the influence of the length of the conical portion in terms of the angle of the cyclone.

In section 7.2.1, we investigated three values of R_c which corresponded to values of the cyclone angle α^*= 10.1°, 20° and 29.6°, respectively, whilst the three values of Z_c, in section 7.2.2, correspond to α^*=28.5°, 20° and 14.5°, respectively. Table 7.2 shows the separation efficiency for the different cyclones with these different angles.

$\alpha^*(^\circ)$		10.1	14.5	20.0	28.5	29.6
$d_{50}(\mu)$	n=0.5	9.3	6.2	7.3	9.0	5.6
	n=1	9.4	6.0	7.0	8.0	5.0
	eqn (7.2.1)	17.5	8.8	5.8	10.5	7.4

Table 7.2: d_{50} cut size for different cyclone angles.

The results are significantly different to those predicted by equation (7.2.2). As mentioned earlier, equation (7.2.2) is an angle free formula so if it is applied here then all the efficiencies with the same Z_c will be the same provided the loss factors are the same. Hence we obtain d_{50} from equation (7.2.1) and the results are shown in Table 7.2 and this shows that there is no clear tendency as to how, in general, α^* affects the efficiency. So we conclude the following:

d_{50} decreases as α^* increases by means of increasing the diameter of the cyclone;

d_{50} increases as α^* increases by means of decreasing the length of the conical portion of the cyclone.

From equation (7.2.1), $d_{50} \propto 1/(R_c Z_c^{1/2})$ which is, to some extent, in reasonable agreement with the results obtained here.

7.2.4 Influence of the Length of the Cylindrical Portion of the Cyclone

There are only a few investigators who have looked at the

influence of the length of the cylindrical portion of the cyclone on the separation efficiency. However, since the separation does occur, more or less, in this part of the cyclone it is worth investigating numerically this influence on the separation efficiency. In this section we will consider the cylindrical portion to have lengths $h_0=0.5h_{0k}$, h_{0k} and $1.5h_{0k}$, where h_{0k} is the length used by Kelsall (1952). All other parameters are the same as those used by Kelsall (1952) and we investigate the influence of this length on the separation efficiency of the cyclone. Table 7.3 shows the value of d_{50} for the different values of h_0 and index n.

h_0		$0.5h_{0k}$	h_{0k}	$1.5h_{0k}$
$d_{50}(\mu)$	n=.5	7.3	7.3	7.2
	n=1.	6.5	7.0	7.0

Table 7.3: d_{50} for different lengths of the cylindrical portion of the cyclone.

It is concluded that the effect of changing h_0 is quite negligible and this has been observed experimentally (see, for example, Bradley (1958) and Bradley and Pulling (1959) where the formulae (7.2.1) and (7.2.2) for d_{50} are independent of the value of h_0). Fig.7.2 shows the efficiency curves for $C=1/R_E^{0.5}$ and $1/R_E$ for these three values of h_0. It is clear that the influence of h_0 is small on the separation efficiency for all values of the particle diameters (not just d_{50}) and this influence may therefore be neglected.

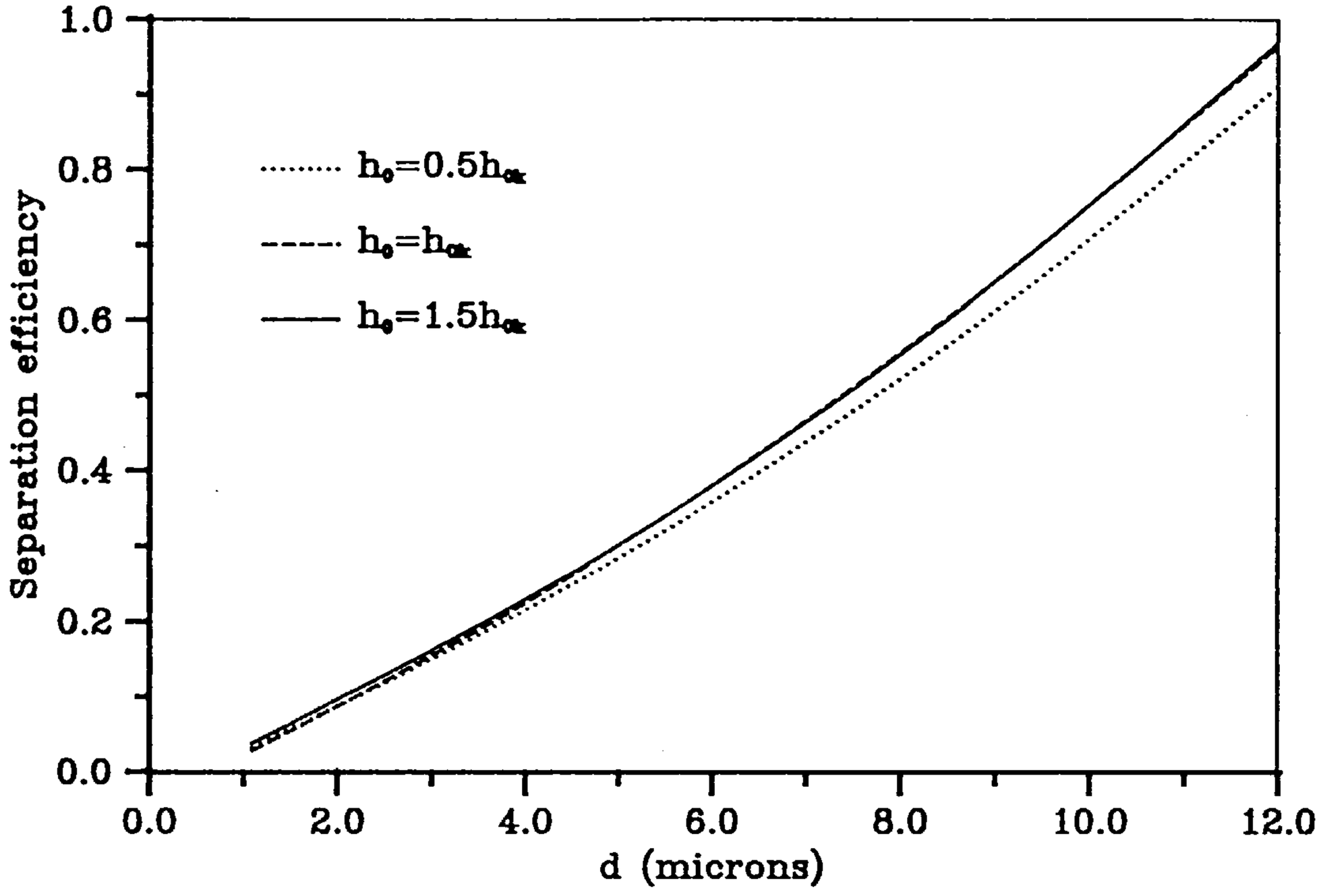

Fig.7.2 The efficiency curves for three different lengths of cylindrical portion.

7.2.5 Influence of the Length of the Vortex Finder

It is known that the length of the vortex finder, h_1, plays an important role in the cyclone performance and the influence of it on the separation efficiency of the cyclone is now investigated. Again three values of h_1 are taken, namely $h_1=h_k/3$, $2h_k/3$ and h_k where h_k is the value of h_1 used by Kelsall (1952). The value of d_{50} obtained is approximately the same in all cases, e.g. 7μ for $C=1/R_E$ and 7.3μ for $C=(1/R_E)^{0.5}$, but this may be due to the exclusion of the overflow leakage. A longer vortex finder gives particles more chance to be separated and a small amount of leakage and that is why an appropriately longer vortex finder gives a higher efficiency in practice. However an overlong vortex finder will increase the energy losses and therefore will decrease the efficiency.

7.2.6 Influence of the Overflow Radius

Three values of the overflow radius were taken in order to investigate its influence on the efficiency, namely $0.5R_{ok}$, R_{ok} and $1.5R_{ok}$, where R_{ok} is the radius of the overflow tube used by Kelsall (1952). The numerical estimates obtained for d_{50} are shown in Table 7.4.

R_o		$0.5R_{ok}$	$1.0R_{ok}$	$1.5R_{ok}$
$d_{50}(\mu)$	n=.5	6.7	7.3	8.0
	n=1.	6.5	7	7.5

Table 7.4: d_{50} for different overflow radius.

Hence the smallest overflow radius gives the highest efficiency and a further decrease in the overflow radius suggests an even higher

efficiency. This is not true in practice because near the axis of the cyclone the viscosity of the fluid becomes more important and the flow rotates as a solid body and the spin velocity tends to zero as R tends to zero. This contradicts the free vortex model assumed here where the spin velocity tends to infinity as R tends to zero.

7.3 The Influence of the Operating Conditions

In this section we investigate how different operating conditions, e.g. flux rates for a given spin velocity and for a given inlet area, affect the separation efficiency for a given cyclone. This time all the results were only obtained with $C(R_E)=(1/R_E)^{0.5}$ since we have seen that the difference between the results obtained using $C=(1/R_E)^{0.5}$ and those obtained using $C=1/R_E$ are insignificant in all the cases considered.

7.3.1 Different Flux Rates for a Given Spin Velocity at Entry

When the spin velocity at the entry is given, an increase in the flux rate means increasing the inlet area. Thus the flow field and the efficiency will be changed because the right hand side of the equation (6.2.23) is a function of D_i. The three flux rates used for the numerical investigation were $Q=Q_k$, $Q=2Q_k$ and $Q=3Q_k$, where Q_k is the flux rate used by Kelsall (1952). **Fig.7.3** gives the cyclone efficiency as a function of the particle size and it is observed, maybe surprisingly, that a larger flux rate gives a lower efficiency. It should be noted that increasing the separation efficiency by means of increasing the flow rate is true only when the spin velocity at the entry also increases at the same time.

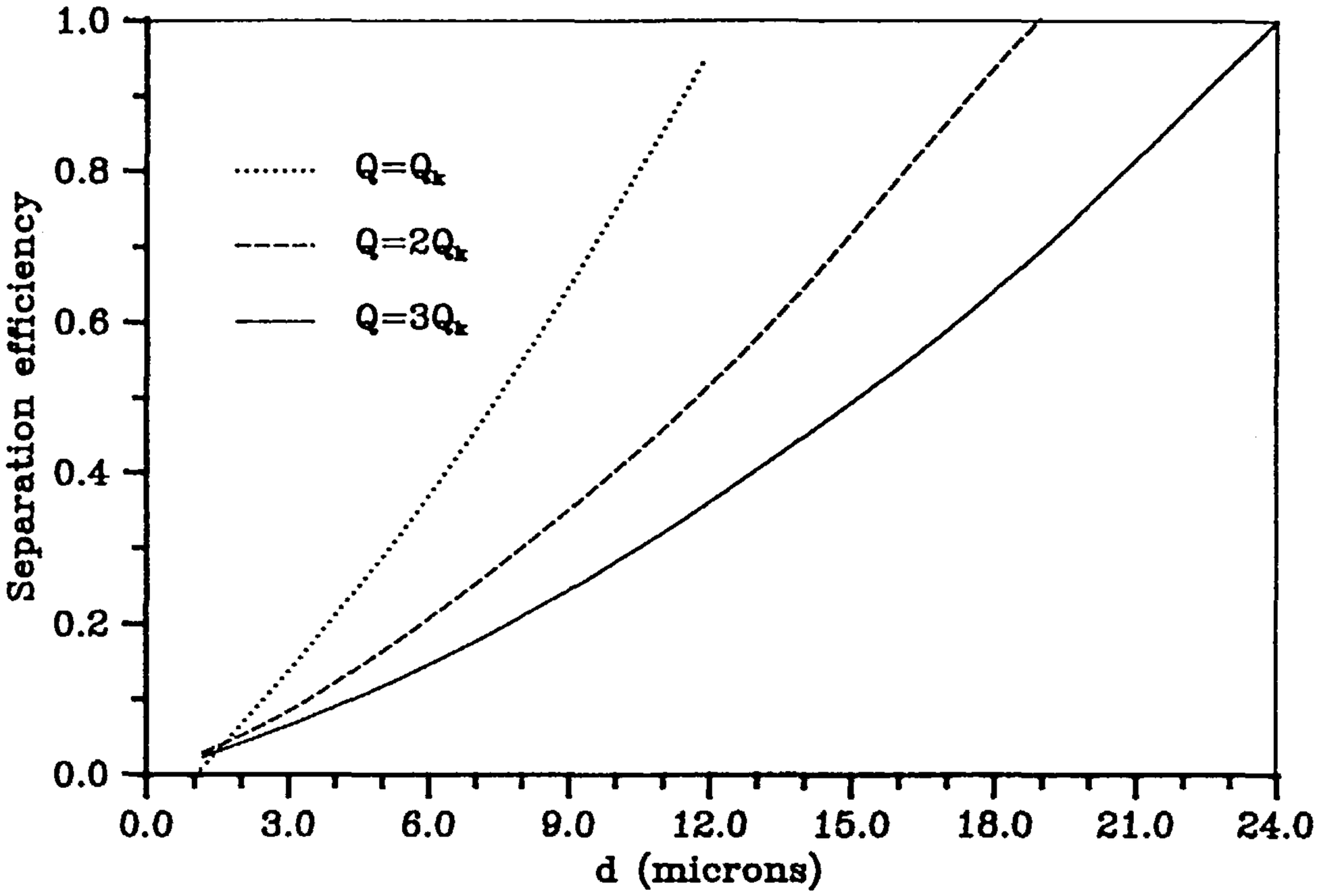

Fig.7.3 The efficiency curves for 3 different flow rates with W_0 unchanged (n=0.5).

Table 7.5 shows the numerically predicted values of d_{50} and those predicted by equation (7.2.1). Note we have taken the value predicted by equation (7.2.1) for $Q=Q_k$ to be 7.3μ and then based on this value worked out values for $Q=2Q_k$ and $Q=3Q_k$. This is because we are mainly interested here in the change in the value of d_{50} with different flow rates and not the exact values of d_{50}. On the other

Q		Q_k	$2Q_k$	$3Q_k$
$d_{50}(\mu)$	Numerical	7.3	11.7	15.0
	Eqn. (7.2.1)	take 7.3	10.3	12.6

Table 7.5: d_{50} for different flow rates.

hand, comparison between the exact values predicted by the numerical method and those predicted by equation (7.2.1) may be meaningless, because the loss factor has been taken to be 0.6 which may not be the real value of the loss factor for the geometry and operating conditions of the cyclone we used here.

We may conclude that increasing the flow rate by increasing only the inlet diameter results in a decrease in the separation efficiency.

7.3.2 The Different Flux Rates for a Given Inlet Area

If the inlet diameter, or more precisely the inlet area, of a cyclone is given, changing the flow rate implies changing the spin velocity at the entry to the cyclone. As will be seen in section 7.4, the cross plane flow streamlines do not depend on Q but the efficiency will improve, in this case, since increasing the flow rate by a factor δ would result in an increase in the spin velocity at the cyclone entry by a factor δ and consequently the value of W_2^2/Q would change by a factor δ. As an example, if Q is doubled then the centrifugal force applied on a particle with the same size would also be doubled so that the separation efficiency in this case would certainly increase. For the numerical test, as in section 7.3.1, the efficiency curves for $Q=Q_k$, $2Q_k$ and $3Q_k$ are plotted in Fig.7.4 and it is observed that the values of d_{50} for Q_k, $2Q_k$ and $3Q_k$ are 7.3μ, 5.3μ and 4.4μ, respectively. In reality it may be expected that the values of d_{50} would be little different from those of d_{50} predicted numerically here since the loss factors for different flux rates will be different.

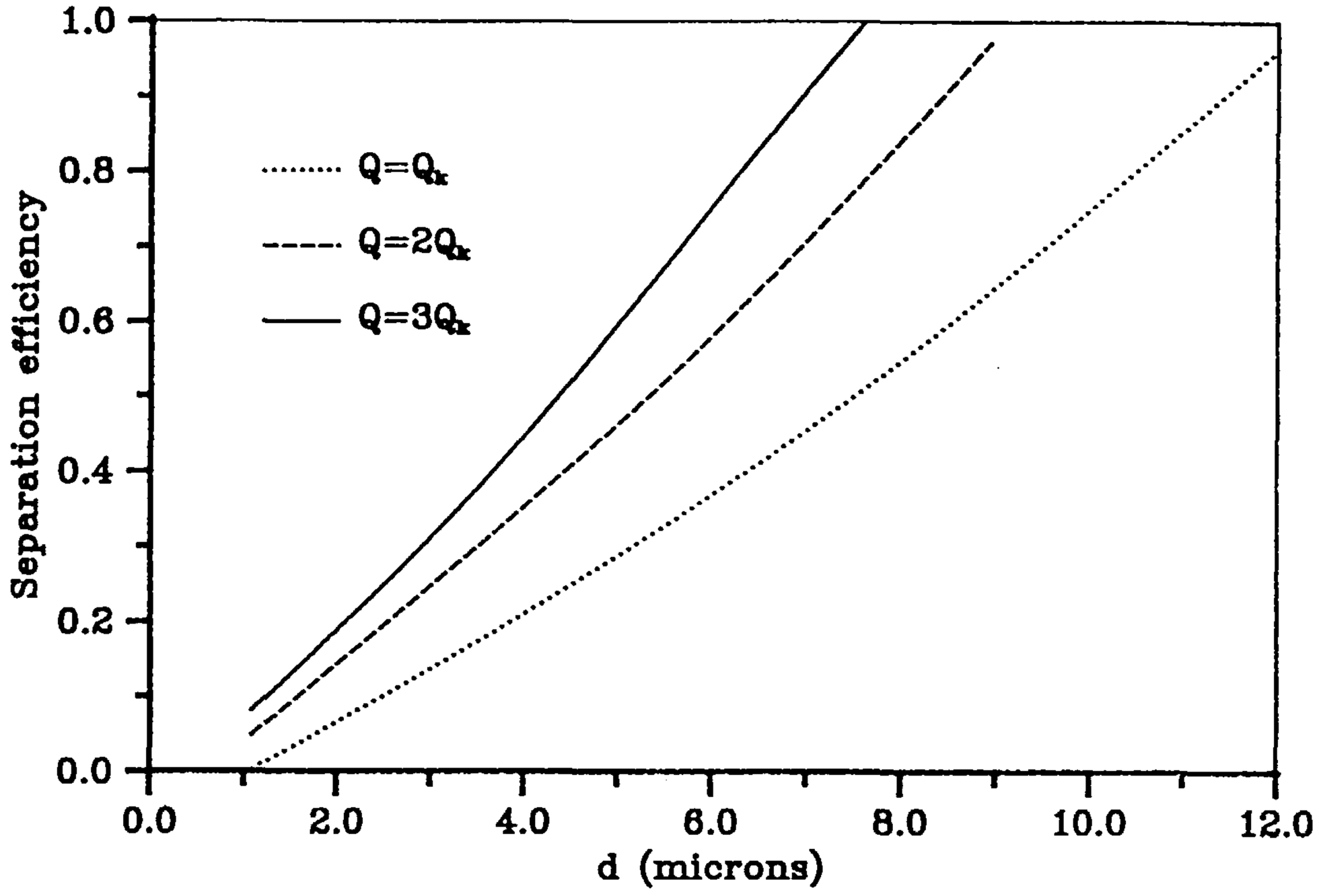

Fig.7.4 The efficiency curves for different flow rates with the cross area of the inlet unchanged (n=0.5).

From this section we conclude that:

(i) increasing the flow rate by increasing the inlet area only gives no improvement in the separation efficiency of a cyclone;

(ii) increasing the flow rate by increasing the spin velocity at cyclone entry results in an increase in the separation efficiency of a cyclone provided that the values of the loss factor are the same for different flow rates and spin velocities at the cyclone entry.

7.4 The 'Similarity' of Cyclones

In this section we assume that the properties of the fluid and particle and the loss factor are unchanged for two cyclones, say

cyclone 1 and cyclone 2 and discuss some problems which are, to some extent, related to the similarity of cyclones or velocities and to investigate how these similarities affect the flow field and the separation efficiency. So a certain kind of performance of a cyclone may be reached for a required separation efficiency.

7.4.1 Effect of Different Flow Rates

Here we investigate differences which may exist in the velocity distributions (u and v) obtained with a flux rate Q_1 compared with a flux rate Q_2. Physically, we expect that any two different flow rates which operate on a given cyclone will yield two different velocity distributions. However, the mathematics predicts that, except for the different scales for the two distributions, the non-dimensional velocity distributions are the same for these two flow rates because the resulting governing equations (6.2.23) and boundary conditions (6.2.24)-(6.2.27) are identical and so their solutions are the same.

7.4.2 Two Similar Cyclones

In this section we investigate what kind of operating conditions are required for cyclone 1 and cyclone 2, if:

i) all the geometrical lengths of cyclone 2 are a factor β different from these of the cyclone 1,

ii) the same efficiency is required for the two cyclones.

It can be seen that if the governing equations of (6.2.23) and (6.4.5) for these two cyclones are exactly the same then the efficiencies will also be the same.

First, we assume that the loss factors for these two cyclones

are the same and using subscripts 1 and 2 to denote those quantities in cyclones 1 and 2, respectively, then $\beta=Z_{c2}/Z_{c1}=R_{c2}/R_{c1}=h_{02}/h_{01}=\ldots$, and from (6.2.23) and (6.4.5) we have

$$(W_{01}/Q_1)^2=\beta^4(W_{02}/Q_2)^2 \qquad (7.4.1)$$

$$R_{c1}W_{01}^2/Q_1=\beta R_{c1}W_{02}^2/Q_2 \qquad (7.4.2)$$

i.e.

$$W_{02}=\beta W_{01} \qquad (7.4.3)$$

$$Q_2=\beta^3 Q_1. \qquad (7.4.4)$$

For example if $\beta=2$, then cyclone 2 needs eight times the flux and twice the spin velocity at the inlet to that required in cyclone 1 for same efficiency. This gives us a way of determining how to operate two 'similar' cyclones to obtain the same efficiency, and a way of changing the cyclone geometry without changing the separation efficiency.

Furthermore if there are two different loss factors, α_1 and α_2, for cyclone 1 and cyclone 2, respectively, then equation (7.4.2) becomes

$$\alpha_1^2 R_{c1}W_{01}^2/Q_1=\alpha_2^2\beta R_{c1}W_{02}^2/Q_2 \qquad (7.4.5)$$

which, when combined with equation (7.4.1), gives

$$W_{02}=\frac{\alpha_1^2\,\beta}{\alpha_2^2}\,W_{01} \qquad (7.4.6)$$

$$Q_2=\frac{\alpha_1^2\,\beta^3}{\alpha_2^2}\,Q_1 \qquad (7.4.7)$$

It is now clear from expressions (7.4.6) and (7.4.7) how the loss factor affects the relationship between Q_1, W_{01} and Q_2, W_{02} respectively. A smaller loss factor requires both a larger flux Q_2 and a larger spin velocity at the entry to the cyclone.

7.4.3 Two Cyclones 'Similar' in One Direction

Let us first consider that all the geometrical lengths in the R-direction of cyclone 2 are scaled by a factor β in comparison to those of the cyclone 1 whilst in the z-direction both cyclones have the same dimensions. We now investigate the effect of β on the cyclone efficiency given that the flow rate and the loss factors for these two cyclones are the same.

For the numerical investigation, we take Kelsall's (1952) cyclone and consider the effects of scaling all the parameters that occur in the R-direction by a factor β. The numerical predicted efficiency curves for these three cyclones (with $C=(1/R_E)^{0.5}$) are shown in **Fig.7.5**, where cyclone 1, 2 and 3 refer to β=0.5, 1 and 2, respectively. It is clear that the cyclone which is smaller in the R-direction gives a lower efficiency if the total flux through the cyclone is fixed and therefore one can improve the separation efficiency by making the cyclone larger in the R-direction.

Furthermore we consider the efficiencies of similar cyclones for which all the geometrical lengths in the z-direction of cyclone 2 are scaled with the same factor β compared with those of cyclone 1 whilst in the R-direction all dimensions are the same. We now investigate the cyclone efficiency if the flow rates and all other factors for these two cyclone are assumed to be the same. Again, as an example, we take Kelsall's cyclone and operating conditions.

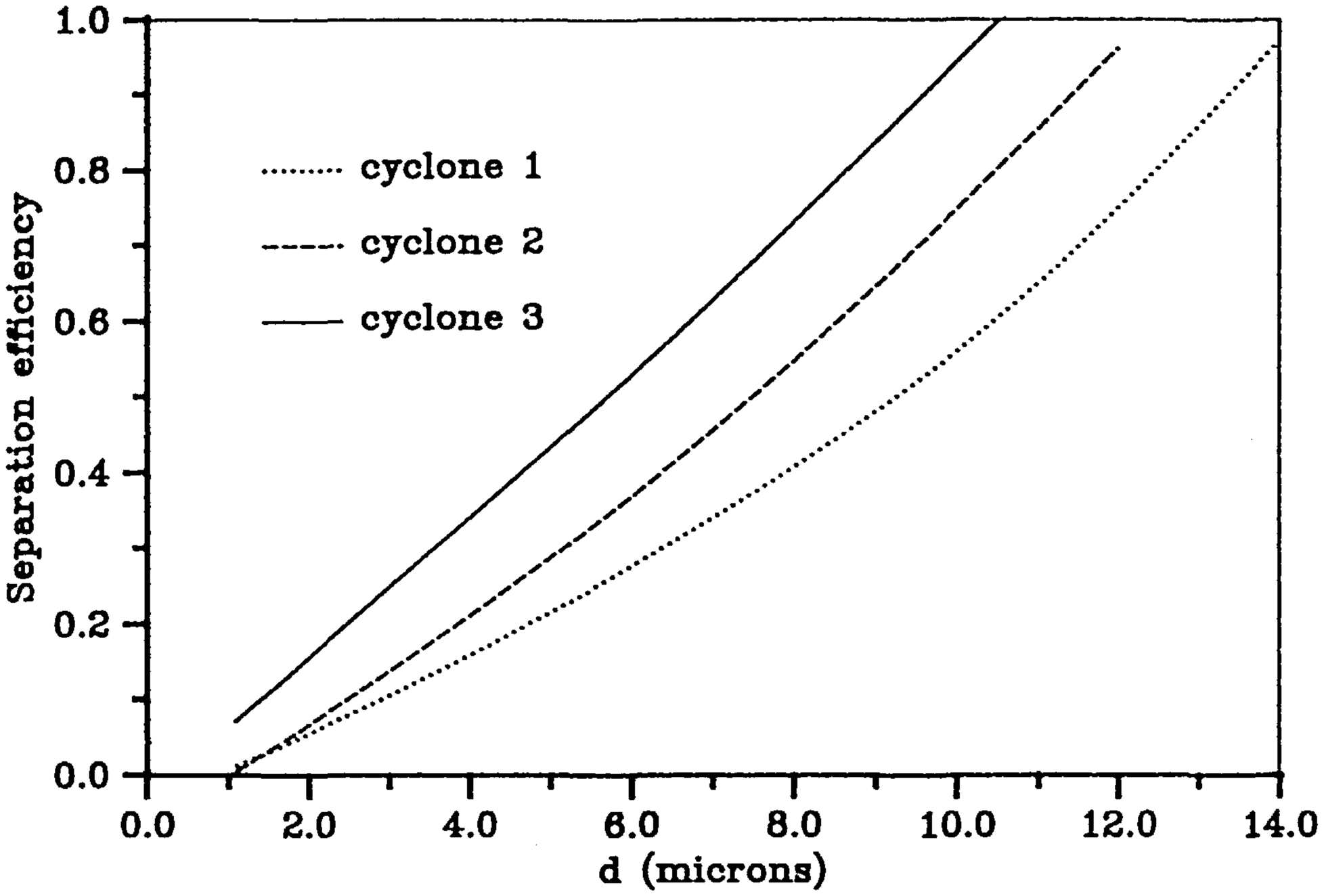

Fig.7.5 The efficiency curves for different cyclones which are similar to each other in the R-direction (n=0.5).

Using Z_k to denote a typical length in the z-direction in Kelsall's cyclone, then the above three cyclones have the lengths of $0.5Z_k$, $1.0Z_k$ and $1.5Z_k$ in the z-direction. The numerical predicted values of d_{50} for these three cyclones with $C=(1/R_E)^{0.5}$ are shown in Table 7.6. So the longer the cyclone the more efficient it is. This is because a longer cyclone gives the particles more opportunity to

Z		$0.5Z_k$	$1.0Z_k$	$1.5Z_k$
$d_{50}(\mu)$	n=.5	11	7.3	6.2

Table 7.6: d_{50} for cyclones similar in the z-direction.

be separated. On the other hand, a cyclone with an over long size in the z-direction could cause too much loss of energy as the flow goes down to the cyclone and as a result the separation efficiency may be lower than that predicted here, or in other words the loss factor has increased.

7.5 Conclusions

In this chapter various aspects of the influence of cyclone dimensions, operating conditions and similarities of cyclones on the separation efficiency have been investigated numerically. With the assumption of the validation of the Stokes drag law and a known value of the loss factor the following conclusions may be obtained:

- Increasing the cyclone diameter with all the other parameters remaining unchanged yields an increase in the separation efficiency;
- The length of the cylindrical portion has little influence on the efficiency;
- Increasing the length of the conical portion of the cyclone with all other quantities remaining unchanged gives a higher efficiency;
- For a fixed values of Z_c, d_{50} decreases as α^* increases by means of increasing the cyclone diameter;
- For a fixed cyclone diameter, d_{50} increases as α^* increases by means of decreasing the conical length;
- Increasing the overflow diameter gives a lower efficiency if all other parameters are unchanged;
- Two 'similar' cyclones can give the same efficiency if Q and W_0 are chosen as given in section **7.4** and the overflow

leakage is neglected;

- If two cyclones are 'similar' in the R-direction then the larger the value of R_c, the higher the efficiency;
- If two cyclones are 'similar' in the z-direction then the longer the cyclone, the higher is the efficiency;
- Increasing the flow rate Q by increasing the inlet area does not increase the efficiency if leakage is ignored;
- Increasing the flow rate Q by increasing the inlet spin velocity yields an increase in the efficiency.

CHAPTER 8 AN INVESTIGATION INTO SOME EXPERIMENTAL WORK

8.1 Introduction

Knowing the details of the influence of the cyclone geometry, of the operating conditions and of the similarities on the separation efficiency of the cyclone, we may need to investigate further how the model we used can be applied to cyclones in practice. In this chapter we will investigate some available experimental data in which the full dimensions of the cyclone were included and compare our numerical results with this experimental data.

It has been noted that the most important factors measuring a cyclone performance may be the loss factor and d_{50}, the 50% cut diameter. Through numerical investigation of some experimental work, in this chapter, a relationship between d_{50}, the loss factor, α, and other parameters such as cyclone diameter, flow rate and the spin velocity at entry to the cyclone etc. is presented by using a regression analysis method. Finally at the end of this chapter the leakage of fluid to the overflow is investigated.

8.2 Investigation of Experimental Work

In this section some experimental work, in which the full dimensions of the cyclone were included, is numerically investigated and the ways in which the mathematical model described in chapters 6

and 7 works for the cyclone in practice are shown.

8.2.1 Stairmand's Work

Stairmand (1951) suggested two kinds of cyclones, namely, one with a high efficiency and another with a high gas flow rate. The first (with an inlet Reynolds number of about 50,000) was chosen to test the methods discussed in chapter 6. Due to the absence of detailed knowledge of how to determine the loss factor at the entry to the cyclone, a loss factor α=0.45 was assumed here. The value of d_{50} for α=0.45 is about 2μ which is in reasonable agreement with the experimental data. A further investigation however, shows that in order to obtain an efficiency curve which is also in reasonable agreement with the experimental data it is not just a matter of finding a loss factor which gives the appropriate value of d_{50} but it must also make the slope of the efficiency curve fit with the experimental data. As mentioned in chapter 6, the free vortex spin velocity tends to infinity as $R \rightarrow 0$ but in practice the spin velocity tends to zero as $R \rightarrow 0$. Hence if we use the free vortex spin velocity to calculate the separation efficiency, the spin velocity will be higher than that which occurs in practice. In reality, the spin velocity takes a maximum value at a small value of R and after that falls very quickly to zero. This suggests that in the region where R is small little separation takes place. Based on this a cut-off region, $R \leq R_{ns}$, within which no separation takes places, is assumed. On introduction of such a region the numerically predicted efficiency curve gives a much better agreement with the experimental data. For Stairmand's work, it was found that if R_{ns}=0.35 and α=0.666 then the numerical efficiency curve is in reasonable

agreement with the experimental data, especially for particles smaller than d_{80}. The efficiency curve as predicted by the numerical method and that obtained by Stairmand are shown in Fig.8.1. There is reasonable agreement; the differences in the results at larger values of d may be due to the leakage and this will be discussed in section 8.5.

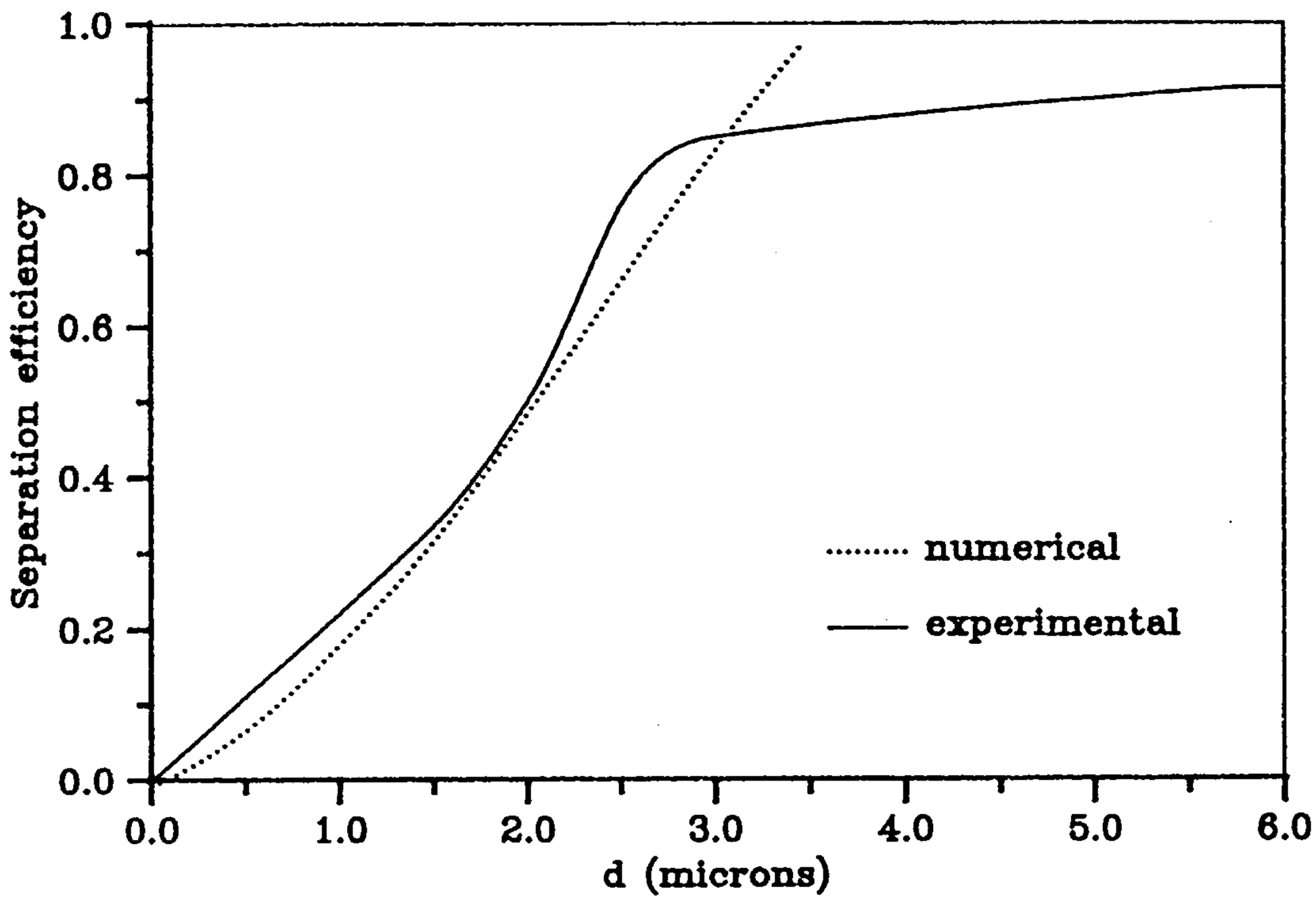

Fig.8.1 The efficiency curves for Stairmand's work.

8.2.2 Kim and Lee's Work

Kim and Lee (1990) obtained experimental results for nine different cyclones, each with three flow rates, and these are summarized in Table 8.1.

Cyclone No.	R_c (m)	R_o (m)	h_0 (m)	h_1 (m)	Z_c (m)	Cyclone angle* α (°)
KI-1	0.01095	0.0040	0.045	0.036	0.15860	7.9
KI-2	0.01095	0.0050	0.045	0.036	0.15860	7.9
KI-3	0.01095	0.0068	0.045	0.036	0.15860	7.9
KI-4	0.01095	0.00875	0.045	0.036	0.15860	7.9
KII-1	0.01555	0.0040	0.045	0.036	0.096584	18.3
KII-2	0.01555	0.0050	0.045	0.036	0.096584	18.3
KII-3	0.01555	0.0068	0.045	0.036	0.096584	18.3
KII-4	0.01555	0.0875	0.045	0.036	0.096584	18.3
KIII-2	0.02055	0.0050	0.045	0.036	0.07874	29.25

Table 8.1: Dimensions of the cyclones of Kim and Lee (1990).

Three flow rates were used for each cyclone, namely Q_1, Q_2 and Q_3 which have values of 0.00014667 (8.8 lpm), 0.00026667 (12.4 lpm) and 0.000306667 (18.4 lpm) m^3/sec, respectively, and the corresponding spin velocities at the inlet are 2.0389, 2.0873 and 4.263 m/sec, respectively. The numerically predicted efficiency curves were obtained for most of the cyclones except those which have a very large overflow diameter (cyclones with very large overflow diameters will give a low separation efficiency and so are not of interest to us) and these curves are shown in Figs.8.2, 8.3 and 8.4. It can easily be seen that the efficiency curves as obtained from the numerical calculations give a reasonable agreement with those obtained experimentally except in the upper region of the curves where larger differences are observed. This may be due to the exclusion of the overflow leakage. The values of R_{ns}, which defined the cut-off region, and the values of loss factor which were

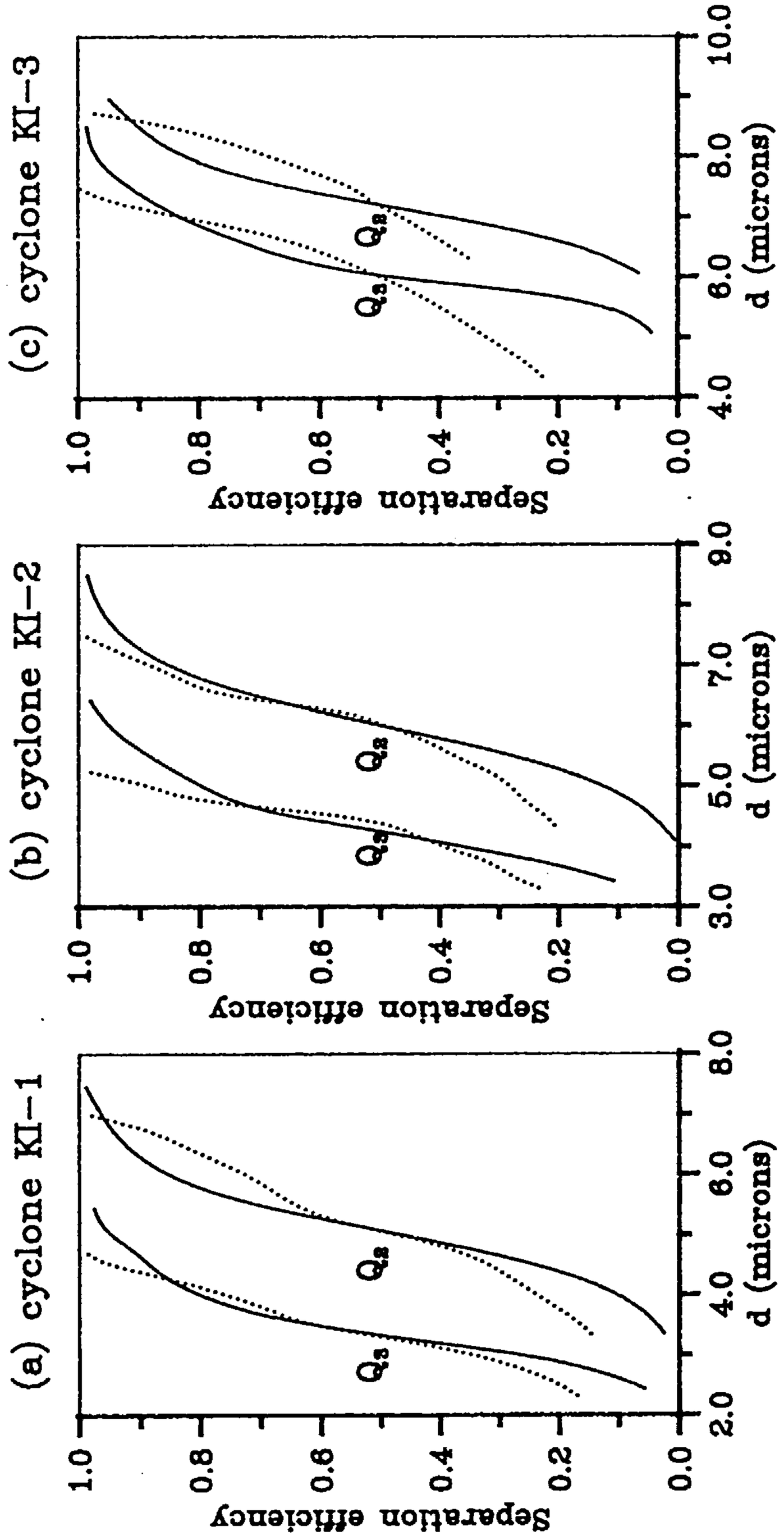

Fig.8.2 The efficiency curves for cyclones KI.
..... numerical results, — experimental results
(Q_s=12.4 lpm, Q_s=18.4 lpm).

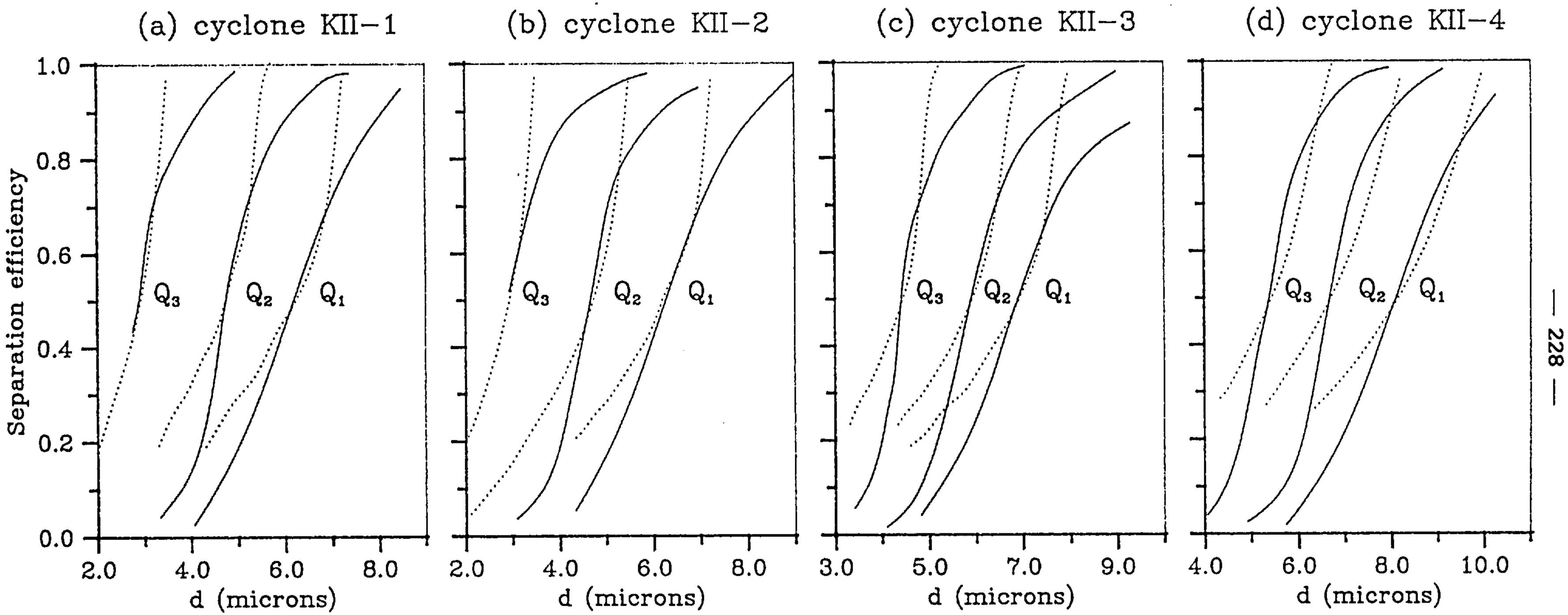

Fig.8.3 The efficiency curves for cyclones KII.

····· numerical results, — experimental results

(Q_1= 8.8 lpm, Q_2=12.4 lpm, Q_3=18.4 lpm).

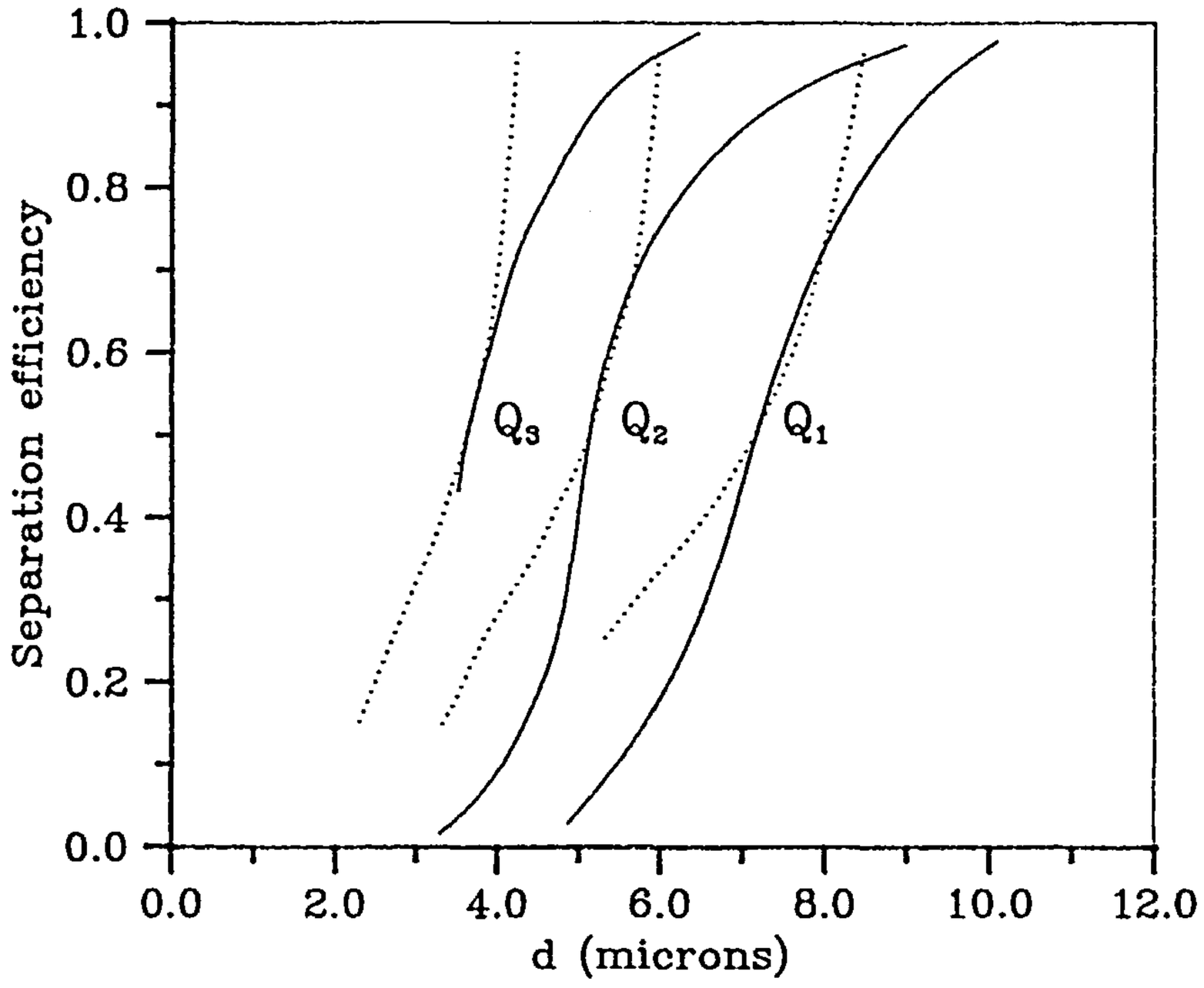

Fig.8.4 The efficiency curves for cyclone KIII-2. ——— numerical results, ——— experimental results (Q_1=8.8 lpm, Q_2=12.4 lpm, Q_3=18.4 lpm).

determined according to d_{50exp} (the experimental values of d_{50}) used for these results are shown in Table 8.2.

As $Q_3>Q_2>Q_1$, it is clear from Table 8.2 that for Kim and Lee's experiments the value of the loss factor increases as the flow rate increases for most of the cyclones considered and this implies that the energy loss for a given cyclone with a higher flow rate is less than that with a lower flow rate. However, due to the complexity of cyclone performance the relationship between the flow rate and loss factor is much more complicated than the above implies. It can also be seen from Table 8.2, viewed with Table 8.1, that for a given cyclone, the difference between the loss factors for two given flow

Cyclone No.	Flow rate	R_{ns}	α	$\alpha(Q_i)-\alpha(Q_j)\equiv\alpha_{ij}$
KI-1	Q_2	0.26	0.1822	
	Q_3	0.26	0.2300	α_{32}: 0.0478
KI-2	Q_2	0.32	0.1848	
	Q_3	0.32	0.2117	α_{32}: 0.0269
KI-3	Q_2	0.44	0.2029	
	Q_3	0.44	0.1997	α_{32}: -0.0032
KII-1	Q_1	0.18	0.1990	
	Q_2	0.18	0.2202	α_{21}: 0.0212
	Q_3	0.18	0.2935	α_{31}: 0.0945
KII-2	Q_1	0.21	0.2173	
	Q_2	0.21	0.2437	α_{21}: 0.0264
	Q_3	0.21	0.3325	α_{31}: 0.1152
KII-3	Q_1	0.31	0.2449	
	Q_2	0.31	0.2410	α_{21}: -0.0039
	Q_3	0.31	0.2651	α_{31}: 0.0202
KII-4	Q_1	0.39	0.2466	
	Q_2	0.39	0.2515	α_{21}: 0.0049
	Q_3	0.39	0.2563	α_{31}: 0.0097
KIII-2	Q_1	0.17	0.1899	
	Q_2	0.17	0.2231	α_{21}: 0.0332
	Q_3	0.17	0.2593	α_{31}: 0.0694

Table 8.2: Cut-off regions and loss factors for the cyclones of Kim and Lee (1990).

rates varies as the overflow diameter changes, with R_o/R_c within the range $0.2\leq R_o/R_c\leq 0.35$ giving the larger differences. From this point of view, if one wants to increase the separation efficiency by increasing the flow rate (in fact, here by increasing the spin velocity at the entry to the cyclone), he/she should increase the flow rate when $0.2\leq R_o/R_c\leq 0.35$ since this will give a better improvement in the separation efficiency for a certain amount of

increment of the flow rate. From the work of Kim and Lee (1990), it can be seen that doubling the flow rate results in almost halving the value of d_{50} for the cyclones with $0.2 \leq R_o/R_c \leq 0.35$ (I-1, II-1, II-2 and III-2 in Kim and Lee's work (1990)), while doubling the flow rate for II-4 ($R_o/R_c \approx 0.56$, see Kim and Lee's work (1990)) only results in a 24% decrease in d_{50}.

The question now is how to choose the value of R_{ns} and hence the value of the loss factor. We will return to this question in section 8.3.

8.2.3 Smith *et al*'s Work

Smith *et al.* (1979) investigated, experimentally, a five stage cyclone in which five cyclones with different geometries are used under different conditions such as temperature, density of the particles etc. Because most cyclones normally perform at room temperature we investigate here only those used by Smith *et al.* (1979) which operated at 25°C and with a flow rate Q=0.0004717 m^3/sec (28.3 lpm) to see how the numerical model developed here predicts the separation efficiency. The geometries of the cyclones we investigated are shown in Table 8.3:

Cyclone No.	R_c (m)	R_o (m)	h_0 (m)	h_1 (m)	Z_c (m)	Cyclone angle α^* (°)
SRI-1	0.02235	0.0075	0.0224	0.0157	0.08129	30.8
SRI-2	0.01830	0.00525	0.0211	0.0157	0.07274	28.3
SRI-3	0.01555	0.00415	0.0140	0.0108	0.04645	37.0
SRI-4	0.01270	0.00295	0.0103	0.0058	0.02865	47.8
SRI-5	0.00760	0.00180	0.0047	0.0043	0.02884	29.5

Table 8.3: Dimensions of the cyclones of Smith *et al.* (1979).

It is found that if the values of R_{ns} and the loss factor α were chosen as those shown in Table 8.4 then the efficiency curves from the numerical model again show good agreement with those obtained experimentally, see **Fig.8.5.**

Cyclone No.	Flow rate	R_{ns}	α
SRI-1	0.0004716667	0.235	0.2988
SRI-2	0.0004716667	0.200	0.4580
SRI-3	0.0004716667	0.187	0.4987
SRI-4	0.0004716667	0.163	0.5552
SRI-5	0.0004716667	0.167	0.3920

Table 8.4: Cut-off regions and loss factor for the cyclones of Smith *et al.* (1979).

All the cyclones here have the same flow rate but have different geometries and this gives us an opportunity to see how the loss factor and d_{50} change with changing geometries. It is clear that the values of the loss factor are, generally, larger than those obtained in section 8.2.2. As has been stated in the last section the difference between two loss factors corresponding to two flow rates for one cyclone is larger when $0.2 \leq R_o/R_c \leq 0.35$. The flow rate here is higher than those in the last section and all the values of R_o/R_c are within this range and hence a larger loss factor is produced. The values of α for SRI-1 and SRI-5 are relatively smaller than those for cyclones SRI-2, SRI-3 and SRI-4; this may be because the values of R_u/R_c for these two cyclones are larger than those for the other three cyclones. As a result the particles which flow down the side wall may have more chance of being picked up again by the air and delivered to the overflow, so the separation efficiency,

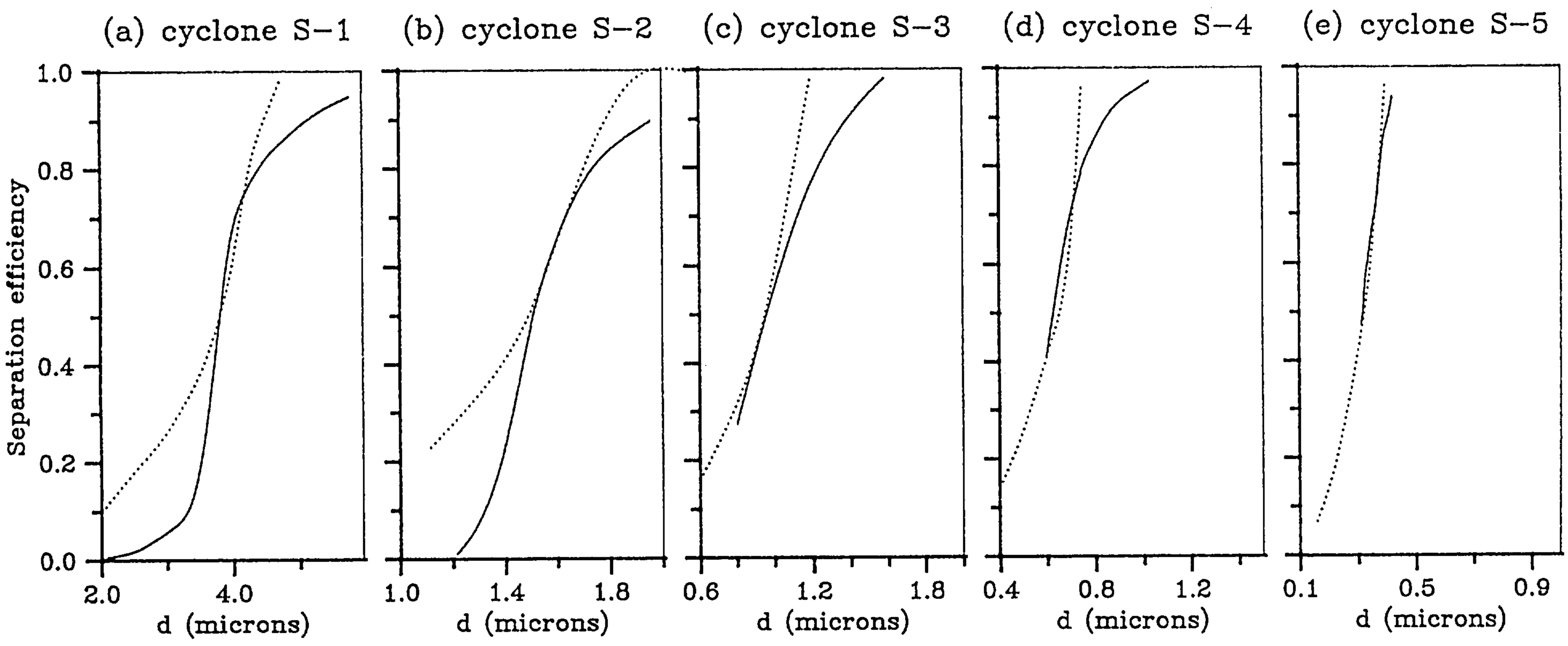

Fig.8.5 The efficiency curves for Smith et al's cyclones (Q=28 lpm).

····· numerical results, — experimental results.

and hence the loss factor, may be lower than that for a larger value of R_u/R_c. It can also be seen from Table 8.4 that SRI-4 has the largest loss factor. The reason for this could be that both R_o/R_c and R_u/R_c for this cyclone are the smallest of those considered and as a result particles in this cyclone have more chance of being separated than those in the other cyclones. It is not sufficient to state the relationship between the spin velocity at the inlet of the cyclone and the loss factor without considering other factors such as the geometry of the cyclone, because a very large value of W_o may give rise to a large energy loss due to the sudden expansion. This can be seen from SRI-5, where W_o for this cyclone was 66.7 m/sec but its loss factor was smaller than that of SRI-4 where the spin velocity was only about 23 m/sec. The reason for this may be due to the differences in the geometries of the cyclones considered.

8.3 Determination of R_{ns} and α

In section 8.2 we have obtained many efficiency curves which compared well with the related experimental data. However, these agreements depend on the choice of the value of the loss factor, α, and R_{ns} (non-dimensional) which defines a cut-off region, $0 \leq R \leq R_{ns}$, such that within which no separation is assumed. Almost a hundred runs with different combinations of α and R_{ns} revealed that the cut-off region could be defined by $R_{ns} \approx 0.7 R_o/R_c$, i.e a value of about seventy percent of the overflow radius. The values of R_{ns} in the numerical results of the work of Kim & Lee (1990) and Smith *et al.* (1979) were all about $0.7 R_o/R_c$, with the loss factor obtained after prescribing the values of R_{ns} and d_{50} from the experimental data. Of course this cut-off region will depend on

other parameters, but in practice we may take R_{ns} a little larger than that we have suggested if R_u/R_c is very large (≥ 0.6, say), while an over small value of R_u/R_c may have little effect on the choice of R_{ns}.

Tarjan (1962) suggested for a water cyclone that there exists an air core along the axis of the cyclone of radius R_a such that $0.06R_c \leq R_a \leq 0.33R_c$ in the vicinity of the axis within which, of course, no separation occurred. Further, Fontein *et al.* (1962) reported that the diameter of the air core increases with increasing the overflow diameter. The results here show a reasonable agreement with that suggested by Fontein *et al.* (1962); indeed the cut-off region for different cyclones investigated here is proportional to the overflow diameter.

8.4 Correlations for d_{50} and the Loss Factor

Using the information obtained in sections 8.2 and 8.3, from the experimental data we may obtain correlations for both d_{50} and the loss factor α by using regression analysis method and hence to have some general ideas on how the geometrical parameters of a cyclone and operating conditions affect on d_{50} and α.

8.4.1 Correlation for d_{50}

An important factor in measuring the separation efficiency of a cyclone, d_{50}, the 50% cut size, has been studied by many authors. By assuming that there is an equilibrium surface Bradley (1958) obtained the formula (7.2.1). In another experiment Bradley and Pulling (1959) gave another formula, equation (7.2.2), for d_{50} which is said to be suitable for cyclones with any included angle. In

investigating 9° and 20° cyclones, Dahlstrom (1949) worked out a correlation for d_{50}, namely,

$$d_{50}=81\ \frac{(2R_c D_i)^{0.68}}{Q^{0.53}}\left\{\frac{1.73}{\rho_p-\rho}\right\}^{0.5} \qquad (8.4.1)$$

where D_i and R_c are measured in inches, Q in U.S. gallon, ρ_p and ρ in g/cm^3, etc. In a study of a cylindrical gas cyclone, Vaughan (1988) gave d_{50} as

$$d_{50}=K/Q^N \qquad (8.4.2)$$

with K and N being constants determined by the cyclone performance.

Saltzman and Hochstrasser (1983) were able to find the following relationship between d_{50}, R_c and R_e, the outlet Reynolds number of cyclone performance, namely,

$$d_{50}/(2R_c)=K_d\left(\frac{1000}{R}\right)^{0.713} \qquad (8.4.3)$$

where K_d is a constant which varies over a small range of values for all the 15 cyclones he considered with a constant diameter. Later Saltzman (1984) used the same method to work out a similar formula for a total of 30 different cyclones and obtained $0.0001429 < K_d < 0.0004461$ with the exponent on the right hand side of expression (8.4.3) changing from 0.713 to 0.83. Although K_d is small and varies over a small range, the ratio of the maximum to the minimum value of K_d is greater than 3 and this suggests that the use of formula (8.4.3) to predict the separation efficiency for a pre-designed cyclone is not very useful.

As cyclone designs depend on of some 10 parameters, a small change in even one of those parameters may make a large change in

one or more of the parameters that appear in all the present d_{50} correlations. For this reason it may be very difficult to obtain a universal formula for cyclones. Nevertheless in this section we try to use regression analysis on some of the experimental data available, namely, Smith *et al.* (1979), Saltzman and Hochstrasser (1983), Saltzman (1984) and Kim and Lee (1990), to evaluate the relationship between d_{50} and some other quantities such as R_c, Z_c, W_0 etc. for small air cyclones.

In a similar manner to the empirical formulae (7.2.1), (7.2.2), (8.4.1) and (8.4.2), we assume that d_{50} has the following form

$$d_{50}=\alpha_0 R_c^{\alpha_1} R_o^{\alpha_2} R_u^{\alpha_3} Z_c^{\alpha_4} (1+h_0/Z_c)^{\alpha_5} (1+h_1/Z_c)^{\alpha_6} \cdot Q^{\alpha_7} W_0^{\alpha_8} (\rho_p-\rho)^{\alpha_9} \qquad (8.4.4)$$

where α_0, α_1,...α_9, are constants which have to be determined by using the available experimental data. A linear regression analysis gives:

$$d_{50}=27.688 R_c^{-0.3275} R_o^{0.6177} R_u^{0.5239} Z_c^{0.03616} (1+h_0/Z_c)^{-36.23} (1+h_1/Z_c)^{17.032} Q^{0.02120} W_0^{-0.8055} (\rho_p-\rho)^{-1.2755} \qquad (8.4.5)$$

where all the quantities used in this formula are measured in SI units.

It should be noted that the quantity Z_c is not the general length of the conical portion of the cyclone, but the mathematical length of the conical portion, i.e $Z_c=R_c Z_{rc}/(R_c-R_u)$ provided that Z_{rc} is the conical length of the cyclone.

From equation (8.4.5) it can be seen that the value of d_{50} decreases as R_o and R_u decreases whilst it increases as the cyclone

radius decreases. This agrees with section 7.2.1 where we have assumed a loss factor α=0.6 for different values of R_c.

Although it seems from expression (8.4.5) that d_{50} is proportional to $Q^{0.02120}$, i.e the value of d_{50} will be almost independent of the value of Q, it must be remembered that the inlet diameter of the cyclone is not involved in the formula so if the inlet diameter is kept constant then the spin velocity at entry to the cyclone will increase as Q increases. As a result a higher flow rate gives a higher efficiency, or in other words, a smaller value of d_{50}. On the other hand, if the value of W_0 is kept constant as Q increases then the value of d_{50} will remain almost unchanged. This also suggests that if one wishes to increase the separation efficiency of the cyclone by increasing the flow rate, as already pointed out in section 7.3, one should increase the flow rate by increasing the spin velocity at the entry to the cyclone rather than by making the inlet diameter larger and keeping W_0 constant.

The exponent for $(\rho_p-\rho)$ in expression (8.4.5) is -1.2755 and this is different from that (for water cyclones) in equations (7.2.1) and (7.2.2) where it was shown to be -0.5. The reason for this is not clear but clearly the gas cyclones are, to some extent, different from liquid cyclones.

Table 8.5 shows some quantities of the experimental data used in the determination of expression (8.4.5) and the values of d_{50} predicted by this formula.

It can easily be seen from Table 8.5 that almost all the errors for the predicted values of d_{50} are within about 20% of the measured values. Bearing in mind the complexity of the cyclone geometries involved in expression (8.4.5) this agreement is good and

one can therefore use it with confidence in the design of small gas cyclones.

It should be noted that the experimental data used here is limited and may be only suitable for small gas cyclones (diameters

Cyclone	Flow rate (m^3/Sec.) ($\times 10^4$)	Cyclone diameter (m) ($\times 10^2$)	d_{50} (Exp) (m) ($\times 10^6$)	d_{50} (Pred) (m) ($\times 10^6$)	$1-\frac{d_{50}(pred)}{d_{50}(exp.)}$ $\times 100$ %	Data Ref.
KI-1	3.0667	2.19	3.3	3.673	11.29	Kim & Lee (1990)
	2.0667		5.1	5.005	-1.86	
	1.3003		6.7	6.549	-2.25	
KI-2	3.0667		4.3	4.215	-1.97	
	2.0667		6.0	5.745	-4.26	
	1.3003		7.3	7.517	2.97	
KI-3	3.0667		6.0	5.097	-15.05	
	2.0667		7.2	6.946	-3.53	
KI-4	3.0667		6.7	5.956	-11.10	
	2.0667		8.5	8.117	-4.51	
KII-1	3.0667	3.11	2.9	3.216	10.91	
	2.0667		4.7	4.384	-6.73	
	1.3003		6.2	5.735	-7.49	
KII-2	3.0667		2.9	3.692	27.30	
	2.0667		4.7	5.032	7.06	
	1.3003		6.2	6.583	6.18	
KII-3	3.0667		4.4	4.464	1.45	
	2.0667		5.9	6.084	3.12	
	1.3003		6.9	7.959	15.36	
KII-4	3.0667		5.4	5.216	-3.41	
	2.0667		6.7	7.108	6.08	
	1.3003		8.1	9.301	14.83	
KIII-2	3.0667	4.11	3.6	3.344	-7.10	
	2.0667		5.1	4.558	-10.62	
	1.3003		7.1	5.964	-16.00	
SRI-I	4.7167	4.47	3.8	3.277	-13.76	Smith *et al* (1979)
	2.3583		5.9	5.644	-4.34	
SRI-II	4.7167	3.66	1.5	1.662	10.78	
	2.3583		2.4	2.862	19.24	
SRI-III	4.7167	3.11	0.95	0.830	-12.64	
	2.3583		2.1	2.421	15.28	
SRI-IV	4.7167	2.54	0.64	0.754	17.75	
	2.4583		1.5	1.298	-13.47	
	1.1782		2.5	2.244	-10.22	
SRI-V	4.7167	1.52	0.32	0.433	35.31	
	2.4583		0.85	0.746	-12.27	
	1.1782		1.5	1.284	-14.38	

Table 8.5: Some of the experimental data and the calculated values of d_{50}.

Cyclone	Flow rate (m^3/Sec.) ($\times 10^4$)	Cyclone diameter (m) ($\times 10^2$)	d_{50} (Exp) (m)	d_{50} (Pred) (m) ($\times 10^6$)	$1-\frac{d_{50}(pred)}{d_{50}(exp.)}$ $\times 100$ %	Data Ref.
S&H-1	3.1767	1.905 with different values of R_c & Z_c	2.09	2.133	2.04	Saltzman and Hochstrasser (1983)
	3.8667		1.82	1.822	0.09	
S&H-2	1.6667		3.30	3.437	4.16	
	2.7667		2.29	2.310	0.87	
	3.8667		1.87	1.776	-5.00	
S&H-3	1.6667		3.42	3.375	-1.33	
	2.7667		2.43	2.268	-6.68	
	3.8667		1.97	1.744	-11.47	
S&H-4	1.9833		2.55	2.749	7.81	
	2.2167		2.50	2.566	2.64	
	3.3167		1.67	1.906	14.16	
	3.8667		1.58	1.628	3.06	
S&H-5	1.6667		2.79	3.073	10.14	
	2.7667		2.02	2.065	2.22	
	3.8667		1.43	1.588	11.06	
S&H-6	1.6667		3.07	3.017	-1.74	
	2.7667		1.90	2.027	6.69	
	3.8667		1.46	1.559	6,78	
S&H-7	2.0167		2.30	2.364	2.76	
	2.2167		2.32	2.243	-3.31	
	3.3167		1.72	1.661	-3.45	
S&H-8	1.6667		2.42	2.677	10.61	
	2.7667		1.65	1.799	9.01	
	3.8667		1.37	1.383	0.97	
S&H-9	1.6667		2.35	2.628	11.82	
	2.7667		1.47	1.766	19.98	
	3.8667		1.40	1.358	-2.30	
S&H-10	2.7667		2.23	2.117	-5.05	
	3.8667		1.71	1.628	-4.77	
S&H-11	1.6667		2.80	3.073	9.75	
	2.7667		2.09	2.065	-1.20	
	3.8667		1.63	1.588	-2.57	
S&H-12	1.6667		3.02	3.017	-0.11	
	2.7667		2.10	2.027	-3.47	
	3.8667		1.55	1.559	0.58	
S&H-13	2.7667		1.92	1.844	-3.94	
	3.8667		1.71	1.418	-17.05	
S&H-14	1.6667		2.65	2.677	1.01	
	2.7667		1.87	1.799	-3.81	
	3.8667		1.62	1.383	-14.61	
S&H-15	1.6667		2.90	2.628	-9.39	
	2.7667		1.89	1.766	-6.57	
	3.8667		1.63	1.358	-16.68	

Table 8.5 (cont.): Some of the experimental data and the calculated values of d_{50}, where S&H-i stands for the ith cyclone used by Saltzman & Hochstrasser (1983).

between 15.2-44.7 mm). The prediction of (8.4.5) for cyclone conditions beyond the range of cyclone geometries and flow rates etc. used here may be not as good.

8.4.2 Correlation for the Loss Factor

Although d_{50} is a very popular measure of the performance of a cyclone, a cyclone may not be designed just on the basis of d_{50} but we require the performance of a cyclone for all values of d. We now try to use some of the experimental data to work out the relationship between the loss factor and the operating conditions, fluid and particle properties and the dimensions of the cyclone. If the loss factor for a cyclone is known then it is straightforward to obtain the efficiency curve for the cyclone by using the numerical method as described in this thesis.

We first use the values of d_{50} and other experimental data in Smith *et al.* (1979), Saltzman and Hochstrasser (1983) and Kim and Lee (1990), by using the numerical method mentioned earlier in this thesis, to obtain the values of the loss factor for each cyclone performance (with $R_{ns}=0.7(R_o/R_c)$, as used in sections 8.2.2 and 8.2.3, the value of R_b being 0.8, see section 8.5). We then use all the values of the loss factor and other data in Smith *et al.* (1979), Saltzman and Hochstrasser (1983), Saltzman (1984) and Kim and Lee (1990), by applying regression analysis, to obtain the relationship between α and the operating conditions, fluid and particle properties and the dimensions of the cyclone.

The plot of α against other cyclone parameters suggests that the loss factor may have the following form,

$$\alpha=k_0\cdot\exp(k_1R_c+k_{11})\cdot\exp(k_2R_o+k_{21})\cdot\exp(k_3R_u+k_{31})\cdot$$

$$\exp(k_4Z_c+k_{41})\cdot\exp(k_5h_0+k_{51})\cdot\exp(k_6h_1+k_{61})\cdot$$

$$\exp(k_7Q+k_{71})\cdot\exp(k_8W_0+k_{81})\cdot\exp(k_9\mu+k_{91}) \qquad (8.4.6)$$

or, alternatively,

$$\alpha=K\cdot\exp(k_1R_c)\cdot\exp(k_2R_o)\cdot\exp(k_3R_u)\cdot\exp(k_4Z_c)\cdot\exp(k_5h_0)\cdot$$

$$\exp(k_6h_1)\cdot\exp(k_7Q)\cdot\exp(k_8W_0)\cdot\exp(k_9\mu) \qquad (8.4.7)$$

where K, k_i (i=1, 2,...9) are constants to be determined. By using the loss factors we obtained from the numerical methods and the experimental data of Smith *et al.* (1979), Saltzman and Hochstrasser (1983) and Kim and Lee (1990), regression analysis gives

$$\left.\begin{aligned} &K=\exp(-40.183),\ k_1=-52.109,\ k_2=21.400\\ &k_3=-152.30,\ k_4=-9.2345,\ k_5=136.18,\ k_6=1.356\\ &k_7=597.6,\ k_8=0.010646,\ k_9=1984047. \end{aligned}\right\} \qquad (8.4.8)$$

It is now easy to see how the value of the loss factor varies with the cyclone geometry and the fluid viscosity for small gas cyclones. We will not discuss in detail these variation here but give some comparisons of the experimental values of the loss factor and the numerical values as predicted by expression (8.4.7) in Table 8.6.

As in section 8.4.1, it is evident that almost all the errors for the predicted values of the loss factor are within 20% of those obtained from the numerical methods. As noted in section 8.4.1, expression (8.4.7) may be only suitable for those gas cyclones whose diameters (for instance) are in the range we have investigated.

Cyclone	R_c (m) ($\times 10^2$)	Z_c (m) ($\times 10^2$)	Q (m^3/S.) ($\times 10^4$)	W_o (m/S.)	α Num.	α Eqn. (8.4.7)	$1-\frac{\alpha(\text{unm.})}{\alpha(\text{pred})}$ ×100%	Ref
KI-1	1.095	15.860	3.0667	4.263	.24408	.21160	-13.31	Kim & Lee (1990)
			2.0667	2.873	.19419	.19639	1.13	
			1.4667	2.039	.17756	.18780	5.77	
KI-2			3.0667	4.263	.22851	.21617	-5.40	
			2.0667	2.873	.20196	.20064	-0.65	
			1.4667	2.039	.19961	.19186	-3.88	
KII-1	1.555	9.6854	3.0667	4.263	.32271	.29447	-8.75	
			2.0667	2.873	.24720	.27365	10.70	
			1.4667	2.039	.22684	.26135	15.22	
KII-2			3.0667	4.263	.37661	.30084	-20.11	
			2.0667	2.873	.28928	.27957	-3.36	
			1.4667	2.039	.26606	.26701	0.36	
KII-3			3.0667	4.263	.29121	.31265	7.36	
			2.0667	2.873	.26988	.29055	7.66	
			1.4667	2.039	.27994	.27749	-0.87	
KII-4			3.0667	4.263	.28421	.32597	14.70	
			2.0667	2.873	.28515	.30293	6.34	
			1.4667	2.039	.28636	.28932	1.03	
KIII-2	2.055	7.874	3.0667	4.263	.29696	.27405	-7.72	
			2.0667	2.873	.26408	.25467	-3.56	
			1.4667	2.039	.23106	.24323	5.27	
SRI-I	2.235	8.129	4.7167	3.723	.32823	.33663	2.56	Smith *et al.* (1979)
			2.3583	1.862	.31170	.28664	-8.04	
SRI-II	1.830	7.274	4.7167	5.887	.50720	.57601	13.57	
			2.3583	2.944	.46695	.48485	3.83	
SRI-II	1.555	4.645	4.7167	10.676	.55284	.49259	-10.90	
			2.3583	5.338	.45424	.40420	-11.02	
SRI-IV	1.270	2.865	4.7167	23.089	.59961	.54390	-9.29	
			2.4583	11.545	.37657	.41777	10.94	
			1.1782	5.743	.33605	.36600	8.91	
SRI-V	0.760	2.884	4.7167	66.727	.41215	.39813	-3.40	
			2.4583	33.364	.22593	.24242	7.30	
			1.1782	16.682	.18955	.18915	0.21	
S&H-1	0.9525	7.617	3.3167	8.731	.22242	.21408	-3.75	Salt-man (1984)
			3.8667	10.661	.23531	.22582	-4.03	
S&H-2		3.808	1.6667	4.595	.27235	.26386	-3.12	
			2.7667	7.628	.29773	.29104	-2.25	
			3.8667	10.661	.30415	.32102	5.54	
S&H-3		2.286	1.6667	4.595	.31296	.30368	-2.96	
			2.7667	7.628	.33344	.33495	0.45	
			3.8667	10.661	.34279	.36946	7.78	

Table 8.6: Some experimental data, numerical and predicted values of the loss factor (to be continued).

Cyclon	R_c (m) ($\times 10^2$)	Z_c (m) ($\times 10^2$)	Q ($m^3/S.$) ($\times 10^4$)	W_o (m/Sec)	α Num.	α Eqn. (8.4.7)	$1-\frac{\alpha(num.)}{\alpha(pred)}$ ×100%	Ref
S&H-4	0.9525	7.617	1.9833	5.468	.20270	.18773	-7.39	Salt-man (1984)
			2.2167	5.974	.19458	.19139	-1.64	
			3.3167	8.731	.23518	.21049	-10.50	
			3.8667	10.661	.22903	.22204	-3.05	
S&H-5		3.808	1.6667	4.595	.27882	.25944	-6.95	
			2.7667	7.628	.29288	.28616	-2.29	
			3.8667	10.661	.34642	.31563	-8.89	
S&H-6		2.286	1.6667	4.595	.30991	.29859	-3.65	
			2.7667	7.628	.38052	.32935	-13.45	
			3.8667	10.661	.41394	.36327	-12.24	
S&H-7		7.617	2.0167	5.560	.18981	.18511	-2.48	
			2.2167	5.947	.17743	.18811	6.02	
			3.3167	8.731	.19174	.20694	7.93	
S&H-8		3.808	1.6667	4.595	.26682	.25506	-4.41	
			2.7667	7.628	.29571	.28133	-4.86	
			3.8667	10.661	.29571	.31031	4.94	
S&H-9		2.286	1.6667	4.595	.30433	.29355	-3.54	
			2.7667	7.628	.36686	.32379	-11.74	
			3.8667	10.661	.32163	.35714	11.04	
S&H-10		7.617	2.7667	7.628	.19487	.20130	3.30	
			3.8667	10.661	.21279	.22204	4.35	
S&H-11		3.808	1.6667	4.595	.27963	.25944	-7.22	
			2.7667	7.628	.28443	.28616	0.61	
			3.8667	10.661	.30492	.31563	3.51	
S&H-12		2.286	1.6667	4.595	.31588	.29859	-5.47	
			2.7667	7.628	.34481	.32935	-4.49	
			3.8667	10.661	.39081	.36327	-7.05	
S&H-13		7.617	2.7667	7.628	.16960	.19791	16.69	
			3.8667	10.661	.19177	.21829	13.83	
S&H-14		3.808	1.6667	4.595	.24127	.25506	5.72	
			2.7667	7.628	.25674	.28133	9.58	
			3.8667	10.661	.24653	.31031	25.87	
S&H-15		2.286	1.6667	4.595	.27167	.29355	8.06	
			2.7667	7.628	.31893	.32379	1.52	
			3.8667	10.661	.30959	.35714	15.38	

Table 8.6 (cont.): Some experimental data, numerical and predicted values of the loss factor (see related references).

In practice, if the loss factor for a cyclone is unknown we may use expression (8.4.7) to obtain the loss factor first, and then

substitute into our numerical procedure to obtain both the value of d_{50} and the efficiency curve for the cyclone performance.

8.5 The Overflow Leakage

Up to now almost all that we have discussed has been based on the assumption that the overflow 'leakage' may be neglected. The 'leakage' is the amount of fluid which does not take part in the full separating procedure. Instead, it takes a short circuit to the overflow carrying with it some of the suspended particles. Leakages of the order of 10% to 15% exist in many situations and it is therefore worth discussing here the influence of the leakage on the overall separation efficiency. Because of the very small amount of knowledge available on how to estimate the leakage in this work, we will give two practical ways to treat leakage.

8.5.1 A Simple Model

First, we assume that only a flux of fluid $Q_s = (1-Le)Q$, where $0<Le<1$, actually flows through the cyclone and the separation efficiency in the top boundary-layer is neglected. This means that LeQ is the flux of fluid through the top boundary-layer. With these assumptions and the assumption that the particle distribution is homogeneous at entry to the cyclone, it is straightforward to work out the overall separating efficiency of the cyclone, E_o, by using the Stokes drag law, if the separation efficiency for the flux Q is known.

Let $E(d_1)$ be the efficiency of a particle with diameter d_1 for the flow rate Q and the corresponding spin velocity at the entry to the cyclone is W_0. The flow fields (solutions of equation (6.2.23))

are the same for Q and W_0 as those for $Q_s=(1-Le)Q$ and $W_{0s}=(1-Le)W_0$. From equation (6.4.5), we observe that in order that the efficiency for the particle with diameter d_2 for given Q_s and W_{1s} is equal to $E(d_1)$, the particle with diameter d_2 must satisfy the equation

$$\frac{W_{0s}^2 d_2^2}{Q_s} = \frac{W_0^2 d_1^2}{Q}, \qquad (8.5.1)$$

giving

$$d_2 = d_1 (1-Le)^{1/2}. \qquad (8.5.2)$$

Then, if $d_x(Q_s, W_{0s})$ is the x% cut size (diameter) for a cyclone with flow rate Q_s and spin velocity at entry to the cyclone W_{0s}, then $d_{x(1-Le)}$ will be x(1-Le)% cut size for the total flow rate Q which has a leakage of LeQ. For example, in section 7.2.1 we predicted a value of d_{50} of 7.3μ and this would give rise to a value of d_{50}=8.9μ if Le=10%, and d_{50}=9.5μ if Le=15%.

For Stairmand's experimental work (1951) the overall efficiency, E_o, as a function of the particle diameter is plotted in Fig.8.6 and it is clear that the agreement between theory and experiment is reasonable.

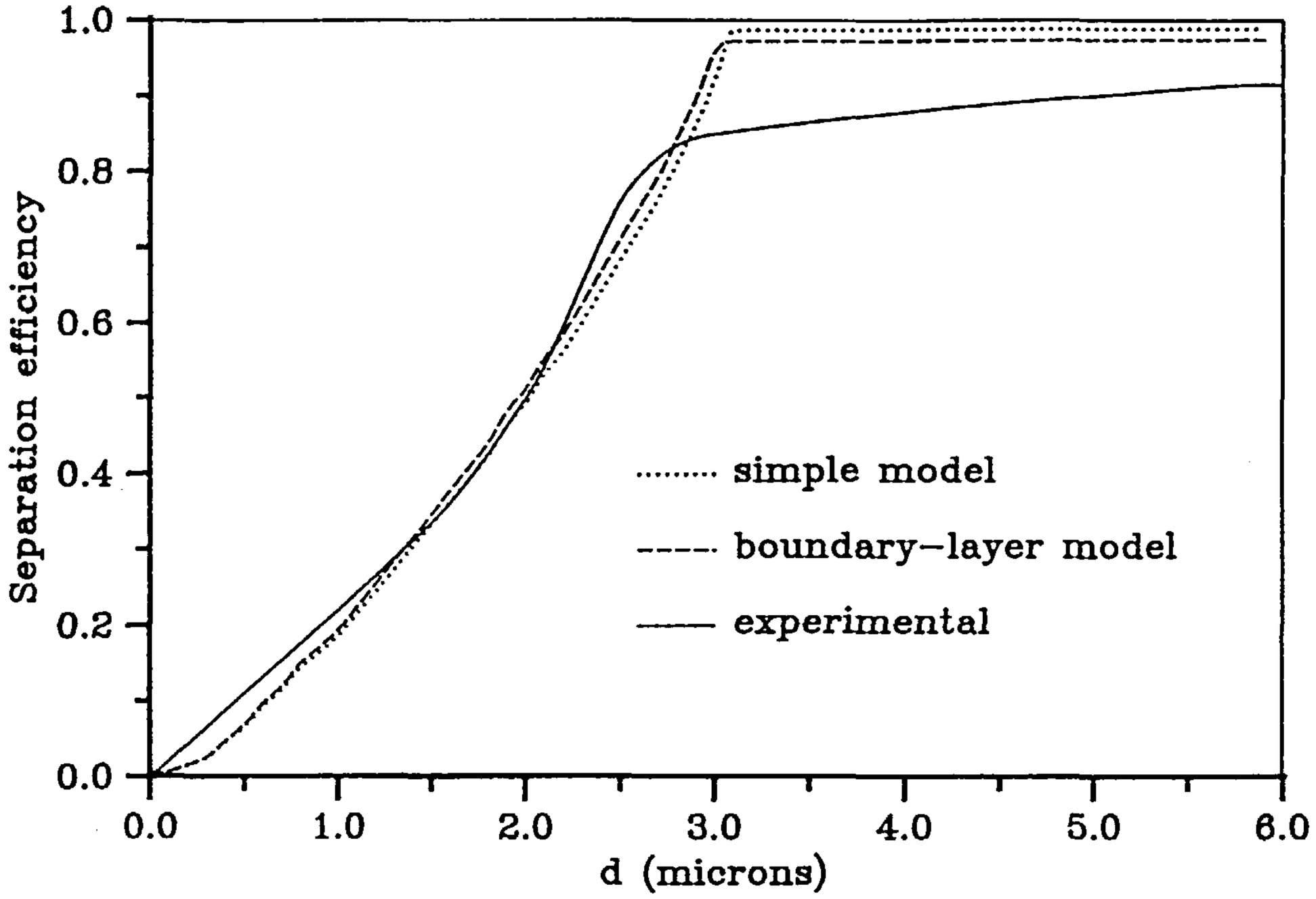

Fig.8.6 The overall efficiency for Stairmand's work.

8.5.2 A Boundary-layer Model

Secondly, we try to seek the leakage of fluid through the boundary-layer at the top wall of the cyclone and then the leakage of a particle with a given diameter.

Assume that across the top boundary-layer the velocities u and w have the forms (Bloor and Ingham (1983)),

$$u=U\ f(\eta) \qquad w=W\ g(\eta) \tag{8.5.3}$$

where U and W are the u and v outflow velocities at the outer edge of the boundary-layer respectively, and

$$\left.\begin{aligned} f&=\gamma\eta^3-(1+2\gamma)\eta^2+(2+\gamma)\eta \\ g&=2\eta-\eta^2 \end{aligned}\right\} \tag{8.5.4}$$

with γ being a constant determined by the scale of the outflow at the outer edge of the boundary-layer.

In terms of the dimensionless meridional leakage flux Q'_L and the thickness of the boundary-layer $\delta'=\delta'(R)$ which have been non-dimensionlized by $(\mu/\rho_p)^{1/(1+\omega)}(W_0R_c)^{1/(1+\omega)}R_c\equiv S_{QL}$ and $(\mu/\rho_p)^{\omega/(1+\omega)}(W_0R_c)^{-\omega/(1+\omega)}R_c\equiv\delta_{QL}$, respectively, the governing equation in the top boundary-layer can be written (see Bloor and Ingham (1983)) in the form

$$\frac{dQ'_L}{dR} = D_1c_1\left\{\frac{R}{\delta'}\right\}^{\omega} \tag{8.5.5}$$

$$D_2\frac{d}{dR}\left\{\frac{Q'^2_L}{R\delta'}\right\}+D_3\frac{\delta'}{R^2} - \frac{Q_L}{RC_0\delta'}\frac{dQ'_L}{dR} -\frac{Q'_L}{C_0^2}\frac{d}{dR}\left\{\frac{Q'_L}{R\delta'}\right\}=- \frac{c_2Q'_L}{R\delta'}\left\{\frac{R}{\delta'}\right\}^{\omega} \tag{8.5.6}$$

where

$$\left.\begin{aligned} c_1&=2\\ c_2&= 12(\gamma+2)/(\gamma+8)\end{aligned}\right\} \tag{8.5.7}$$

$$\left.\begin{aligned} C_0&=\int_0^1 f(\eta)d\eta\\ D_1&=C_0/\int_0^1 f(1-g)d\eta\\ D_2&= \frac{1}{C_0^2}\int_0^1 f^2d\eta\\ D_3&= \int_0^1 (1-g^2)d\eta\end{aligned}\right\} \tag{8.5.8}$$

with $\eta=n'/\delta'(R)$ (n' is the boundary coodinate which is normal to the top wall of the cyclone but in the opposite direction to the z-direction) and $\omega=1$ (for a laminar boundary-layer).

The boundary conditions for equations (8.5.5) and (8.5.6) are

$$Q'_L = \delta'=0 \qquad \text{at } R=1. \tag{8.5.9}$$

The fourth order Runge-Kutta method was used to solve equations (8.5.5) and (8.5.6) with the singularity at R=1 being treated in the way suggested by Bloor and Ingham (1983).

As pointed out by Bloor and Ingham (1983), Q_L' and δ' are fairly insensitive to the value of γ in the range of $-\infty<\gamma\leq-25$. In practice γ is a large negative quantity so we have taken the value of γ to be -80 in all the computations performed here.

The trajectory of the particle in the boundary-layer may be determined by the equivalent of equation (6.4.5), namely,

$$\frac{d\eta}{dR} = \frac{\frac{Q_L'}{\delta'}\frac{d\delta'}{dR}\eta f(\eta) - \frac{dQ_L'}{dR}\int_0^{\eta} f(\eta)d\eta}{Q_L' f(\eta) + \frac{(\rho_p-\rho)d^2W_0}{18\eta R_c} g^2(\eta)\delta' \int_0^1 f(\eta)d\eta} - \frac{\eta}{\delta'}\frac{d\delta'}{dR} \qquad (8.5.10)$$

It is found from the numerical solution of equation (8.5.10) that if a particle enters the boundary-layer through its outer edge then instead of being released to the main flow again it will be discharged to the overflow through the inner part (the region near the wall) of the boundary-layer. We assumed earlier that if a particle in the main flow has not been separated then it will be discharged to the overflow. Further due to the complexity of the flow at the entry to the cyclone near R=1, we also assume that all the particles that enter into the top boundary-layer do so in an area near R=1.

Because in this section we are only interested in the particles which are discharged to the overflow through the boundary-layer, from the above assumptions we may choose a position which is near to R=1 where the complexity of the flow near the entry to the cyclone

is assumed to have been sufficiently diminished, say R_b=0.8, to obtain the leakage flux of fluid Q'_L through this position, i.e. $Q'_L(R_b)$. $Q'_L(R_b)$ consists of two parts: one part, Q'_{Lv}, in which fluid flows towards the vortex finder and another part, Q'_{LR_0}, in which fluid flows in the opposite direction, i.e. $Q'_L(R_b)=Q'_{Lv}+Q'_{LR_0}$ (see Fig.8.7). Physically the flow near the entry to the cyclone is very complicated and it is very difficult to know what exactly happens there. Nevertheless, we may assume that within the cyclone the separation efficiency can be obtained by combining the separation efficiency in the top boundary-layer and that in the main flow. The separation efficiency in the main flow has been discussed earlier in this thesis while the separation efficiency in the top boundary-layer may be calculated in the following way.

We assume that the separation in the top boundary-layer is achieved by the fluid which flows towards the vortex finder in the upper part of the top boundary-layer. The amount of this fluid may be shown to be (see Bloor and Ingham (1983)):

$$Q_{Lv}(R_c R_b)\equiv -2\pi S_{QL} Q'_{Lv}(R_b)=-2\pi S_{QL} R\delta'(R_b)U\int_0^{\eta_0} f(\eta)d\eta \qquad (8.5.11)$$

where $0<\eta_0<1$ and satisfies $f(\eta_0)=0$ (see equation (8.5.4) and Fig.8.7).

Now, given a particle with diameter d, we can find an equilibrium point at $R=R_b$, where the drag force applied on the particle is balanced by the centrifugal force due to the rotation of the flow, say $\eta=\eta_d$. Therefore η_d satisfies

$$Q'_L f(\eta)+\frac{(\rho_p-\rho)d^2 W_0}{18\eta R_c}g^2(\eta)\delta'\int_0^1 f(\eta)d\eta=0 \qquad (8.5.12)$$

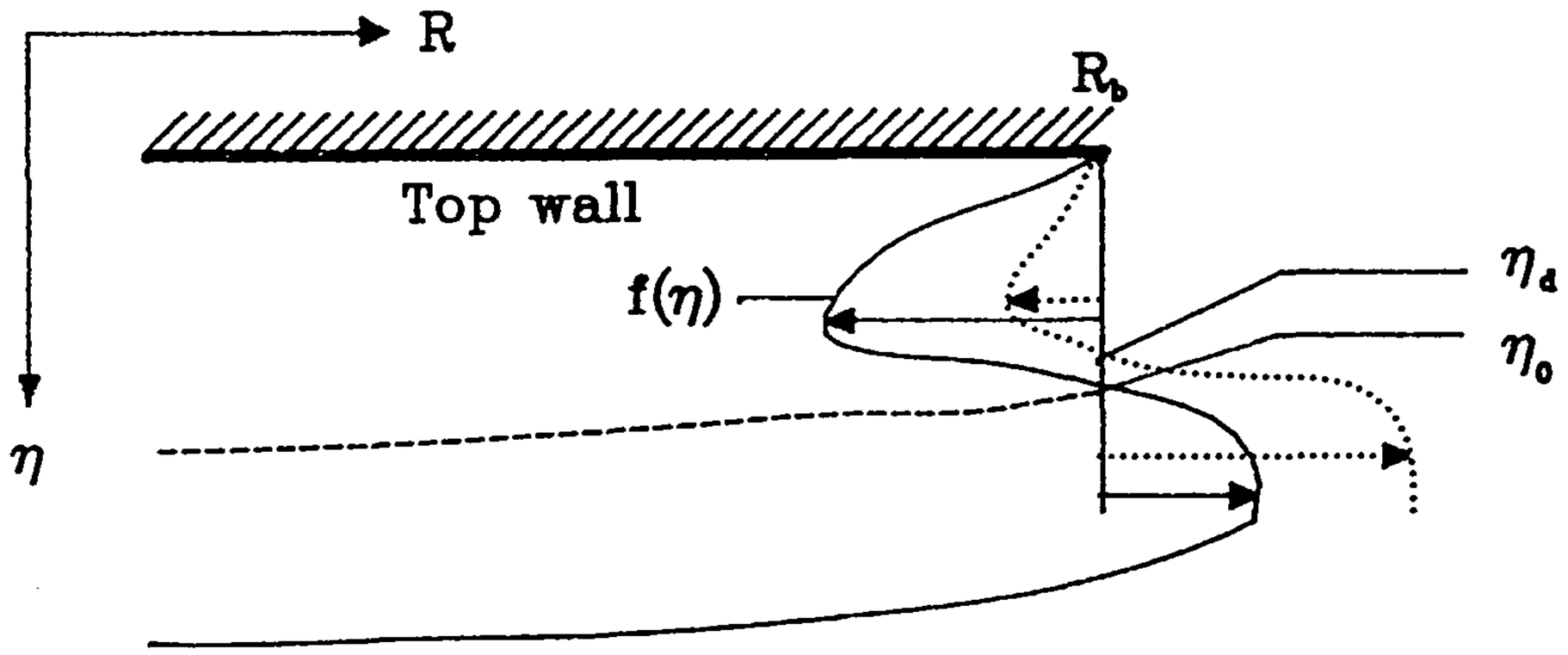

Fig.8.7 Details of the flow structure at the top boundary-layer near $R = R_b$.

By assuming that the particle distribution is homogeneous in the upper part of the top boundary-layer, the separation efficiency for the particle with diameter d can now be shown to be

$$E_b(d) = \int_0^{\eta_d} f(\eta)d\eta \Big/ \int_0^{\eta_0} f(\eta)d\eta. \qquad (8.5.13)$$

The flux of fluid in the main flow of the cyclone, Q_s, can now be written as $Q_s = Q - Q_{Lv}(R_c R_b)$ and the separation efficiency in the main flow, E_m, can be obtained by using the method provided in chapters 6 and 7.

It is now straightforward to work out the overall separation efficiency for a given cyclone,

$$E_o(d) = \frac{E_m(d)Q_s + E_b(d)Q_{Lv}(R_c R_b)}{Q}. \qquad (8.5.14)$$

As an example, the overall efficiency curve for the experimental data of Stairmand (1951) is shown in Fig.8.6. It is clear that this curve shows a better agreement with the experimental data than that obtained in section 8.5.1 where we assumed that all the particles in the leakage flow are discharged to the overflow.

8.6 Conclusions

Various experimental data has been investigated numerically and it is found that the numerical methods used in this thesis predicts the experimental findings reasonable well. Correlations for both the loss factor and d_{50} have been obtained from some experimental data available which predict well both the loss factor and d_{50}. Unlike some other formulae which characterize the cyclone performance, the formula for d_{50} developed here contains no constants which need to be determined from the cyclone performance so it may be used to predict d_{50} if the cyclone geometry and operating conditions are known.

With a given cyclone geometry one may use these correlations to predict both the values of the loss factor and d_{50} and hence to predict the efficiency curve numerically providing the predicted (or otherwise obtained) value of the loss factor is available.

The leakage to the overflow has also been treated in two practical ways and the efficiency which takes account of the separating process in the boundary-layer has been calculated.

CHAPTER 9 A NUMERICAL INVESTIGATION INTO THE EFFICIENCY OF SMALL PERSONAL CYCLONES

9.1 Introduction and Previous Work

In the last 3 chapters we have investigated both the fluid flow in the cyclone and the factors which affect the separation efficiency. In chapter 7 various aspects which affect the separation efficiency were studied providing we known the value of the loss factor. In chapter 8 investigations into some available experimental data were mainly on the larger cyclones and therefore the validation of the conclusions reached may be limited because the diameters of the cyclones used were, typically, greater than 10mm, see for example Smith *et al.* (1979) and Kim and Lee (1990).

From the fluid dynamics point of view the model used in the last 3 chapters should also predict the flow field in small cyclones. On the other hand, some experimental work has been reported on the separation efficiency (or in other words the penetration) for small gas cyclones (although the full dimensions of the cyclones used were, sometimes, not reported), see for example, Bartley & Breuer (1982), Kenny *et al.* (1987) and Lidèn & Kenny (1990).

Ogden *et al.* (1983) studied the flow dependence of the Casella cyclone and found that the relationship between the penetration, P_{en}, and flow rate through the cyclone has the form

$$(1-P_{en})^{0.5} = aQ^{N}d_{ae} \qquad (9.1.1)$$

where d_{ae} is the aerodynamic diameter of the particle which penetrates through the cyclone, Q is the flow rate and a and N are constants which have to be determined (in the case that particles are spherical and in the Stokes regime $d_{ae}=d(\rho_p/\rho_w)^{1/2}$, where ρ_w is the density of water, see Vincent (1989)). They found for the flow rates they investigated that if $(1-P_{en})^{0.5}$ was plotted against the aerodynamic diameter of the particle, a straight line was obtained and the penetration curve compared well with the BMRC definition for respirable dust.

Using a regression analysis method Lidèn and Kenny (1990) gave an empirical model which can predict the penetration curve for 5 versions of the British gas cyclone by applying the so called Blachman-Lippman equation (Blachman and Lippman (1974))

$$P_{en} = 0.5(1-\tanh(k_1x + k_2x^2))$$

$$= 1/[1 + \exp(2(k_1x + k_2x^2))] \qquad (9.1.2)$$

where $$x = \frac{d_{ae}-d_{50}}{d_{ae}}, \qquad (9.1.3)$$

By using a regression analysis they were able to predict the constants k_1 and k_2 in equation (9.1.2) and then the penetration curves for 4 versions of the British small gas cyclone, namely, Higgine BCIRA, Danish version, SIMPEDS 1-hole and two SIMPEDS 4-holes. They found that their model gave good agreement with their experimental investigation. Lidèn and Kenny (1990) found for the SIMPEDS (1-hole) cyclone that the value of d_{50} decreases at a rate

almost inversely proportional to the flow rate through the cyclone. They claimed that the penetration curves for the British cyclones investigated had some differences in shape with those obtained by several earlier investigators, see Higgens and Dewell (1967), Maguire *et al.* (1973) and Ogden *et al.* (1983), who found that the penetration curves appeared to follow the BMRC definition of respirable dust, although with a d_{50} slightly less than 5μ.

Kenny *et al.* (1987) investigated several different samplers, including the Casella cyclone, and again by using regression analysis, found that the relation between the penetration, the separation efficiency E and aerodynamic diameter is

$$0.5 \ln(E/P_{en}) = k_0 + k_1 d_{ae} + k_2 d_{ae}^2 \qquad (9.1.4)$$

with k_0, k_1 and k_2 constants which may vary with the flow rate and are to be determined from the experimental data. They also found that their curves were different in shape to the BMRC definition of respirable dust. It can be seen that the penetration curves of Kenny *et al.* (1987) fitted well with their experimental data, but the constants in the regression equation (9.1.4) need also to be determined from the experimental data, as we have seen from Lidèn and Kenny (1990). Also, for different flow rates, different regression equations may be obtained, i.e. one can obtain the penetration curve only after the experiments have been performed.

Bartley and Breuer (1982) investigated the possibility of optimizing the performance of the 10mm cyclone. The model which was used to predict the efficiency curve was as follows (see also Held and Cooper (1979))

$$E(d_{ae}) = \int_0^{d_{ae}} \frac{\exp[-\ln(d'-\mu_c)/(2\sigma_c^2)]}{\sigma_c\sqrt{2\pi}\ d'}\, dd'$$

$$= 0.5 + 0.5\,\mathrm{erf}[(\ln(d_{ae})-\mu_c)/(\sigma_c\sqrt{2})] \qquad (9.1.5)$$

where μ_c and σ_c are constants to be determined. It is clear that the parameters μ_c and σ_c characterize the cyclone performance and the 50% cut-off diameter d_{50} is given by

$$d_{50} = e^{\mu_c} \qquad (9.1.6)$$

where σ_c is related to the sharpness of the cut since

$$d\left.\frac{\partial E}{\partial d}\right|_{d=d_{50}} = \frac{1}{\sigma_c\sqrt{2\pi}}. \qquad (9.1.7)$$

Again using regression analysis the values μ_c and σ_c were determined by fitting expression (9.1.5) to the experimental data (certainly μ_c and σ_c will vary for different flow rates). It was found by Bartley and Breuer (1982) that the recommended flow rate for the 10mm cyclone investigated (MSA cyclone) was not the best one which fitted the BMRC definition for respirable dust but a flow rate of 1.2 lpm seemed to follow the definition quite well. In order to determine the values of the characterizing parameters μ_c and σ_c in the vicinity of a fixed flow rate Q_0, they used a truncated Taylor's series in lnQ. Expanding about $\ln Q_0$, this gives

$$\mu_c(Q) = \mu_c(Q_0) + \alpha_\mu \ln(Q/Q_0) \qquad (9.1.8)$$

$$\sigma_c(Q) = \sigma_c(Q_0) + \alpha_\sigma \ln(Q/Q_0) \qquad (9.1.9)$$

so the flow dependence is then characterized by the constants α_μ and α_σ which must then be determined from the experimental data which

depends in turn not only on the flow rate Q but also on the flow rate Q_0.

As d_{50} is a very important parameter for the performance of a cyclone many authors have paid particular attention to it. One of the most popular empirical formulae for d_{50} is

$$d_{50} = kQ^{-N} \qquad (9.1.10)$$

where k and N are constants which characterize the cyclone performance in a similar way that μ_c and σ_c did in Bartley and Breuer's work (1982). Usually the values of k and N differ from cyclone to cyclone, see for example Ogden *et al.* (1983). For Casella cyclones Ogden *et al.* (1983) found that the value of the index N is about 0.7.

It seems that in order to predict the cyclone penetration (or separation efficiency) curve appropriately one may need at least 2 parameters which will characterize the cyclone performance. This is because, mathematically, in order to determine the shape of the curve one needs at least its slope and another parameter, say for example d_{50}.

In order to investigate the cyclone performance more fundamentally, Boysan *et al.* (1982), Ferguson (1989) and Wen *et al.* (1990) have solved the full governing flow equations in order to study the fluid dynamics in the cyclone. In the last 3 chapters we have been able to predict the cyclone performance reasonably well for those cyclones with diameters which are typically greater than 10mm. Although many experimental investigations are available for small gas cyclones, it is, nevertheless, worth studying the

performance of this kind of personal cyclone further by numerical techniques, as performing calculations form a cost effective alternative to performing the corresponding experimental work.

In this chapter we use a similar numerical technique to that described in the last 3 chapters of this thesis in order to investigate the small gas cyclone (10mm in diameter) and to see whether the previous work in this thesis is valid for this kind of personal cyclone. Details of the techniques used here may be found in the previous chapters and only the extra information that is required will be presented here. For the geometry of the cyclone and the computational domain of the problem see **Fig.1.4** and **Fig.6.1**, respectively.

9.2 Mathematical Model and Numerical Techniques

All details of the mathematical model and the numerical techniques used in this chapter are similar to those used in the last 3 chapters and hence will not be described again here.

9.3 Results and discussion

The Casella 10mm personal cyclone with different flow rates has been investigated in this chapter. The mesh size used in the numerical results are 1/80 in both the R- and z-directions since a further decrease in the mesh size results in almost no difference in the separation efficiency. Although in the last chapter we gave an empirical formula for predicting the value of the loss factor, it is only appropriate for cyclones for which the diameter is much greater than 10mm and it is not therefore suitable to use it for cyclones which have diameters of 10mm that have been investigated in this

chapter. The numerical model employed earlier in this thesis requires a value of d_{50} or of the loss factor (which may be obtained from the experimental data or by other means). In this chapter the value of d_{50} used is obtained from the experimental results (Kenny *et al.* (1987)) and hence the loss factor may be found. Then the separation efficiency can be determined by the numerical method described in chapters 6, 7 and 8.

Fig.9.1 shows the penetration curve obtained from the numerical technique using $R_{ns}=0.7R_u/R_c$ (R_u is the under-flow radius of the

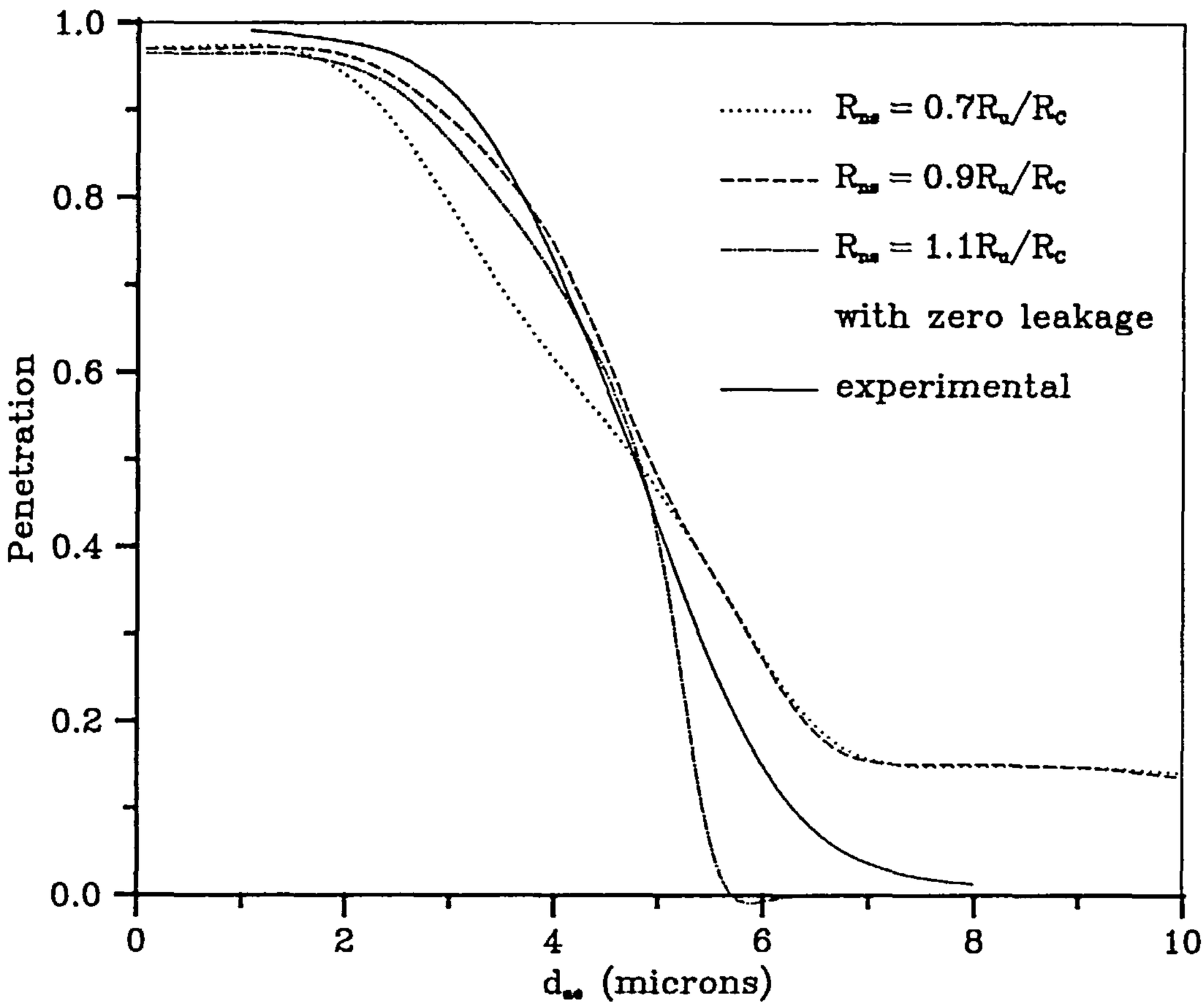

Fig.9.1 Penetration curves obtained from the numerical technique and from the experimental data of Kenny *et al.* (1987).

cyclone) and including the effects of leakage as predicted in chapter 8 of the thesis. Also shown in **Fig.9.1** is the experimental data given by Kenny *et al.* (1987) with a flow rate of 1.9 lpm for the PVA particle. The horizontal axis in **Fig.9.1** is the aerodynamic diameter (in microns, μ) whilst the vertical axis is the penetration, P_{en}, which has the following relationship with the separation efficiency E

$$P_{en}=1-E \qquad (9.3.1)$$

It can be seen from **Fig.9.1** that the penetration curve obtained from the numerical technique for a solid aerosol particle shows rather a poor agreement with that obtained from the experimental data (Kenny *et al.* (1987)). The upper portion of the penetration curve obtained from the numerical technique is well below that obtained from the experimental data. This suggests that a further increase in the value of R_{ns} (which define the cut-off region such that if $R<R_{ns}$ there will be no separation (see chapter 8)), above $0.7R_u/R_c$ may be needed. Another observation from **Fig.9.1** is it is clear that the leakage for this kind of cyclone seems to be very small and in fact is almost negligible. On increasing the value of R_{ns} to $0.9R_u/R_c$, the upper portion of the penetration curve as obtained from the numerical technique becomes closer to that obtained from the experimental data but the lower portion of the curve is still higher than that obtained from the experimental data. This may mean there is a small (or zero) leakage for this kind of the cyclone. The numerical penetration curve obtained from the numerical method by putting $R_{ns}=1.1R_u/R_c$ and a zero leakage is also shown in **Fig.9.1** and, clearly, in this case the agreement between

the numerical results and the experimental data is much better than that in the situations where a smaller value of R_{ns} has been used. This suggests that a value of $1.1R_u/R_c$ for R_{ns} is required and that a leakage of zero may be required for small cyclones.

In order to confirm if the above suggestions are valid for other kinds of aerosols and flow rates, numerical results with $R_{ns}=1.1R_u/R_c$ and a zero leakage are compared with the experimental results of Kenny *et al.* (1987). **Fig.9.2** shows the penetration curves for different flow rates from 1.3 lpm to 2.5 lpm by using the numerical technique described in the last 3 chapters of this thesis with $R_{ns}=0.7R_u/R_c$ and including a leakage. The corresponding experimental results for liquid particles (Silicone oil, S200) are drawn from the work of Kenny *et al.* (1987) and are also shown in **Fig.9.2** for comparison. Again, as in the situation for solid particles, it can be seen that the numerical penetration for the particles with diameters larger than d_{50} is lower than that obtained experimentally whilst that for the particles with a diameter smaller than d_{50} is higher than that obtained experimentally. A further increase of R_{ns} from $0.7R_u/R_c$ to $0.9R_u/R_c$ gives the numerical

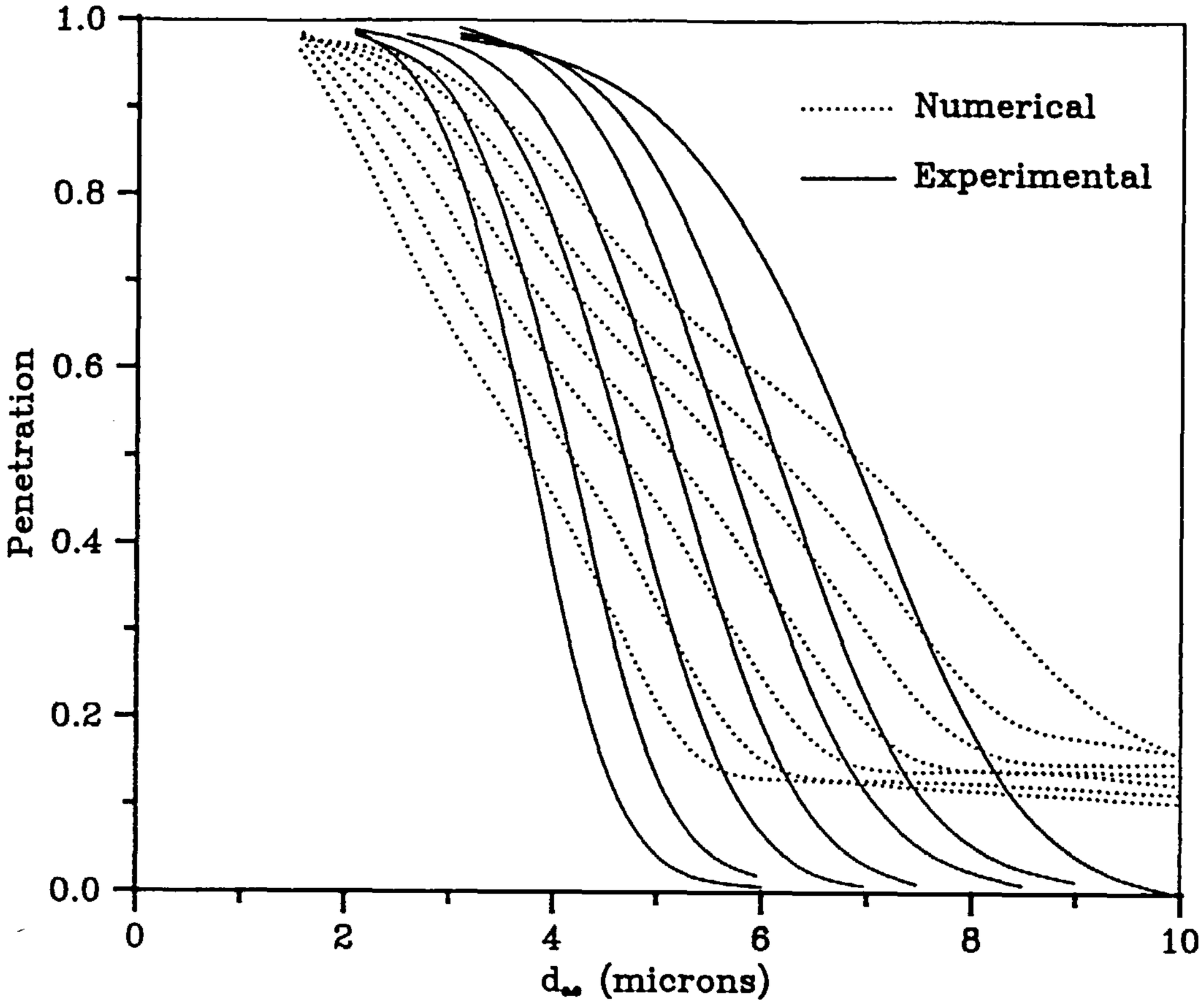

Fig.9.2 Penetration curves obtained from the numerical technique with $R_{ns}=0.7R_u/R_c$ and with a leakage obtained by the method shown in section 8.5 for different flow rates and from experimental data of Kenny *et al.* (1987). The flow rates for the penetration curves (from right to left) are 1.3, 1.5,..., 2.5 lpm respectively.

penetration in better agreement with the experimental data as shown in Fig.9.3.

The numerical results obtained with $R_{ns}=1.1R_u/R_c$ and a zero leakage are shown in Fig.9.4 where again it may be seen, as in the case of solid aerosols, that the numerical penetration gives much

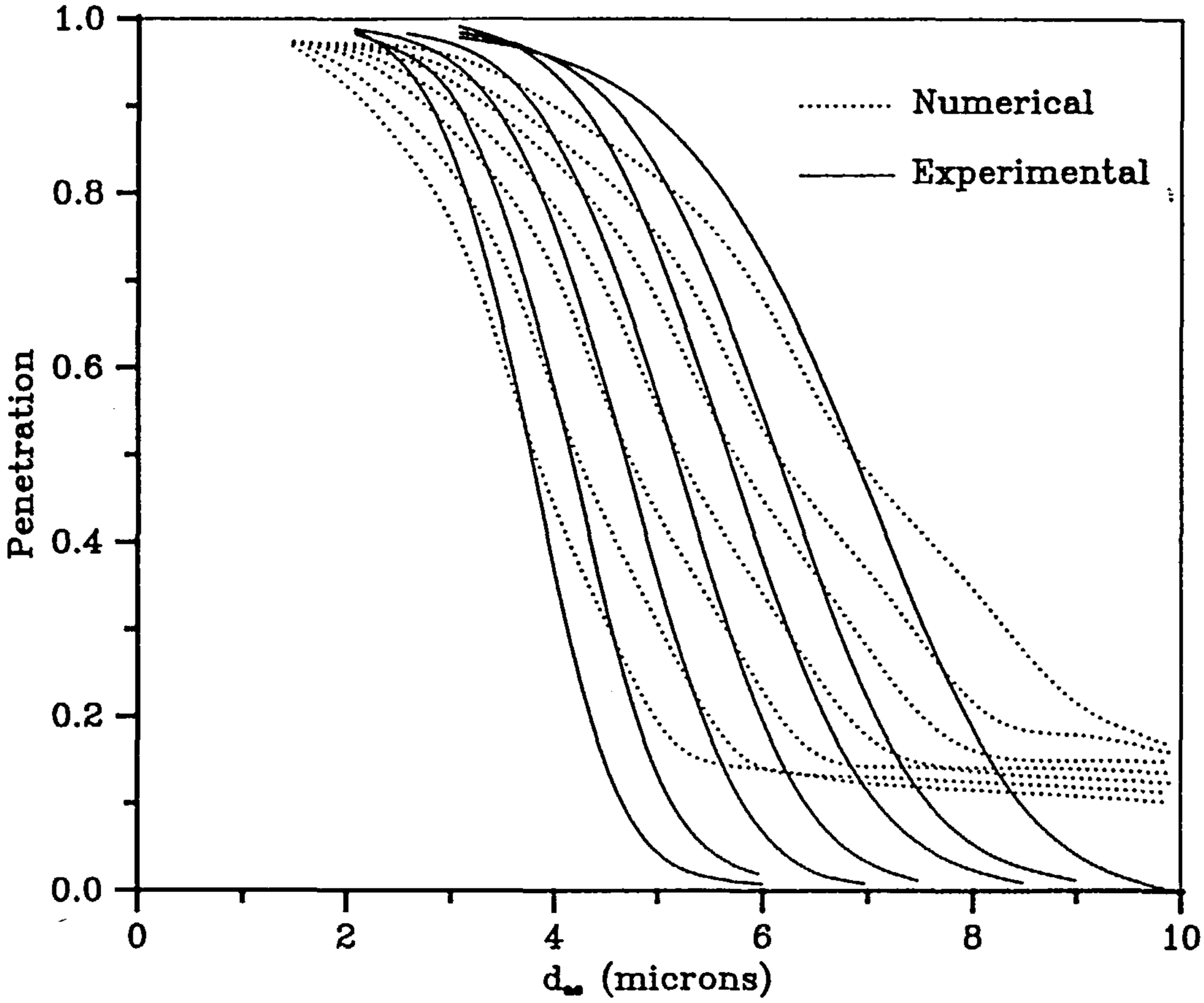

Fig.9.3 Penetration curves obtained from the numerical technique with $R_{ns}=0.9R_u/R_c$ and with a leakage obtained by the method shown in section 8.5 for different flow rates and from experimental data of Kenny *et al.* (1987). The flow rates for the penetration curves (from right to left) are 1.3, 1.5,..., 2.5 lpm respectively.

better agreement with the corresponding experiments (Kenny *et al.* (1987)).

Kenny *et al.* (1987) have also studied the penetration curve at the same flow rate for different versions of the Casella cyclone and argued that the difference between the penetration curves of the cyclone with 1 inlet hole and that with 4 inlet holes was not

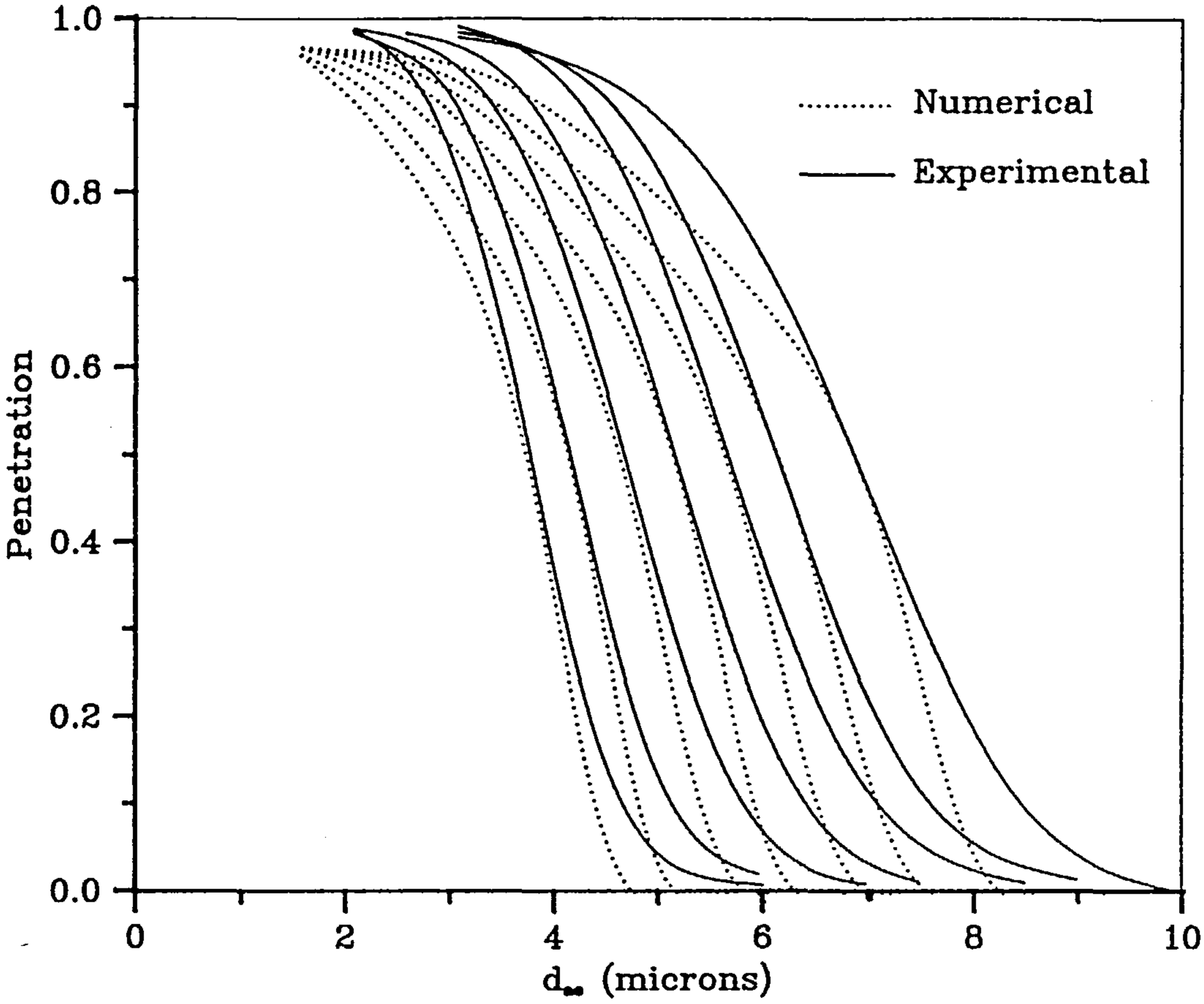

Fig.9.4 Penetration curves obtained from the numerical technique with $R_{ns}=1.1R_u/R_c$ and with a zero leakage for different flow rates and from experimental data of Kenny *et al.* (1987). The flow rates for the penetration curves (from right to left) are 1.3, 1.5,..., 2.5 lpm respectively.

significant. So at this stage we may confirm that a symmetrical inviscid flow model within the cyclone may be considered a valid assumption for a small gas cyclone, i.e the techniques used in the last 3 chapters can be used for small gas cyclones but the value of R_{ns} should be $1.1R_u/R_u$ and a zero leakage must be assumed.

The inviscid flow model used in this thesis was based on the

assumption that the Reynolds number at the inlet of the cyclone is sufficiently large that the spin velocity in the cyclone may be assumed to have the form

$$wR = \text{constant} + \varepsilon \qquad (9.3.2)$$

where ε is a very small positive quantity. For small cyclones the values of the Reynolds number may not be sufficiently large to assume that the flow may be treated as inviscid and some adjustments due to the viscosity of the fluid may be required. It is well known (Bloor and Ingham (1987)), that if the viscosity is included in the azimuthal direction, the spin velocity is governed by an ODE whose solution is such that near R=0 the spin velocity is zero.

For large values of the Reynolds number the solution of the ODE is in good agreement with expression (9.3.2) for most values of R (except those very near R=0) whilst for small values of the Reynolds number the agreement between the numerical solution and expression (9.3.2) is only good away from R=0. This phenomenon is shown schematically in **Fig.9.5** and it is probable that this is the reason why we need to take a larger value of R_{ns} for the small cyclones than that required for the larger cyclones studied earlier in this thesis.

It should be noted that the numerical model used here requires all the dimensions of the cyclone and the operating conditions. Due to the lack of information about all the dimensions of the cyclones used in many of the experimental investigations we can not, at the moment, compare our mathematical model with any other experimental data.

It is also of interest to note that the results obtained

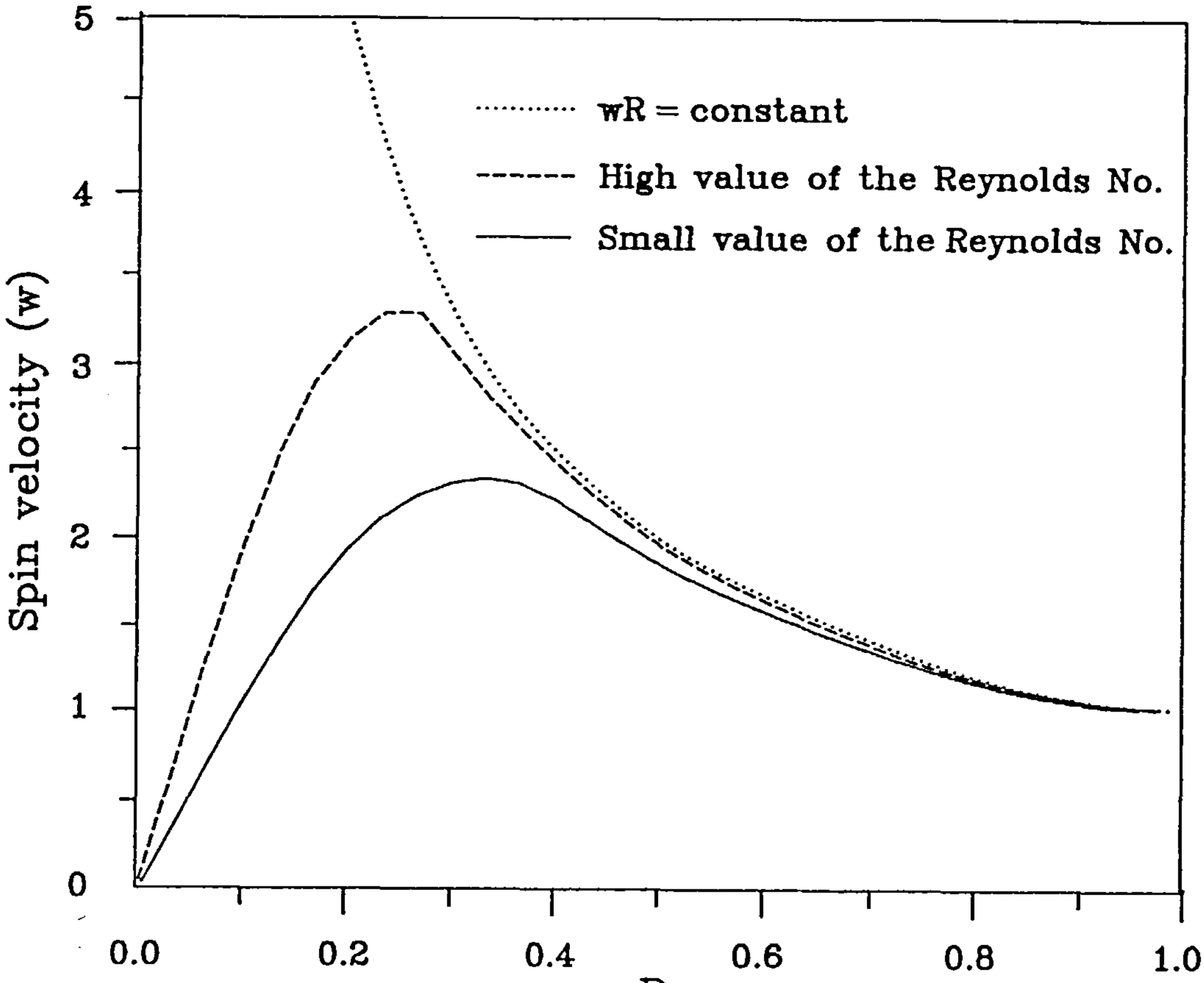

Fig.9.5 The spin velocity in a cyclone for different values of the Reynolds number (schematic).

experimentally for different kinds of aerosols (physical properties such as shape, solid or liquid) are usually different, see for example Kenny *et al.* (1987), where a value of d_{50} for the liquid aerosol was 5.2μ whilst a value 4.8μ was obtained for the solid aerosol for the same cyclone and the same operating conditions. The numerical method used here disregards the difference in the physical properties of the particles and only requires the diameter and density of the particle. In order to study these differences further investigation on the interaction between the fluid and the particle will be required.

9.4 Conclusions

The mathematical model and numerical techniques used in the last 3 chapters have again been employed in order to investigate the separation efficiency of small gas cyclones whose diameters are, typically, about 10mm. The numerical results show a reasonable agreement with those obtained experimentally.

It is found that in order to use the model and numerical methods for small gas cyclones, the cut-off region which we introduced in chapter 8 needs to be larger than when the diameters of the cyclones were greater than 10mm. Due to the absence of the full dimensions in the experimental work, we are unable to compare the present model with any other experimental data. However, the results we have obtained for the small gas cyclone suggest that the cut-off region should be about $1.1R_u/R_c$ rather than $0.7R_u/R_c$ as used for the larger cyclones.

CHAPTER 10 CONCLUSIONS

10.1 Oscillatory Flows

In the first part of this study, the two-dimensional, incompressible viscous fluid flow induced by oscillating cascades of cylinders with different cross-sectional shapes have been studied. All problems involve solving numerically the Navier-Stokes equations in terms of the streamfunction and vorticity. Most of the numerical solutions have been obtained using a second-order-accurate finite-difference scheme which is based on a modified procedure to preserve accuracy and iterative convergence at large values of the Reynolds number. The main difficulties encountered in obtaining accurate numerical solutions are, (i) the presence of the singularity in vorticity near the sharp corners of the body; (ii) the satisfactory treatment of the boundary conditions at large distances from the bodies, and (iii) the development of efficient numerical techniques which are suitable for the different geometries of the cascade. To overcome the first difficulty the appropriate forms of the analytical solution in the vicinity of the singularity have been derived and some constants involved in the analytical solutions have been determined using the information in the vicinity of the singularity. In order to satisfactorily deal with the boundary conditions at large distances from the cascade appropriate asymptotic solutions which are valid at large distances from the cascade have been developed and put into an easily usable form for

numerical calculations. In order to overcome the third difficulty, transformations have first been introduced in order to ensure that there are more mesh points near to the cascade, where the flow changes dramatically, than at large distances from it. Then a second-order-accurate finite-difference scheme, which is based on a modified procedure to preserve accuracy and iterative convergence at large values of the Reynolds number, and which is suitable for a wide range of two-dimensional incompressible, viscous, unsteady flow problems has been developed. Using this numerical scheme accurate results have been obtained to a variety of problems and they show good agreement with those obtained in some related experimental investigations. Further, for moderate values of the frequency Reynolds number, R_b, a series truncation and a numerical technique have been used to investigate the cascade flow (chapter 3) and the results from these two methods show good agreement.

By using a conformal mapping technique and the Boundary Element Method the secondary flows induced by cascades of square and circular cylinders have been investigated for $R_s \geq O(1)$ in chapters 4 and 5, respectively. At higher values of the streaming Reynolds number, the streaming flow induced by the cascade of circular cylinder becomes asymmetrical, and a stability analysis has been derived. The theoretical predictions of when instabilities first appear are in good agreement with some related experimental investigations. The numerical results and stability analysis have not been presented here for the streaming flow induced by an oscillating cascade of bodies with other shapes but, in principle, the numerical methods derived in this chapter may be applied to these types of cascades.

As the Reynolds number increases, say R_e in chapter 2 or R_s in chapters 4 or 5, then finer mesh sizes are clearly required in order to obtain accurate solutions. However, the computer time is too expensive to obtain convergent and accurate solutions for large values of the Reynolds number if the present methods are used. So, clearly, improvements that could be made to the present work in the future is the introduction of more efficient solvers, such as the multi-grid technique, when solving the present problems at large values of the Reynolds number.

Another possible extension of the present work is to investigate the stability of the steady cascade flow, as in the case investigated by Ingham *et al.* (1990a), and the unsteady cascade flow, as studied in chapter 2. It is postulated that the stability analysis presented in chapter 5 for the streaming cascade flow can be used in these two cases without encountering many difficulties.

So far most of the theoretical investigations on the fluid flow induced by harmonically oscillating bodies are based on perturbation and/or boundary-layer techniques. In most cases the perturbation parameter chosen is ε, which is assumed to be very small, and then attention is directed as to how the flow changes with another independent parameter, say R_b, when ε is very small. However, the experimental results of Tutsuno (1974) showed for a given value of R_b that there are large changes in the flow structure as ε increases from being very small to a small finite value. In order to investigate how the flow changes with ε when R_b is very large it may be interesting to use the quantity $1/R_b$, in which R_b is assumed to be very large, as the perturbation parameter and study how the structure of the flow changes as a function of ε.

10.2 Industrial Cyclones

In the second part of this thesis systematic investigations on the fluid flow in the cyclone and the separation efficiency of the cyclone have been performed. In particular,

(i) An accurate numerical model for the simulation of the flow in the cyclone at very high values of the Reynolds number has been presented. It has been found that the functional form of the angular momentum given to the fluid at the entry to the cyclone is described well in this model since any small perturbation in its value produces only a small change in the predicted separation efficiency. The theoretical efficiency curves based on the flow model have been given which also compare well with those which have been obtained experimentally.

(ii) The effects of changing the various parameters that occur in the problem on the separation efficiency of the cyclone have been investigated. The most important factors which affect the fluid flow and the separation efficiency of the cyclone have been identified. This provides us with a basic understanding of how the geometry of the cyclone affects the separation efficiency and therefore gives a clear guide as to how the cyclone should be designed.

(iii) Using a regression analysis correlations of the value of d_{50} and the loss factor for the the cyclone are obtained and again these results show reasonable agreement with the experimental data. Unlike some previously published formulae which characterize the cyclone performance the formula developed here contain no constants which need to be preassigned and hence it may be used with confidence to predict d_{50} given the geometry of the cyclone and the operating conditions.

(iv) The differences in the performance between large industrial and small personal cyclones (typically 10mm in diameter) have been identified.

In this thesis the spin velocity in the main body of the cyclone has been assumed to be a free vortex flow, i.e wR=constant, and this assumption has been shown to be in reasonable agreement with most of the available experimental data. However, this agreement becomes worse as R tends to zero since the viscous effects near the axis of the cyclone become more important and eventually dominate the flow. Thus it is not appropriate to use the free vortex flow for the spin velocity in the vicinity of R=0 in order to calculate the separation efficiency of the cyclone. In order to overcome this difficulty a value of $R=R_{ns}$ was assumed such that no separation occurs in the region $0\leq R\leq R_{ns}$, the quantity R_{ns} is actually unknown and its value must be obtained empirically. In reality separation does occur to some extent in the region $0<R<R_{ns}$ and therefore a better model is required for determining the spin velocity near the axis of the cyclone. This model should take into account the effects of viscosity near the axis on the cyclone in a manner similar to that described by Bloor and Ingham (1983). The spin velocity as determined by Bloor and Ingham (1983) has been shown to be in good agreement with some related experimental data even in the region near to the axis and hence could be used. The estimation of the vorticity in the recirculation region in the upper part of the cyclone can then be performed in a similar way to that as described in chapter 6 since the flow can still be treated as inviscid in the region of flow not close to the axis of the cyclone and hence the theory of Batchelor (1956) is still valid.

Alternatively, an improvement in the prediction of the spin velocity can be achieved by using an inviscid model, as shown in this thesis, in the main body of the cyclone, and a viscous model, as developed by Ferguson (1989), in the vicinity of R=0, and then matching these two solutions. Clearly the model of Bloor and Ingham (1983) will be easier to apply than the alternative model described above but the alternative model has the advantage that the viscous effects can be taken into account in both the spin and the cross-plane velocity components. Hence an improvement in the agreement between the theoretical and experimental results for the cross-plane velocities, u and v, will also be achieved.

In the mathematical model used in this thesis the three-dimensional flow at the entry to the cyclone is modelled by a two-dimensional axisymmetric flow, and the distribution of the velocity in the cyclone depends critically on this entry condition. The distribution of the velocity in the main body of the cyclone from this model has been shown to be in good agreement with some related experimental data. However, in practice the flow near the entry to, or more precisely in the upper part (in the cylindrical portion, say) of the cyclone is three-dimensional, especially for those small cyclones which operate with low flow rates. Hence a full three-dimensional investigation is needed in order to model the flow in this part of the cyclone (but not including the flow in the overflow pipe) more accurately. As indicated by some experimental data the flow in the lower part and in the region of the overflow pipe of the cyclone is almost axisymmetric. Hence the axisymmetric model used in this thesis, or alternatively that developed by Bloor and Ingham (1983), can be used to model the flow in this region of

the cyclone. The solutions in these two region must then be matched. The three-dimensional investigation would require a large amount of computer storage and time and hence an adaptive mesh algorithm together with a multi-grid technique would be essential if accurate solutions are to be found. This adaptive algorithm could allow a fine mesh to be used in regions of the flow where high gradients occur, such as near to the entry to the cyclone, and relatively coarse mesh in regions of the flow where small gradients occur, such as far from the walls of the cyclone. The size of the mesh can be determined by estimating the gradients of the velocity of the flow in different directions. Special care is needed in the entry region of the cyclone since the flow in this region is very complicated and therefore the treatment of the boundary conditions here requires special attention. Energy losses due to the sudden expansion of the flow in the entry of the cyclone need to be estimated and some information about the flow even in the inlet pipe near to the entry is also required since the vorticity in the entry to the cyclone must be determined.

REFERENCES:

Andres, J.M. and Ingard, U., 1953a, Acoustic Streaming at High Reynolds Number, *J. Acous. Soc. Amer.*, **25**, 928-931.

Andres, J.M. and Ingard, U., 1953b, Acoustic Streaming at Low Reynolds Number, *J. Acous. Soc. Amer.*, **25**, 932-938.

Andrade, E.N.Da.C., 1931, On the Circulations Caused by the Vibration of Air in a Tube, *Proc. Roy. Soc.*, **A134**, 445-470.

Amin, Norsarahaida, 1988, Low-frequency Oscillation of a Cylinder in a Viscous Fluid, *Quart. J. Mech. & Appl. Maths.*, **41**, 195-201.

Badr, H., Dennis, S.C.R., Bates, S. and Smith, F.T., 1985, Numerical and Asymptotic Solutions for Merging Flow Through a Channel with an Upstream Splitter Plate, *J. Fluid Mech.*, **156**, 63-81.

Bartley, D.L. and Breuer, G.M., 1982, Analysis and Optimization of the 10mm Cyclone, *Amer. Ind. Hyg. Assoc.*, **43**, 520-528.

Batchelor, G.K., 1956, On Steady Laminar Flow with Closed Streamlines at Large Reynolds Number, *J. Fluid Mech.*, **1**, 177-190.

Batchelor, G.K., 1967, *An Introduction to Fluid Dynamics,* Cambridge University Press.

Bertelsen, A., Svardal, A. & Tjotta, S., 1973, Nonlinear Streaming Effects Associated with Oscillating Cylinders, *J. Fluid Mech.*, 59, 493-511.

Bertelsen, A.F., 1974, An Experimental Investigations of High

Reynolds Number Steady Streaming Generated by Oscillating Cylinders, *J. Fluid Mech.*, **64**, 589-597.

Betchov, R. and Criminale, W.O., *Stability of Parallel Flows*, 1967, Academic Press, New York, London.

Bittleston, S.H., 1986, *Flows Pass Arrays of Cylinders*, Ph.D Thesis, Bristol University.

Blachman, M.W. and Lippmann, M., 1974, Performance Characteristics of the Multicyclone Aerosol Samplers, *Amer. Ind. Hyg. Assoc. J.*, **35**, 311-316.

Bloor, M.I.G. and Ingham, D.B., 1973a, Theoretical Investigation of the Flow in a Conical Hydrocyclone, *Trans. Instn. Chem. Engrs.* **51**, 36-41.

Bloor, M.I.G. and Ingham, D.B., 1973b, On the Efficiency of the Industrial Cyclone, *Trans. Instn. Chem. Engrs.* **51**, 173-176.

Bloor, M.I.G. and Ingham, D.B., 1974, The Theoretical Analysis of the Conical Cyclone, *Proc. 1st European Conf. on Mixing & Contrifugal Separation,* E6-95-E6-106, Cambridge, England.

Bloor, M.I.G. and Ingham, D.B., 1975, Turbulent Spin in a Cyclone, *Trans. Instn. Chem. Engrs.* **53**, 1-6.

Bloor, M.I.G. and Ingham, D.B., 1976, Boundary Layer Flows on the Side Walls of Conical Cyclones, *Trans. Instn. Chem. Engrs.* **54**, 276-280.

Bloor, M.I.G., Ingham, D.B. and Laverack, S.D., 1980, An Analysis of Boundary Layer Effects in a Hydrocyclone, *Proc. 1st Inter. Conf. on Hydrocyclones*, 49-62, 1-3 October, Cambridge, England.

Bloor, M.I.G. and Ingham, D.B., 1983, Progress in Filtration and Separation 3, Edited by R.J. Wakeman, 57-148, Elsevier.

Bloor, M.I.G. and Ingham, D.B., 1987, The Flow in Industrial

Cyclones, *J. Fluid Mech.*, **178**, 507-519.

Boysan, F., Ayers, W.H. and Swithenbank, J., 1982, A Fundamental Mathematical Modelling Approach to Cyclone Design, *Trans. Instn. Chem. Engrs.*, **60**, 222-230.

Bradley, D., 1958, *Ind. Chemists & Chem. Manufacturer*, pp.473.

Bradley, D., 1965, *The Hydrocyclone*, 1st Ed., Pergammon, Oxford. (a) 14-16.

Bradley, D. and Pulling, D.J., 1959, Flow Patterns in the Hydraulic Cyclone and Their Interpretation in Terms of Performance, *Trans. Instn. Chem. engrs.*, **37**, 34-45.

Bramley, J.S. and Dennis, S.C.R., 1984, The Numerical Solution of 2-dimensional Flow in a Branching Channel, *Computers & Fluids*, **12**, 339-355.

Carrière, Z., 1929, Analyse Ultramicroscopique Des Vibrations Aériennes, *J. Phys. Radium*, **10**, 198-208.

Dahlstrom, D.A., 1949 Cyclone Operating Factors and Capacities on Coal and Refuse Slurries, *A.I.M.A., Mining Trans.*, **184**, 331-343.

Davidson, B.J., and Riley, N., 1972, Jets Induced by Oscillatory Motion, *J. Fluid Mech.*, **53**, 287-303.

Dennis, S.C.R. and Hudson, J.D., 1978, A Difference Method for Solving the Navier-Stokes Equations, *Proc. 1st Conf. Num. Methods Laminar & Turbulent Flow*, 69-80, Swansea (July 1978): Pineridge Press.

Dennis, S.C.R. and Smith, F.T., 1980, Steady Flow Through a Channel with a Symmetrical Constriction in the Form of a Step, *Proc. Roy. Soc. Lond.*, **A372**, 393-414.

Duck, P.W. and Smith, F.T., 1979, Steady Streaming Induced Between

Oscillating Cylinders, *J. Fluid Mech.*, **91**, 93-110.

Dvorak, V., 1874, Ueber die Entstehungsweiseder Kundt's chen Staubfiguren, *Ann. der Phys. & Chemie*, **31**, 634-638.

Faraday, M., 1831, On a Peculiar Class of Acoustical Figures and on Certain Forms Assumed by Groups of Particles upon Vibrating Elastic Surfaces, *Phil. Trans.*, **121**, 299-340.

Fearn, R.M., Mullin, T. & Cliffe, K.A., 1990, Nonlinear Flow Phenomena in a Symmetrical Sudden Expansion, *J. Fluid Mech.*, **211**, 595-608.

Ferguson, J.W.J., 1989, Swirling Flows in Conical Vessels, Ph.D Thesis, Leeds University, England.

Fontein, F.J. and Dijksman, C., 1953, The Hydrocyclone, its Application and its Explanation, *Proc. of the Symp. on Recent Developments in Mineral Dressing, Instn. Min. & Metall.*, London, 229-246.

Fontein, F.J., Van Kooy, J. & Leniger, H.A., 1962, The Influence of Some Variables upon Hydrocyclone Performance, *Brit. Chem. Engrs.*, **7**, 410-421.

Gary, J. and Helgason, R., 1970, A Matrix Method for Ordinary Differential Eigenvalue Problems, *J. Comp. Phys.*, **5**, 169-187.

Gordon, D., 1978, Numerical Calculations on Viscous Flow Fields Through Cylinder Arrays, *Computer & Fluids*, **6**, 1-13.

Haddon, E.W. & Riley, N., 1979, The Steady Streaming Induced Between Oscillating Circular Cylinders, *Quart. J. Mech. Appl. Maths.*, **32**, 265-282.

Hayes, J.G. and Halliday, J., 1974, The Least-squares Fitting of Cubic Spline Surfaces to General Data Sets, *J. Instn. Maths. Applics*, **14**, 89-103.

Held, J.T. and Cooper, D.W., 1979, Theoretical Investigation of the Effects of Relative Humidity on Aerosol Respirable Fraction, *Atmospheric Environ.*, 13, 1419-1425.

Higgins, R.I. and Dewell, P., 1967, A Gravimetric Size-selecting Personal Dust Sampler, *Inhaled Particles & Vapours II* (Edited by C.N. Davies), 576-586, Pergamon Press, Oxford.

Holtsmark, J., Johnsen, I., Sikkeland, T. and Skavlem, S., 1954, Boundary Layer Flow Near A Cylindrical Obstacle in an Oscillating Incompressible Fluid, *J. Acous. Soc. Amer.*, 26, 26-39.

Ingham, D.B., Tang, T. and Morton, B.R., 1990a, Steady Two-dimensional Flow through a Row of Normal Flat Plates, *J. Fluid Mech.*, 210, 281-303.

Ingham, D.B., Yan, B. and Morton, B.R., 1990b, The Fluid Flow Induced by Large Amplitude Oscillations of a Cascade, Accepted for Publication in *Computer & Fluids*.

Ingham, D.B. and Yan, B., 1989, The Fluid Flow Induced by an Oscillating Cascade, *Proc. 6st Conf. Num. Methods Laminar & Turbulent Flow*, 723-733, Swansea (July 1989): Pineridge Press.

Ingham, D.B. and Yan, B., 1991, Fluid Flow Induced by a Small Amplitude Harmonically Oscillating Cascade, Accepted for Publication in *Acta Mechanica*.

Irani, M.B., 1982, *Finite Element Analysis of Viscous Flow & Rigid Body Interaction*, Masters Thesis, Univ. of British Columbia.

John, P., 1984, *Plane-Sudden Expansion Flows & Their Stability*, Ph.D Thesis, Imperial College, London, England.

Kelsall, D.F., 1952, A Study of the Motion of Solid Particles in a Hydraulic Cyclone, *Trans. Instn. Chem. Engrs.*, 30, 87-108.

Kenny, L.C., Berry, R.D. and Lidèn, G., 1987, Experimental Techniques for the Measurement of Cyclone Penetration Curves, Section Paper of *Health & Safety Executive Research & Laboratory Services Division.*

Kim, J.C. and Lee, K.W., 1990, Experimental Study of Particle Collection by Small Cyclones, *Aerosol Sci. & Technol.*, 13.

Kim, S.K. and Troesch, A.W., 1989, Streaming Flows Generated by High-Frequency Small-amplitude Oscillations of Arbitrarily Shaped Cylinders, *Phys. Fluids*, A1, 975-985.

Knowles, S.R., Woods, D.R. and Feuerstein, I.A., 1973, The Velocity Distribution within a Hydrocyclone Operating without an Air Core, *The Canadian Journal of Chem. Engrs.*, 51, 263-271.

Lane, C.A., 1955, Acoustical Streaming in the Vicinity of a Sphere, *J. Acous. Soc. Amer.*, 27, 1028-1086.

Laverack, S.D., 1980a, The Effect of Particle Concentration on the Boundary Layer Flow in a Hydrocyclone, *Trans. Instn. Chem. Engrs.* 58, 33-42.

Laverack, S.D., 1980b, *The Effect of Solids on the Boundary Layer in a Hydrocyclone*, Ph.D Thesis, University of Leeds, Leeds, England.

Lidèn, G. and Kenny, L.C., Comparison of Respirable Dust Sampler Penetration Curves with Sampling Conventions, private communication to T.L. Ogden (1990).

Lugt, H.J. and Schwiderski, E.W., 1964, Flows Around Dihedral Angles, *Proc. Roy. Soc.*, A285, 382-412.

Maguire, B.A., Barker, D. and Wake, D., 1973, Size Selection Characteristics of the Cyclone Used in the Simpeds 70 Mk 2 Gravimetric Dust Sampler, *Staub.*, 33, 95-99.

Manzoor, M., 1984, *Heat Flow Through Extended Surface Heat Exchangers*, Lecture Notes in Engineering 5, Springer-Verlag.

Moffatt, K.H., 1964, Viscous and Resistive Eddies near a Sharp Corner, *J. Fluid Mech.*, **18**, 1-18.

Morton, B.R. and Ingham, D.B., 1991, Private Communication.

Motz, H., 1946, The Treatment of Singularities of Partial Differential Equations by Relaxation Methods, *Quart. Appl. Maths.*, **4**, 371-377.

Ogden, T.L., Barker, D. and Clayton, M.P., 1983, Flow Dependence of the Casella Respirable-dust Cyclone, *Ann. Occup. Hyg.*, **27**, 261-271.

Ohsai, H. and Maeda, S., 1958, Motion of Water in a Hydraulic Cyclone, *Chem. Engrs.* (in Japanese), 22, 200-207.

Osborne, M.R., 1967, Numerical Methods for Hydrodynamic Stability Problems, *SIAM J. Appl. Maths.*, **15**, 539-557.

Pattani, P.G. & Olson, M.D., 1987, Periodic Solutions on Rigid Body-Viscous Flow Interaction, *Inter. J. Num. Methods in Fluids*, 7, 653-695.

Pattani, P.G. & Olson, M.D., 1988, Force on Oscillating Bodies in Viscous Fluids, *Inter. J. Num. Methods in Fluids*, 8, 519-536.

Rancey, W.P., Corelli, J.C. & Westervelt, P.J., 1954, Acoustical Streaming in the Vicinity of a Cylinder, *J. Acous. Soc. Amer.*, **26**, 1006-1014.

Rayleigh, Lord, 1883, On the Circulations of Air Observed in Kundt's Tubes and on Some Allied Acoustical Problems, *Phil. Trans.*, **A175**, 1-21.

Rietema, K., 1961, Performance and Design of Hydrocyclones-I General Consideration, *Chem. Engrs. Sci.*, **15**, 298-302, 1961.

Riley, N., 1965, Oscillating Viscous Flows, *Mathematika*, 12, 161-175.

Riley, N., 1967, Oscillatory Viscous Flows, Review & Extension, *J. Instn. Maths. Applics.*, 3, 419-434.

Riley, N., 1975, The Steady Streaming Induced by a Vibrating Cylinder, *J. Fluid Mech.*, 68, 801-812.

Riley, N., 1981, High Reynolds Number Flow with Closed Streamlines, *J. Engrs. Maths.*, **15**, 15-27.

Rott, N., 1964, *Laminar Flow Theory*, Section D, Chapter 2, Princeton.

Saltzman, B.E., 1984, Generalized Performance Characteristics of Miniature Cyclones for Atmospheric Particulate Sampling, *Amer. Ind. Assoc. J*, **45**, 671-680.

Saltzman, B.E. and Hochstrasser, J.M., 1983, Design and Performance of Miniature Cyclones for Respirable Aerosol Sampling, *Environ. Sci. & Technol.*, **17**, 418-424.

Schlichting, H., 1932, Berechnung Ebener Periodischer Grenzschichtströmungen, *Physikalische Zeit*, 33, 327-335.

Segel, L.A., 1961, Application of Conformal Mapping to Viscous Flow Between Moving Circular Cylinders, *Quart. Appl. Maths.*, **18**, 335-353.

Smith, F.T., 1985, On Large-scale Eddy Closure, *J. Maths. & Phys. Sci.*, **19**, 1-80.

Smith, W.B., Wilson, R.R. and Harris, D.B., 1979, A Five-stage Cyclone System for in Situ Sampling, *Environ. Sci. & Technol.*, **13**, 1387-1392.

Sobey, I.J. & Drazin, P.G., 1986, Bifurcations of Two-dimensional Channel Flows, *J. Fluid Mech.*, **171**, 263-287.

Stairmand, C.J., 1951, The Design and Performance of Cyclone Separators, *Trans. Instn. Chem. Engrs.*, 29, 356-372.

Stuart, J.T., 1963, Unsteady Boundary Layer. In: *Laminar Boundary Layers*, Oxford University Press, London.

Stuart, J.T., 1966, Double Boundary Layers in Oscillating Viscous Flows, *J. Fluid Mech.*, 24, 673-687.

Svarovsky, L., 1984, *Hydrocyclones*, Holt, Rinehart and Winston, London, England.

Tabakova, S.S. and Zapryanov, Z.D., 1982, On the Hydrodynamic Interaction of Two Spheres Oscillating in a Viscous Fluid -I. Axisymmetrical Case, *J. Appl. Maths. & Phys.* [ZAMP]., 33, 344-357.

Tamada, K. and Miyagi, T., 1974, Secondary Flow Around an Oscillating Cylinder, *J. Phys. Soc. Japan*, 37, 249-253.

Tartan, G., 1962, Discussion of Paper by Lilge, *Trans. Instn. Min. & Metall*, 71, 539-546.

Tatsuno, M., 1973, Circulatory Streaming Around an Oscillating Circular Cylinder at Low Reynolds Numbers, *J. Phys. Soc. Japan*, 35, 915-920.

Tatsuno, M., 1974, Circulatory Streaming in the Vicinity of an Oscillating Square Cylinder, *J. Phys. Soc. Japan*, 36, 1185-1191.

Tatsuno, M., 1980, Secondary Flows Around Oscillating Asymmetrical Cylinders, *Reports of Research Institute for Appl. Mech.*, 28, No.89, 35-47.

Tatsuno, M. and Bearman, P.W., 1990, A Visual Study of the Flow Around an Oscillating Circular Cylinder at Low Keulegan-Carpenter Numbers & Low Stokes Numbers, *J. Fluid*

Mech., 221, 157-182.

Tetionis, D.P., 1981, *Unsteady Viscous Flows*, Springer-Verlag, New York.

ter Linden, A.J., 1949, Investigations into Cyclone Dust Collectors, *Proc. Instn. Mech. Engrs.*, 160, 233-240.

Thomes, L.H., 1953, The Stability of Plane Poiseuille Flow, *Phys. Review*, 91, 780-783.

Thompson, J.F., Thames, F.C. and Mastin, C.W., 1974, Automatic Numerical Grid Generation of Body Fitted Curvilinear Coordinate System For Field Containing Any Number of Arbitrary Two Dimensional Bodies, *J. Comp. Phys.*, 15, 299-319.

Vaughan, N.P., 1988, Construction and Testing of an Axial Flow Cyclone Preseparators, *J. Aerosol Sci.*, 19, 295-305.

Vincent, J.H., 1989, *Aerosol Sampling,* 29-30, John Wiley & Sons, Chichester.

Wang, C.Y., 1968, On High Frequency Oscillatory Viscous Flows, *J. Fluid Mech.*, 32, 55-68.

Wen, X., Bloor, M.I.G., Ferguson, J.W.J. and Ingham, D.B., 1990, A Numerical Study of The Fluid and Particle Collection in Cyclones, *Proc. 4th Ann. Conf. Aerosol Soc.*, 53-58, University of Surrey, April 1990.

Williamson, C.H.K., 1985, Sinusoidal Flow Relative to Circular Cylinders, *J. Fluid Mech.*, 155, 141-174.

Wilson, S., 1969, The Development of Poiseuille Flow, *J. Fluid Mech.*, 38, 793-806.

Woods, L.C., 1954, A Note on the Numerical Solution of Fourth Order Differential Equations, *Aero. Quart.*, 5, 176-184.

Yan, B., Bloor, M.I.G., Ferguson, J.W.J. and Ingham, D.B., 1990, A

Numerical Investigation into the Fluid Dynamics in a Cyclone, *Proc. 4th Ann. Conf. of the Aerosol Soc.*, University of Surry, April 1990, U.K.

Yan, B. and Ingham, D.B., 1991, Streaming Flow Induced by an Oscillating Cascade of Circular Cylinders, *Proc. 7st Conf. Num. Methods Laminar & Turbulent Flow*, 1407-1417, Stanford (July 1991), U.S.A.

Yan, B., Ingham, D.B. and Morton, B.R., 1991, Streaming Flow Induced by an Oscillating Cascade of Cylinders, Submitted to *J. Fluid Mech.*

Zapryanov, Z., Kozhoukharova, Zh. and Iordanova, A., 1988, On the Hydrodynamic Interaction of Two Circular Cylinders Oscillating in a Viscous Fluid, *J. Appl. Maths.* & *Phys.* (ZAMP), 39, 204-220.